UNIVERSITÉ DE STRASBOURG

Université Nationale Taras Shevchenko de Kiev

ÉCOLE DOCTORALE DE PHYSIQUE ET CHIMIE-PHYSIQUE

Institut Charles Sadron

THÈSE présentée par :

Viktoriia MEKLESH

soutenue le : **20 septembre 2017**

pour obtenir le grade de : **Docteur de l'université de Strasbourg**

Discipline/ Spécialité : Physique

EFFECT OF CONFINED POLYMER ON THE PROPERTIES OF LYOTROPIC LAMELLAR MESOPHASES

THÈSE dirigée par :

M. KÉKICHEFF Patrick	Directeur de Recherches, Institut Charles Sadron
M. BULAVIN Leonid	Professeur, Université Nationale Taras Shevchenko de Kiev

RAPPORTEURS :

Mme FRAGNETO Giovanna	Chaire Grands Instruments Européens Université Grenoble Alpes
M. FREYSSINGEAS Eric	Maître de Conférences, École Normale Supérieure de Lyon

---

AUTRES MEMBRES DU JURY :

M. CHARITAT Thierry	Professeur, Université de Strasbourg
Mme BARZOUKAS Marguerite	Professeur, Université de Strasbourg

Résumé

Les mésophases lamellaires lyotropes sont des cristaux liquides à une dimension, constitués d'un mélange eau/tensioactif. Comme le nom l'indique, la matière s'organise en couches avec un empilement alterné de lamelles d'eau séparées par des membranes de tensioactifs. Au cours de cette thèse, un système analogue a été étudié, dans lequel des macromolécules hydrosolubles de polyoxyéthylène (PEO) peuvent être dissoutes dans des mésophases lamellaires lyotropes de tensioactifs de dodécylsulfate de sodium (SDS) mélangés à un co-tensioactif (octanol). La présence des macromolécules modifie les interactions entre membranes et peut aller jusqu'à déstabiliser la phase lamellaire. Le but est de comprendre comment le polymère modifie les interactions entre membranes.

Les phases lamellaires enrichies en polymère sont à la base de nombreuses applications (industrie cosmétique, pharmaceutique, élaboration de pneus, peintures...) mais bien souvent leur emploi se fait de manière empirique et les propriétés particulières qui en découlent ne sont pas toujours bien contrôlées. De plus, confiner ainsi des polymères permet d'obtenir des «galettes» de polymère à deux dimensions, ce qui présente des intérêts pour l'élaboration de nouveaux matériaux légers et résistants.

Le système étudié dans cette thèse a d'abord été étudié par Ficheux et al. [44–46]. Ce travail s'inscrit également dans la lignée directe des travaux menés par Kékicheff et al. [74], Javierre et al. [69, 70] et Herrmann et al. [55–57]. Le diagramme de phase (Figure 1) de ce système révèle l'existence de deux phases lamellaires de périodicités différentes L_α/L_α. Cela signifie que le polymère dissous dans les lamelles d'eau de la structure lamellaire peut la déstabiliser. Sur les limites de la région biphasique de coexistence des deux structures lamellaires, il y a deux points critiques P_{s1} et P_{s2}. Ce type de diagramme de phase permet de suivre la solubilité du polymère dans la phase lamellaire faite de bicouches d'une composition donnée en fonction de l'espacement lamellaire d. La composition du système est definie par deux variables: la fraction massique Φ_m de tensioactif et la fraction

massique C_p (wt. %) de polymère dans l'eau. Tracer d en fonction $1/\Phi_m$ à C_p constant revient à suivre des chemins qualifiés [44] de droites de dilution.

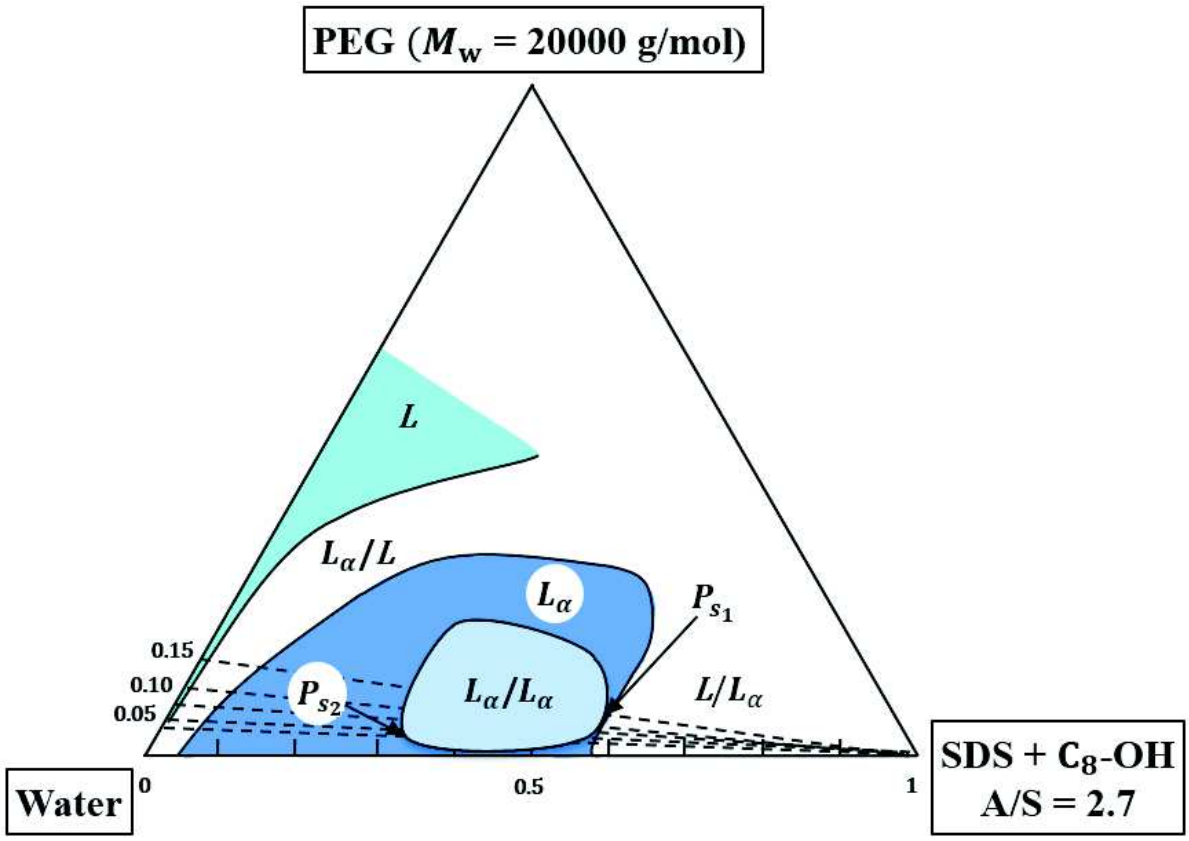

Figure 1: Diagramme de phase pour le système SDS/C_8OH/ H_2O/PEG correspondant au coupe A/S = 2.7 (rapport molaire alcool/tensioactif) et $T = 25°C$ [44]. Les compositions sont données en fractions massiques (wt. %). L désigne une phase isotrope, L_α désigne une phase lamellaire. L_α/L_α désigne le domaine diphasique. P_{s1} et P_{s2} sont deux points critiques.

Les mécanismes conduisant à la coexistence des deux phases lamellaires sont aujourd'hui incompris. La clé pour obtenir des informations sur les propriétés des mésophases lamellaires consiste à comprendre les interactions intermembranaires. Afin d'obtenir une meilleure compréhension du mécanisme de déstabilisation de la structure lamellaire, les modifications des propriétés élastiques des membranes sont étudiées au fur et à mesure que le polymère dissous remplace l'eau des lamelles entre membranes.

Comme pour tout matériau organisé, il est important de mesurer ses propriétés structurales. Ainsi, la périodicité de l'empilement, d, et l'épaisseur des membranes, δ, qui dépendent de la concentration en polymère confiné sont déterminées par diffusion de rayons X aux petits angles (SAXS). La Figure 3 montre la période smectique d de mé-

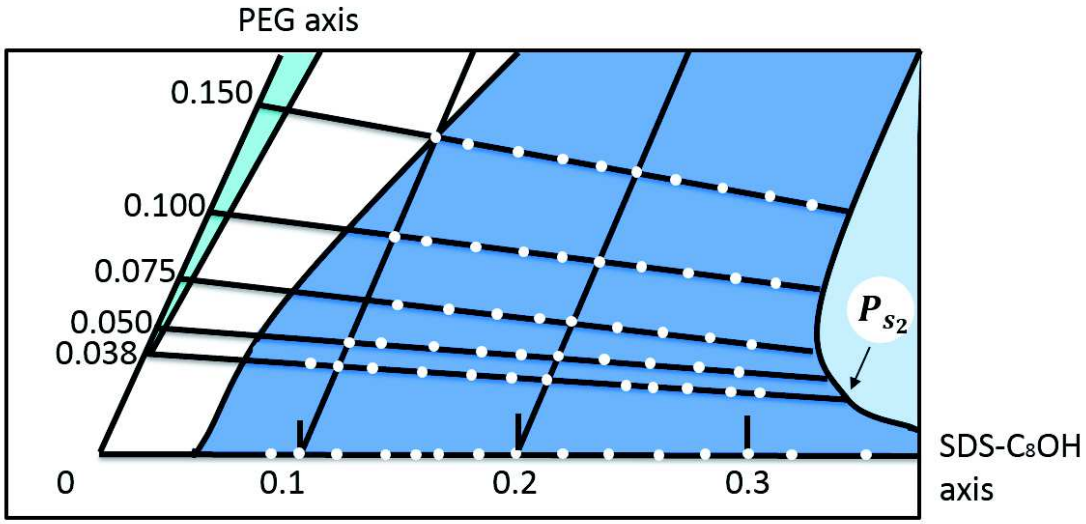

Figure 2: L'encadré du diagramme de phase (Figure 1) représente les échantillons (points blancs) préparés pour étudier l'effet du polymère le long de six lignes de dilution.

sophases lamellaires en fonction de l'inverse de la fraction volumique ϕ_m de membranes à concentrations croissantes de polymère dans les lamelles d'eau: $C_p = 0$; 3.8 ; 5 ; 7.5 ; 10 ; 15 wt. %. Il suit la loi de dilution prévue pour une structure lamellaire $d = \delta/\phi_m$. De la pente, une épaisseur de membrane δ est extraite.

La Figure 4 montre que l'épaisseur de la membrane δ diminue de 2.51 ± 0.05 nm en l'absence de polymère à 2.31 ± 0.02 à $C_p = 15$ wt. %. Cette diminution est susceptible d'être liée à l'adsorption des chaînes macromoléculaires sur les membranes. Certaines chaînes s'intercalent à proximité des têtes polaires du tensioactif/alcool à l'interface des bicouches. Cela peut entraîner une sorte d'étirement des bicouches lamellaires. En conséquence, la membrane devient plus mince. Le même effet a déjà été observé dans [45].

Ainsi, la grande partie de ma thèse a été la mesure du module élastique de courbure des membranes, κ, qui est relié à l'amplitude de leurs ondulations thermiques. Son évolution a été étudiée le long de lignes de dilution du diagramme de phase (Figure 2) par RMN solide du deutérium des molécules perdeutérées d'octanol qui mélangées avec le SDS forment les bicouches de tensioactifs. Le module élastique de courbure des phases lamellaires a été extrait selon le modèle de Auguste et al. [5]. Les couplages quadrupolaires résiduels sont directement liés aux paramètres d'ordre orientationnel des molécules de cotensioactif flexibles dans la phase lamellaire L_α. Contrairement à d'autres méthodes expérimentales, comme la diffraction des rayons X, la ^{2}H RMN donne la valeur du module de courbure

indépendamment de la connaissance du module de compressibilité, et les échantillons ne doivent pas être orientés.

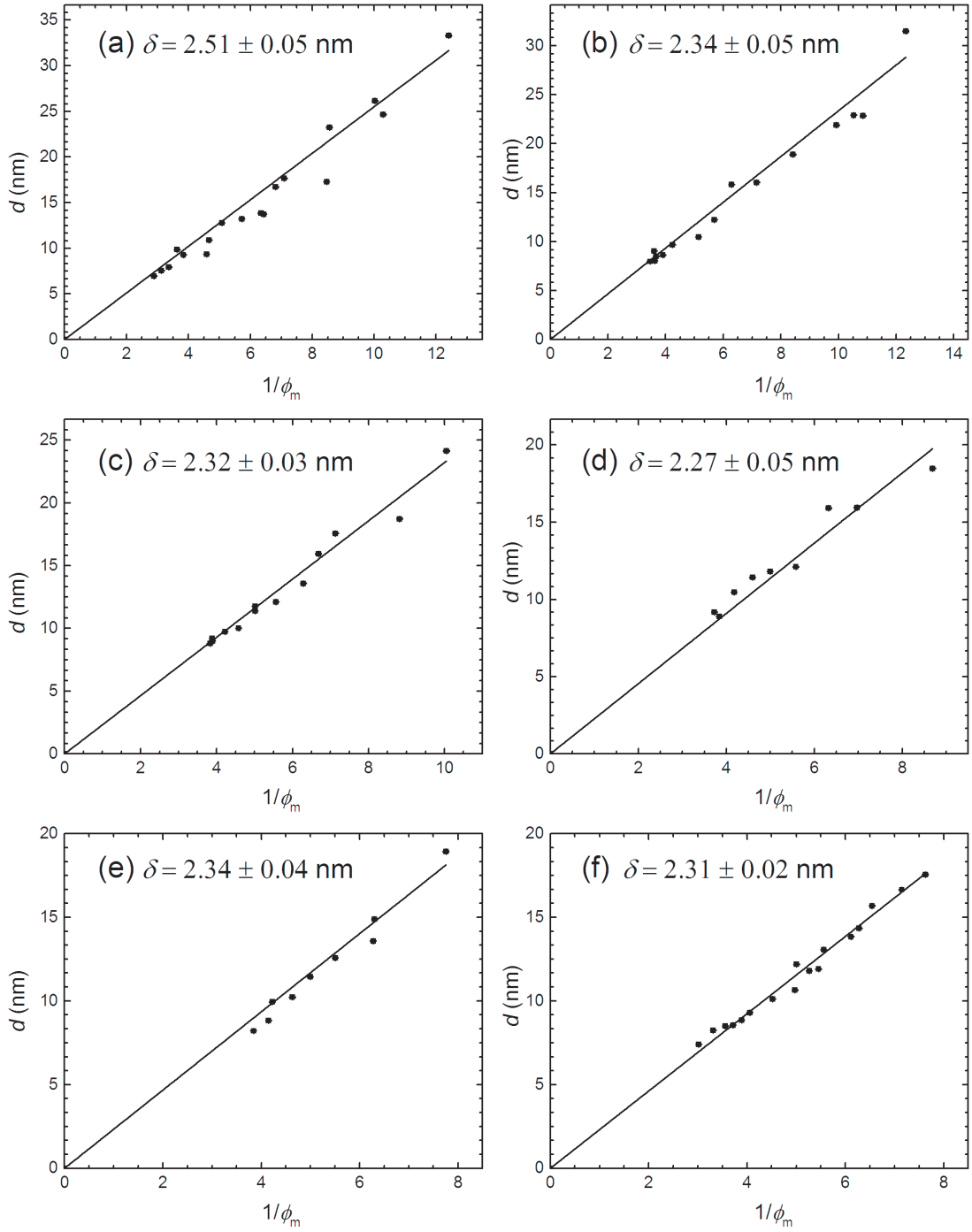

Figure 3: Période smectique d de mésophases lamellaires en fonction de l'inverse de la fraction volumique ϕ_m de membranes à concentrations croissantes de polymère dans les lamelles d'eau: (a) $C_p = 0$ wt. % ; (b) $C_p = 3.8$ wt. %, (c) $C_p = 5$ wt. %; (d) $C_p = 7.5$ wt. %; (e) $C_p = 10$ wt. %; (f) $C_p = 15$ wt. %. Une épaisseur de membrane δ est extraite.

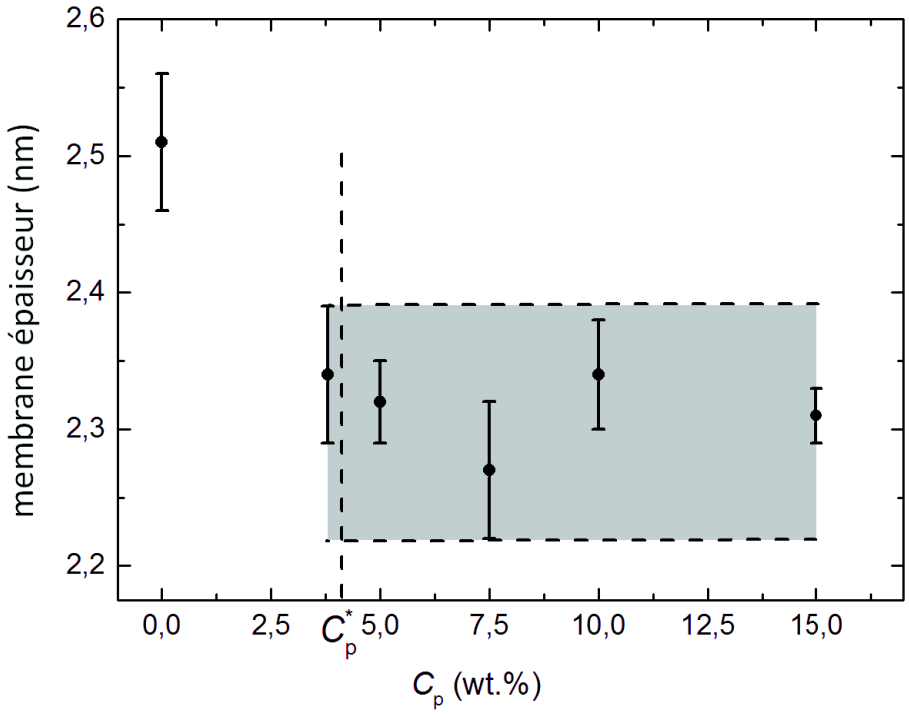

Figure 4: Évolution de l'épaisseur de la membrane δ avec la fraction massique du polymère C_p.

Un exemple de spectre obtenu pour une concentration en polymère de $C_p = 10$ wt. % à fraction de membrane 26 wt. % est présenté à la Figure 5. On peut distinguer quatre éclatements quadrupolaires $\Delta\nu_{Qa-d}$, où $\Delta\nu_{Qa}$ correspond au groupement CD_3 de bout de chaîne de la molécule d'octanol, tandis que les éclatements $\Delta\nu_{Qb-d}$ comprennent les contributions des groupes CD_2 le long de la chaîne d'octanol. Il apparaît que certains deutérons se comportent de manière équivalente du point de vue de la dynamique de mouvement, donnant naissance à des lignes de résonance superposées. Il est donc difficile d'identifier et d'affecter des pics spécifiques dans le spectre. C'est pourquoi toutes les données ont été analysées en utilisant une méthode supplémentaire de simulation des spectres (Figure 8). De manière remarquable les deux méthodes aboutissent au même résultat d'évolution du module élastique de courbure des membranes avec l'addition de polymère. Comme le montre la Figure 6, celui-ci reste inchangé tant que le polymère dissous dans les lamelles d'eau est en régime dilué. Par contre un accroissement d'environ 20 % est observé dès que le régime devient semi-dilué.

Cette évolution du module élastique de courbure est discutée en rapport aux prédictions théoriques. Une rigidification des interfaces est prédite par de Gennes [36], mais son amplitude n'est pas calculée. Dans un cadre de champ moyen Brooks et al. [15, 16] mon-

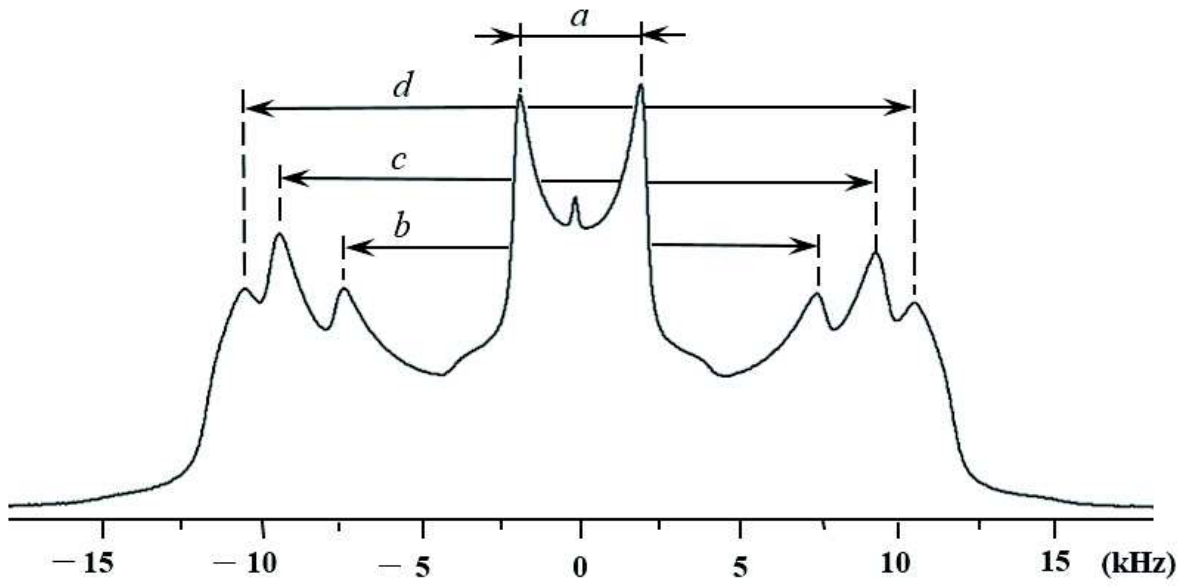

Figure 5: Spectre RMN obtenu pour une concentration en polymère C_p = 10 wt. % à fraction de membrane 26 wt. % pour SDS/octanol perdeutéré/ H_2O/PEG. On peut distinguer quatre éclatements quadrupolaires $\Delta\nu_{Qa-d}$.

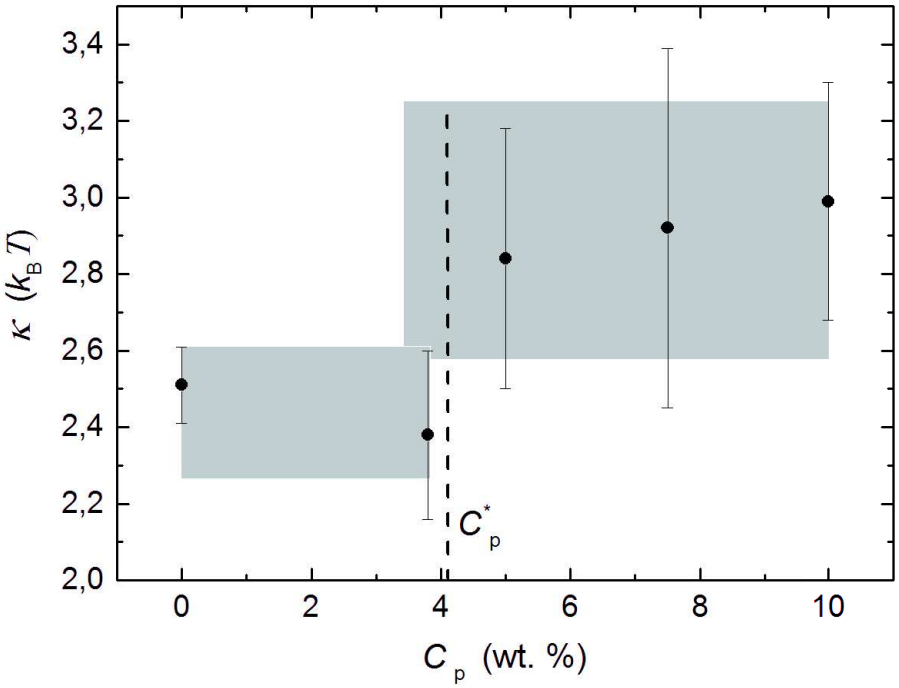

Figure 6: Variation du module de courbure κ (en unité k_BT) en fonction de la concentration en polymère C_p wt. %.

trent que la contribution de polymère adsorbé diminue le module élastique de courbure. Mais l'effet calculé est très faible (de l'ordre du dixième de k_BT). Skau et al. [9] montrent, à partir de précédentes études théoriques, qu'à adsorption fixée mais plus grande que celle

à l'équilibre, la diminution devient plus faible conduisant à un accroissement de la rigidité de courbure. Les auteurs mentionnent qu'une adsorption irréversible des chaînes de polymère sur les membranes conduirait à un effet plus prononcé, bien qu'ils n'aient pas développé le calcul. L'effet de l'adsorption de polymères sur le module élastique reste donc incertain au vu des théories existantes.

Des spectres RMN, qui présentent un comportement biphasique des mésophases dans la partie diluée du diagramme de phase nous a poussé à investiguer cette région par microscopie électronique (Figure 7). Comme Auguste et al. [6] nous avons observé la présence de vésicules multilamellaires (sphérulites) dans la région diluée proche de la limite de phase lamellaire. La quantité de chaque phase, ou plus précisément, la quantité de noyaux de deutérium occupant chaque phase dans un échantillon est proportionnelle à l'intégrale de cette partie dans le spectre. La simulation des spectres, nous a permis de mesurer le montant relatif de chaque phase dans les mésophases (Figure 8). Selon nos observations les vésicules multilamellaires coexistent avec la phase lamellaire dans la gamme de la fraction massique de la membrane de 10 à 20 wt. %. Il semblerait que le polymère induit la courbure spontanée de la bicouche et crée des sortes de "poches d'eau" avec une forte concentration de polymère.

Les effets induits par le confinement du polymère dans les lamelles d'eau dépendent de la tendance de celui-ci à s'adsorber ou non aux interfaces eau/tensioactifs. Une étape importante de mon travail a été d'étudier la dynamique des chaînes de polymères confinées. La technique utilisée est la FRAPP (Fluorecsence Recovery After Photobleaching Pattern), qui permet de mesurer le coefficient de diffusion de chaînes polymères marquées par fluorescence. Nous avons obtenu le coefficient d'autodiffusion des chaînes de PEG dans l'eau en fonction de la concentration du polymère et une dépendance à la loi de puissance très proche du régime de croisement. En ce qui concerne les mésophases lamellaires, nous avons montré qu'environ 50 à 70 % des chaînes de PEG contribuent à la fraction immobile, qui peut être due à un polymère partiellement adsorbé sur les membranes et/ou des polymères confinés dans les domaines lamellaires. La décroissance de l'intensité du contraste présente plusieurs populations de polymères diffus: on suggère qu'il y a une population qui diffuse environ trois fois plus lentement que les chaînes de polymères libres et deux autres populations qui diffusent beaucoup plus lentement. On peut interpréter les populations très lentes comme les échanges de chaînes entre la population de polymères non adsorbée, qui est présente au milieu de l'espacement intercalaire et la population de

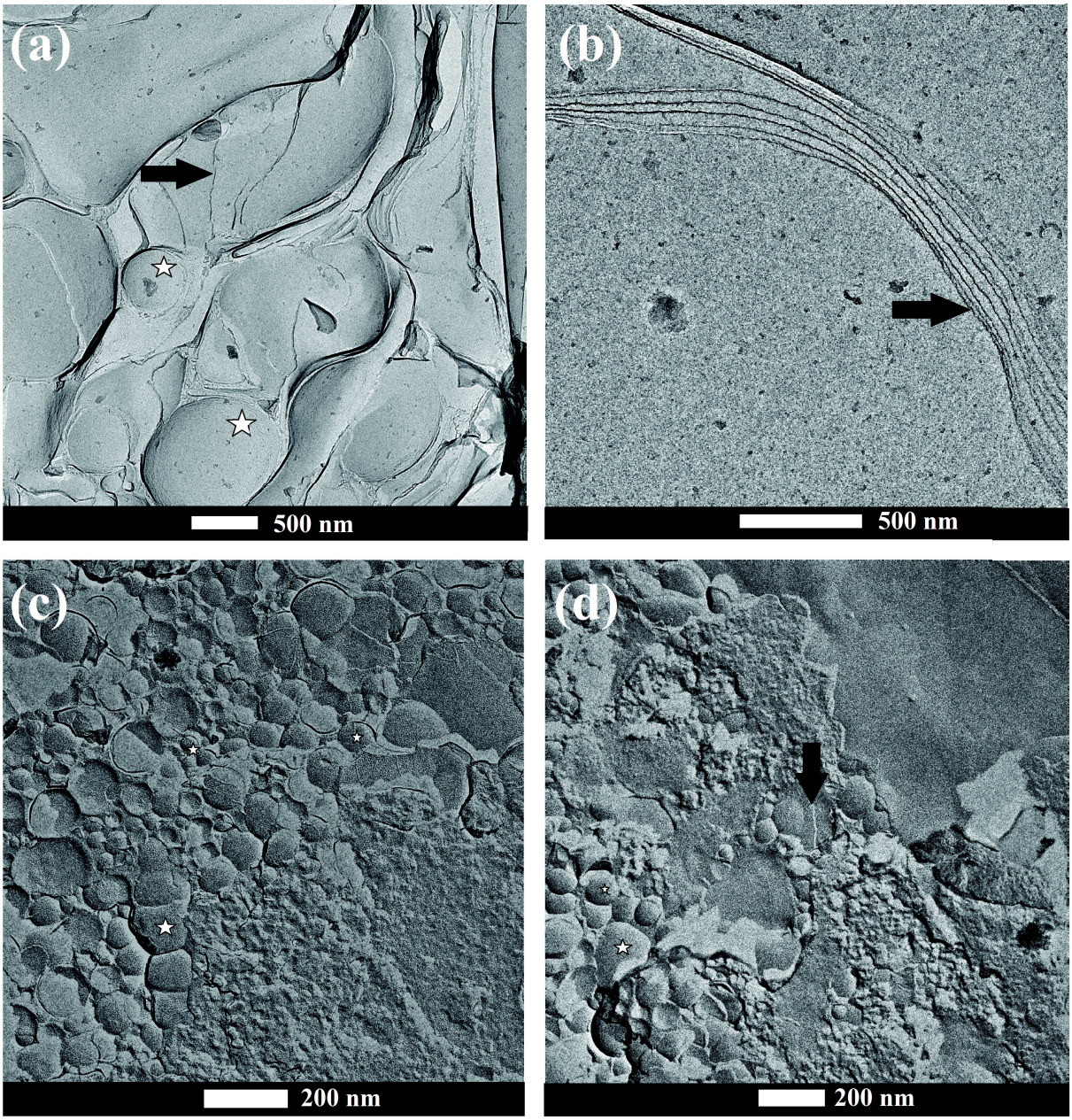

Figure 7: Micrographes obtenus par microscopie électronique après cryofracture pour des mésophases en fraction de membrane constante $\Phi_m = 10$ wt. % et différentes proportions de polymère contenues: (a) $C_p = 0$ wt. %, piles de lamelles planaires (flèche) et les régions où les bicouches sont courbées (étoiles); (b) $C_p = 0$ wt. %, texture en gradins (flèche) caracteristique d'une phase lamellaire; (c) et (d) $C_p = 15$ wt. %, vésicules unilamellaires (étoiles) dispersées dans la matrice lamellaire (flèche).

polymères adsorbés, qui est immobile.

La principale difficulté dans le travail avec les mésophases lamellaires était double: il faut obtenir des membranes parfaitement alignées et deuxièmement, il faut séparer différentes fractions mobiles de PEG dans la mésophase lamellaire, ce qui devient plus

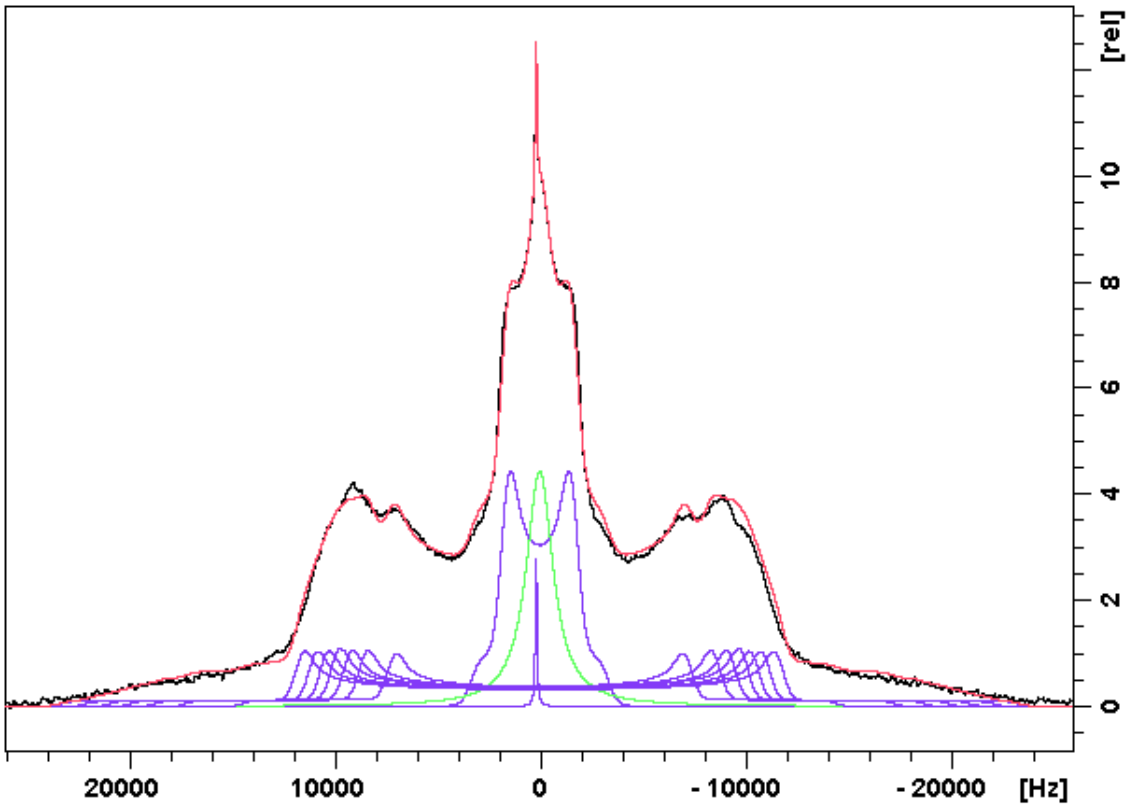

Figure 8: Spectre expérimental (en noir) et calculé (en rouge) pour l'échantillon en Φ_m = 10 % sans polymère. Paramètres de la simulation: les couplages quadrupolaires (CD_3 et 7 CD_2 liaisons), le déplacement chimique de l'eau DHO et la phase isotrope (en vert). La quantité de phase isotrope dans la mésophase est d'environ 9,6 %.

compliqué si des oscillations à longue portée apparaissent dans le signal FRAPP. Par conséquent, une nouvelle géométrie de mise en place a été proposée afin d'obtenir un meilleur alignement et de contrôler l'épaisseur de l'intervalle de l'échantillon confiné en utilisant des entretoises de mica d'épaisseur connue. Malheureusement, le laser s'est effondré l'année dernière et, par manque d'argent, il n'a pas encore été remplacé. Par conséquent, les résultats n'ont pas pu être complétés dans le cadre de cette thèse de doctorat. D'autres recherches expérimentales sont appelées à tirer des conclusions définitives sur tous les effets susmentionnés.

En parallèle, le module élastique de compressibilité $\bar{B}$, qui est directement relié au potentiel d'interaction entre membranes, est mesuré par la technique de mesure directe des forces à l'échelle moléculaire (Surface Force Apparatus, SFA). C'est la continuité des travaux de Herrmann et al. [57], afin d'extraire le coefficient de la loi de puissance attendue: $\bar{B}_{pol} \sim C_p^{\alpha}$. En présence de polymère, au fur et à mesure que les macromolécules remplacent le contenu en eau, le module de compressibilité de l'empilement lamellaire chute,

c'est la signature d'une interaction attractive due à la présence des macromolécules. De plus, des comportements très intéressants ont été mis en évidence: la présence de dislocations de très grands vecteurs de Burgers à grandes séparations ainsi que des phénomènes d'avalanches.

Les phases lamellaires dopées par des polymères sont des objets d'étude intéressants, tant pour des questions fondamentales que pour des applications pratiques. Le polymère qui est confiné dans une mésophase lamellaire induit de nombreux effets. Les membranes sont légèrement amincies, les fluctuations de courbure s'effectuent par adsorption des chaînes polymères à l'interface membrane / eau. Certaines poches polymère-eau peuvent même être créées entre des membranes adjacentes et probablement la distribution de molécules d'alcool le long de l'interface tensioactif est modifié. En outre, la dynamique des chaînes polymères est ralentie lors de l'enfouissement dans les couches d'eau. Tous ces effets locaux se combinent pour déstabiliser la pile lamellaire de manière macroscopique et conduire finalement à la coexistence de deux phases lamellaires de différentes périodicité, comme cela a été observé dans le diagramme de phase. Ce travail de thèse de doctorat a apporté une certaine lumière à ces effets déstabilisateurs, même si l'on demande plus de travail pour une compréhension globale du comportement de la phase lamellaire du polymère dopé.

Contents

List of Symbols

d	periodicity
δ	bilayer thickness
$\bar{d}$	interlayer spacing
D	surface separation
F_n	force
$\bar{B}$	elastic compressibility modulus at constant chemical potential
κ	elastic bending modulus
$\bar{\kappa}$	Gaussian curvature elastic modulus
Φ_m	membrane mass fraction
$\bar{\Phi}$	polymer volume fraction in water
C_p	polymer mass fraction in water
M_W	molar mass
R_G	gyration radius
ϕ_m	membrane volume fraction
B_0	strength of the magnetic field
$\Delta\nu_Q$	quadrupolar splitting
ν_Q	quadrupolar coupling constant
S_{C-D}	order parameter of CD group
τ_q	relaxation time
l_n	parabolae minima
l_n^i	inward jump position

Chapter 1

Introduction

1.1 Surfactants. Liquid mesophases

Surfactants are material that are made up of two different parts, namely hydrophilic and hydrophobic parts, covalently linked. It is known that hydrophilic molecules are characterised by their high affinity to polar solvents [61]. These molecules create hydrogen bonds with water molecules without perturbing too much the local structure. However, the hydrophobic molecules such as hydrocarbons, disrupt strongly the structure [61]. Their interaction with water is unfavourable from an energetic point of view. Therefore, they condense in solution in order to minimize the contact area with the solvent.

Surfactants are so-called "amphiphilic molecules". This particular organization gives them unique properties of self-assembly. Depending of their charge characteristics, surfactant molecules can be ionic (cationic or anionic), non-ionic or zwitterionic surfactants (Table 1.1). For example, sodium docedyl sulfate is an anionic surfactant (see Figure 1.1). When it is dissolved in water, the polar head releases the Na^+ counterion and becomes negatively charged.

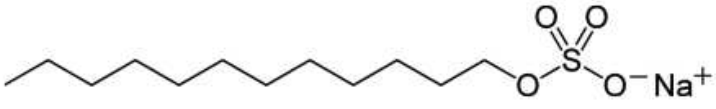

Figure 1.1: Surfactant molecule of sodium dodecyl sulfate ($C_{12}H_{25}SO_4^-Na^+$).

At low concentrations the molecules are dispersed in the solvent. Beyond a critical concentration (the critical micellar concentration or CMC), molecules aggregate to form spherical micelles in order to avoid any contact between the hydrophobic tails and water. The shape of the aggregates varies depending on the concentration of amphiphilic molecules. For this reason such systems are called lyotropic (*lyo* - dilution, *tropos* - form).

Table 1.1: Different types of amphiphilic molecules.

Type	Structure of amphiphile		CMC (M)
anionic	$C_{12}H_{25}\ SO_4^-\ Na^+$	sodium sodecyl sulfate (SDS)	$8.1 \cdot 10^{-3}(25°C)$
cationic	$C_{18}H_{29}\ N(CH_3)_3^+\ Cl^-$	cetylpyridinium chloride (CPCl)	$0.9 \cdot 10^{-3}(30°C)$
neutral	$C_{12}H_{25}(OCH_2CH_2)_6OH$	hexaethylene glycol dodecyether ($C_{12}E_6$)	$8.7 \cdot 10^{-5}(25°C)$
zwitterionic	$(C_{15}H_{31}COO)CHCH_2 OPO_3CH_2CH_2NMe_3 (C_{15}H_{31}COOCH_2)$	dipalmitoylphosphatidylcholine (DPPC)	$5 \cdot 10^{-10}(41°C)$

Additionally micelles can form only above a certain temperature known as the Krafft temperature or "Krafft point" [80]. The Krafft temperature (T_K) corresponds to the temperature at which the surfactant solubility equals the CMC. The Krafft point is strongly dependent on the alkyl chain length of the surfactants and on the head group structure, hence the packing efficiency in the solid crystalline state [80].

The Krafft temperature for SDS is equal to 22°C (Figure 1.2). It corresponds to the temperature at which all the hydrocarbon chains solidify, forming the inflexible, all-trance configurations. Below this temperature surfactants precipitate out in the form of hydrated crystal. In other words the solubility limit of SDS molecules is less then CMC. At this point, it is energetically unfavourable for the molecules to assemble into spherical micelles. Figure 1.2 illustrates that the CMC increases very slightly as the temperature is raised to 40° for SDS [89].

In order to form a micelle the surfactant molecules should have sufficiently flexible hydrocarbon chains to undergo the contortions demanded by micelle shape. The temperature has to be high enough for the chains to be in a melted or liquid state, so that the molecule is not rigid.

Interactions between micellar surfaces are repulsive (from electrostatic or hydration forces), so that as the number of aggregates increases and micelles get closer to one another, the only way to maximize separation is to change shape and size. This explains the sequence of surfactant phases observed in the concentrated regime. Such phases are known as mesophases or lyotropic liquid crystals. With increasing the concentration of surfactants in water solution the following sequence of structures are commonly observed: spherical micelle → cylindrical micelle → cylindrical micelles packed in a two-dimensional hexagonal lattice (hexagonal phase) → connected cylinders or membranes in regular three-dimensional lattices (e.g., bicontinuous cubic phase) → planar membranes (lamellar phase) (see Figure 1.3).

Figure 1.4 shows the phase diagram of SDS extensively studied in the work of Kékicheff et. al [73] in the concentrated regime by high sensitivity differential scanning calorimetry.

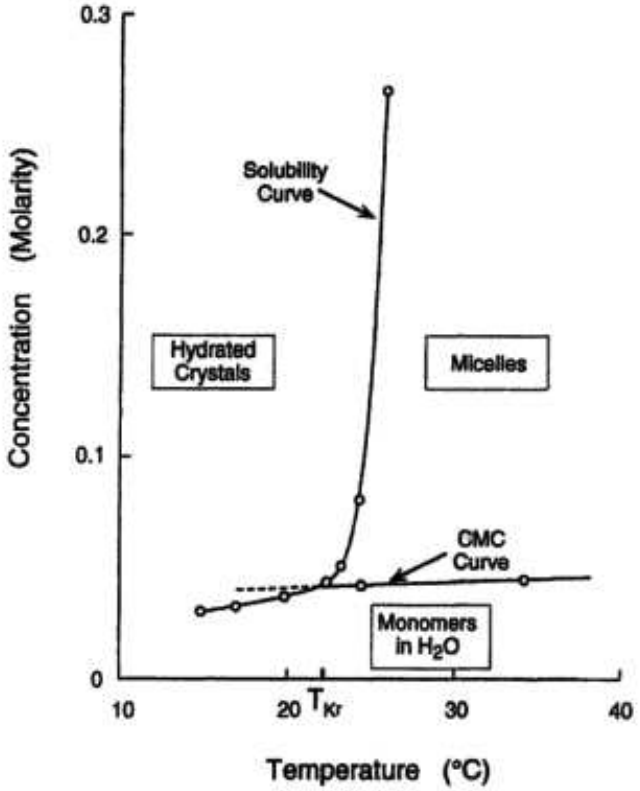

Figure 1.2: Temperature dependence of SDS solubility in the region of the Krafft temperature. At temperatures below T_K, hydrated surfactant crystals precipitate out of solution before micelles form. Above T_K the solubility increases dramatically and monomers assemble to form micelles [89].

It can be seen from the diagram that besides the lamellar (L_α) and hexagonal (H_1) phases (hexagonal is denoted as H_α) there are several intermediate phases that exist over a narrow range of concentration. Hexagonal appears at 37 % in co-existence with a micellar solution and then at 40 % as a single phase. A lamellar phase is the major phase between 69 and 86 % surfactant and appears even at higher temperatures. Between hexagonal and lamellar phases a number of intermediate phases exist. Above 87 % surfactant the lamellar phase co-exists with a crystal phase.

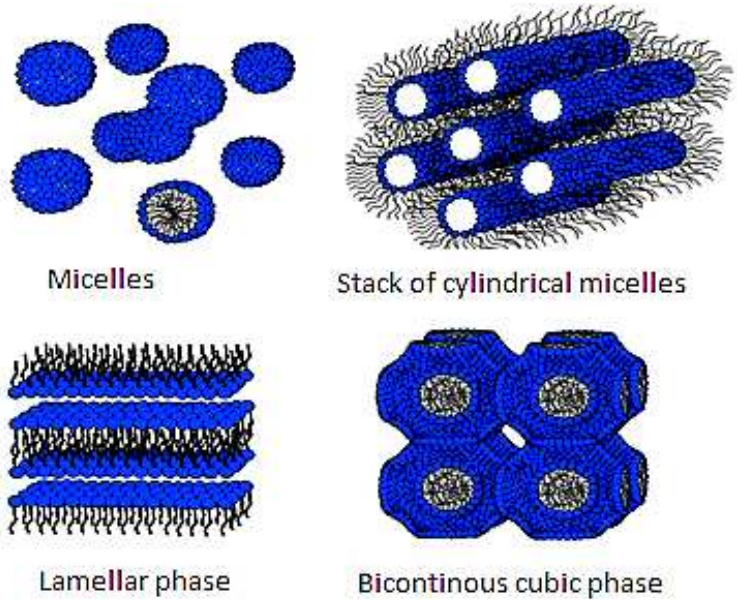

Figure 1.3: Formation of various structures in surfactant solutions [1].

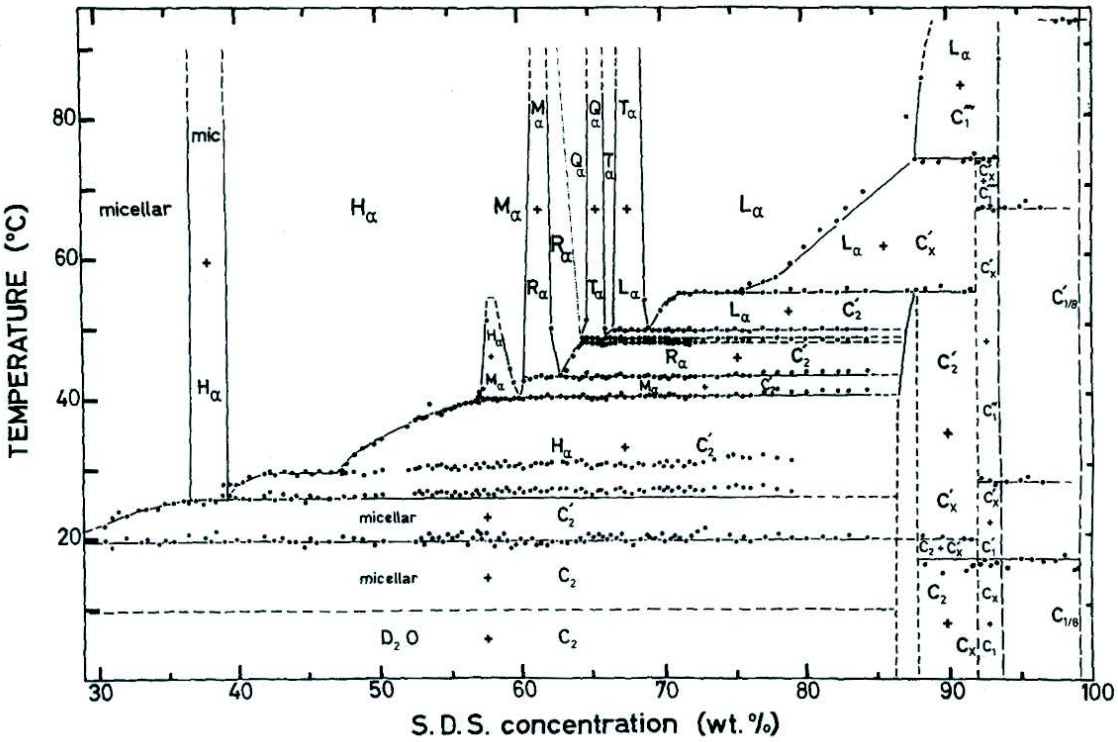

Figure 1.4: Phase diagram for SDS – D_2O system established in 1989 by Kékicheff [73]. In Luzzati's terminology the mesophases: H_α, hexagonal phase; M_α, two-dimensional monoclinic phase; R_α, rhombohedral phase; C_α, cubic phase; T_α, tetragonal phase; L_α, lamellar phase (α – quasi-liquid state for paraffinic chain).

1.2 Physical properties of isolated membrane

1.2.1 Elasticity of a membrane

The curvature elasticity plays a major role in the elastic properties of fluid membranes, as evidenced by Helfrich (1973 [54]). The most general form of curvature free energy F_{curv} per unit area of a bilayer with two local principal curvatures R_1 and R_2 can be written in terms of the mean $(1/R_1 + 1/R_2)$ and Gaussian $(1/R_1\ R_2)$ curvatures defined as:

$$f_{curv} = \frac{1}{2}\kappa\left(\frac{1}{R_1} + \frac{1}{R_2} - C_0\right)^2 + \bar{\kappa}\frac{1}{R_1 R_2}, \tag{1.1}$$

This form for curvature free energy states that the mean curvature that minimizes the free energy has a value of C_0, termed the spontaneous curvature of the membrane. The energy cost of deviating from the spontaneous curvature is the bending or normal elastic modulus, κ, which is always positive. A parameter $\bar{\kappa}$, known as the Gaussian bending elastic modulus is related to the topological changes and measures the energy cost of saddle-like deformations; it can be positive or negative. The Gaussian modulus $\bar{\kappa}$ gives the topology of the surface at equilibrium [54].

The energy cost associated to the membrane deformation in the vicinity of the equilibrium position can be written:

$$f_{def} = \frac{1}{2}\kappa\left(\frac{1}{R_1} + \frac{1}{R_2} - C_0\right)^2, \tag{1.2}$$

According to the value of the elastic bending modulus one can distinguish two categories of membranes:

- rigid membranes whose bending elastic modulus is large compared to k_BT. Its is usually the case of phospholipid membranes, such as the biological membranes.
- flexible membranes, composed of one tail surfactant molecules, with bending elastic modulus of the order of k_BT. For such systems the thermal fluctuations are significant.

We will consider only flexible membranes, which are easier to bend and thermally undulate a lot, such as surfactant bilayers in lamellar phase L_α.

1.2.2 Elastic constants renormalization

When κ is of the order of k_BT the amplitude of membrane fluctuations in the direction normal to its equilibrium position is of the order of its lateral extension, the membrane undulates to occupy the maximum space. The amplitude of these fluctuations is such that the membrane is in a crumpled state, then we have lost local normal correlations to the membrane. It is possible to define a characteristic length, below which this correlation exists and the membrane can be considered as flat. This length is called the persistance length ξ_k. This concept, introduced by De Gennes (1979 [34]) for polymers was resumed to characterize the changing shape of the membrane (De Gennes, Taupin, 1982 [37]).

$$\xi_k = a \exp\left(\frac{4\pi\kappa}{3k_BT}\right) \tag{1.3}$$

where a is the average distance between two surfactants in the monolayer. Thus, for scales below ξ_k, the membrane is considered as planar. For a distance ξ larger than ξ_k, the elastic constants are renormalized as follows:

$$\kappa = \kappa_0 \left[1 - \frac{3k_BT}{4\pi\kappa_0} \ln\left(\frac{\xi}{a}\right)\right] \tag{1.4}$$

$$\bar{\kappa} = \bar{\kappa_0} \left[1 + \frac{5k_BT}{6\pi\bar{\kappa_0}} \ln\left(\frac{\xi}{a}\right)\right] \tag{1.5}$$

The logarithmic term can be understood as an entropic correction not negligible, due to fluctuations of the membrane. On spatial scales larger than ξ_k the membrane is gaining in entropy by bending itself. This entropic effect is at the origin of stabilizing undulation interactions, particularly for diluted non-charged lamellar phases.

1.3 Lamellar phase structure and interactions

A lamellar phase L_α (Figure 1.5) takes the form of stacks of bilayers (or membranes) of thickness δ separated by solvent layers. The membranes can have many components (typically an amphiphile molecule and a co-surfactant). A co-surfactant is a water soluble molecule but which, in the presence of aggregates, prefer to be inserted therein. The polar heads are not ordered, and the amphiphiles diffuse quite freely in each monolayer. There is no order in the acyl chains either (they are melted).

The L_α phase is a smectic liquid crystal: parallel to the planes of the bilayers, the molecules are distributed as in a liquid; perpendicularly to the bilayers, there is a long-range positional order. The smectic periodicity d ranging from dozens up to several thousand angstroms have been observed [26].

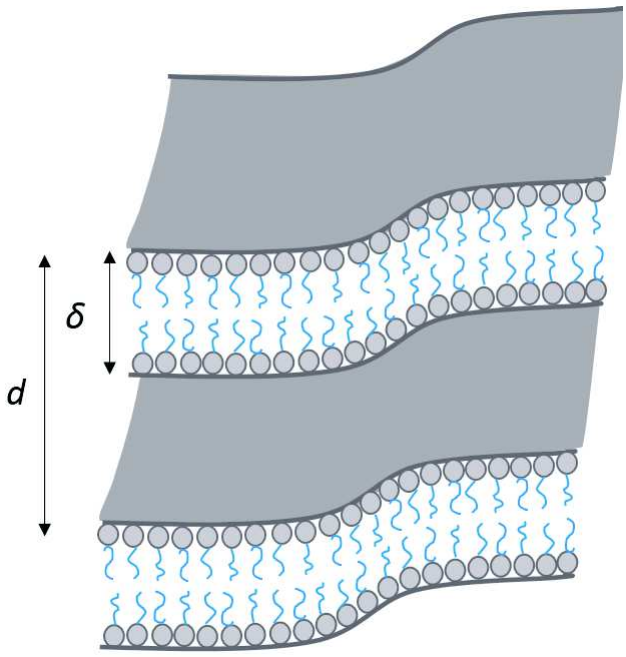

Figure 1.5: Structure of lamellar phase L_α: bilayers of δ thickness, stacked along one direction, with a smectic periodicity d. For geometric reasons, it is seen that $d = \delta/\phi_m$, with ϕ_m membrane volume fraction.

For a homogeneous sample, the periodicity of the lamellar phase is related to the volume fraction of membrane from simple geometric considerations, by the expression:

$$d = \frac{\delta}{\phi_m} \tag{1.6}$$

where ϕ_m is the volume fraction of membrane in the sample. The existence of fluctuations (undulations) brings a logarithmic corrections to this purely geometrical relationship [109]:

$$d = \frac{1}{\phi_m}(A - B \ln \phi_m) \tag{1.7}$$

This is attributed to the excess area coming from the undulations [109].

There are four types of interactions between the bilayers leading to the stability of the lamellar phase:

- the van der Waals interactions. These forces are due to dipole/dipole induced interactions. They are generally attractive. The potential interaction per unit area between two flat membranes is expressed as follows [67]:

$$V_{VDW} = -\frac{A_H}{12\pi}\left(\frac{1}{d^2} + \frac{1}{(d+2\delta)^2} - \frac{2}{(d+\delta)^2}\right) \tag{1.8}$$

  where A_H is a Hamaker constant for a given system, it is in the order of $k_B T$;

- the hydration interactions. They are repulsive and short range [85]. The origin of these interactions arises from the structuring of water molecules through hydrogen bonds.

$$V_{hydr} = F_0 e^{-\frac{d}{L_H}} \tag{1.9}$$

F_0 is an energy per unit area and L_H the interaction range (typically a few Å). This force is dominant for membranes that are closely packed and can be neglected for the diluted lamellar phases. In contrary, it becomes important for gels phases.

- the electrostatic interactions. This force exists only for charged surfactant molecules. It is a long-range interaction. In the absence of added salts, the interaction potential for large values of d, is given by [110] :

$$V_{elec} \backsim \frac{\pi k_B T}{4 L_B d}\left(1 - \frac{c}{L_B d^2} + \frac{c^2}{L_B^2 d^2}\right) \tag{1.10}$$

With a Bjerrum length $L_B = \dfrac{e^2}{4\pi\varepsilon_r\varepsilon_0 k_B T}$ ($\backsim$ 7 Å for water at room temperature) and c is a coefficient related to the surface area per charged polar head. Addition of salts reduces the range of this interaction. The interaction potential becomes:

$$V_{elec} = E_0 e^{-\frac{d}{\lambda_D}} \tag{1.11}$$

where E_0 is an energy per unit area. The range of the interaction is then determined by the Debye screening length $\lambda_D = \sqrt{\dfrac{\varepsilon_r\varepsilon_0 k_B T}{\sum_i Z_i^2 e^2 C_0}}$ with C_0 the ion concentration of the solution, Z_i their valence, the ε_0 is the dielectric permittivity of the vacuum, ε_r is the relative permittivity of the solvent ($\varepsilon_r = 80$ for water) and e the electron charge.

- the steric interaction comes from the significance of the thermally induced fluctuations of the membranes. A membrane undulating between its two neighbours is confined in a space that is restricted compared to the space it would occupy alone. The origin is thus steric and entropic. This interaction is long range. It is become important for flexible membrane (small κ). The interaction potential can be written as [54]:

$$V_{und} = \frac{3}{128}\frac{\pi^2 k_B^2 T^2}{\kappa(d-\delta)^2} \tag{1.12}$$

Therefore, the Van der Waals attractive interaction is balanced by the repulsive interactions, comprised of the electrostatic interaction of the charged membranes, the hydration interaction and the steric undulation interaction. The hydration interaction is significant for the weak interlayer spacing (1 nm). In the our system, the periodicities are in a range between 6 nm and 24 nm: as a consequence only steric undulation and electrostatic repulsion interactions may play a role to balance the ever present attractive

Van der Waals interaction.

1.4 Elasticity of a lamellar phase

1.4.1 Two-component lamellar phase

The thermodynamic stabilisation of the lamellar phase results in equilibrium between the elastic properties of interfacial film separating the hydrophilic and hydrophobic regions and the interactions created by amphiphiles. It is highlighted in this section the important role of the elasticity of the interface in the thermodynamical description of the lamellar phase.

The elastic properties of the lamellar phase can be described considering that lamellar phase is a smectic A phase of two incompressible constituents. As explained above, the equilibrium state of a lamellar phase is characterized by a periodic stacking of periodicity, d, of membranes of thickness, δ. In this state the equilibrium corresponds to an energy per unit volume $f_{eq} = V(d)/d$. The energy cost of any deviation from this equilibrium reads:

$$f = f_{eq} + \frac{B}{2}(\partial_z u)^2 + \frac{K}{2}(\bigtriangledown_\perp u)^2 + \frac{1}{2}\chi^{-1}\delta c^2 + C\delta c\partial_z u, \tag{1.13}$$

where $u(\mathbf{r})$ is a displacement of a bilayer in the stacking direction relative to its equilibrium position (Figure 1.6), δc is a local variation of thickness (concentration) of the bilayer. B and K are the elastic constants of the system, defined respectively as the compression modulus of the bilayers at the constant concentration and the bending elastic modulus ($K = \kappa/d$). χ is the osmotic compressibility at the constant periodicity and C is a coupling constant between the layers displacement and the fluctuations of concentration.

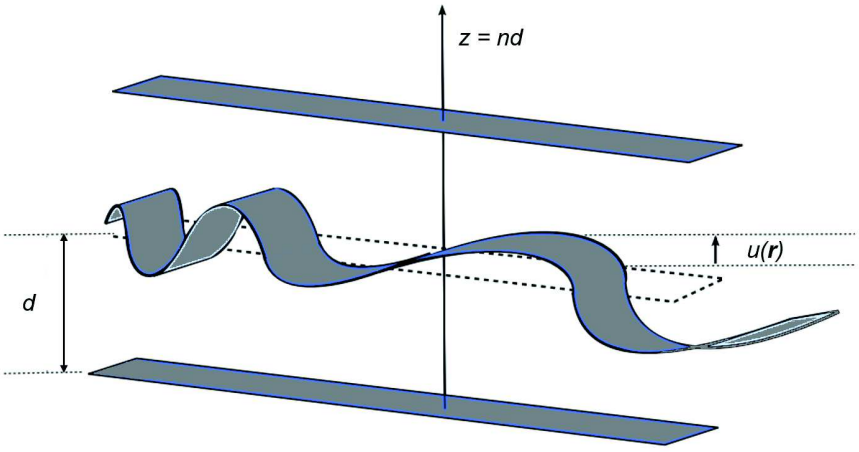

Figure 1.6: Membrane fluctuations.

The significance of the elastic constant B implied in this binary system that the compression of the layers include also the compression of the membrane, keeping the concentration of surfactant constant. One can define $\bar{B}$ the compression elastic modulus at constant chemical potential of surfactant :

$$\bar{B} = B - \chi C c^2 \tag{1.14}$$

$\bar{B}$ is related directly to the interactions between membranes and can be measured by Surface Force Apparatus, Dynamic Light Scattering and X-ray Scattering.

1.4.2 Three-component lamellar phase

In 1994, Nallet et al. classified [100] the three-component lyotropic L_α lamellar phases in three distinct types:

- two-solvent lamellar phase: it occurs when the amount of surfactant bilayers becomes comparable to the amount of solvent separating them;
- doped-bilayer lamellar phase: arises when the surfactant bilayer hosts a colloidal component;
- doped-solvent lamellar phase: arises when the solvent is now hosting a colloidal component while the surfactant bilayer remains “pure”.

We consider polymer doped-solvent lamellar phases. The nature of the interactions polymer/polymer and polymer/solvent is determined by the quality of the solvent towards the polymer and the temperature, independently from the presence of the membranes. However, the interface membrane/solvent may alter the polymer behavior: depending on the hydrophobicity or hydrophilicity, the polymer may adopt an adsorbing or non-adsorbing behavior towards the membranes.

Previous studies have shown that the polymer molecules can occupy a variety of locations; they can be:

- confined in the interlayer solvent and do not adsorb onto and not incorporate into the surfactants bilayers [87, 88, 120];
- completely localized in the membrane [106];
- localized both in the bilayers and in the solvent [132];
- adsorb onto the bilayers [44, 56].

The presence of a polymer changes the elastic properties of the membranes and makes complicated the thermodynamic description of the lamellar phases.

If we assume that the system is not compressible, and for small fluctuations around the equilibrium position, the free energy density is given by [3]:

$$f = f_{eq} + \frac{\bar{B}}{2}\left(\frac{\partial u}{\partial z}\right)^2 + \frac{K}{2}\left(\frac{\partial^2 u}{\partial x^2} + \frac{\partial^2 u}{\partial y^2}\right)^2 + \frac{1}{2}\bar{\chi_p}^{-1}\delta\tilde{c_p}^{\,2} + \frac{1}{2}\bar{\chi_t}^{-1}\delta\tilde{c_t}^{\,2}, \tag{1.15}$$

where $\bar{\chi_t}^{-1}$ (resp. $\bar{\chi_p}^{-1}$) is related to the surfactant (resp. colloidal particle) osmotic compressibility and $\delta\tilde{c_t}$ (resp. $\delta\tilde{c_p}$) is the fluctuation of surfactant (resp. colloidal particle) mass fraction around the equilibrium. $\bar{B}$ is the elastic compressibility modulus at constant chemical potential of the surfactant and guest component, which is related to the intermembrane interaction potential. K is the normal curvature elastic constant, which describes the energy required to bend the bilayers together: $K = \frac{\kappa}{d}$, where d is the periodicity of the layered stack.

1.5 Polymer-doped lamellar phase

1.5.1 Polymer dilution. Poly(ethylene) glycol

In our study polymer chains of poly(ethylene glycol) are dissolved in the water layers of lamellar mesophases. The polymer dilution and some aspects of polymer which is considered are presented below.

When the amount of polymer in solution is very small, each chain occupies a volume usually described as a sphere of radius R_G, the radius of gyration. The polymer coils are far from each other and thus do not interact. This is the dilute regime (Figure 1.7a). The characteristic length is the gyration radius, $R_G \approx aN^{\nu}$ (a is the monomer length; $\nu = 3/5$ for polymer in a good solvent [34]).

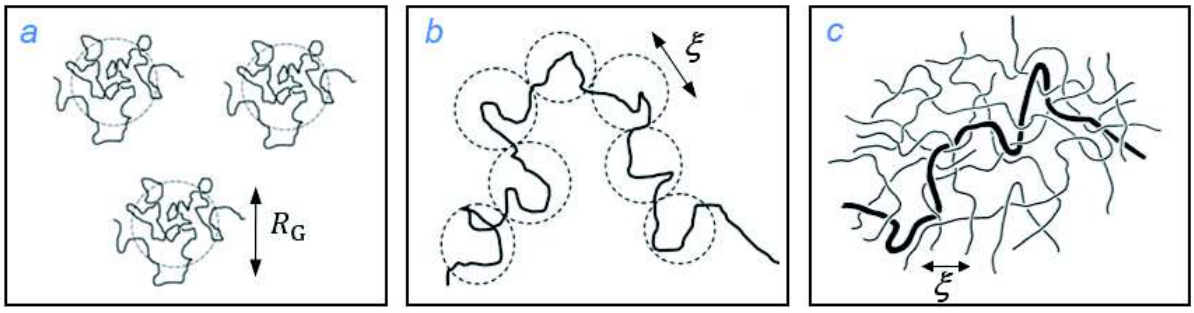

Figure 1.7: Schematisation of the regimes. a) $\bar{\Phi} < \bar{\Phi}^*$ dilute solution; b) $\bar{\Phi} = \bar{\Phi}^* = Na^3/R_G^{3/5} = N^{-6/5}$ overlap concentration; c) $\bar{\Phi} > \bar{\Phi}^*$ semi-dilute solution.

With increasing the concentration, the coils get closer until they rich a critical concentration $\bar{\Phi}^*$, the concentration at which the chains begin to overlap. The resulting net

is characterised by its mesh size ξ,

$$\xi(\bar{\Phi}) = R_G \left(\frac{\bar{\Phi}}{\bar{\Phi}^*}\right)^{-\nu/3\nu-1} = R_G \left(\frac{\bar{\Phi}}{\bar{\Phi}^*}\right)^{-3/4} \tag{1.16}$$

where $\bar{\Phi}$ is the polymer volume fraction in the solvent. Physically, this means that two monomers of the same chain cannot see each other when they are separated by a distance superior to ξ: their interactions are screened by the other monomers. ξ is independent of the chain-length. This is the semi-dilute regime.

The limit between both regimes corresponds to the situation where the coils are in contact but do not overlap (Figure 1.7b), that is to say when $\xi = R_G$, and this how we define the overlap concentration: $\xi(\bar{\Phi}/\bar{\Phi}^*) = R_G$.

Poly(ethylene oxide)(PEO), or also poly(ethylene glycol)(PEG) is a neutral, hydrosoluble, linear polymer. Besides purely academic interest in the unusual behaviour of PEO [66], it has attracted attention because of its practical importance. PEO is biocompatible and inhibits protein adsorption. These specific features makes polymeric micelles with a PEO corona good candidates for drug delivery purposes [84].

The repeat units of the polymer is $-CH_2 - CH_2 - O-$, this macromolecule has an unusual interaction with water [41] arising from its unexpected water solubility or "hydrophilicity". While, poly(butylene oxide), $-(CH_2 - CH_2 - CH_2 - O-)_n-$, having one more methylene (CH_2) group is hydrophobic and insoluble in water. This observation suggests that a refined balance between hydration forces at the hydrophobic interfaces of these polymers determines their solubility. Indeed, PEO appears to form thin monolayers at the air-water interface possessing thereby also the hydrophobic character [66]. PEO when free in solution, can be attracted to the surfaces of certain kind of surfactant micelles, vesicles, cells resulting in polymer adsorption [17, 79].

1.5.2 Polymer confinement regimes

We consider now the situation where polymer coils are confined in the water layers separating the membranes of the lamellar mesophase. Satisfying the following conditions : i) the polymer does not penetrate through the membranes, so that the confinement is effective; ii) the polymer shows no specific interaction with the membrane so that the strong adsorption regime is avoided, one realize a situation similar to the confinement in infinite slits. Such a situation has been theoretically addressed by Daoud and de Gennes [28] and studied experimentally by Ligoure et al. [87, 88]. From scaling arguments, these authors have found four regimes of confinement (sketched in Figure 1.8), depending on the polymer volume fraction $\bar{\Phi}$ in the solvent and on the width of the slit $\bar{d}$:

- $\bar{d} > R_G$ and $\bar{\Phi} < \bar{\Phi}^*$: three-dimensional dilute solution of polymer chains (3D D regime). The chains do not overlap and stay in their spherical coil conformation.

- $\bar{d} > a\bar{\Phi}^{-3/4}$ and $\bar{\Phi} > \bar{\Phi}^*$: three-dimensional semi-dilute solutions of polymer chains (3D S-D regime). The chains overlap but still remains unsqueezed.
- $a/(N\bar{\Phi}^2) < \bar{d} < a\bar{\Phi}^{-3/4}$ and $\bar{\Phi} > \bar{\Phi}^*$: two-dimensional semi-dilute regime (2D S-D regime). The chains both overlap and are squeezed by the slits.
- $\bar{d} < R_G$ and $\bar{\Phi} < \bar{\Phi}^*$, or $\bar{d} < a/(N\bar{\Phi}^2)$ and $\bar{\Phi} > \bar{\Phi}^*$: the two-dimensional dilute solution of polymer chains (2D D regime). The chains do not overlap, but are squeezed (flat pancakes of thickness $\bar{d}$).

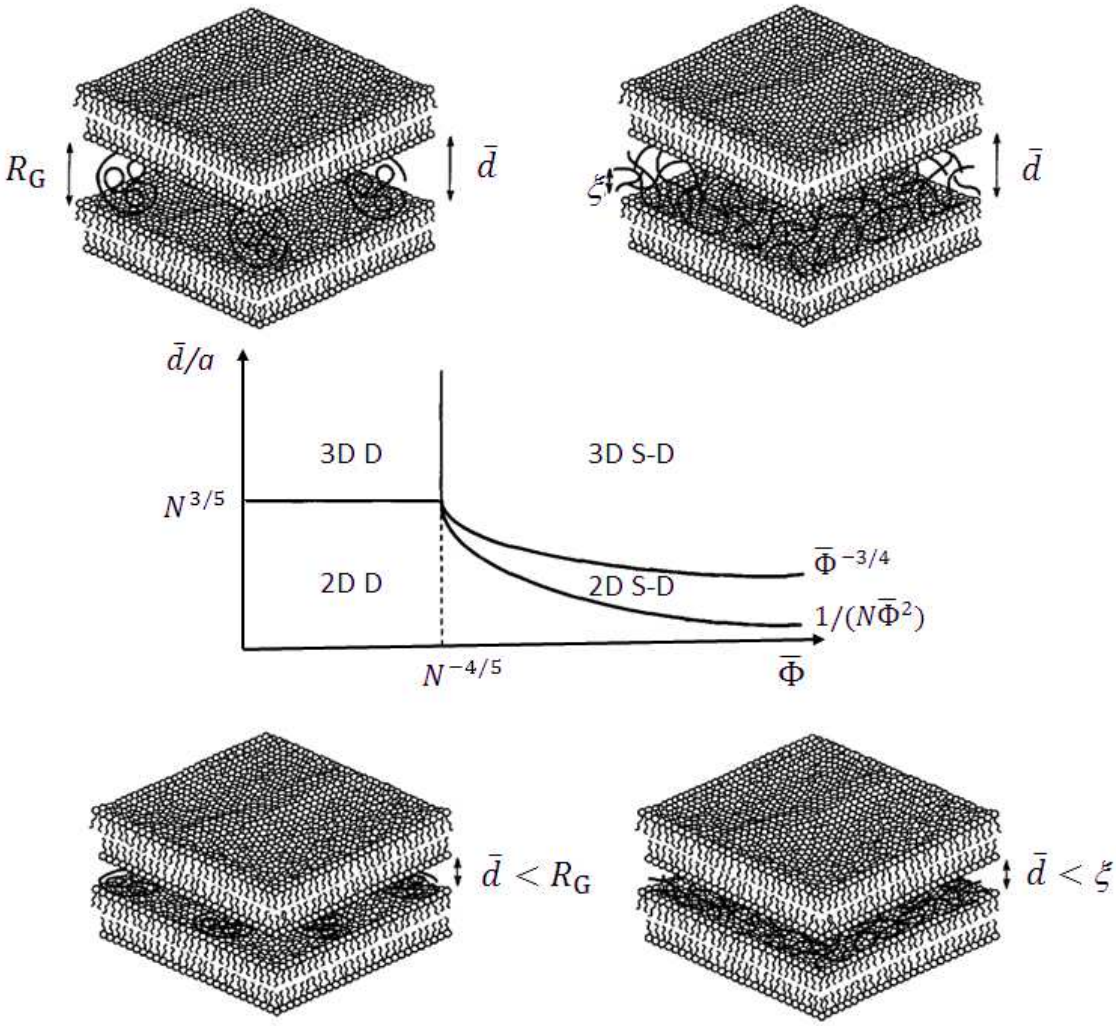

Figure 1.8: Polymer confinement regimes [88]. $\bar{\Phi}$ is the volume fraction of polymer in the solvent; N is the polymerization index; $\bar{d}$ is the width of the slit ($\bar{d} = d - \delta$) and a is the monomer length.

1.6 Bending elastic moduli

Much emphasis has been placed on the characterization of the elastic properties of the membranes which play a major role in determining the intermembrane interactions and the overall topology assumed by the membrane. The bending moduli of membranes have been extensively studied both theoretically and experimentally, since their values are typically of a few k_BT or less, and therefore their effects can be probed by analysis of the thermal fluctuations.

Up to now, the bending elastic moduli of the membrane have been measured by dynamic light scattering [99], high-resolution small-angle X-ray scattering by analysis of lineshapes [110] or of the peak position [123], electron spin resonance and ^{2}H NMR spectroscopy [5, 12].

Small-angle X-ray scattering (SAXS) and neutron scattering have been recognized as a powerful tool for the study of the organization as well as the fluctuations of various self-assembling systems. Quantitative treatment of the SAXS or neutron scattering pattern of a lamellar phase, allow to measure the dimensionless number, η, called Caillé exponent [19] characterizing the power-law singularities at the Bragg peaks.

The profile of the Bragg diffraction peaks is analyzed through the structure factor of the smectic stack. In the case of the oriented samples the asymptotic behaviour of the structure factor in the direction parallel ($\|$) and perpendicular ($\perp$) to the layer normal is given by simple power laws [110] (Eq.(1.16, 1.17)). In our case, the lamellar mesophases are not oriented, thus the structure factor is given by Eq. (1.18).

$$S(0,0,q_{\|}) \sim \frac{1}{|q_{\|} - q_n|^{2-\eta_n}} \tag{1.17}$$

$$S(q_{\perp},0,q_n) \sim \frac{1}{|q_n - q_{\perp}|^{4-2\eta_n}} \tag{1.18}$$

$$S(q) \sim \frac{1}{|q - q_n|^{-1+\eta_n}} \tag{1.19}$$

where q_n is the position of the $n-th$ harmonic of the structure factor ($q_n = nq_0$, $n = 1, 2, \dots$) and the η_n is the power law Caillé exponent related to the bending elastic constants $\bar{B}$ and K:

$$\eta_n = n^2 q_0^2 \frac{k_BT}{8\pi\sqrt{\bar{B}K}} \tag{1.20}$$

To clearly separate increases in the strength of intermembrane interaction ($\bar{B}$) from changes in rigidity (K) require a more formal analysis. SAXS and neutron scattering are good methods to obtain the structure of lamellar mesophases, but thay have also

disadvantages. In particular only the product of the two elastic constants $\bar{B}$ and K is measured.

New techniques were proposed by Auguste et al. [5] to study the bending elastic modulus by use of the deuterium solid state NMR spectroscopy. ^{2}H NMR technique gives a valuable information on the angular fluctuations of the membranes in lyotropic lamellar phases. The bending elastic modulus κ can be extracted from the measurement of the quadrupolar splitting. The compressibility modulus $\bar{B}$ appears only as a logarithmic correction of the κ dependence.

We will focus our experimental studies on the NMR spectroscopy measurements. The theoretical background of this technique is presented in Chapter 2.

1.7 Motivation and scope of the thesis

The lamellar phase has proven to be a good experimental and theoretical model to study amphiphilic bilayers, and their interactions with polymers [44, 56]. For instance, the presence of polymer (PEO) attached to the surface of liposomes enhances steric interaction that stabilize the lipid bilayer against approaching macromolecules or cells [79], increasing its lifetime in the bloodstream and allowing for the targeting of tumors [97]. Nevertheless, the interactions of polymers with amphiphilic bilayers are still poorly understood. Several questions arise:

- How do polymers influence the interbilayer interactions [56]?
- How do large hydrophilic polymers permeate through membranes [124]?
- How does the lamellar phase release the constraint imposed by a dopant?
- Does a lamellar phase consist of pores in the bilayers? Many experimental observations would be easier to interpret if the presence of pores in amphiphilic bilayers (e.g. the permeation of molecules through bilayers [25]) is assumed. Experimentally, pores are difficult to observe directly, the molecular dynamics simulations were done to study transient pores appearing in the bilayers [92].

The first experiments of polymer confined to lyotropic lamellar phases was reported by Kékicheff et al. in 1984 [74]. Studies on phase diagrams by deuterium NMR and X-ray scattering were performed in order to investigate the dissolving properties of polymer PEO in a lamellar phase made of SDS bilayers. Firstly, the authors have found that the solubility limit of PEO molecules is surprisingly large (one-fourth of the water of mesophase can be replaced by polymer), and does not depend on the molecular weight of PEO. Secondly, they observed the shrinking of the thickness of water layers $\bar{d}$ caused by polymer adsorption on SDS/water interfaces.

In this work, the authors show also (neutron scattering) that the smaller macromolecules are arranged according to the periodicity of the lamellar mesophase and are therefore located in the water layers. For the larger ones, they spread in two or more water layers, and this crossing must be associated with some deformations of the bilayers. The authors show one possible model for these deformations (Figure 1.9), the deformation is a localized pinching of the SDS bilayer coupled with the passage of one PEO strand across the bilayer. This brings a minimal perturbation to the center of the bilayer, while releasing the confinement of the macromolecule.

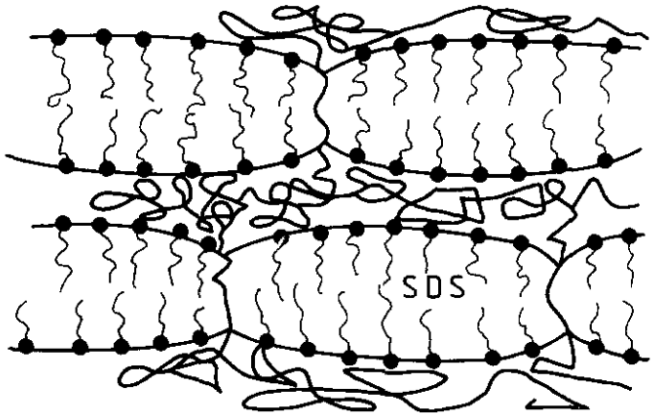

Figure 1.9: A model for the deformation of a SDS bilayer. PEO strands cross from one water layer into the next [74].

The early investigations of polymer-doped lamellar phases concentrate on a polymer-induced phase separation [87]. Small angle X-ray scattering and neutron scattering study of a three-component lamellar phase composed of water, nonadsorbing water-soluble polymer (polyvynilpyrolidone), fluid membranes made of a cationic surfactant (cetylpiridiumchloride) and cosurfactant (hexanol) provide detailed information on polymer contribution to the smectic compressibility modulus $\bar{B}$ [11]. In this work, the authors have shown that the presence of a nonadsorbing polymer in the solvent induce effective destabilizing interaction between the bilayers, which is of purely entropic origin, similar to the depletion interaction between colloidal particles in a polymer solution. In all regimes of polymer confinement (see Figure 1.8) they have obtained a negative polymer contribution to the layer compression modulus inferred from the Caillé parameter, η, meaning that the polymer-mediated interaction tends to destabilize the smectic order. However, the authors found that in the absence of added salt, and for highly charged membranes this destabilizing interaction cannot compete with the stabilising electrostatic interaction. However, the lamellar/lamellar phase separation were achieved by adding salt and thereby screening the electrostatic interaction.

M.-F. Ficheux in her PhD work has investigated the phase diagrams of the quaternary system composed of SDS/octanol/water/PEG [44–46]. In this system neutral water-soluble polymer PEG partially adsorbs onto the negatively charged surfactant bilayers.

Ficheux established the phase diagrams for several molar ratios alcohol/surfactant (A/S) and for several PEG molar masses. Large amounts of PEG can be solubilized in the mesophase: up to 50 % of the water can be replaced by the polymer. What is remarkable is the appearance of a two-phase region in the phase diagram for both PEG of molar masses M_w = 8000 and 22600 g/mol without salt addition. Two lamellar phases with different periodicities coexist in this region. The extent of this region, that is bounded by two critical points, is polymer size dependent, and is less wide for the PEG 8000. The periodicity d and bilayer thickness δ decrease when the concentration of polymer in water increases, as already observed (for d) and assumed (for δ) by Kékicheff in 1984. The observed decrease of δ is attributed to a slight increase of the average area per polar head in the bilayer. They focused then on the system SDS/octanol/water/PEG 22600 (A/S=2.7). In a first study [45], they qualitatively show that an increase in the polymer concentration in water leads to a decrease of the elastic compressibility modulus $\bar{B}$. In a second study the authors investigated the approach of the critical point by studying the Caillé exponent η (neutron scattering [46]). They found that this exponent apparently diverges at the critical point, which leads to the decrease and disappearance of $\bar{B}$ at this special point.

Javierre in her PhD work has studied the effect of addition of PEG on ternary SDS/hexanol/water and quaternary water-dodecane-hexanol-SDS mixtures [69]. It was possible to replace up to 16 % of water contained in the lamellar phase (made of SDS-hexanol-water) with PEG. This amount is smaller that previously found in the SDS-octanol-water-PEG (50 %). The comparison shows that the polymer solubility in lamellar phase and the extent of the two-phase area increase with alcohol chain length. The study of inverse structures has shown most striking results - it is not possible to incorporate PEG in the classical sponge phase, even if the thickness of the water layer in this structure is identical to that present in the lamellar phase. Clearly, the topology of the bilayers appears as a crucial parameter for the solubilization of PEG within the inverted bilayers [70].

Freyssingeas [47, 48] studied the system consisting of SDS/pentanol/water/PEG system. The compressibility modulus of a lamellar stack containing guest polymer molecules was measured by Surface Force Apparatus [48]. The lamellar phase was induced from a micellar phase. This avoided problems resulting from the viscosity and turbidity characteristic of the lamellar samples. Increasing the amount of polymer resulted in a marked decrease in the layer compressibility modulus $\bar{B}$. The possible origins discussed for this enhanced attractive contribution are the adsorption of the PEG at the interfaces which could lead to a bridging interaction; or the altering of the classical electrostatic interaction due to the PEG (the charge distribution could change); or both effects are superimposed.

Herrmann L. in her PhD thesis [55] continued the study of SDS/octanol/water/PEG phase diagram. She investigated the smectic compressibility modulus by Surface Force Apparatus technique. Keeping the membrane volume fraction constant the PEG dissolu-

tion results in a marked decrease in the elastic compressibility modulus, $\bar{B}$. This indicates a softening of the repulsive interactions between the lamellae mediated by polymer adsorption on the bilayers/ aqueous solution interface. Insights into the behavior of the mesophases in confined geometries and thereby their stabilization mechanism are gained by noting a plastic contribution due to the presence of edge dislocations in the wedge-like geometry [57]. In [56] the authors demonstrate that despite many intricacies, the interaction between charged surfaces in aqueous solutions with monovalent counterions is fully accounted for by electrostatics at distances larger than a few nanometers, provided the weak coupling theory for electrostatics is implemented.

The role of added polymers between the lamellar bilayers was investigated theoretically by Daoud and de Gennes [28] in 1977 and revisited by Brooks and Cates [14]. They classified the situations of the polymer confinement into four regimes and derived the corresponding free energy for each regime. On the basis of these works Ligoure et al. [88] have calculated the polymer contribution to the elastic compressibility modulus. The overall mechanism for this was found to be a softening of the repulsive interactions between the bilayers due to the presence of polymer in the solvent. Note that in all these theoretical works, the polymer is a homopolymer that does not adsorb on the membranes.

The influence of an adsorbing homopolymer on the curvature moduli has been investigated in several theoretical papers by de Gennes [36], Brooks [15,16], Clement [23] (using a meanfield approach). The theoretical prediction is a decrease in the bending modulus when polymer is adsorbed onto the membranes. Note, that the strongest assumption in this theory is the homogeneous, non-penetrating adsorption of the polymer. A work of Blokhuis et al. investigates the interaction between two planar, polymer-adsorbing plane using a self-consistent field theory [9].

More recent experiments report the effect that seems to be not in agreement with theoretical studies:

- Warriner et al. [132] have been investigated the influence of polymer molecular weight in lamellar gels based on PEG-lipids (PEG-DMPE mixtures). In the system the linear polymer chains anchor with one end to the membranes. They observe a phase transition from the lamellar to gel phase which occurs with increasing the polymer content. This effect is explained by the changes of the membrane elastic constants [131,132].

- Yang et al. [136] report an increase of κ, for the case of polysoaps addition. The long chain of polysoaps is anchored with sidechains to the membrane. Interestingly, the authors claim that the contribution of the increased layer thickness by the polymer can be neglected.

- addition of non-adsorbing polymers to a lamellar phase was studied by Bouglet et al. [12]. The authors find that the bending elastic modulus κ is insensitive to the amount of polymer in the lamellar phase while saddle-splay modulus $\bar{\kappa}$ is strongly decreased (cryo-

TEM study).

- the effect of rigid inclusions (a triblock peptide) on the bending rigidity of lamellar phase was studied in the work of Tsapis et al. [130]. The Caillé parameter, η, was found to decrease with peptide concentration. Since the peptide decorated lamellar phase stabilized by thermal fluctuations, this decrease was interpreted as an increase of the bilayer effective thickness. The measurements of bending rigidity have shown that small amounts of peptide induce a dramatic stiffening of the lamellar phase.

- Palomares et al. have shown that a polymer (PEG) induces a topology transition of the bilayers of an anionic surfactant system (SDS-hexanol-brine), provided that the electrostatic interactions between the membranes are screened. The main effect of increasing the polymer concentration in the solvent of the lamellar and sponge phases is to produce a phase transformation into the vesicular phase [63]. The study of the effect of PEG on the bending elastic modulus of surfactant membranes [62] have shown the measured increase in κ (DLS), which is not expected from the available theories.

Therefore, in this thesis we focus on the effect of adsorbing polymer (PEG) on the structure and elastic properties of lyotropic lamellar mesophases. The theoretical background of deuterium NMR is presented in the second chapter. In the third chapter the materials and experimental methods are described. The fourth chapter deals with experimental results obtained from SAXS and NMR: the structural parameters of lamellar mesophases and the bending modulus calculations. The special behaviour of the mesophases (microscopy study) in the diluted part of the phase diagram is discussed as well in the fourth chapter. The fifth chapter is dedicated to the study of diffusion coefficient of polymer in confinement by FRAPP technique. In the sixth chapter the elastic compressibility modulus $\bar{B}$ is discussed (SFA measurements).

Chapter 2

NMR: Theoretical background

This chapter outlines the theory behind the measurements and calculations. An introduction to the general aspects of ^{2}H NMR spectra together with the quadrupolar echo technique is given first. Then in more details are described the NMR spectra from deuterons in liquid crystalline unoriented samples together with the definition of the carbon-deuterium bond order parameter. Afterwards, the technique which is used to calculate the bending elastic modulus from the measured quadrupolar splitting is presented.

2.1 Introduction

Nuclear magnetic resonance (NMR) spectroscopy is a powerful analytical tool. The observable measured in NMR is magnetization and its evolution over time. ^{2}H NMR applied to lipid membranes has been discussed in excellent reviews by Seelig [115, 116] and Davis [31]. It provides valuable information about the phase behaviour of lyotropic liquid crystalline systems (Kekicheff, 1989 [73]).

Let us first begin with some common concepts about nuclear magnetism. A nucleus with nonzero spin, I, behaves as a small bar magnet, with a magnetic moment, μ, given by:

$$\mu = \gamma\hbar\sqrt{I(I+1)} \tag{2.1}$$

where $\hbar$ is the reduced Planck's constant and γ is the gyromagnetic ratio, an inherent property of the nucleus equals to $4.1 * 10^7$ T^{-1} s^{-1} for ^{2}H.

The observed value of the magnetic moment is the projection of μ on the z axis, μ_z. According to the results of quantum mechanics it is:

$$\mu_z = m_I\gamma\hbar \tag{2.2}$$

where m_I is the magnetic quantum number. The allowed value of m_I are $I, (I-1), ..., 0, ..., (-I+1), -I$ giving rise to $2I+1$ possible states for the nucleus.

In the absence of the magnetic field the energy of the nucleus is independent of the m_I, but degeneracy is removed when an external field is applied. In a magnetic field of magnitude B_0, where direction defines the z axis, the energy is given by Zeeman interaction hamiltonian, $\hat{H}_{Zeeman} = -\gamma\hbar B_0 \hat{I}_z$:

$$E = -\mu_z B_0 = -m_I \gamma \hbar B_0 \tag{2.3}$$

While the Zeeman interaction is useful for identifying different types of nuclei placed in magnetic fields, structural and dynamic information may be obtained by considering other magnetic and electrical interactions coupling with the nucleus. These interactions are perturbations to the Zeeman interaction. Thus, the full NMR hamiltonian may be expressed as:

$$\hat{H} = \hat{H}_{Zeeman} + \hat{H}_J + \hat{H}_{CS} + \hat{H}_{DD} + \hat{H}_Q \tag{2.4}$$

where $\hat{H}_{Zeeman}$ is the Zeeman interaction, $\hat{H}_J$ is the J coupling or scalar interaction, $\hat{H}_{CS}$ is the chemical shift coupling, $\hat{H}_{DD}$ is the dipolar coupling and $\hat{H}_Q$ is the quadrupolar coupling and reveal the tensorial character. All of these interactions result in small perturbations of the resonance away from the Larmor frequency:

$$\nu_0 = \frac{\gamma}{2\pi} B_0 \tag{2.5}$$

it depends on the strength of the magnetic field and the nucleus of interest (in our spectrometer $B_0 = 7.05$ T and $\nu_0 = 46.1$ MHz for Deuterium). The magnitude of the quadrupolar interaction for Deuterium with a spin $I = 1$ relative to the strengths of the dipole-dipole, scalar and chemical shift interactions is sufficiently large to permit its accurate measurement and interpretation (i.e. the order of magnitude $\hat{H}_{DD}$ is 10^3 Hz and $\hat{H}_Q$ around 10^5 Hz). Therefore, only Zeeman and quadrupolar coupling interactions have to be taken into account.

The charge distribution around the nucleus with a spin greater than 1/2 is no longer spherical, thus, it necessarily possesses an electric quadrupole moment and electric quadrupoles interact with electrical field gradients (EFG). Therefore by definition the quadrupolar interaction is an interaction between the nuclear spin $I \geqslant 1$ and the electric field gradients surrounding it. The quadrupolar interaction depends on the orientation of the nucleus with respect to the magnetic field, so that ^{2}H NMR can be used to gain information about the positions of deuterons in the sample and the quadrupolar hamiltonian can be written in tensorial form as:

$$\hat{H}_Q = \frac{eQ}{6I(2I-1)\hbar} \mathbf{I} \cdot e\mathbf{q} \cdot \mathbf{I} \tag{2.6}$$

where Q is the electrical quadrupolar moment which depends on the nature of the

considered nucleus, **I** is the nuclear spin operator, e is the electron charge. The tensor $e\mathbf{q}$ describes the EFG, where each component $eq_{\alpha\beta}$; $\alpha, \beta = x, y, z$ represents the gradient of the α component of an electric field in the direction β. The EFG tensor $e\mathbf{q}$ is traceless. The asymmetry parameter, η, is defined from the principal axis system (see Figure 2.1):

$$\eta = \frac{q_{xx} - q_{yy}}{q_{zz}} \tag{2.7}$$

where eq_{zz} corresponds to the largest principal component of the electric field gradient. In the absence of axial symmetry, i.e. $q_{xx} \neq q_{yy} \neq q_{zz}$, the quadrupolar hamiltonian in Eq. (2.6) may be expressed to the first order in the applied field $\mathbf{B}_0$ [42] as

$$\hat{H}_Q = \frac{3e^2Qq_{zz}}{8I(2I-1)\hbar}(3cos^2\theta - 1 + \frac{1}{2}\eta \sin^2\theta \cos 2\phi)(3\hat{I}_z^2 - \hat{I}^2) \tag{2.8}$$

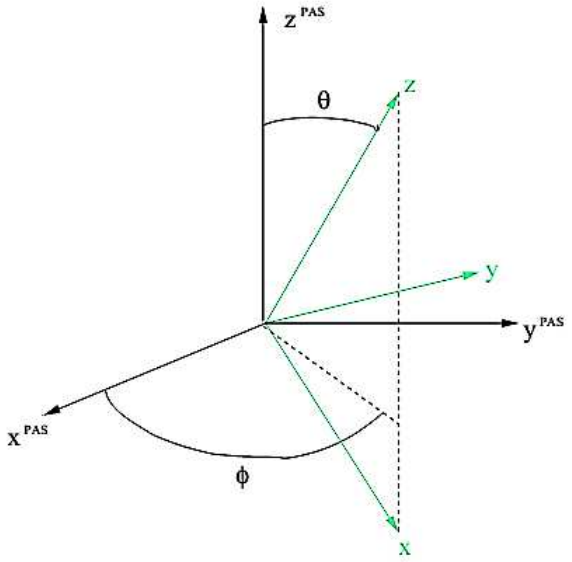

Figure 2.1: Principal axis system of the electric field gradient.

At the fields of several tesla commonly employed in NMR, the quadrupolar Hamiltonian results in only a small shift of the Zeeman energy levels. The energy levels for ^{2}H in a magnetic field parallel to the z component $eq_{zz} = eq$ of the electric field gradient tensor are:

$$E_m = -\frac{\gamma h B_0 m}{2\pi} + \frac{e^2Qq}{4}(3m^2 - 2) \tag{2.9}$$

As a result of the quadrupolar interaction the frequencies of the allowed transitions are thus displaced from the Larmor precession frequency $\nu_0 = \gamma B_0/2\pi$ by $\pm\, 3e^2qQ/4h$ for deuterium. Resulting in a doublet of separation $\Delta\nu_Q = 3e^2qQ/2h$. This is the maximum obtainable splitting, since B_0 was defined as being parallel to eq_{zz}. The energy levels diagram is presented in Figure 2.2.

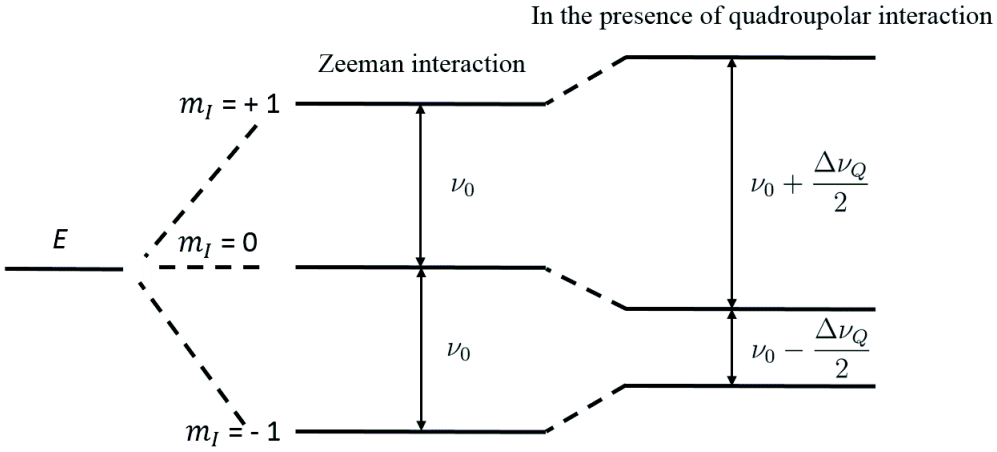

Figure 2.2: Alignment of spins in a magnetic field where $I = 1$, without and with the influence of the quadrupole interaction.

For a powder sample, consisting of a random distribution of eq_{zz}, the NMR spectrum is made up of contributions from all orientations of the molecule-fixed eq_{zz} with respect to the external B_0. For a given orientation the splitting is given by:

$$\Delta\nu_Q = \frac{3}{4}\nu_Q(3\cos^2\theta - 1 - \eta\sin^2\theta\cos 2\phi) \tag{2.10}$$

where $\nu_Q = e^2Qq/h$ is termed the "static quadrupolar coupling constant" which varies according to the chemical environment.

^2H is a spin-1 nucleus with a relatively small electric quadrupole moment ($Q = 0.28$ e$\cdot$ fm^2) which gives rise to the quadrupole coupling constant, ν_Q, in the range 140-220 kHz in organic compounds for instance. Also pertaining to C-D bonds eq_{zz} is essentially parallel to the bond direction and η, the asymmetry parameter, is very close to zero so that the second term in Eq. (2.10) may be ignored. According to Eq. (2.9) and (2.10) the resonance frequency shows the following dependence on the orientation angle θ:

$$\nu_\pm = \nu_0 \pm \frac{\Delta\nu}{2} = \frac{\gamma B_0}{2\pi} \pm \frac{3e^2qQ}{4h}\left(\frac{3\cos^2\theta - 1}{2}\right) \tag{2.11}$$

It is convenient to introduce a "reduced" resonance frequency $\xi_\pm$:

$$\xi_\pm = \frac{\nu_\pm - \frac{\gamma B_0}{2\pi}}{\frac{3e^2qQ}{4h}} = \pm\frac{3\cos^2\theta - 1}{2} \tag{2.12}$$

Thus the orientation dependence of the splitting is given by the factor $(3\cos^2\theta - 1)/2$, where $1 \geq \xi_+ \geq -1/2$ and $-1 \leq \xi_- \leq 1/2$.

The probability of finding a number of nuclei N oriented between angle θ and $\theta + d\theta$ with respect to B_0 is given by the area of a zone of the sphere, $2\pi r^2 \sin\theta d\theta$, multiplied by

the spin surface density:

$$dN = \frac{N}{4\pi r^2} 2\pi r^2 \sin\theta d\theta = \frac{1}{2} N \sin\theta d\theta \tag{2.13}$$

thus, the probability density $p(\theta)$ is given by

$$p(\theta) = (1/2)\sin\theta, \int_0^\pi p(\theta) d\theta = 1 \tag{2.14}$$

The fraction of spins with the reduced resonance frequency is described by $p(\xi)d\xi$, so that the two probability densities $p(\theta)$ and $p(\xi)$ are related to each other according to

$$p(\xi) = p(\theta)\frac{d\theta}{d\xi} = \frac{1}{2}\sin\theta\frac{d\theta}{d\xi} = -\frac{1}{2}\frac{d\cos\theta}{d\xi} \tag{2.15}$$

The NMR spectrum contains two resonances ξ_+ and ξ_-, which correspond to the spin transitions $m_I = 0 \leftrightarrow 1$ and $m_I = -1 \leftrightarrow 0$, so that

$$p(\xi) = p(\xi_+) + p(\xi_-). \tag{2.16}$$

Combining Eq. (2.12) and (2.15) it then follows

$$p(\xi_\pm) \sim \frac{1}{\sqrt{(\pm 2\xi_\pm + 1)}} \tag{2.17}$$

Figure 2.3 illustrates a typical powder NMR spectra, the probability densities $p(\xi_+)$ and $p(\xi_-)$ correspond to the two possible spin transitions: $+1 \leftrightarrow 0$ and $0 \leftrightarrow -1$ and $p(\xi)$ diverges at frequencies $\xi = \pm 1/2$, which corresponds to nuclear sites inclined at $\theta = 90°$ with respect to B_0. The frequency separation $\Delta\nu_Q$, called the quadrupolar splitting, of the most intense absorptions peaks (at $\xi = \pm 1/2$) in the powder lineshape is:

$$\Delta\nu_Q = \frac{3}{4}\nu_Q \tag{2.18}$$

The total absorption intensity depends on transition probability $I(\xi_\pm)$, taking the assumption that it is equal for both deuterium transitions $I(\xi_\pm) = I$, it reads:

$$S(\xi) = Ip(\xi) \tag{2.19}$$

NMR resonance lines are generally broadened due to magnetic interactions between neighbouring nuclei [115]. The shape of an individual resonance line centered at ξ^* quite often can be approximated by a normalized Gaussian of the form:

$$I(\xi - \xi^*) = \frac{1}{\sqrt{2\pi\sigma}} \exp[-(\xi - \xi^*)^2/2\sigma^2)] \tag{2.20}$$

A Lorentzian lineshape or the Gaussian together with Lorentzian broadening can be assumed [115]. In a powder-type spectrum the total absorption $S(\xi)$ at a frequency ξ is given by the convolution of the lineshape function $I(\xi - \xi^*)$ with the corresponding probability function $p(\xi^*)$:

$$S(\xi) = \int_{-\infty}^{+\infty} I(\xi - \xi^*) p(\xi^*) d\xi^* \tag{2.21}$$

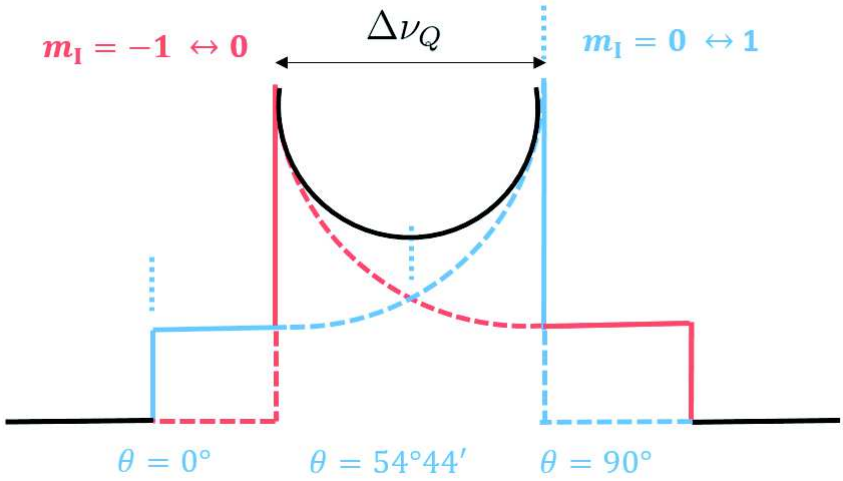

Figure 2.3: The form of a $^2H(I = 1)$ quadrupole powder pattern. There are two possible transitions for a spin-1 nucleus ($m_I = +1$ to $m_I = 0$ and $m_I = 0$ to $m_I = -1$), which give rise to the mirror image line shapes.

The convolution is equivalent to the sum of Lorentzian (Gaussian) line shapes located at every frequency weighted by the intensity of the given frequency. The broadening can be expressed in hertz, and it is the reciprocal of the spin-spin relaxation time T_2 [8].

2.2 Quadrupolar echo technique

The main instrumental limitation in NMR experiment which has to be taken into account is the recovery time of the receiver. The finite 'dead-time' of the receiver following the radiofrequency pulse causes the initial data points of the free induction decay (FID) to be lost, and the Fourier-transformed spectrum is thus inaccurate. For a ^{2}H NMR spectrum with a width of 250 kHz this would require a receiver dead-time (plus one half of the pulse width) to be shorter than $1/(2\pi \cdot 500\ \text{kHz}) \sim 0.3\ \mu\text{s}$.

The only practical solution to this dead-time problem is to translate t = 0 to well beyond the spectrometer recovery time. To do this the quadrupolar echo pulse sequence was proposed in the lipids study by Davis et al. (1976 [30]), which consists of a pair of pulses separated by a time τ longer than the spectrometer recovery time, and 90° out of phase with one another. The echo 90°_x - τ - 90°_y - τ is illustrated in Figure 2.4. The powder pattern is then obtained by Fourier transformation of the last half of the echo.

2.3 ^{2}H NMR of Lyotropic Liquid Crystals

The lyotropic liquid crystals exhibit a variety of stuctures, among them lamellar phase is the most appropriate model of a biological membrane. The soap/water mixtures form a

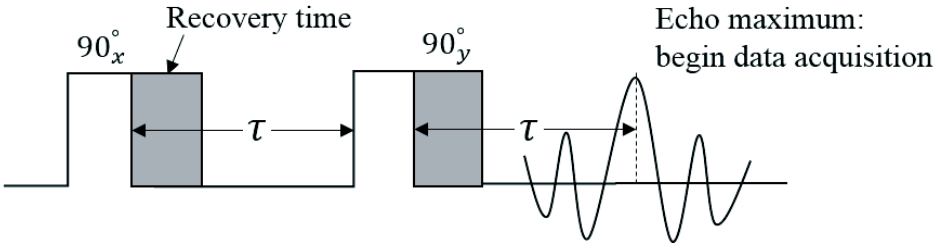

Figure 2.4: The quadrupole echo pulse sequence 90°_x - τ - 90°_y - τ. Fourier transformation begins at the top of the echo.

lamellar phase over a range of water concentrations. These systems are attractive because with them it is possible to study the order and dynamics of independent hydrocarbon chains in a lamellar structure. Deuteron NMR is a standard method for investigating the structure and dynamics of membranes, phospholipid bilayers and related model system.

The ^{2}H NMR spectrum of a liquid crystalline anisotropic phase containing D_2O confined in the water layers of a stack of membranes exhibits a quadrupolar splitting characteristic of the water molecules (Kekicheff, 1989 [73] Figure 2.5a). Despite the rapid motion of water molecules, a small degree of orientational order remains enforced by the orientation of the anisotropic liquid crystalline phase. Spectra of isotropic phases like, for example, cubic liquid crystalline phases exhibit zero splitting. Both lamellar and hexagonal phases produce splittings. Figure 2.5b shows the powder patterns obtained for an isotropic phase (iso), a hexagonal phase (hex), and a lamellar phase (lam) [127]. The lamellar and hexagonal spectrum can be distinguished because the ^{2}H powder pattern for the hexagonal phase of amphiphilic rods has a splitting that is roughly half of that for the corresponding lamellar phase [127]. This is due to lateral diffusion about the rod generating one more axis of symmetry for further averaging of the quadrupolar interaction.

2.3.1 The acyl chain order parameter

Deuterium NMR can be used to reveal anisotropic motions. For anisotropic motions each deuteron contributes a doublet due to the quadrupole moment of the deuterium nucleus, while for rapid isotropic motions the deuterium NMR spectrum of deuteron consists of one single line as the splitting is averaged to zero [116].

Lamellar phase is characterized by the tendency to align the constituent surfactant molecules parallel to the long molecular axes. Due to this packing, rotations perpendicular to the long axis are restricted while those around this axis are not hindered leading to anisotropic motions. In order to define the average order in the system a macroscopic sample of lamellar mesophase can be considered such as composed of a large number of microdomains ($\simeq$ 20 μm). In one microdomain the average orientation of the ensemble of molecules is characterized by its director, the optical axis of $\mathbf{n}_0$. Around this axis

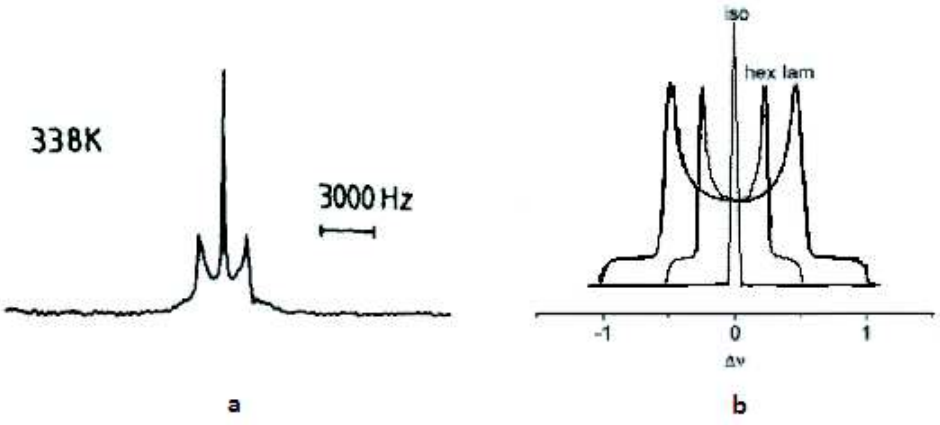

Figure 2.5: a) The spectrum of D_2O molecules for a sample in the 3-phase region of the phase diagram (lamellar + isotropic + hydrated crystal). The D_20 molecules in the lamellar phase give rise to the doublet, and those in the isotropic phase to the sharp central line [73]. b) Illustration of the powder patterns obtained for isotropic (iso), hexagonal (hex),and lamellar (lam) liquid crystalline phases.

the movements of the surfactant molecules are considered to have a cylindrical symmetry. The molecular origin of membrane flexibility is due to the fluctuations around the director axis [116].

The perturbation depends on the orientation of the electrical environment of the D nuclei (CD bonds) with respect to the external magnetic field of the experiment $\mathbf{B}_0$. A perdeuterated cosurfactant molecule embedded in the lamellar mesophase (see Figure 2.6) that is placed in a magnetic field experiences different movements [5]:

- intramolecular motions, i.e. isomerisations of CD_2 groups around the molecular axis (angle θ_I);
- molecular motions, due to anisotropic reorientation of the molecule with respect to the normal to the local surface, $\mathbf{n}$ (angle θ_M);
- fluctuations of bilayer domains, i.e. fluctuations of $\mathbf{n}$ with respect to the optical axis of the smectic liquid crystal $\mathbf{n}_0$ (angle θ_F).

This angular dependence is described by second-order spherical harmonics. The observed quadrupolar splitting $\Delta\nu_Q$ is expressed by:

$$\Delta\nu_Q = \frac{3}{2}\nu_Q \left(\frac{3cos^2\theta_L - 1}{2}\right) S_{C-D} \tag{2.22}$$

where the angle θ_L represents the orientation of the normal to the membrane $\mathbf{n}_0$ with respect to the magnetic field direction $\mathbf{B}_0$, ν_Q is the quadrupolar coupling constant, S_{C-D} is the orientational order parameter of the $C-D$ bond accounting for the fast (in the

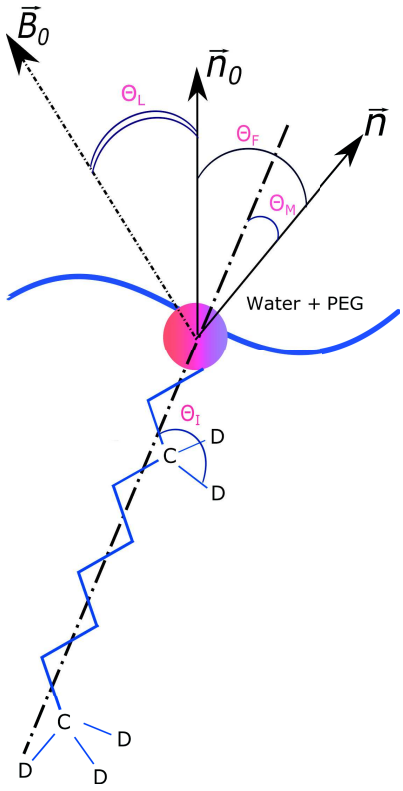

Figure 2.6: Schematic view of the various axially symmetric motions of an amphiphilic molecule in a lamellar phase. The quadrupolar splitting becomes scaled according to the angle between the particular $C-D$ bond and the axis of motional averaging [5].

NMR time scale) contributions of anisotropic motional averages in the bilayer, and given by:

$$S_{C-D} = S_I S_M S_F = \left\langle \frac{3cos^2\theta_I - 1}{2} \right\rangle \left\langle \frac{3cos^2\theta_M - 1}{2} \right\rangle \left\langle \frac{3cos^2\theta_F - 1}{2} \right\rangle \tag{2.23}$$

The angular brackets denote a time-space average. To derive the Eq. (2.23), it is assumed that molecular motions operate at different time scales (see Table 2.1). The term S_F accounts for the fluctuations of the bilayers in the lamellar mesophase.

Collective fluctuations of the membranes (angle θ_F) and intermolecular motions (angles θ_I, θ_M) must be uncorrelated. We shall only assume that for the time being the product $S_I S_M$ remains constant once the composition of the membrane is fixed. It is fulfilled here since collective motions are known to occur at much slower time scales than molecular motions. Only the motions slower than 10^{-5} s (a characteristic time of the quadrupolar interaction) have to be taken into account.

Table 2.1: Characteristic times of the molecular motions in comparison to the time of the observation (logarithmic scale) [72].

Time, s:	**Molecular motions**
10^3	Flip-flop time for 1 SDS molecule in a bilayer
$10^{-3} - 3 \cdot 10^{-4}$	Diffusion time for water molecules over 1 μm (a characteristic size of the crystallites observed by microscope)
$3 \cdot 10^{-5}$	Characteristic times of the quadrupolar interactions
10^{-8}	Diffusion time of a SDS molecule along a curved interface (time during which a SDS molecule rotates by 1 radian)
10^{-9}	Average time between 2 conformations for a SDS molecule
10^{-10}	Exchanging time between adsorbed/free water
10^{-11}	Time between 2 elementary jumps of a water molecule between 2 hydration sites
10^{-12}	Rotation of the bond

2.3.2 Thermal undulations of the bilayers in a lamellar phase

The fluctuations of the membranes can be described by the local displacement $U_i(\mathbf{r})$ of the $i-th$ membrane at position $\mathbf{R} = (\mathbf{r}, id)$ with respect to the ideal undistorted network of planes, where d is the period of the lyotropic lamellar phase. $\boldsymbol{R}$ denotes the 3-d vector and $\mathbf{r}$ its projection on the (x, y) plane, z is the optical axis.

The energy of the fluctuations can be expanded at the lowest order in terms of the compression and bending. Instead of $U_i(\mathbf{r})$, a continuous variable $\tilde{u}(\mathbf{R})$ is generally used (de Gennes [33]).The continuous description implies that $\tilde{u}(\mathbf{R})$ is coarse-grained variable fluctuating at wavelengths longer than some cutoff length L_1 of the order of d. Note that the cutoff length L_1 satisfies $a \leq L_1 \leq L$ in which a is a molecular size parallel to the film and L the size of the sample. The free energy of the fluctuations is given by:

$$\Delta F[\tilde{u}] = \int_{\pi/L}^{\pi/L_1} \frac{d^3q}{(2\pi)^3} \left(\frac{\bar{B}}{2} q_z^2 + \frac{K}{2} q_\perp^4 \right) |\tilde{u}(q)|^2 \tag{2.24}$$

where $\bar{B}$ denotes the compressibility modulus and K is the bending elastic modulus.

The disorientation $\tilde{\theta}_F(\mathbf{R})$ which arises from $\tilde{u}(\mathbf{R})$ can be calculated [33]:

$$cos^2\tilde{\theta}_F(\mathbf{R}) = \frac{1}{1 + (\nabla_\perp \tilde{u})^2} \tag{2.25}$$

The order parameter S_F can be expressed as:

$$S_F \approx \frac{1}{2}\left(\frac{3}{1+\langle(\nabla_\perp \tilde{u})^2\rangle)+\langle(\nabla_\perp u_i^2\rangle}-1\right) \tag{2.26}$$

where $u_i(\mathbf{r}) = U_i(\mathbf{r}) - \tilde{u}(\mathbf{R})$ is the deviation of the film from the smooth sheet at position $\tilde{u}(\mathbf{r}, z = id)$.

Within a simple Gaussian theory Auguste et al. have calculated [5]:

$$\langle(\nabla_\perp u_i)^2\rangle = \frac{1}{8\pi}\frac{k_B T}{\kappa}\ln\left(1+\frac{\kappa\left(\frac{\pi}{a}\right)^4 d}{\bar{B}}\right) \tag{2.27}$$

Inserting this result in Eq. (2.22), and for $\theta_L = \pm\pi/2$, one obtains the effect of thermal fluctuations of the membrane upon the recorded quadrupolar splitting:

$$\Delta\nu_Q = \alpha\left(\frac{3}{1+\frac{1}{8\pi}\frac{k_B T}{\kappa}\ln\left(1+\frac{\kappa\left(\frac{\pi}{a}\right)^4 d}{\bar{B}}\right)}-1\right) \tag{2.28}$$

where α (corresponding to $\frac{3}{4}\nu_Q S_I S_M$) is related to the internal properties of the amphiphilic molecule in the membrane.

Thus $\Delta\nu_Q$ is directly related to the bending modulus of the membrane κ and also to the compressibility modulus $\bar{B}$ which is related to the intermembrane interactions.

Chapter 3

Materials and methods

3.1 Materials

3.1.1 Sodium dodecylsulfate

The anionic surfactant, sodium dodecylsulfate (SDS), was purchased from Sigma-Aldrich as an ACS reagent, 99 %. The CAS number is 151-21-3. The molar mass is 288.8 g/mol and the density 1.16 g/cm^3 at room temperature.

3.1.2 Octanol

- The aliphatic octanol was purchased from Sigma-Aldrich as an 1-octanol ($C_8H_{18}O$), anhydrous, $\geqslant$ 99 %. The CAS number is 111-87-5. The molar mass is 130.23 g/mol and the density 0.827.
- The perdeuterated aliphatic alcohol, N - Octanol (D17, 98 %), was purchased from Euriso-Top (SKU:DLM-620-1). The molar mass is 148.37 g/mol. Molecular formula: $CD_3(CD_2)_7OH$.

3.1.3 Water

The water is Milli-Q water (apparatus from Millipore), of resistivity 18.2 MΩ.cm at 25°C.

3.1.4 Poly(ethylene glycol)

The poly(ethylene glycol) (PEG), a linear water-soluble non-ionizable polymer, was purchased from VWR as "polyethylene glycol" ($HO(C_2H_4O)_nH$) for synthesis, of average molecular weight $\sim$ 20 000 g/mol" of brand Merck. The CAS number is 25322-68-3.

The gel permeation chromatography gives a molar mass of M_w =18 713 g/mol and a polydispersity index $M_n/M_w = 1.05$ [55, 57].

The radius of gyration is determined thanks to the set of data given in [18,74](the R_G versus M_w relation was determined by neutron scattering). For a polymer of molar mass M_w = 18 713 g/mol, a radius of gyration of 56 Å is inferred (Figure 3.1).

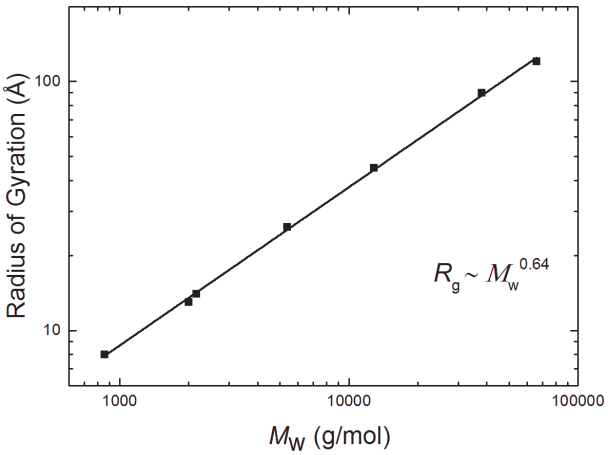

Figure 3.1: Radii of gyration of isolated PEO in D_2O: as deduced from a R_G vs M_w relation, which was determined by neutron scattering in [18].

The overlap concentration is estimated with $c^* = M_w/\frac{4\pi}{3}N_A R_G^3$ [52], which gives $\sim$ 42 g/L for PEG with the gyration radius of R_G = 56 Å. We can calculate the polymer volume fraction: $\bar{\phi} = C_p\rho_{wat}/(C_p(\rho_{wat} - \rho_{pol}) + \rho_{pol})$, where $\rho_{pol} = 1.2$ g/cm^3 is density of polymer, thus $\bar{\phi} = 0.035$, and the overlap polymer weight fraction $C_p^* = 4.1$ wt. %.

The PEG fluorescently labeled - mPEG-FITC* was purchased from brand Uptima (Cat. number BV1325) of molecular weight 20000 g/mol. See the molecular formula in Figure 3.2). FITC has an emission spectrum peak wavelength of approximately 495 nm **. The hydration radius of the probe is about R_H = 9 Å [98].

*Methoxyl PEG Fluorescein
**http://www.fluorophores.tugraz.at/substance/252

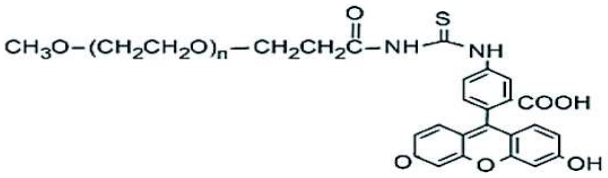

Figure 3.2: Fluorescently labeled mPEG-FITC.

3.1.5 Samples preparation

The samples were prepared following the procedure:

- first the polymer content is weighed and dissolved into Milli-Q water; the aqueous solutions are gently stirred for a few hours at room temperature. The polymer solutions form clear solutions in the whole range of compositions.
- the required quantity of SDS is weighed in a vial (for small amounts of sample); then the corresponding amount needed of polymer solution is taken from the mother solution and added to the SDS. The container is then sealed and attached to a setup that allows the container to rotate slowly. Thus, the SDS dissolves completely in the solution in a few hours;
- finally the required quantity of octanol is added to the mixture; slow rotation of the container is carried out for 3 to 4 weeks in an oven at (25.0±0.1)°C.

This procedure allows to obtain homogeneous mixtures at equilibrium. The samples are then stocked in the same oven at (25.0±0.1)°C before use. The position of the samples in the phase diagram are presented in Figure 3.3.

3.1.6 System studied

In Figure 3.2, the phase diagram established by Ficheux [44, 45] is presented. We have kept her notations: C_p denotes the polymer mass fraction in water, Φ_{memb} denotes the membrane mass fraction.

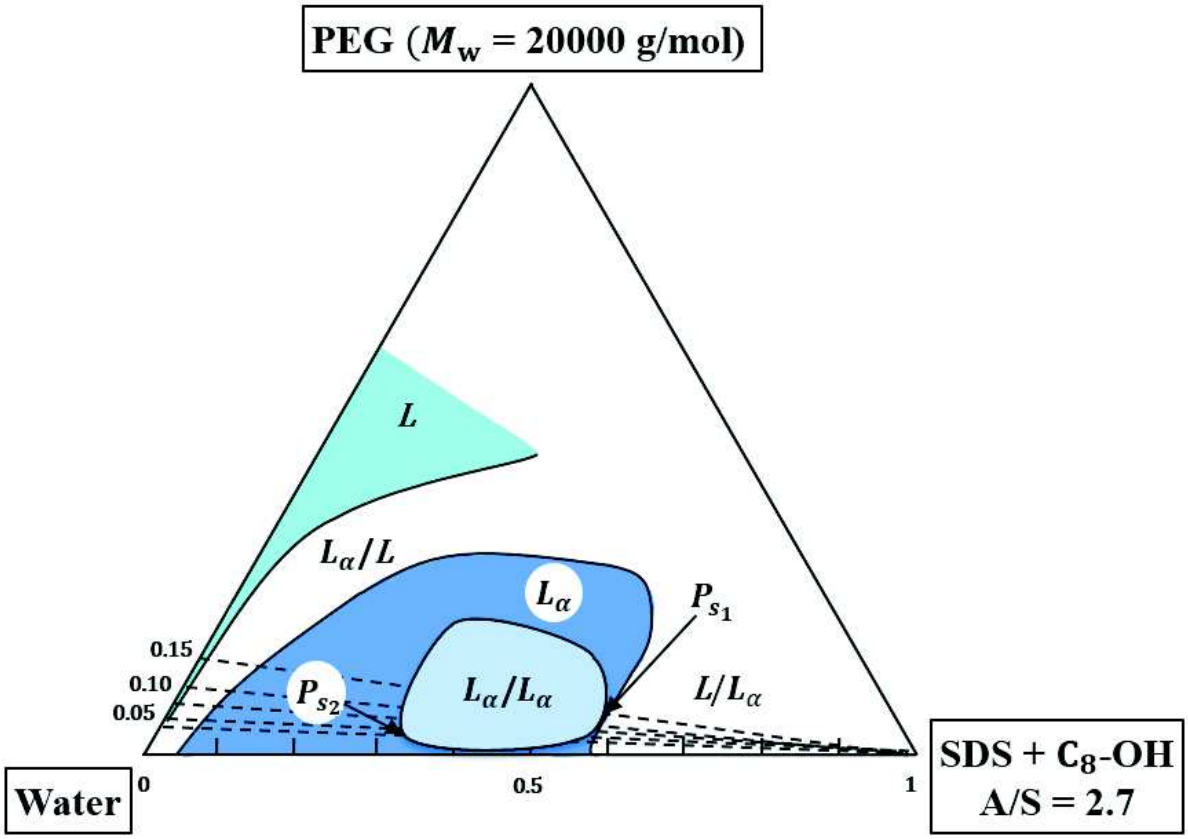

Figure 3.3: Section at constant temperature ($T = 25°C$) and membrane composition (octanol to SDS molar ratio A/S = 2.7) of the quaternary phase diagram water/octanol/SDS/PEG established by Ficheux [12]. Compositions are given as percentage by weight (wt. %) fractions. The "membrane" corner corresponds to SDS and alcohol. L is an isotropic phase, L_α a lamellar phase. L_α/L_α and other similar symbols represent two-phase domains. P_{s1} and P_{s2} are critical points.

Ficheux identified from the splitting Δq between the Bragg peaks positions of the two coexisting lamellar phases two candidates for critical points [44] at $\Phi_{memb} = 58$ wt. % and $C_p = 15$ wt. % for P_{s1} and $\Phi_{memb} = 32$ wt. % and $C_p = 3.8$ wt. % for P_{s2}. In [13], Ficheux et al. show that the Caillé exponent diverges on the approach of P_{s2}, which is attributed to the vanishing of the layer compressibility modulus $\bar{B}$. Therefore, in order to approach this critical point the appropriate samples were prepared. They are located in the phase diagram as presented in Figure 3.4 below:

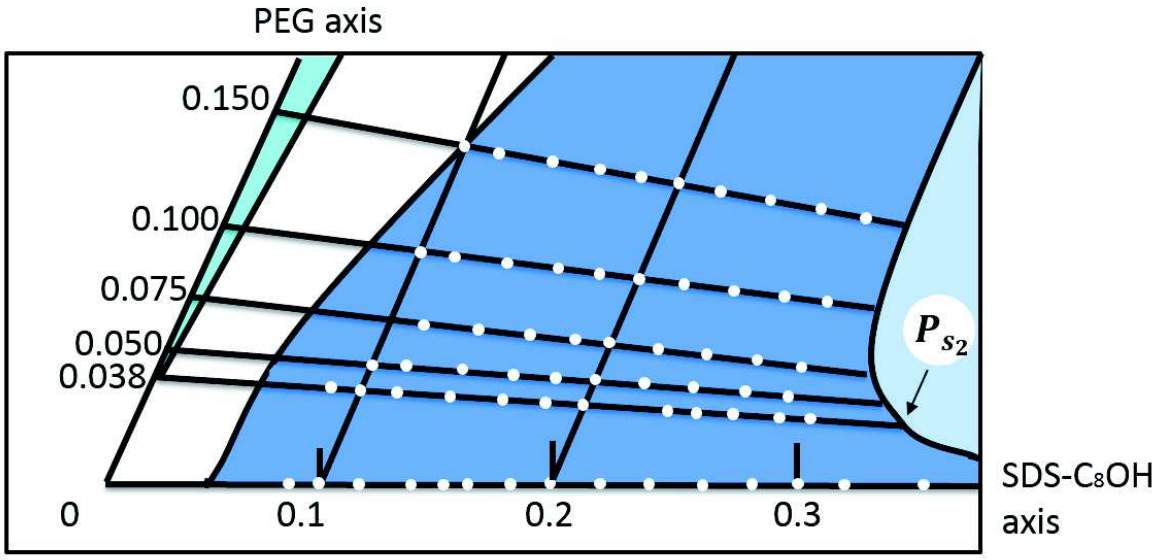

Figure 3.4: Section of Figure 3.3. The inset of the phase diagram represents the samples (white spots) prepared in order to investigate the effect of the polymer along six dilutions lines.

3.2 Methods

3.2.1 Cross-polarized optical microscopy

Polarized optical microscopy is a powerful tool for studying the microstructure of liquid crystal mesophases. It is used to check that the mesophases prepared as explained above are macroscopically homogeneous and located in the lamellar phase of the phase diagram. Indeed, lamellar mesophases are birefringent with characteristic textures that can be observed between crossed polarizers.

Two types of defects exist in Smectic A liquid crystals [101]: the focal conics and the dislocations. The focal conics involve large-scale curvature deformations of the layers. They can be divided into two types depending on the sign of the Gaussian curvature of the layers:

1) in a focal domain of the first type the Gaussian curvature is negative, the two principal radii of curvature (R_1 and R_2) having opposite signs everywhere. An ideal focal domain describes the molecular configuration in such a way that the layer thickness remains constant, except for the two specific lines (Figure 3.5).

2) in a focal domain of the second type, the layers have, on the contrary, a positive Gaussian curvature ($1/R_1R_2 > 0$). These domains are obtained by considering that the physical parts of the layer normals passing through the two conics are the two half-lines

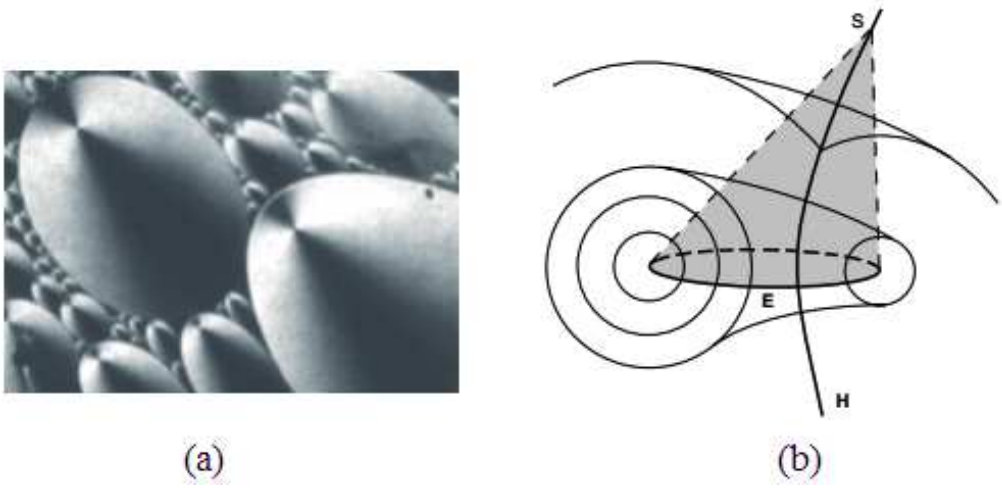

Figure 3.5: a) Focal conics texture seen between crossed polarizers in the polarizing microscope [101]; b) focal domain of the first type (FD1): the two singular lines are an ellipse E and its conjugated hyperbola H. The physical part of an FD1 is contained inside the cone of vertex S and having as base the ellipse E. The texture seen in a) is an association of such cones.

originating on the hyperbola (Figure 3.6 [101]). The domains of the second type are rarely encountered and only develop under very specific experimental conditions or upon approaching the transition toward a direct micellar phase [83]. It was found by Roux and co-workers that spherulites (or MLVs) can be produced from a lyotropic lamellar phase by applying a certain shear rate [119].

Oily streaks are formed by a regular stacking of focal conics and can be interpreted as "giant" dislocations of very large Burgers vector having undergone a structural transformation.

The dislocations, locally breaking the translational order and involving local variations of the layer thickness are classified in two basic types, edge dislocation and screw dislocation [78, 101]. The edge dislocation is more common in lyotropic lamellar systems, and it happens at the location where a membrane layer suddenly stops. These defects are not always visible using polarizing microscopy, but can be revealed by other techniques, for instance by freeze-fracture electron microscopy. The edge dislocation defects will be discussed in more details in section 3.2.5.

3.2.2 Electron microscopy

The samples microstructures were studied by Freeze fracture electron microscopy (FFEM) (Technai G2, FEI). The observation of the surface topography was performed on a Hitachi SU8001 microscope. The experiments were performed by Marc Schmutz through a microscopy platform at Institute Charles Sadron.

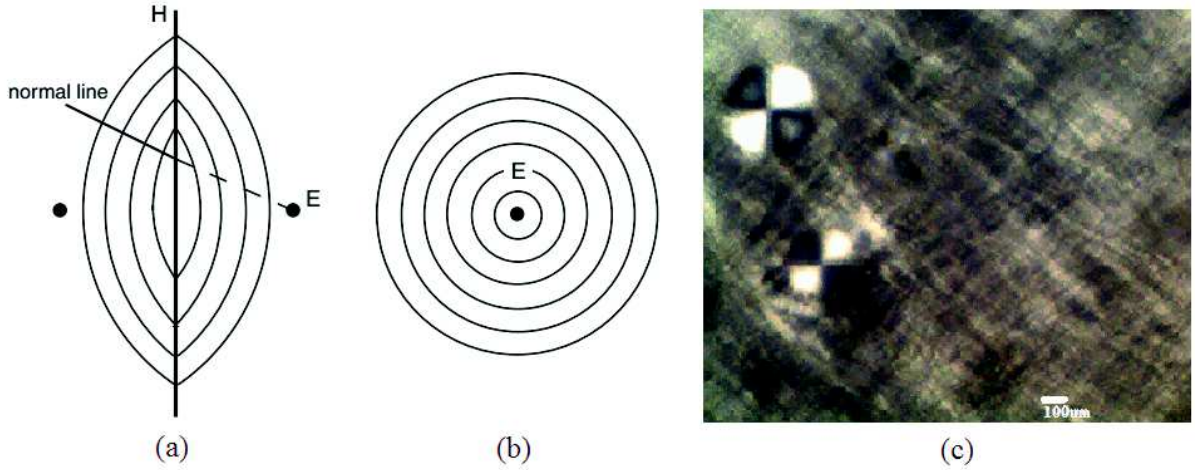

Figure 3.6: a) Focal domain of the second type when the ellipse is a circle and the hyperbola a straight line. b) Spherulite or onion (the ellipse is reduced to a point. [101]; (c) Patterns for spherulites observed under microscope.

The freeze-fracture technique consists of physically breaking apart (fracturing) a frozen sample [118]. After the fracturing the structural details exposed by the fracture plane is visualized by vacuum-deposition of platinum–carbon to make a replica for examination in the transmission electron microscope.

The freeze-fracture replica were prepared in four key steps:

1. rapid freezing - a drop of the mesophase was placed between two small copper holders to form a sandwich, which was then quickly plunged into liquid nitrogen to freeze the sample;

2. fracturing - the copper holder, with the frozen sample, was transferred into a cryo fracture apparatus. The sample was fractured under high vacuum at - 160°C;

3. replication - right away the fracturing a thin layer of platinum (2 nm) was evaporated under a 45° angle and a thick carbon film (20 nm) was deposited at 90° to stabilize the replica. Then the sample was warmed to room temperature under a dry N_2 stream;

4. replica cleaning - the replicas were washed in an organic solvent $CHCl_3$ to remove any remaining component of the original sample.

Finally, the resulting solid replica was collected on 400 mesh copper grids, and observed at 200 kV with a Tecnai G2 FEI transmission electron microscope (FEI France, Merignac, France), the images were recorded with a slow scan EAGLE camera (FEI France, Merignac, France).

In order to avoid a formation of ice crystals upon cryofixation we replaced 30 % of water (in volume) with a cryoprotectant - glycerol. Glycerol is soluble in water viscous alcohol, which is capable of changing the physical properties of water in order to lower the critical rate of freezing [50]. As exposure to glycerol may lead to artefacts in membrane structure, the mesophases were examined by cross-polarized optical microscopy as well.

Freeze-drying and metal shadowing were used in order to study the topology of the mesophases by Scanning Electron Microscope (SEM). Note, that SEM study at high magnification reveal the topography of the mesophases up to 100 μm. The goal is to freeze a hydrated sample, then to freeze-dry it under the vacuum (at - 80°C) and finally to shadow the surface of the specimen by metal evaporation (Platinum). The detailed protocols may be found in [114].

3.2.3 X-ray diffraction

X-Ray diffraction is one of the most reliable techniques for studying liquid crystalline phase structures. Because the wavelength of X-rays is comparable to atomic size it is used to provide the information about molecular arrangement.

X-ray diffraction experiments were performed in our laboratory, within the group of Michel Rawiso, by using a diffractometer (Figure 3.7) developed by Molecular Metrology (Elexience in France). X-rays are produced thanks to a rotating anode tube. The diffractometer operates with a pinhole collimation of the X-ray beam and a two-dimensional gas-filled multiwire detector. A monochromatic ($\lambda = 1.54$ Å with $\Delta\lambda/\lambda < 4\%, K_\alpha$ emission of the copper) and focused X-ray beam is obtained through a multilayer optics designed and fabricated by Osmic. The size of the incident beam on the sample was close to 600 μm. The sample to detector distance was set at 0.71 m, allowing to explore scattering vectors ranging from $q = 0.01$ Å^{-1} to 0.3 Å^{-1}. According to Bragg's law [51]:

$$q_n = 4\pi \sin(\theta/2)/\lambda \tag{3.1}$$

where λ and θ are the wavelength of the incident beam and the scattering angle, respectively. The q resolution related to the beam size of the sample and the beam divergence was close to 0.005 Å^{-1}. The samples were placed in sealed cells made between two Mica windows separated by a teflon spacer of 1 mm thickness. The exposure time was about 2 hours for each sample. Measurements were performed at room temperature.

Because each sample is made of many domains with random orientation with respect to the direction of the incident beam to the sample (Figure 3.8) the X-rays scatter at all angles in space, and the scattered beam produces a cone of diffraction. Indeed, due to the nature of the set of lattice planes, each set of planes gives its own cone of radiation thus concentric cones are formed. These cones create the arcs of rings, known as Debye-Scherrer rings, which are recorded during data collection. The resulting diffracted and

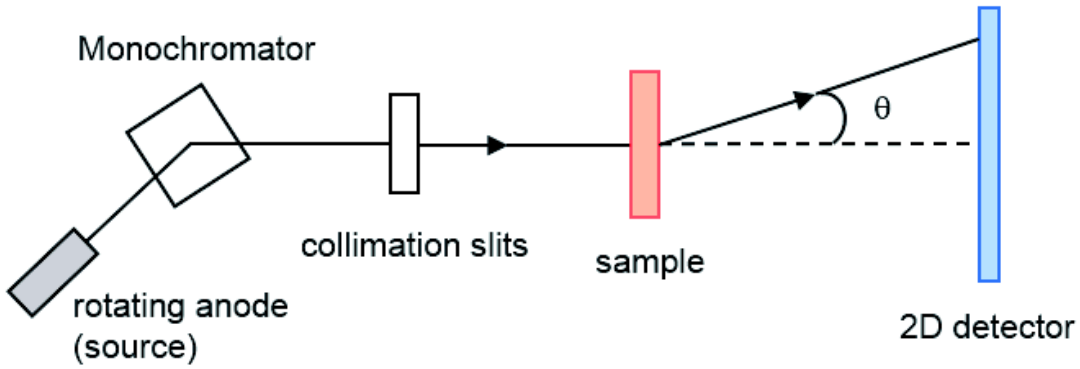

Figure 3.7: Schematic representation of the experimental setup of X-ray diffraction available in the Institute Charles Sadron.

diffused pattern is isotropic due to very nature of the "powder sample".

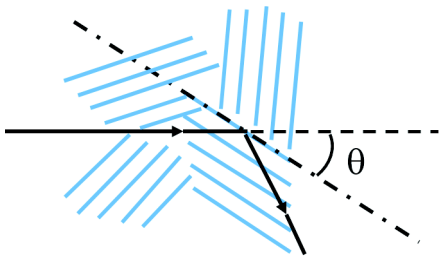

Figure 3.8: "Powder sample": in the absence of the prefered orientation the sample is a set domains randonly oriented. Each set of produces its own cone of diffraction

Figure 3.9 shows an example of the intensity scattered by the lamellar mesophases as a function of the scattering wavevector and corresponding 2D scattering image for the sample with 9.6 wt. % membrane fraction and $C_p = 0$ wt. %. A series of three Bragg diffraction peaks can be seen. Their positions are in the ratio of $1 : 2 : 3$ indicating a one-dimensional smectic A structure of periodicity $d = 10.9 \pm 0.4$ nm.

3.2.4 Deuterium solid state NMR

The measurements of the quadrupolar splittings were performed at the Institute of Chemistry, in the laboratory of Membrane Biophysics and NMR (group of Prof. Burkhard Bechinger). Experiments were carried out on a Bruker Avance 300 wide-bore spectrometer, operating at 46.1 MHz for deuterium. The temperature was regulated to $298 \pm 1K$. The experimental resolution is about ± 15 Hz.

The MAS rotor is made of zirconium oxide (Zirconia); it has a diameter of 4 mm and a sample volume of 200 µL. The rotor cap is made of Kel-F. After the samples were placed into a tube, they were centrifuged in a centrifuge rotor at a speed of 6000 rpm during 10 min prior to NMR experiment in order to remove bubbles.

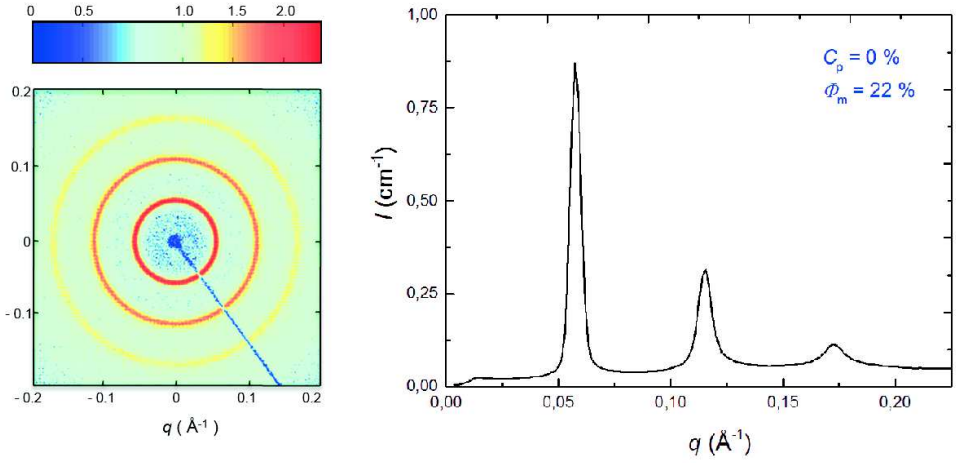

Figure 3.9: 2D diffraction pattern and corresponding plot of intensity scattered by the lamellar mesophase as a function of the wavevector for the sample with $\Phi_m = 22$ wt. % and $C_p = 0$ wt. %. A series of three Bragg diffraction peaks, whose positions are in the ratio $1 : 2 : 3$, allows us to infer the periodicity of the sample: $d = 10.9 \pm 0.4$ nm.

NMR signals were recorded with a quadrupole echo technique: $\pi/2$ pulse width of 3.4 μs, pulse spacing 50 μs with a spectra width of 500 kHz. Quadrupolar splittings were obtained from the free induction decay (FID). During processing, the first 30 points were removed in order to start Fourier transformation at the beginning of the echo and 60-Hz exponential line broadening was applied. The last one is used in order to increase the signal to noise ratio. Then the results were converted to a frequency-domain signal by a Fourier transformation.

3.2.5 Surface force apparatus

An apparatus for measuring surface forces (Surface Forces Apparatus - SFA) was invented in the 1970s by Israelashvili and Tabor [67]. For the first time it made possible to measure the forces which are exerted between two surfaces, separated by a thickness of liquid or gas ranging from a few micrometers up to a few angstroms. The force measurements carried out with SFA technique gave the direct experimental evidence of the Derjaguin-Landau-Verwey-Overbeek force theory (DLVO) [39].

The instrument is depicted schematically in Figure 3.10, which is based on the following principles:

- the sample is confined between two curved mica surfaces, partially reflective, which form the walls of a confinement cell;

- the cell is illuminated by a beam of white light and the mica/mica separation is measured by an interferometric technique, from the transmitted wavelengths;

- the force measurement is made by moving the surfaces with a piezoelectric tube and by simultaneously measuring the deflection of a cantilever of known elastic constant.

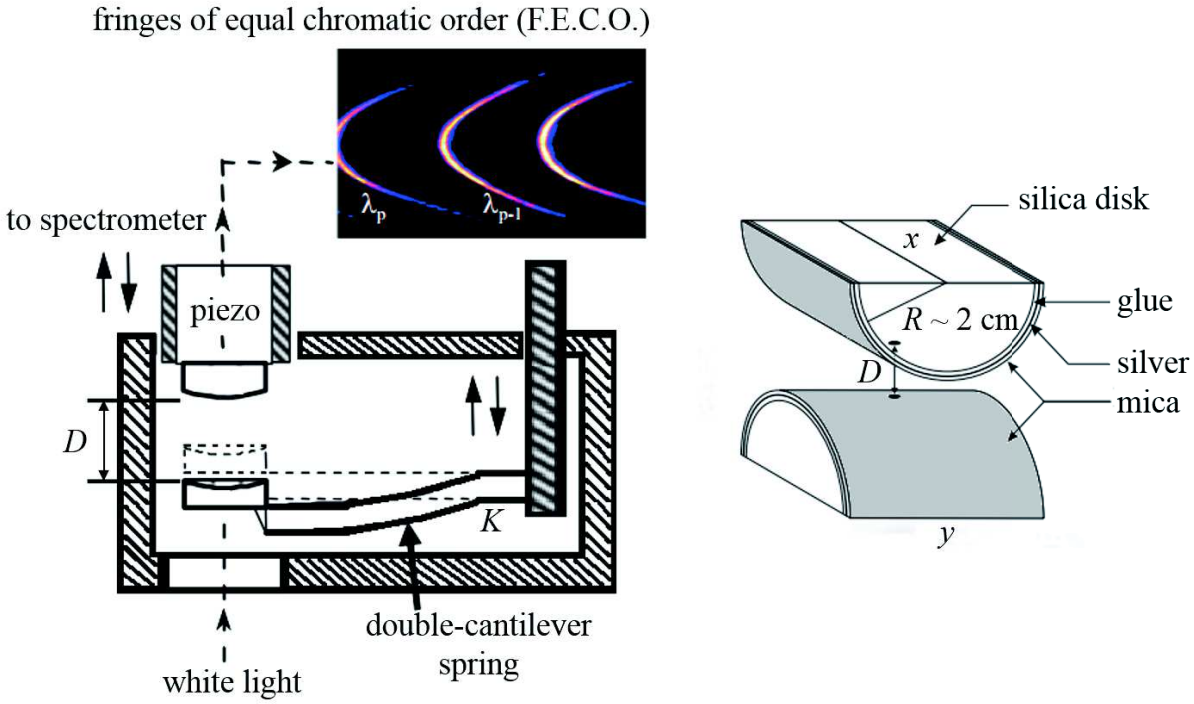

Figure 3.10: A schematic representation of the Surface Force Apparatus (SFA) and the geometry of confinement.

The geometry of confinement

Thin mica sheets freshly cleaved were glued down onto two supporting silica disks of semi-cylindrical shape (radius of curvature $R \simeq 2$ cm) (Figure 3.10). The cylinder axes of the disks are perpendicular to each other and form a confinement geometry known as "crossed cylinders geometry". The disks are completely covered by the two muscovite mica sheets cut from a single sheet of mica of uniform thickness (1 to 3 μm). As a result the two opposite mica sheets have the same thickness in a given experiment. The backing sheet of mica is silvered by vacuum deposition to a thickness of about 50 nm.

The sheets are very flexible and adapt to the curved surface of the disks on which they are bonded by the silver side with a help of glue of the thickness about 10-20 μm. Epikote resin is very suitable as a glue for several reasons: it is transparent, it does not change its volume as it sets and thus prevents any stress in the glued mica sheet upon cooling, and it is not a source for contaminants [49].

The muscovite mica is a naturally occurring mineral consisting of aluminosilicate layers held together by ionic bonds between potassium. It can be cleaved along crystallographic planes into atomically smooth thin sheets, and large enough to cover the surface of the

lenses (~ 1 cm^2). In addition it is chemically pure, although easily contaminated by water vapour and other organic molecules present in the environment. Thus, mica squares are cut with a white-hot platinum wire (0.1 mm diameter) and immediately placed face down on a freshly cleaved, large backing sheet onto which it adheres. In this way the surface of the pieces in contact with the backing sheet are protected from contamination. To ensure a contaminant free surface the whole sample preparation is carried out in a clean room.

The main advantage of crossed-cylinders geometry is the possibility to bring the surfaces into contact at a single point of contact, defined as the point of minimum separation D between the two surfaces of mica (Figure 3.10). If we call x and y the cylinder axes of radius R_x and R_y and r is the distance in the xy plane from the point of contact, the distance h between the surfaces increases with r in the following way:

$$h(x,y) = D + \sqrt{R_x^2 - x^2} + \sqrt{R_y^2 - y^2} \sim D + \frac{r^2}{2R}, r \ll R = \sqrt{R_x R_y} \tag{3.2}$$

Near the point of contact the separation between crossed cylinders is therefore equivalent to the separation between a plane and a sphere of radius R, or between two spheres of radius $2R$.

The crossed cylinder arrangement is also convenient for the comparison of experiment with theory. According to Derjaguin the force between crossed cylinders of equal radius R is equivalent to the free energy $E(D)$ of interaction per unit area between two plane parallel surfaces of the same material [38].

$$\frac{F}{R} = 2\pi E \tag{3.3}$$

For this reason, forces $F(D)$ measured with the SFA between two crossed-cylinders of mean radius of curvature R are routinely plotted as F/R and are therefore implicitly related to the interaction free energy $E(D)$.

The validity of Derjaguin approximation lies on the following requirements: the range of the force is small compared to the radius of curvature of the surfaces. This is always fulfilled in measurements using the SFA ($R \sim 2$ cm and $D \sim 0.1$ nm up to several μm so $R \gg D$). R needs also to be independent of D (the surfaces must remain undeformed) so that $F(D)$ is mathematically well-defined, i.e. single-valued and integrable. This may not always be fulfilled. Especially when the surfaces are being deformed due to the action of strong surface forces the comparison between experiments and theory is no longer straightforward. In some cases the application of equation (3.3) can be questionable. Hence statistical mechanic derivations have to be applied to correctly describe the interactions e.g. for oscillatory structural forces arising between curved surfaces in fluids.

Interferometric measurement of the thickness

The measurement of the distance D between the mica surfaces is calculated by an interferometric technique called "fringes of equal chromatic order" (FECO) [58, 65]. The method consists in measuring the shift of the resonance wavelengths, from the value at the mica/mica contact in the air.

The outer silvered faces of the two mica sheets form an optical cavity (a Fabry-Perot like interferometer). Collimated white light is directed and impinged normal to the surfaces. The infrared components of the light are filtered to prevent the heating of the sample. When the beam passes through the interferometer, only the spectral components resonating with the "cavity" are transmitted. The central part of the transmitted beam passes through the confinement cell near the point of contact and creates Newton's rings, as can be seen through a microscope objective. If a microscope focuses the light emerging from the interferometer on the entry slit of a grating spectrometer, the fringes are split up according to their wavelength. Analysis of this array allows to measure the optical thickness of the film and simultaneously determine the thickness and the refractive index of each layer in the interferometer. We will only consider the case with three-layer (e.g. mica-medium-mica) interferometry, which is the most commonly used setup for SFA experiments.

It should be noted that multiple-beam interferometry requires the presence of two highly reflective thin films separated by one or more dielectric materials of total thickness greater than the wavelength of visible light. The spectrum can be accurately predicted using classical electromagnetic theory, and the FECO wavelengths depend on the thicknesses and the optical properties of the media (refractive indices and their dispersions) [65,128].

An example of deformation of the geometry is given in Figure 3.11 for the adhesion between two mica surfaces in contact in air. Since mica is birefringent, each fringe normally appears as a doublet. Thus one fringe is extinguished by passing the light through a polariser.

Since the gap between the curved surfaces is not uniform, the shape of the observed FECO is a direct representation of the relative geometry of the surfaces (Figure 3.12). The FECO appears parabolic. In order to measure the separation one uses the spectrum profile which corresponds to the centre of the fringe.

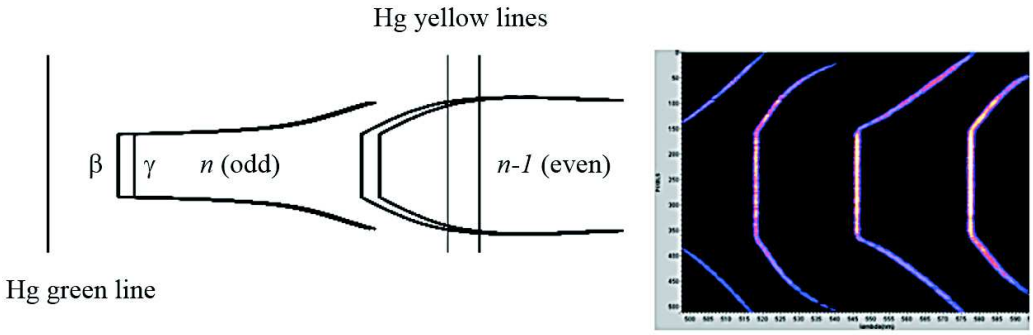

Figure 3.11: A schematic representation (left) corresponds to the two split fringes (β and γ) at contact. The FECO fringes of mica surfaces in air adhesive contact ($D = 0$, right). Note that the contacting parts of the surfaces flatten due to elastic deformations of the mica and supporting glue. The reference lines of mercury are indicated (green and yellow). Reproduced from [22].

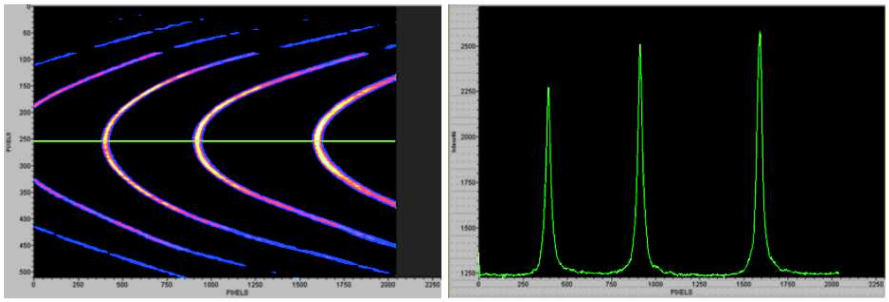

Figure 3.12: FECO at the distance D from the contact and the profile of the fringes. The green line on the image of the fringes corresponds to the line chosen to obtain the profile. Reproduced from [22].

The separation determined by multiple-beam interferometry is an absolute value relative to the predetermined zero separation (measured distance of contact in air, or in an aqueous solution). This is an important advantage over most of the non-interferometric devices such as AFM force measurement. Under optimum experimental conditions a 0.1 nm resolution can be achieved for surface separations larger than 5 nm. Below 5 nm, the resolution is about 0.2 nm.

The lateral magnification is set by the microscope (about x32) that focuses the light emerging from the interferometer to the spectrometer slit.

Force measurement

In the SFA design schematically displayed in Figure 3.10, one of the surfaces is attached to a piezoelectric tube. The other one is mounted at the end of a double force measuring cantilever (of constant stiffness $K_c \sim 50$ N/m) that can be moved to bring the surfaces

to a given separation. Accurate force measurements require precise control of the surface separation. This is usually realised either mechanically by a system of micrometers and differential springs or by piezoelectric devices. The advantage of the latter ones is, that they displace the surfaces smoothly without causing vibrations. However the piezo-actuators are prone to nonlinearity, hysteresis and creep, which have to be corrected by electronic feedback system to provide a subnanometric precision. In the setup of the laboratory an ensemble of piezoelectric actuators (Physik Instruments) has been mounted. The non-linearity and hysteresis are electronically corrected. The range of displacement is 100 µm and the minimum repeatable step is 0.5 nm [55].

Forces between the surfaces of the crossed cylinders are determined from the deflection of the cantilever spring system and calculated by Hookes law with the known spring constant. The spring constant is calibrated with an accuracy of 1 % after each experiment. Small calibrated weights are placed on the hemicylinder attached to the cantilever and the deflection is measured. A double cantilever is preferable to a single leaf spring because it prevents the curved surfaces from rolling and shearing as the load is varied. The force can be determined with a resolution of about 50 nN. When normalised by the radius of curvature of the surfaces, this is equivalent to 0.002 mN/m
citeSadron2013.

A force measurement is started with the surfaces separated well beyond the range of any surface force. Then the surfaces are stepwise approached. After each displacement, the surfaces are allowed to come to rest and their true distance is measured by the optical method. This process is repeated and the measured separation profile as a function of the actuator displacement is recorded. A straight line of slope equal to 1 is obtained at large separations where no force of interaction occurs. Repulsive forces are seen as a continuous deflection away from contact and are limited only by the onset of deformation of the surfaces. Strongly attractive surface interactions lead to a mechanical instability. Similar to AFM it occurs when the slope of the force-distance profile exceeds the cantilever spring constant. As a consequence the technique allows forces to be measured only over the regions where the gradient of the force ($\partial F/\partial D$) is smaller than the spring constant K. Thus only parts of the force curves are directly accessible and the force vs distance profile appears to be discontinuous, with jumps from unstable (e.g. $\partial F/\partial D > K$) to stable mechanical regimes [55].

Instrumentation

The SFA was home-built by the group of Patrick Kékicheff at the Institut Charles Sadron, Strasbourg. The upper surface is attached to the piezo actuator (Physik Instrument) with a max. travel of 100 µm and a precision of 0.5 nm, used for fine approach of the surfaces. The lower surface is placed at the end of a double-cantilever spring made of stainless steel with a force constant around 50 N/m. The sample chamber with a volume of 45

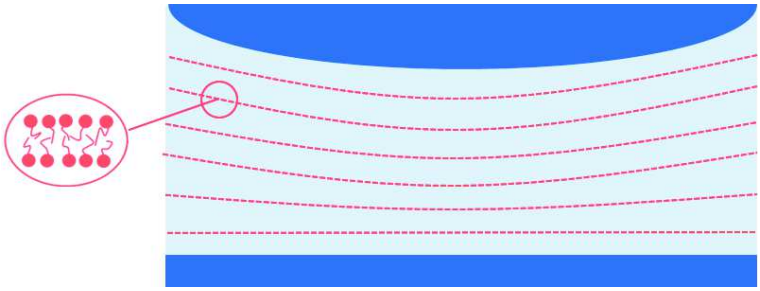

Figure 3.13: A homeotropic alignment of the membranes (in red) between the two mica surfaces (in blue).

cm^3 is also made of chemical inert stainless steel in order to prevent contamination of the sample surfaces or solutions. For coarse alignment the surfaces are moved with screw spindle connected to a computer which allows displacement of the upper surface with a precision of 0.1 μm.

In order to avoid thermal drifts of the mechanics, the temperature of the sample chamber is strictly controlled to 25 °C using a PID controller (Lakeshore 340) which regulates the temperature with a precision of 0.5°C/24 h in the laboratory, 0.05°C/24 h within the plexiglas confinement and 0.004°C/h within the sample chamber. The temperature of the laboratory room is fixed 3° C lower than the desired temperature of the SFA.

Collimated white light from a 150 W halogen lamp is directed in the optical cavity via water liquid core optical fiber (this eliminates IR). The resulting interference pattern is enlarged by a 16x objective and directed to a Jobin-Yvon imaging spectrometer by an imaging optical fiber (composed of 120 000 single fibers) and a doublet adaptator (x2) to enter into the spectrometer. The spectrometer is coupled with a liquid nitrogen cooled CCD camera (2048 x 512 pixels). The spectrometer-camera system is controlled with a computer and the interference patterns are analysed with a home written software [55].

Homeotropic alignment of the lamellar mesophases in SFA

Since lamellar phases are very viscous, usually about two days are required to equilibrate the confined structure after the sample is introduced in the SFA chamber. Afterwards, typically several days are necessary to obtain an homeotropic alignment (see Figure 3.13) of the membranes, that is membranes aligned parallel to the confining mica surfaces. The alignment can be achieved by performing slow movement of the surfaces back and forth over separations of several micrometers. This method, equivalent to shearing the liquid crystal is often used to produce homeotropic alignment in lamellar systems.

As it was mentioned before, the geometry of crossed cylinders of radii R is equivalent to the geometry of a sphere of radius R against a flat plane. Therefore, in a confined medium of nonuniform thickness, exists a conflict between the homeotropic alignment and

the need for a constant layer spacing d: as a result defects must arise. For a wedge-shaped geometry, an array of edge dislocation loops is expected (Figure 3.14). Dislocations are characterized by their Burgers vector (see Figure 3.15). By definition, these defects break the translational symmetry of the lamellar structure and they are difficult to see using the polarizing microscope, since the layer distortions they induce are too small [101].

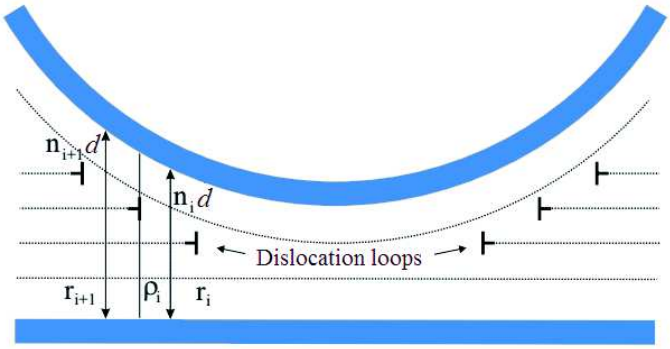

Figure 3.14: Schematic representation of lamellar mesophase confined between a sphere and a flat plane. An array of concentric dislocation loops is introduced in order to compensate the variation in sample thickness. The sample can be modelled as a set of N adjacent torus-like cells. Each cell is delimited by the inner radius, ρ_i, where the thickness, $h(\rho_i)$, is an integral multiple of the reticular distance $h(\rho_i) = n_i d$, and an outer radius, ρ_{i+1}, where the thickness is increased by b layer period: $h(\rho_{i+1}) = (n_i + b)d$, where b is the Burger vector. In this picture every cell of rank $i > 0$ contains one edge dislocation loop $(b = 1)$of radius r_i [107].

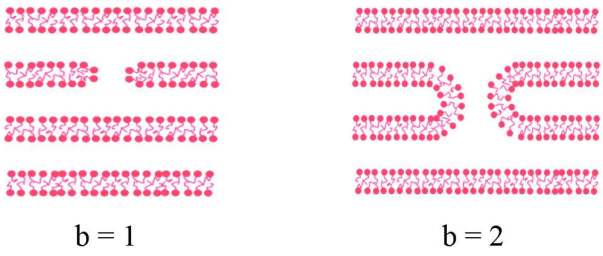

Figure 3.15: Edge dislocations of Burgers vector $b = 1$ (left) and $b = 2$ (right) [55]

Chapter 4

NMR: Experimental results

In the following chapter the lamellar mesophases prepared along dilution lines of polymer PEG (as shown in Figure 4.1) were studied by small angle X-ray scattering and deuterium solid state NMR. Firstly, the x-ray scattering experiments allowed us to get structural information on the samples. Secondly, we extracted from the experimental NMR spectra the values of the quadrupolar splittings. To do so, we used two different methods which will be discussed in the second part of this chapter. Suchwise, the variation of the bending elastic modulus κ with respect to the polymer concentration C_p was obtained in two different ways and compared.

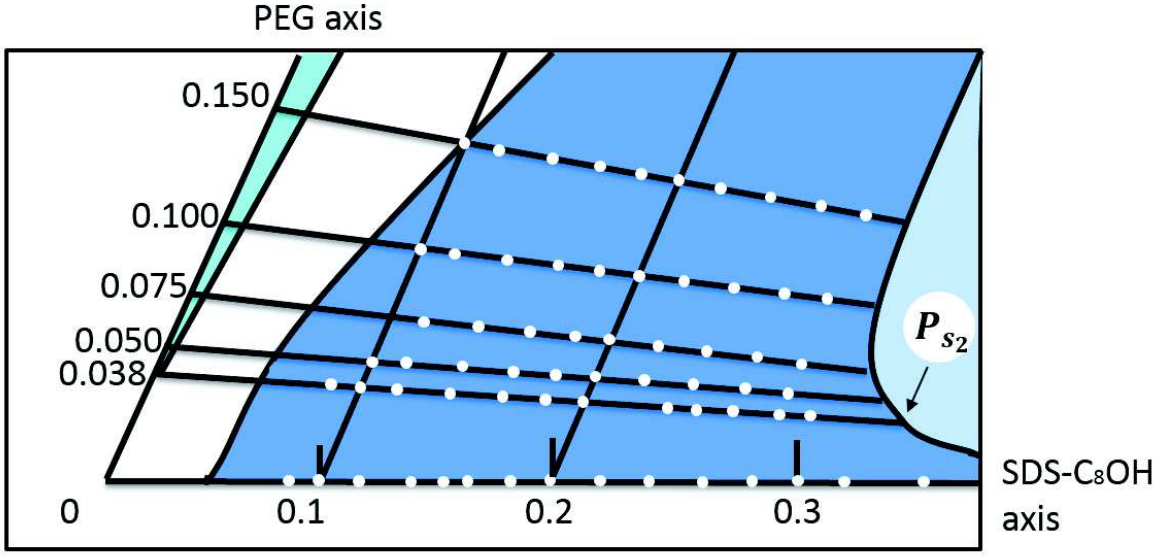

Figure 4.1: The inset of the phase diagram (see Section 3.1.6) represents the prepared mesophases (in white) along the dilutions lines: $C_p = 0$; 3.8; 5; 7.5; 10; 15 wt. % in order to approach the critical point P_{S2}.

4.1 Structural parameters determined by x-ray diffraction

In this part, the diffraction experimental results concerning samples located along six dilution lines, with C_p varying from 0 to 15 wt. % are presented. For each lamellar mesophase the X-ray scattering pattern displays a series of three Bragg diffraction peaks in the ratio 1:2:3 accordingly to 1D smectic order.

As an example, the scattering patterns for powder samples located along the dilution line $C_p = 7.5$ wt. % are presented in Figure 4.2. Three harmonics of the structure factor are always observed, they shift to small angles as Φ_m decreases.

The inset of Figure 4.2 corresponds to 2D scattering image of sample at $\Phi_m = 22$ wt. % without polymer. As can be seen from the 2D SAXS intensity distribution obtained with pinhole collimation there are no indication of preferred orientation (the lattice planes are randomly arranged in space). For this volume fraction the periodicity is $d = 10.9 \pm 0.4$ nm and the diffraction pattern is isotropic constituted of three rings in the ratio 1:2:3. The scattering patterns from all the mesophases can be found in the Appendix A.1.

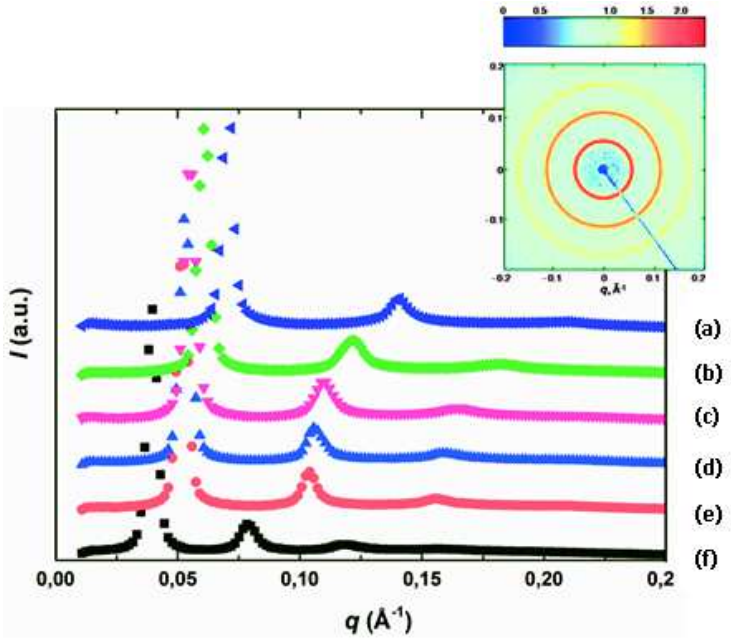

Figure 4.2: Small angle X-ray scattering by mesophases at different membrane concentrations, along the dilution line $C_p = 7.5$ wt. %. Membrane mass fraction Φ_m is 26; 24; 22; 20; 18; 16 wt. % from curve (a) to curve (f). The inset shows a 2D scattering image for a lamellar mesophase with membrane mass fraction $\Phi_m = 22$ % without polymer ($C_p = 0$ wt. %) giving a periodicity: $d = 10.9 \pm 0.4$ nm

The periodicity of lamellar mesophases at different volume fraction has been measured.

Figure 4.3 shows the smectic period d of lamellar mesophases as a function of the inverse membrane volume fraction $1/\phi_m$ for six dilution lines studied: $C_p = 0$; 3.8; 5; 7.5; 10 and 15 wt. %. It follows the expected dilution law for a lamellar structure $d = \delta/\phi_m$. From the slope a membrane thickness δ is extracted. As deduced from the slopes the thickness depends on the polymer content.

Figure 4.4 shows that the membrane thickness δ decreases from 2.51 $\pm$ 0.05 nm in the absence of polymer to 2.31 $\pm$ 0.02 at $C_p = 15$ wt. %. This decrease is likely to be related to the adsorption of the macromolecular chains onto the membranes. Some brands intercalate in the vicinity of the polar heads of the surfactant/alcohol at the interface of the bilayers. They modify the effective charge per polar head of the membrane. This may result in a kind of stretching of the lamellar bilayers: the volume of the surfactant tails is likely to be distributed a little bit differently; they have more space in lateral directions, thanks to the polymer brands that does not penetrate completely the membranes. As a consequence the membrane becomes thinner. This decrease was already observed in [44]. It should be noted however that the variation occurs at very low C_p, and after reaching the overlap concentration ($C_p^* = 4.1$ wt. %) [44] the addition of polymer has no effect, or very little.

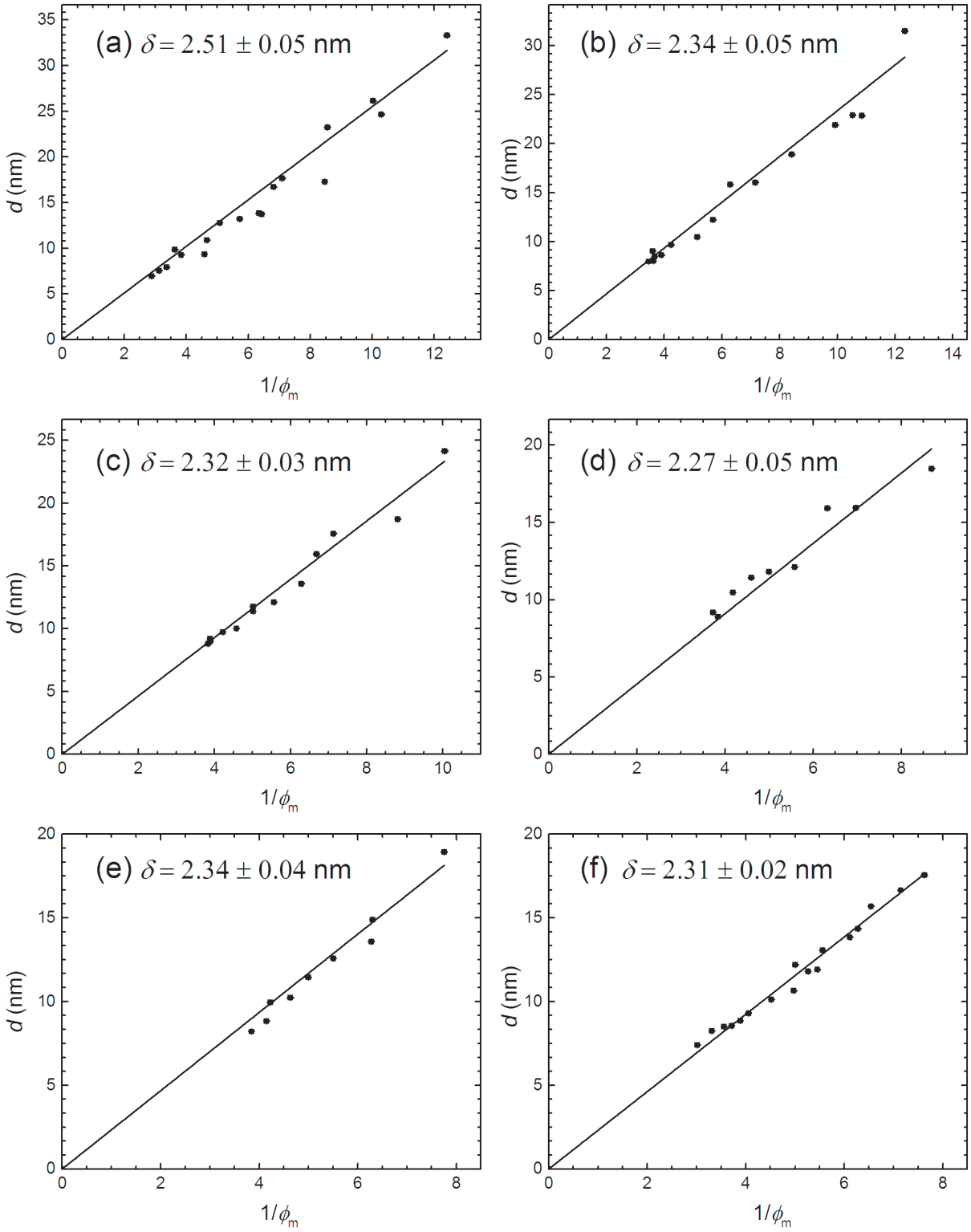

Figure 4.3: Periodicity of the lamellar mesophases as a function of their inverse membrane volume fraction along dilution lines where the polymer content is kept constant: (a) C_p = 0 wt % ; (b) C_p = 3.8 wt %, (c) C_p = 5 wt %; (d) C_p = 7.5 wt %; (e) C_p = 10 wt %; (f) C_p = 15 wt %. The membrane thickness δ is inferred from the slope.

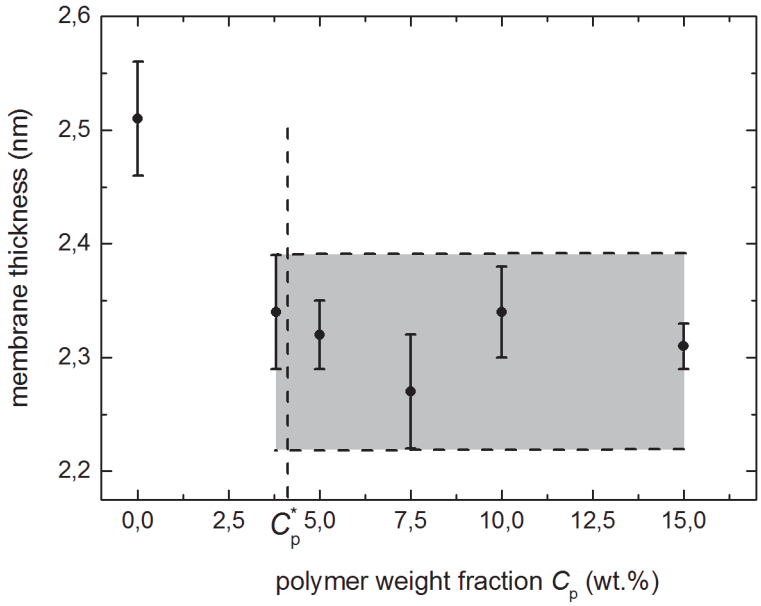

Figure 4.4: Evolution of the membrane thickness δ with the polymer weight fraction C_p.

4.2 NMR spectrum of perdeuterated octanol in a lamellar phase

The ^{2}H NMR spectra of 1-octanol (perdeuterated) are broad powder patterns, characteristic of axially symmetric rotations about the alcohol long axis. Figure 4.5 shows an example of NMR spectra of perdeuterated octanol in the SDS/water/octanol/PEG lamellar system with the membrane fraction of 26 wt. % and polymer mass fraction $C_p = 10$ wt. %. One sees that the spectrum has the right shape - it is a "powder" spectrum, which is easily recognizable due to the presence of both the major peaks and the shoulders respectively corresponding to bilayers oriented at 90° and 0° with respect to the static magnetic field direction.

A peak at the middle of the spectrum, namely at 3.57 ppm, corresponds to the chemical shift of the D_2O or HDO due to the exchange of H and D in the O-D groups of octanol and water molecules in small amount. As mentioned before, the chemical shift interaction is negligible in comparison with the quadrupolar coupling interaction, however we can observe it due to the high resolution of the NMR spectrometer. The chemical shift is of the order of a few ppm, thus it does not affect the quantitative evaluation of the quadrupolar splitting.

The doublets $\Delta\nu_Q$ correspond to the CD_3 and CD_2 of the octanol chain in the lamellar mesophase. One can distinguish four different quadrupolar splittings: the most intense $\Delta\nu_{Qa}$ corresponds to the terminal CD_3 bound (8th position on the octanol chain), which has the maximum freedom and thus the smaller splitting. Only three other splittings

$\Delta\nu_{Qb-d}$ are observed, showing that some of them result from the overlap of close splittings arising from neighboured CD_2 groups along the octanol chain.

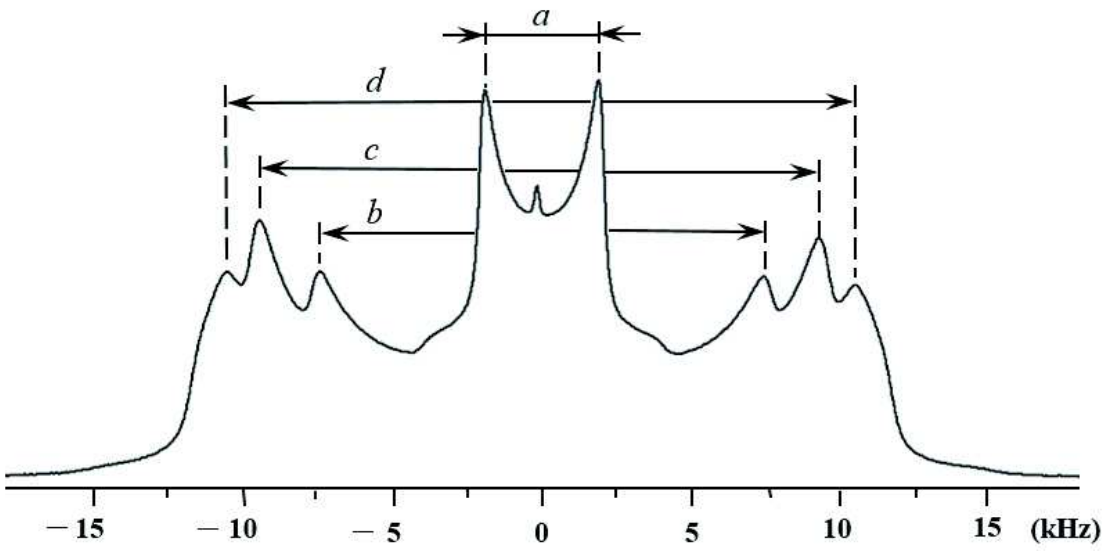

Figure 4.5: NMR spectra of perdeuterated octanol for the sample with 26 wt. % membrane fraction and polymer mass fraction C_p = 10 wt. %. One can distinguish four quadrupolar splittings $\Delta\nu_{Qa-d}$, where $\Delta\nu_{Qa}$ corresponds to the terminal CD_3 and $\Delta\nu_{Qb-d}$ comprise contributions of CD_2 groups along the octanol chain.

Interestingly, if we compare the spectra along the dilution line at constant polymer weight fraction in water $C_p = 10$ wt. % (Figure 4.6) we observe that with increasing the water content in the mesophases, i.e. increasing the spacing between the membranes, one sees a considerable increase of intensity in the center of the spectra. For the mesophase with $\Phi_m = 10$ wt. % the spectrum contains besides the signal from residual ^{2}HOH, some amount of isotropic phase. Because this mesophase is located in the phase diagram close to the L_α - L_α/L phase boundary (see Figure 3.3) we can suggest that isotropic and lamellar phase coexist in this region.

Superimposed NMR spectra in Figure 4.7 shows the variations of the quadrupolar splittings versus a polymer weight fraction C_p for a lamellar mesophases at constant membrane volume fraction Φ_m = 16 wt. %. It can be seen that with increasing the polymer concentration in water layers the mobility of C-D_2 groups of the octanol chain slightly increases (the quadrupolar splitting deacreases).

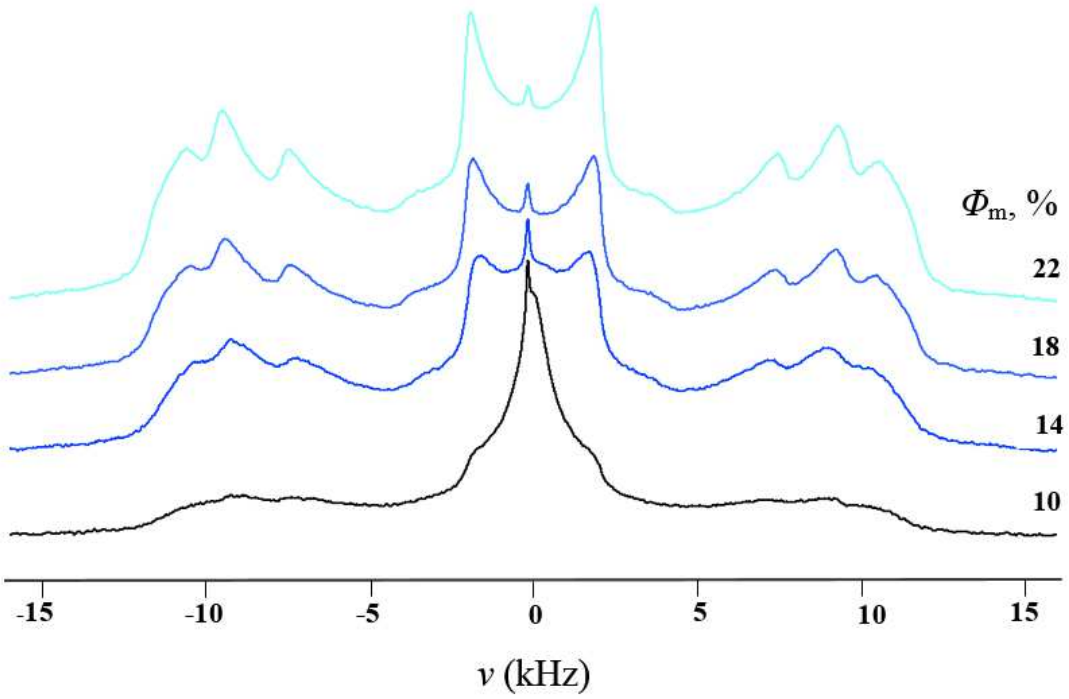

Figure 4.6: NMR spectra of perdeuterated octanol molecule of several lamellar mesophases at fixed concentration of polymer in the water layers, $C_p = 10$ wt. % for Φ_m varying from 10 to 22 wt. %.

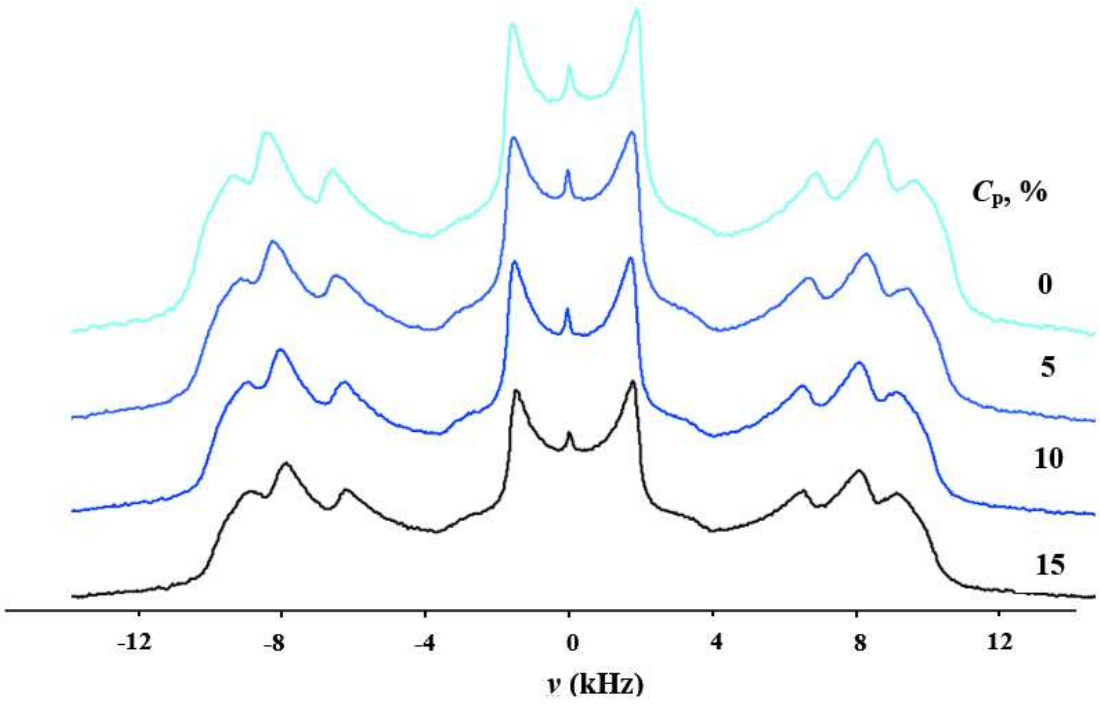

Figure 4.7: NMR spectra of perdeuterated octanol molecule of several lamellar mesophases at fixed membrane mass fraction, $\Phi_m = 16$ wt. % with C_p varying from 0 to 15 wt. %.

4.3 Bending elastic modulus

As we can see the ^{2}H spectrum of perdeuterated octanol is a superimposition of four quite broad powder patterns (the same tendency was found in [126], in a multilamellar dispersions study, where spectrum of perdeuterated octanol contains three broad powder patterns). In this case the determination of the quadrupolar splitting pertaining to the different C-D_2 segments in the molecule is difficult. The exception is the methyl group peak.

Therefore, in order to take the full advantage of spectral data we have analysed the spectra by two different methods. Firstly, the quadrupolar splittings were determined by measuring the peak to peak distance for "a", "b", "c", "d" peaks - Method 1. Secondly, each spectrum was deconvoluted using the Solid Lineshape Analysis tool (SOLA) in TopSpin v3.5 and the value of quadrupolar splitting was assigned to each site in the octanol chain - Method 2.

4.3.1 Results. Method 1

Dilution line of a lamellar phase without polymer

The variation of the quadrupolar splittings are fitted by a damped mean square method (using commercial software OriginPro v.9) which enables to get two parameters: the bending elastic modulus κ and the constant term $\alpha = 3/4\nu_0 S_I S_M$ (Eq. 2.28). In Figure 4.8 measurements of the $\Delta\nu_{Qa}$, $\Delta\nu_{Qb}$, $\Delta\nu_{Qc}$ and $\Delta\nu_{Qd}$ are plotted versus the repeat distance d of the lamellar stack (which was independently measured by x-ray diffraction). One sees that $\Delta\nu_Q$ decreases as d increases, i.e., as the water volume fraction increases. This decrease is linked to the undulations of the membranes, thus to the bending elastic modulus κ [5].

The smectic order for the samples without added polymer is stabilized by long-range electrostatic interaction in pure water, and the corresponding compressibility modulus is [110]

$$\bar{B}_{elec} = \frac{\pi k_B T}{2 l_B} \frac{d}{(d-\delta)^3} \tag{4.1}$$

where $l_B = e^2/(4\pi\epsilon k_B T) \approx 0.7$ nm is the Bjerrum length (for water) and the bilayer thickness $\delta = 2.5$ nm inferred from the SAXS measurements (see section 4.1).

Putting the expression of $\bar{B}$ given by Eq. (4.1) in Eq. (2.28), we have fitted the experimental results for the series of samples along the dilution line without polymer. The four series of splittings $\Delta\nu_{Qa}$, $\Delta\nu_{Qb}$, $\Delta\nu_{Qc}$, $\Delta\nu_{Qd}$ give the values of the bending modulus κ (given in the units of $k_B T$ at T = 298 K) and the product of $S_I S_M$ are plotted

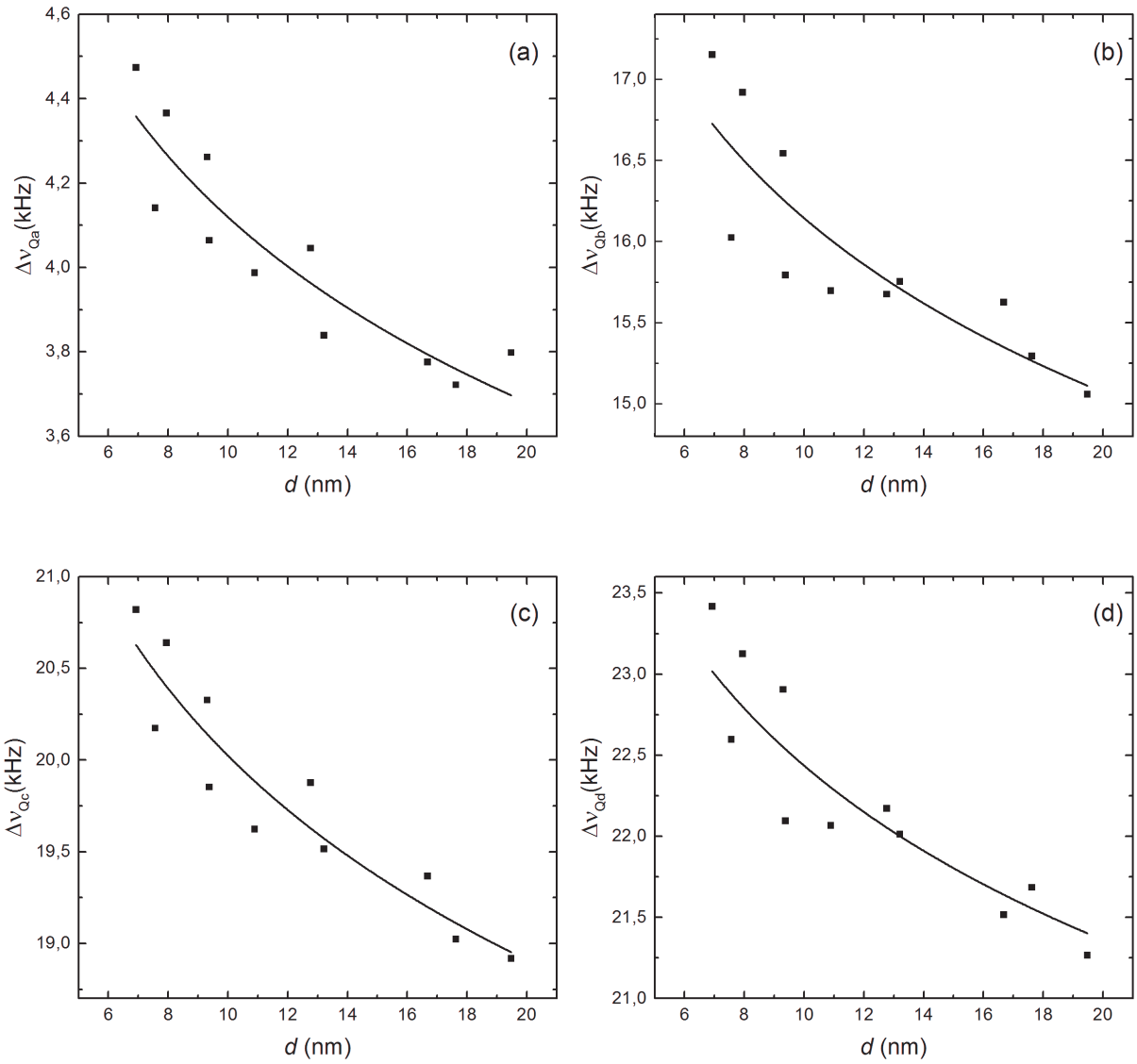

Figure 4.8: Plot of the four different quadrupolar splittings $\Delta\nu_{Qa}$, $\Delta\nu_{Qb}$, $\Delta\nu_{Qc}$, $\Delta\nu_{Qd}$ of the lamellar system SDS/ octanol / water as a function of the smectic period d nm. The plain lines are the fits obtained from Eq. (2.28).

in Figure 4.9.

As it was already mentioned the "a" peak position corresponds to the terminal CD_3 group, which experiences the increased motional averaging produced by rapid reorientation of this group about its three-hold axis. This motion also gives rise to essentially reduced quadrupole splitting for the CD_3 resonance compared to CD_2 groups.

We can suppose that the quadrupolar splittings of the CD_2 groups which located closer to the polar head of molecule reflect more the overall behaviour of the membrane fluctuations than the CD_3 group. Therefore, we present the values of κ_a obtained from $\Delta\nu_{Qa}$ and the values of the bending modulus obtained from $\Delta\nu_{Qb}$, $\Delta\nu_{Qc}$ and $\Delta\nu_{Qd}$ separately. One gets $\kappa_a = 2.01 \pm 0.08 k_B T$. Further, the values of the bending modulus reads: $\kappa_b =$

$2.35 \pm 0.2 k_B T$; $\kappa_c = 2.55 \pm 0.16 k_B T$; $\kappa_d = 2.61 \pm 0.2 k_B T$. Because one may consider the measurement of $\Delta\nu_{Qb}$, $\Delta\nu_{Qc}$, $\Delta\nu_{Qd}$ independent of each other, the inferred corresponding values of κ_b, κ_c, κ_d may be considered independent as well. In this approximation, one may take the average value of these inferred values with an error bar weight averaged. Thus, the final average value of the bending modulus $\kappa_{av} = 2.51 \pm 0.1\ k_B T$.

Figure 4.9 (b) shows the evolution of the product $S_M * S_I$ (molecular and intramolecular motions, angles θ_I and θ_M, see Figure 2.6). It was assumed to be uncorrelated with collective fluctuations of the membrane (θ_F), since these motions occur at different timescales. Interestingly, that the product $S_M * S_I$ is sufficiently low for "a" peak position and the constant for the rest "b", "c", "d" peaks. As it is known, S_I characterizes the intermolecular motions, namely the conformational isomerisation of each segment along the chain (angle θ_I). That is why the free rotation of a methyl group reduces the quadrupolar splitting by -1/3 taking into account a tetrahedral angle θ_I of 109.4 °. The knowlewdge of S_I for each marked position in the chain may allow as well to determine an "aliphatic thickness" of the bilayer, as it was shown if the works of Seelig [115,116]. One can estimate that the molecular order parameter S_M is constant, as the surface area per polar head remains constant along the dilution. Figure 4.9 confirm the invariance of the product $S_M * S_I$ along the dilution for "b", "c", "d" peak positions.

We have fitted the evolutions of quadrupolar splittings as well by taking into account the bilayer thickness δ as a parameter in our fit. This is an important way to check our method by comparison of δ from the fit with the experimental measured value. We have found in all data treatment a good agreement within error of 5 %.

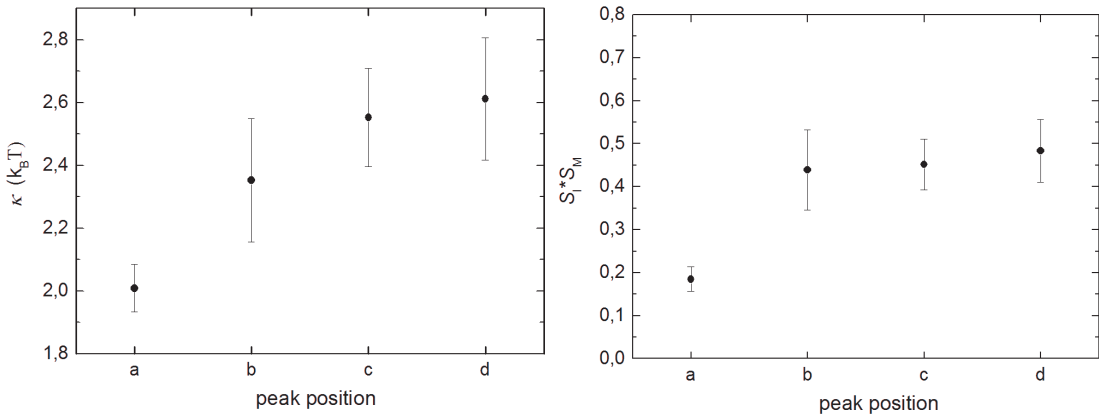

(a) (b)

Figure 4.9: Results of the fits in Figure 4.8. (a): the corresponding variation of bending modulus κ in the energy units of $k_B T$ as a function of peak position; (b): - of the product $S_I * S_M$.

Addition of polymer

The variation of quadrupolar splittings $\Delta\nu_{Qa-d}$ versus the periodicity of the lamellar mesophase at constant polymer concentration $C_p = 3.8$ wt % is plotted in Figure 4.10. For these mesophases the bilayer compression modulus $\bar{B}$ is assumed to be a sum of two terms: $\bar{B} = \bar{B}_{elec} + \bar{B}_{pol}$, where the electrostatic contribution $\bar{B}_{elec}$ is given by Eq. (4.1) and the polymer contribution $\bar{B}_{pol}$, which varies with C_p, is given by Eq. (4.2) [88]:

$$\bar{B}_{pol} \simeq -1.57 k_B T \frac{d}{b(d-\delta)^3} C_p^{3/4} \tag{4.2}$$

where $b \approx 0.35$ nm is the monomer length of a polymer [53]. The layer compression modulus B_{pol} is always negative [88] and the polymer is in the three-dimentional semidilute regime of confinement. Even if Eq. (4.2) is valid only for nonadsorbing polymer, we used it as so far, no other theoretical prediction has been proposed in the literature. Anyway, as we see in Eq. (2.28) $\bar{B}$ appears in the logarithmic correction term of the κ dependence and its absolute value does not affect greatly the final result for κ. For example, if we assume roughly that the $\bar{B}_{pol}$ reduces the compressibility modulus $\bar{B}$ from 50 % of its value, then it would give the contribution to the bending elastic modulus κ of only $0.5 \div 1$ % of its value.

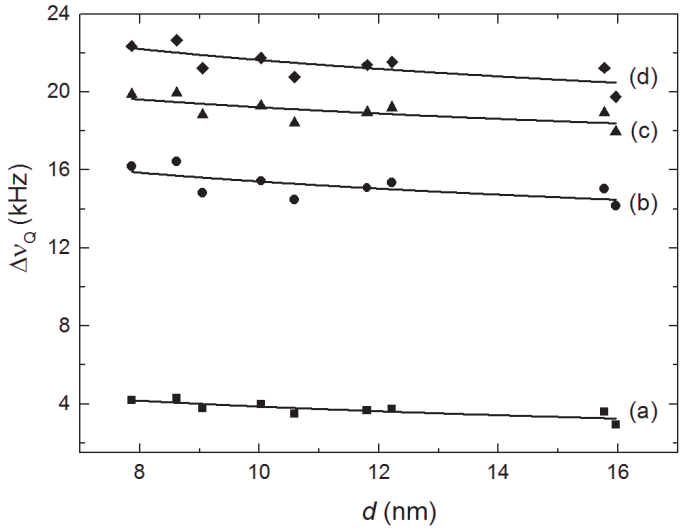

Figure 4.10: Plot of the four different quadrupolar splittings $\Delta\nu_{Qa}$, $\Delta\nu_{Qb}$, $\Delta\nu_{Qc}$, $\Delta\nu_{Qd}$ of the lamellar mesophases at constant $C_p = 3.8$ wt. % as a function of the periodicity d. The plain lines are the best fits obtained from Eq. (2.28).

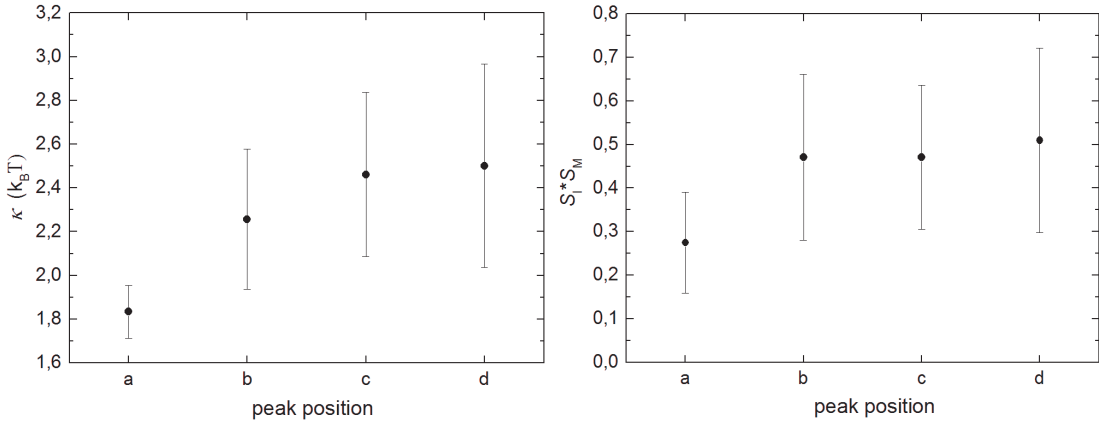

(a) (b)

Figure 4.11: Results of the fits in Figure 4.10. (a): the corresponding variation of bending modulus κ in the energy units of k_BT as a function of peak position; (b): - of the product $S_I * S_M$.

The values of bending elastic modulus κ_a and κ_{av} were extracted using the same procedure for the other dilutions lines: $C_p = 5; 7.5; 10; 15$ wt. % (see Figures 4.12-4.17).

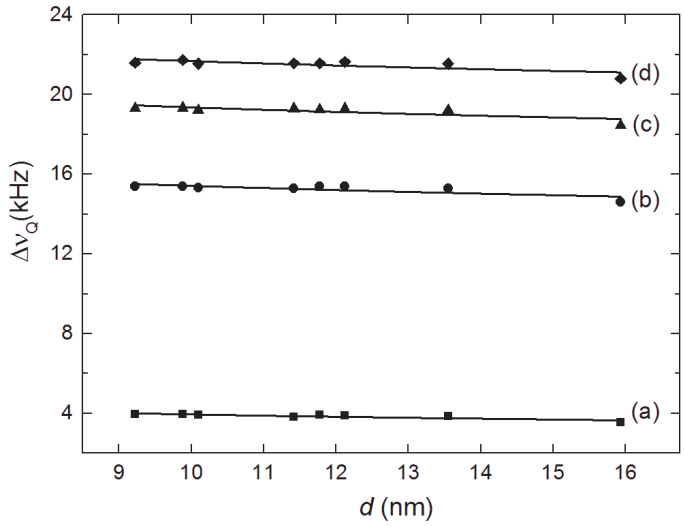

Figure 4.12: Plot of the four different quadrupolar splittings $\Delta\nu_{Qa}$, $\Delta\nu_{Qb}$, $\Delta\nu_{Qc}$, $\Delta\nu_{Qd}$ of the lamellar mesophases at constant $C_p = 5$ wt. % as a function of the periodicity d. The plain lines are the best fits obtained from Eq. (2.28).

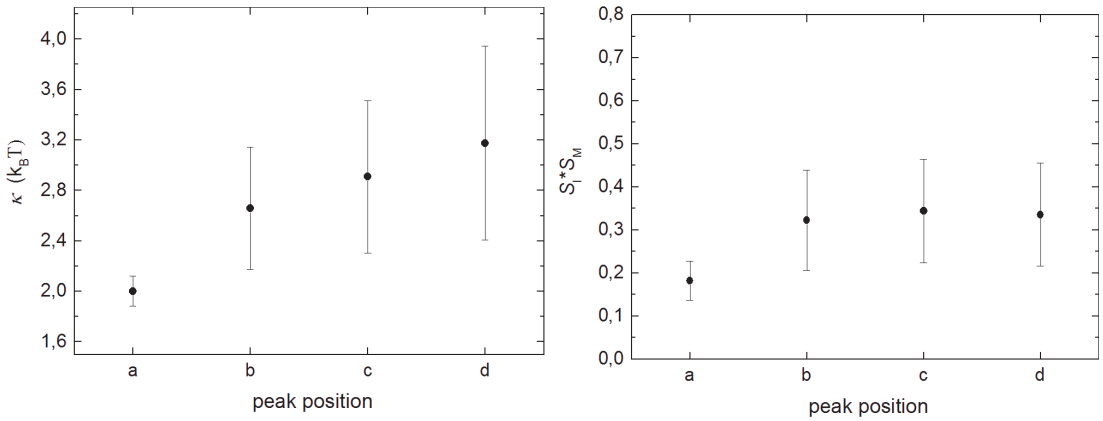

(a) (b)

Figure 4.13: Results of the fits in Figure 4.12. (a): the corresponding variation of bending modulus κ in the energy units of k_BT as a function of peak position; (b): - of the product $S_I * S_M$.

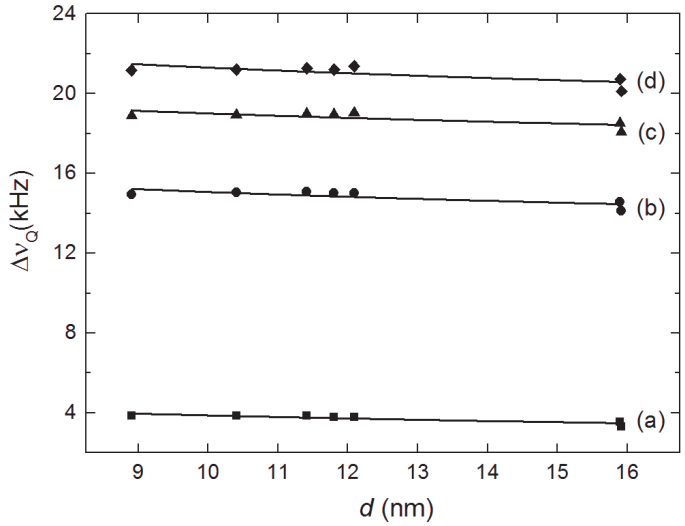

Figure 4.14: Plot of the four different quadrupolar splittings $\Delta\nu_{Qa}$, $\Delta\nu_{Qb}$, $\Delta\nu_{Qc}$, $\Delta\nu_{Qd}$ of the lamellar mesophases at constant $C_p = 7.5$ wt. % as a function of the periodicity d. The plain lines are the best fits obtained from Eq. (2.28).

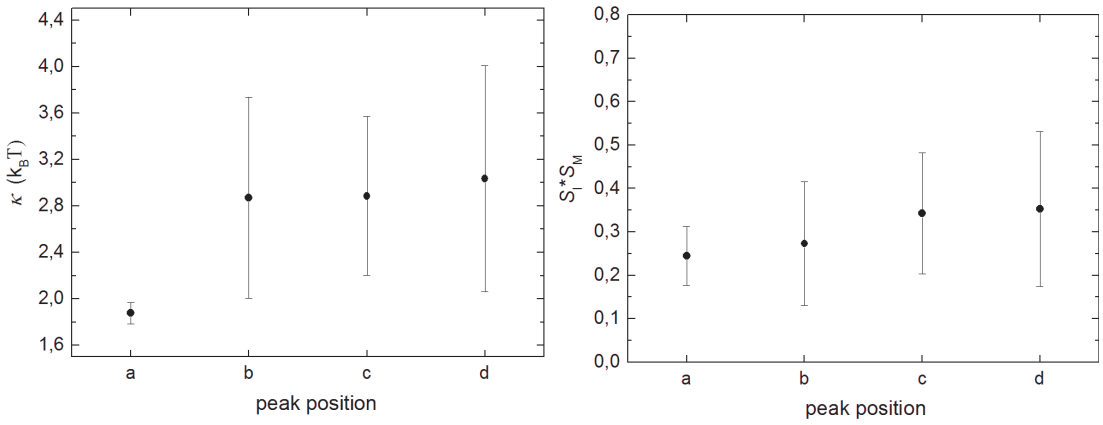

Figure 4.15: Results of the fits in Figure 4.14. (a): the corresponding variation of bending modulus κ in the energy units of k_BT as a function of peak position; (b): - of the product $S_I * S_M$.

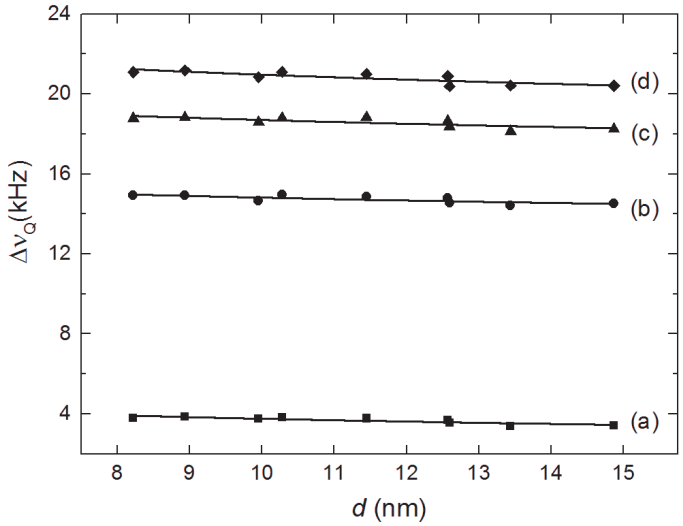

Figure 4.16: Plot of the four different quadrupolar splittings $\Delta\nu_{Qa}$, $\Delta\nu_{Qb}$, $\Delta\nu_{Qc}$, $\Delta\nu_{Qd}$ of the lamellar mesophases at constant $C_p = 10$ wt. % as a function of the periodicity d. The plain lines are the best fits obtained from Eq. (2.28).

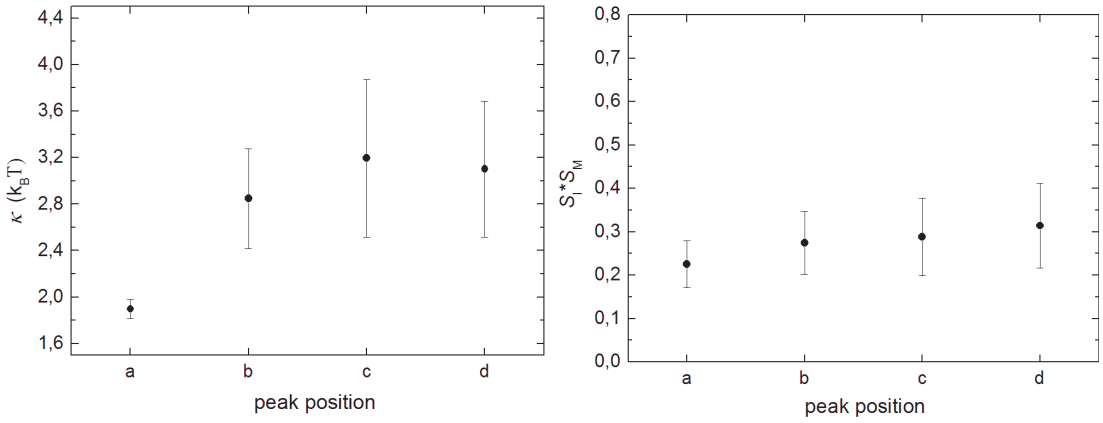

(a) (b)

Figure 4.17: Results of the fits in Figure 4.16. (a): the corresponding variation of bending modulus κ in the energy units of k_BT as a function of peak position; (b): - of the product $S_I * S_M$.

Analysing the results obtained from all measurements Figure 4.18 shows the evolution of the κ_a and κ_{av} *versus* the polymer weight fraction C_p wt.%. One sees that κ_a doesn't change upon polymer addition, whereas κ_{av} slightly increase from 2.51 ± 0.10 to 2.99 ± 0.31 k_BT for $C_p = 0$ and 10 wt. % respectively.

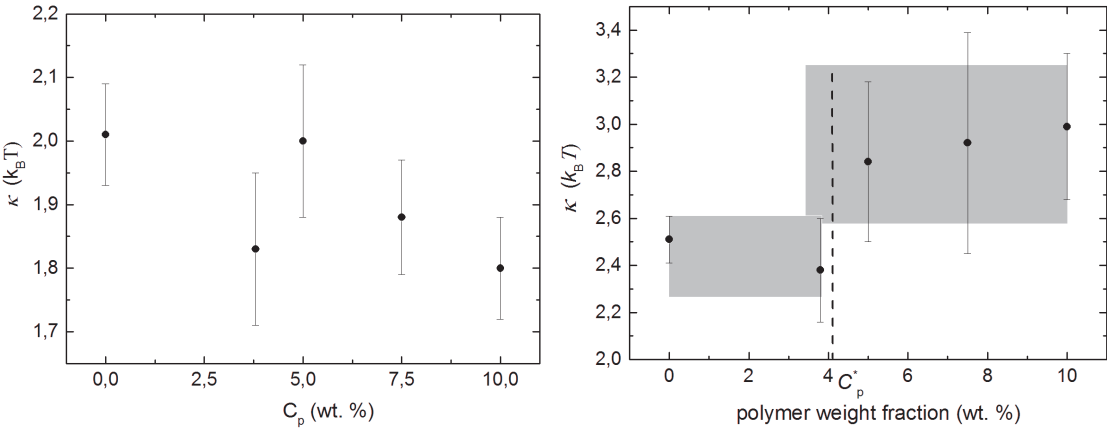

(a) (b)

Figure 4.18: Variation of the bending modulus (a): κ_a and (b): κ_{av} as a function of polymer weight fraction C_p wt. %.

4.3.2 Results. Method 2

Spectrum simulations

The drawback of deuterium magnetic resonance arise in the situation when some deuterons behave in motionally equivalent manner giving rise to overlapped resonance lines. It is

difficult to identify and assign specific peaks in the spectrum (Figure 4.5), and powder pattern spectra simulations are tricky but still promising method. Therefore, to deal with this problem Solid line shape analysis (SOLA) built-in TopSpin software (Bruker) were used to simulate and fit calculated spectra to experimental ^{2}H NMR spectra.

The distribution of intensity in spectra such as in Figure 4.5 can be determined by a computer simulation where the simulated spectrum is made up of a number of overlapping I = 1 quadrupolar powder patterns [30]. Before starting the simulation the experimental spectra were properly phase corrected and baseline corrected. Each line of the simulated solid state NMR spectrum can be characterized by the following parameters [94]: isotropic chemical shift δ_{iso}, amplitude (related to the integrated intensity), asymmetry parameter η (axial symmetry: $\eta = 0$), Gaussian/Lorentzian parameters (the half-width at half-maximum), quadrupolar tensor (ν_Q) and a suplementary parameter for the apodization (Lorenzian broadening). From these parameters, it is then possible to compute the modelled spectrum as the sum of the individual lines choosing the static condition of the experiment (without sample spinning).

The mismatch criterion, which is used in the simulation routine is the least square difference between the experimental and modelled spectrum. The optimization algorithm (Simplex) aims at minimizing the mismatch criterion by varying the parameters of the different lines. The "best overlap %" value displays the calculated overlap area of the lines of the experimental and the modelled spectrum (overlap in % = 100·(1 - ($S_{exp} - S_{calc}$)/S_{exp})).

Starting with an approximate solution, by adjusting the simulation parameters for each CD_2 and CD_3 segments in octanol molecule we compute the calculated spectrum until it approximately fits the experimental spectrum.

An example of computer simulated "powder-type" spectrum is shown in Fig. 4.19. The key parameters in the simulation are listed in Table 4.1. The third column in the table is the line broadening (LB) factor in the units of hertz. The value of 60 Hz was used for exponential apodization (or window multiplication) during the Fourier Transformation. Exponential multiplication is the most often used apodization function in one-dimensional NMR. Its main purpose is to increase the signal to noise ratio of the data and to give greater weight to the Free Induction Decay at small time values, where it has the greatest amplitude (further details in [133]). The Fourier transform of an exponential function yields a signal with a Lorentzian line shape. Thus, an exponential window does not change the lines shape, or its integral but increases the linewidth by LB. During the spectrum simulations we keep constant the value of line broadening for each of resonance doublets.

As it was shown in section 2.1 the NMR resonance lines can be approximated by a Gaussian or Lorentzian or combination of Gaussian and Lorenzian functions [116]. Of the various explanations advanced to interpred the broadening the one given in [20] in

terms of fluctuations in the energy and lifetime of the spin states due to the interactions between neighbouring nuclei. The width of resonance line is characterized by a spin-spin transverse relaxation time T_2. In our case we used the Gaussian broadening of around 800 Hz.

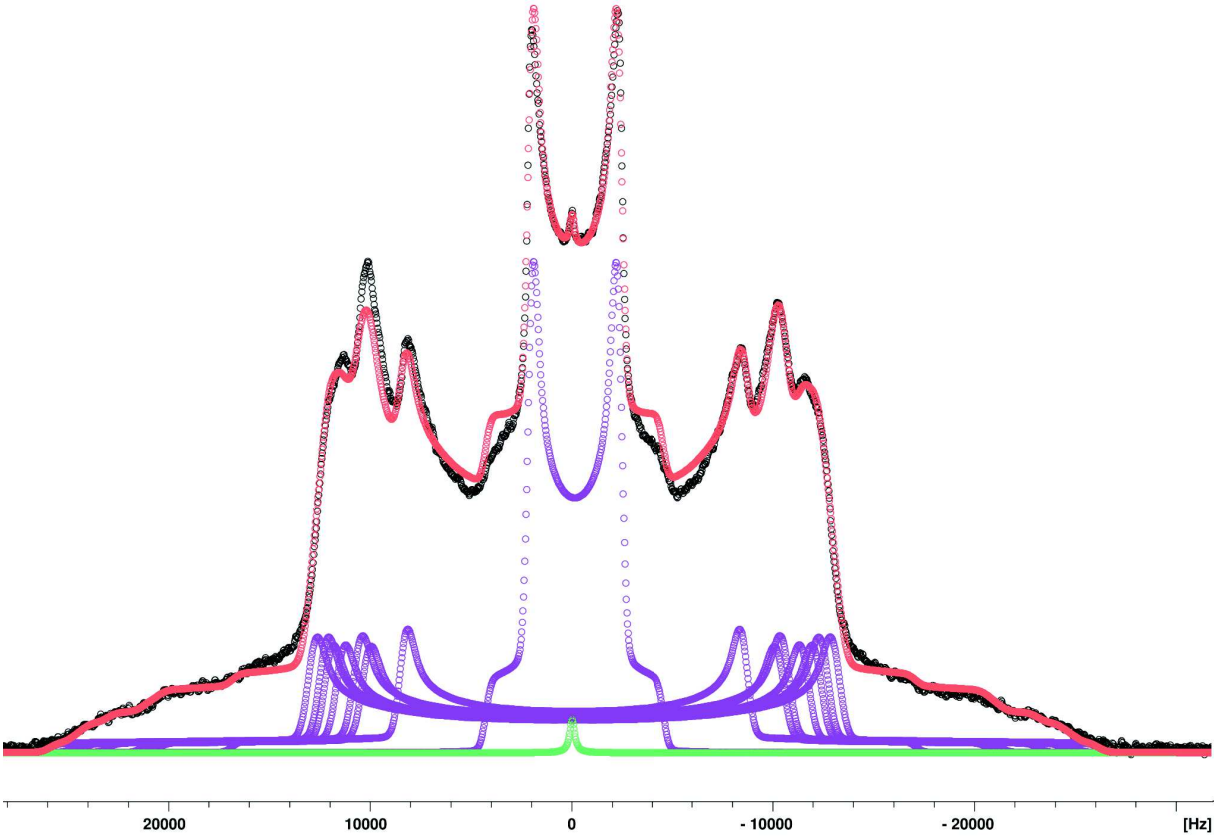

Figure 4.19: . Experimentally recorded (black) and calculated NMR spectrum (red) of sample with $\Phi_m = 26.5$ % and $C_p = 0$ wt. %. The overlap equals to 98 %. The 7 CD2 and 1 CD3 powder patterns are presented in violet, whereas an isotropic chemical shift - in green.

However, we should mention that the fitting by SOLA without manual adjusting/fixing the parameters does not give the physically correct results, even if the value of spectrum overlap is high. The algorithm used in the software does not ensure the unicity of the obtained solution that will only be the closest to the starting point. The procedure of the fitting is fairly robust when close to a final, well defined solution.

At first the spectra fitting was performed as it is shown in Figure 4.20 without careful attention to the intensity of the doublets, especially to the area under the peaks. One sees the marked increase of the intensity at the 4-CD_2 octanol position and decrease at the 7-CD_2, which could not be explained in terms of physics behind, because the area under the doublet is directly proportional to the amount of deuterium, which contribute

Table 4.1: Simulation parameters for the spectrum (Figure 4.13) of the sample with Φ_m = 26.5 % and C_p = 0 wt. %.

Chain position	$\Delta\nu_Q$ (kHz)	Line broadening (Hz)	Gaussian broadening (Hz)	Intensity (a.u)	δ(iso)(ppm)
1-CD_2	26.025	60	800	0.23	0
2-CD_2	24.9	60	800	0.23	0
3-CD_2	24.3	60	800	0.22	0
4-CD_2	23.1	60	800	0.22	0
5-CD_2	21.3	60	800	0.24	0
6-CD_2	20.55	60	800	0.22	0
7-CD_2	16.95	60	675	0.25	0
8-CD_3	4.425	60	477	1.0	0
HDO	0	295	0	0.07	3.700

to corresponding resonance frequency. Simulated spectrum in Figure 4.20 matches as well the experimental one, but the resulting peak assignment is not correct.

Finally, all spectra were adequately simulated as is it shown in Figure 4.19: by including 7 doublets (CD_2 bonds) with equal weightings, the 8th doublet is exceptional (the terminal CD_3) and a peak in the center(chemical shift of water).

The similar line shapes calculations, that were done on lyotropic lamellar systens can be found in the works [8, 29, 102, 115, 126] and the existing de-packe-ing techniques (the calculation of the 'aligned' ^{2}H NMR spectrum from the 'random' powder pattern spectrum) in the works [112, 113, 122].

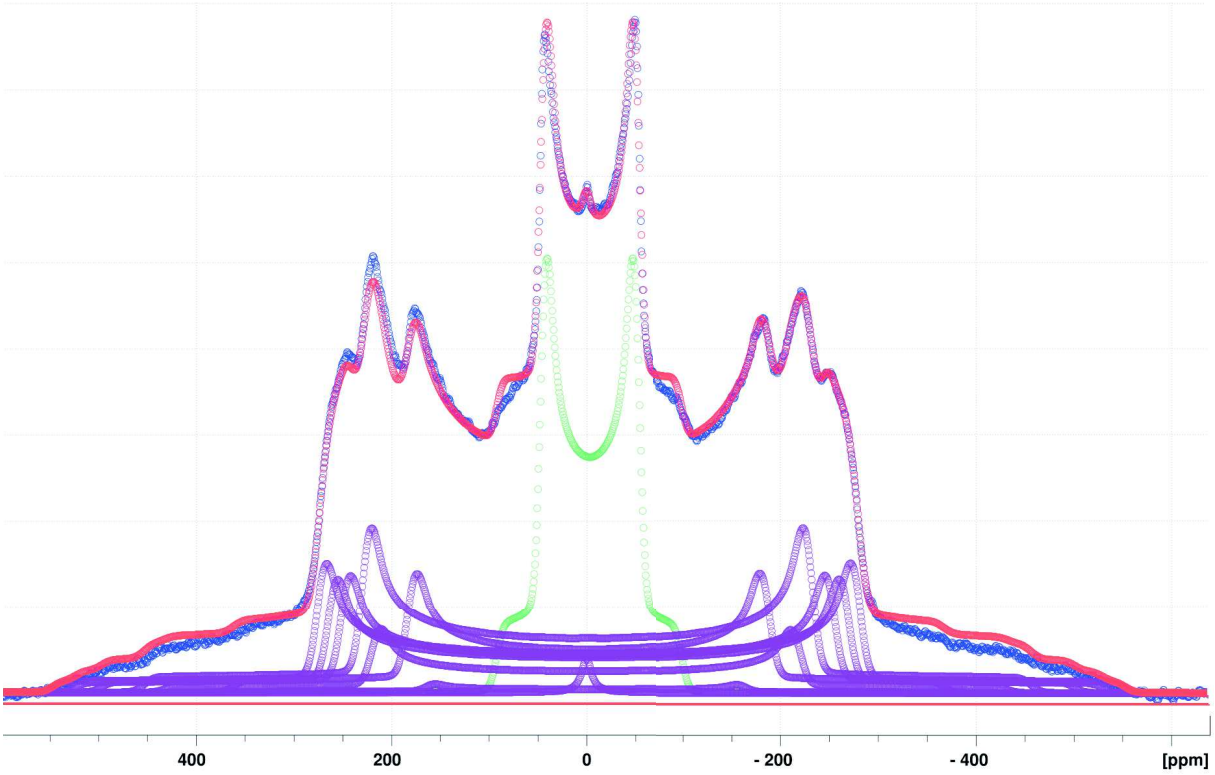

Figure 4.20: Experimentally recorded (blue) and calculated NMR spectrum (red) of sample with $\Phi_m = 26.5$ % and $C_p = 0$ wt. %. The overlap equals to 96 %. The pake patterns are pictured in violet. 1 ppm = 46.1 MHz.

Table 4.2 illustrates the comparison of the quadrupolar splitting values obtained by the Method 1 (peak to peak distance measurement, section 4.2) and the Method 2 (spectrum simulations, Figure 4.19). One sees that the quadrupolar splitting are similar for "a" and "b" peak position to those obtained by Method 2 (a bit smaller due to the broadening of the peaks) since the splitting corresponds to CD_3 group and 7-CD_2 group respectively. Conversely they are different in Method 2 compared to "b" and "d" peaks since the latter are due to superimposed CD_2 groups splitting.

Table 4.2: The assignment of peaks to specific chain position. Comparison of the values of $\Delta\nu_Q$ obtained from the Method 1 and Method 2 for the sample in Figure 4.19.

Peak position	$\Delta\nu_Q^1$ (kHz)	$\Delta\nu_Q^2$(kHz)	Chain position
a	4.262	4.425	8
b	16.544	16.950	7
c	20.328	20.550; 21.300	6; 5;
d	22.906	23.100; 24.300; 24.900; 26.025	4; 3; 2; 1

The order parameter of the octanol in the mesophase

In liquid-crystalline membranes, the quadrupolar splitting corresponds to the order parameters of the surfactant (co-surfactant) molecules. The relationship between $\Delta\nu_Q$ and the order parameter is given by Eq. (2.22): $\Delta\nu_Q = 3/4\nu_Q \mid S_{CD} \mid$.

The results of spectra simulation can help us now to reconstruct the order parameter profile. Figure 4.21 represents the order parameter S_{CD} as a function of the chain position of the mesophase with $\Phi_m = 26.5$ % and $C_p = 0$ wt. % (see Table 4.1). One sees that the order parameter decreases as the distance from the membrane interface increases, which is in accordance with earlier observations for any surfactant chain in a bilayer [73] and for a cosurfactant, such as octanol-D_{17} in the lamellar phase of the potassium oleate-octanol-water system [10].

In the earlier studies of Charvolin and co-workers [21] the binary mixture potassium laurate-water with perdeuterated lauric acid have been studied. The authors used for the measurements a planar oriented specimen. A similar variation of the order parameter as in our case was observed: the order parameter decreases as the distance from the lipid-water interfaces increases. The small irregular variations of the order parameter of specifically deuterated decanol was observed in the ternary mixture sodium decanoate/decanol/water [117]. It may be noted that apart from the small differences the qualitative behaviour of these two lipid phases is similar - the order parameter remains fairly constant for most of the chain and only becomes much smaller for the terminal three or four segments.

The molecular interpretation of the deuterium order parameter is characterized as follows [115]: the close packing of polar heads imposes steric constraints on the hydrocarbon chains reducing the conformational freedom of the individual chain molecules, and it is the reason for the constant order parameter in the upper part of the chain. In the central part of the membrane, where the free ends are located, the steric restrictions are relived and the order parameter decreases.

The evolution of the order parameter profiles along the dilution lines: (a) $C_p = 10$ wt. % (a) and (b) $C_p = 10$ wt. % are illustrated in Figure 4.22. Interestingly, one observes that the order parameter increases with a higher membrane mass fraction. The observed ordering effect seems to correspond with a reduction in the reorientation motion.

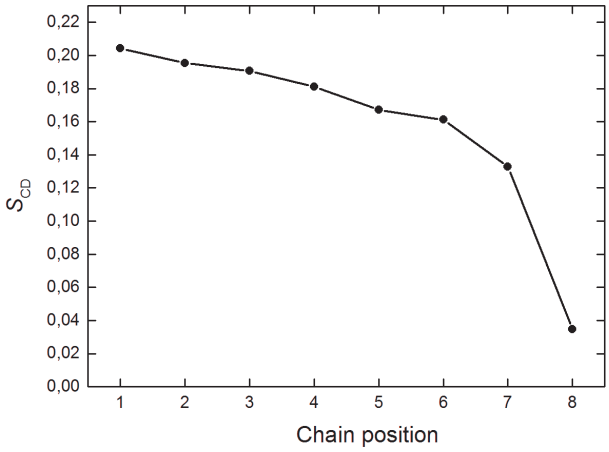

Figure 4.21: Simulated spectrum shown in Figure 4.13 provides position-dependent deuterium order parameter S_{CD}.

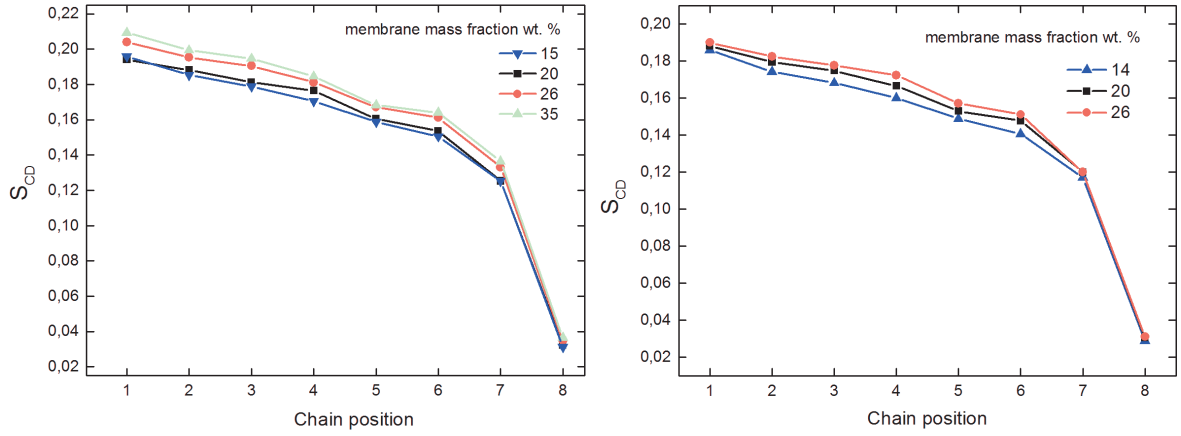

(a) (b)

Figure 4.22: The order parameter S_{CD} as a fuction of chain position along the dilution line (a) without polymer $C_p = 0$ wt. %; (b) $C_p = 10$ wt. % at different membrane mass fractions Φ_m.

Bending elastic modulus: results

Further using the results from spectra simulations we analyse our data in the same way as was explained in section 4.3.1 of this thesis. The Figures 4.23-4.32 show the fitting plots and the obtained values of the bending elastic modulus κ.

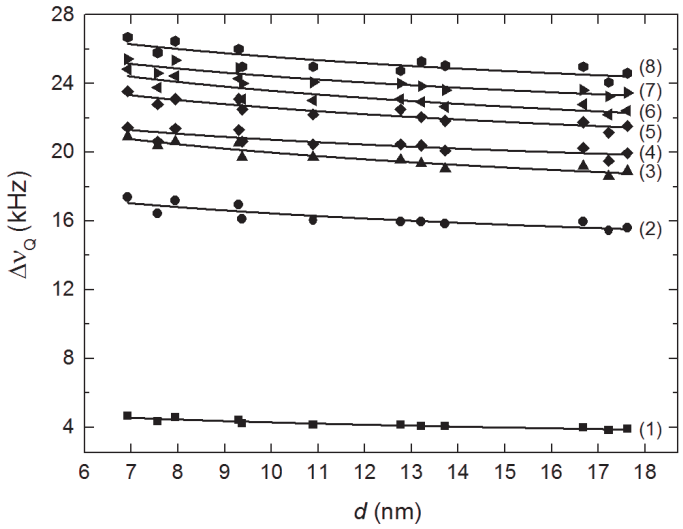

Figure 4.23: Evolution of 8 quadrupolar splitting (8 CD - groups in octanol chain) as a function of the periodicity d at the constant polymer weight fraction $C_p = 0$ wt. %. The plain lines are the best fits obtained from Eq. (2.28).

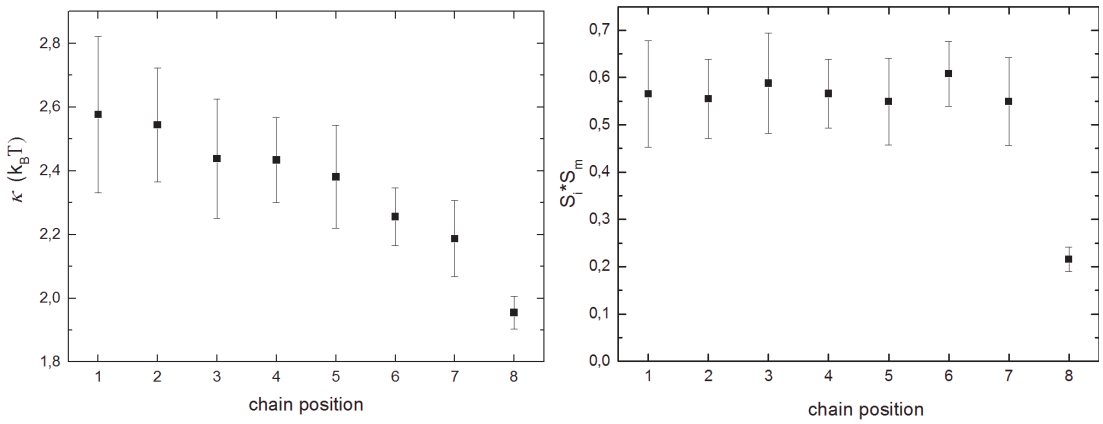

(a) (b)

Figure 4.24: Results of the fits in Figure 4.23. (a): the corresponding variation of bending modulus κ in the energy units of k_BT as a function of peak position; (b): - of the product $S_I * S_M$.

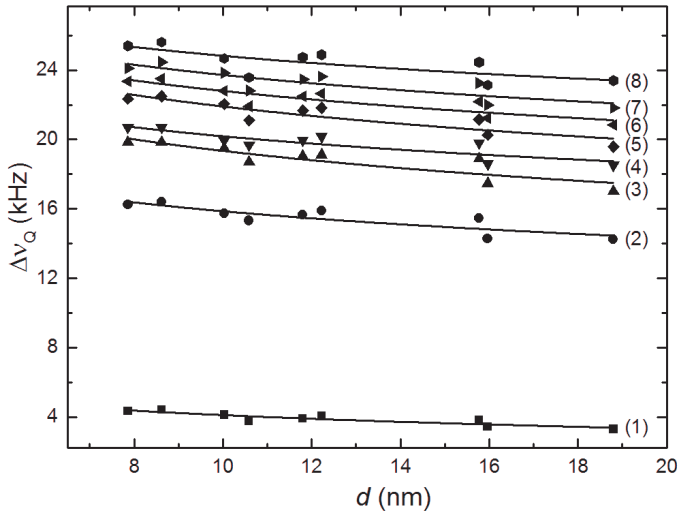

Figure 4.25: Evolution of 8 quadrupolar splitting (8 CD - groups in octanol chain) as a function of the periodicity d at the constant polymer weight fraction $C_p = 3.8$ wt. %. The plain lines are the best fits obtained from Eq. (2.28).

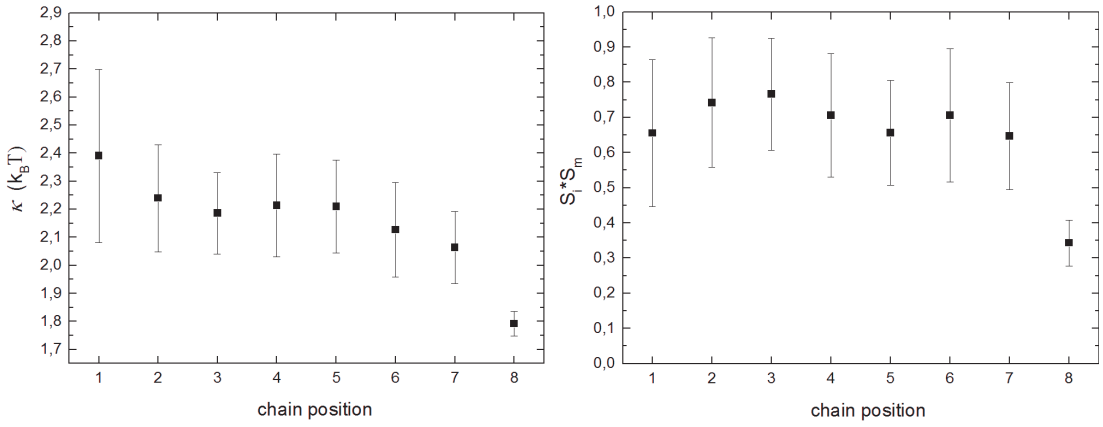

(a) (b)

Figure 4.26: Results of the fits in Figure 4.25. (a): the corresponding variation of bending modulus κ in the energy units of k_BT as a function of peak position; (b): - of the product $S_I * S_M$.

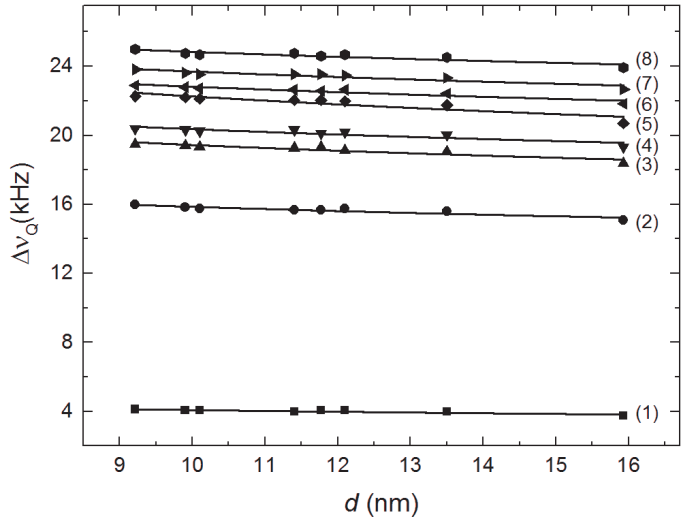

Figure 4.27: Evolution of 8 quadrupolar splitting (8 CD - groups in octanol chain) as a function of the periodicity d at the constant polymer weight fraction $C_p = 5$ wt. %. The plain lines are the best fits obtained from Eq. (2.28).

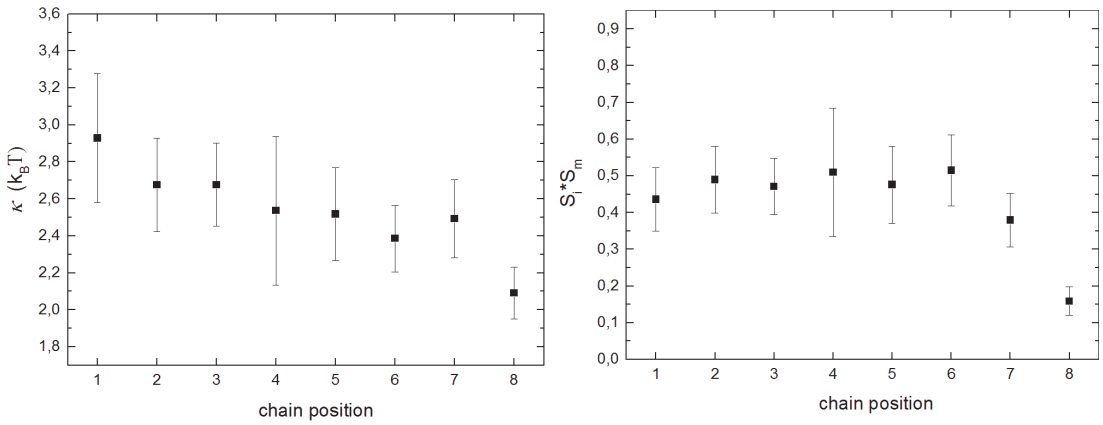

(a) (b)

Figure 4.28: Results of the fits in Figure 4.27. (a): the corresponding variation of bending modulus κ in the energy units of k_BT as a function of peak position; (b): - of the product $S_I * S_M$.

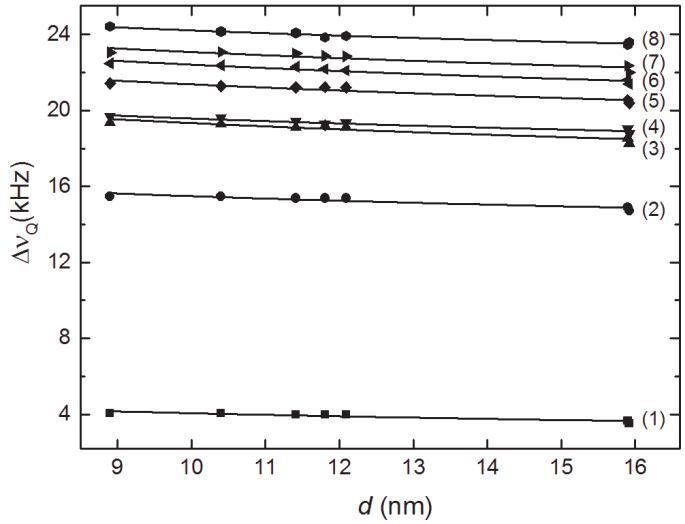

Figure 4.29: Evolution of 8 quadrupolar splitting (8 CD - groups in octanol chain) as a function of the periodicity d at the constant polymer weight fraction $C_p = 7.5$ wt. %. The plain lines are the best fits obtained from Eq. (2.28).

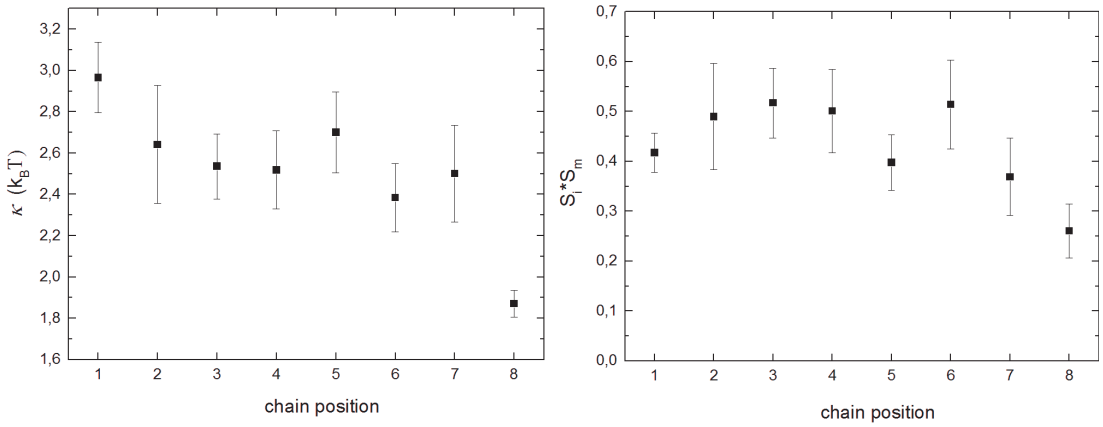

(a) (b)

Figure 4.30: Results of the fits in Figure 4.29. (a): the corresponding variation of bending modulus κ in the energy units of k_BT as a function of peak position; (b): - of the product $S_I * S_M$.

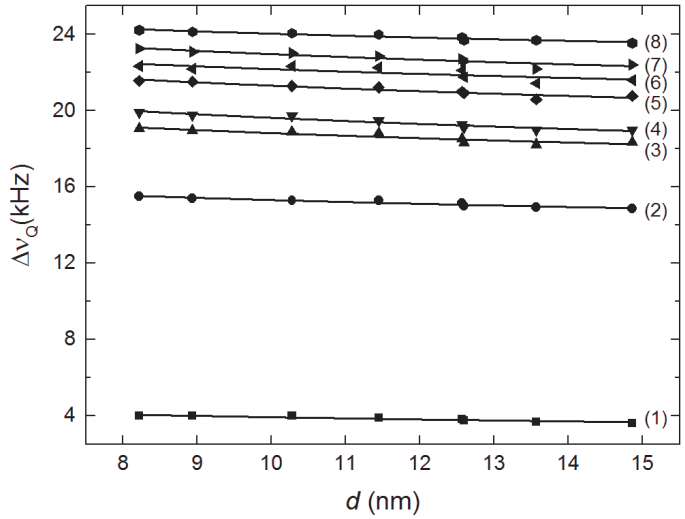

Figure 4.31: Evolution of 8 quadrupolar splitting (8 CD - groups in octanol chain) as a function of the periodicity d at the constant polymer weight fraction $C_p = 10$ wt. %. The plain lines are the best fits obtained from Eq. (2.28).

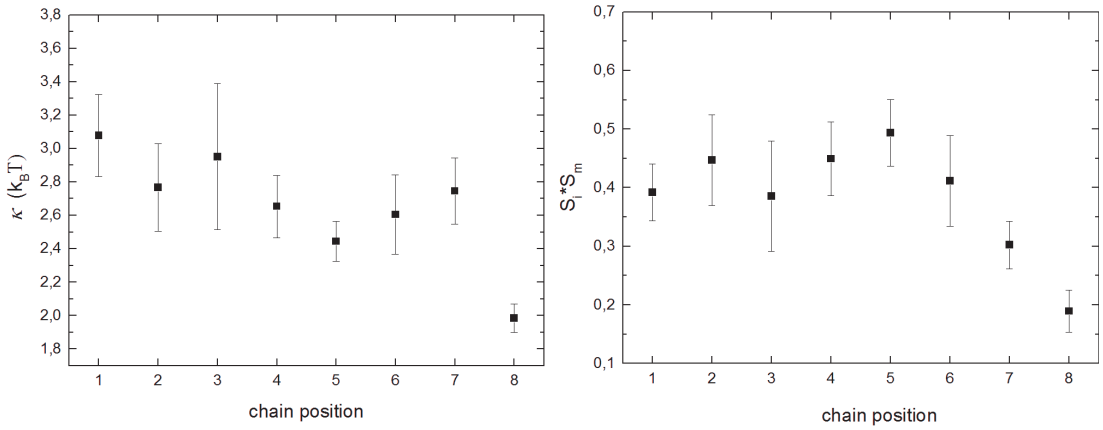

(a) (b)

Figure 4.32: Results of the fits in Figure 4.31. (a): the corresponding variation of bending modulus κ in the energy units of k_BT as a function of peak position; (b): - of the product $S_I * S_M$.

Figure 4.33 shows the variation of the bending modulus κ_{CD3} which correspond to 8-CD_3 chain position in octanol and κ_{av} - the average value (here we have taken as average of the values from 1-CD_2, 2-CD_2, 3-CD_2 - the chain position closer to the polar head).

4.4 Discussion

Figure 4.33 shows the same result that was obtained by Method 1, that κ has a tendency to increase when the polymer gets more concentrated. If we consider the samples along

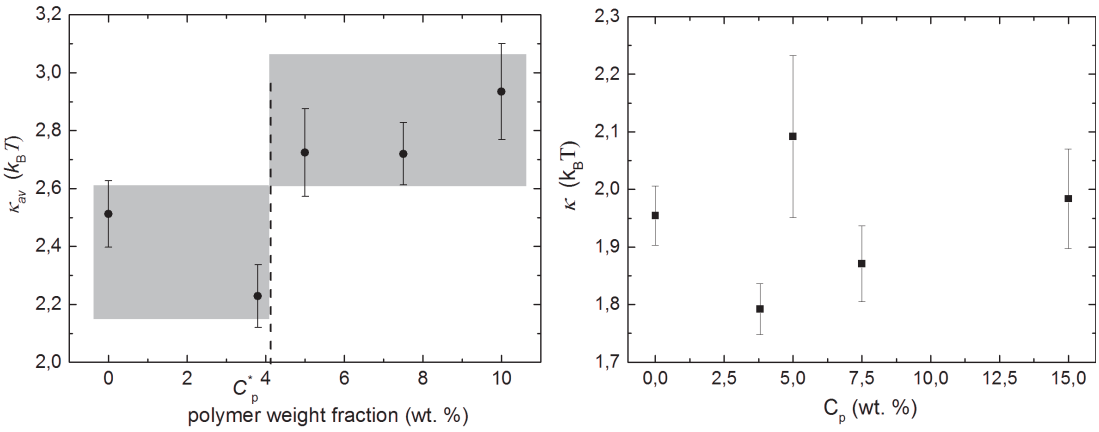

(a) (b)

Figure 4.33: Variation of the bending modulus (a): κ_{av} and (b): κ_{CD3} as a function of polymer weight fraction C_p wt. %.

the dilutions lines: without polymer $C_p = 0$ wt. %, at the constant amount of polymer in the water $C_p = 3.8$ wt. % and $C_p = 10$ wt % the bending modulus takes the values $\kappa = 2.51 \pm 0.12\ k_BT$, $\kappa = 2.23 \pm 0.11\ k_BT$ and $\kappa = 2.93 \pm 0.17\ k_BT$ respectively. The non-monotonic variation at $C_p = 3.8$ wt. % can be interpreted in the following way: since the samples located along this dilution line approach the critical point P_{s2}, we may attribute the changes in the bending elastic modulus to the progressive structural evolution of the lamellar mesophases in the vicinity of it. The increase in the bending modulus is small, but remains unexpected from the available theories which will be discussed below.

The process of macromolecules interaction with internal interfaces has important implications in colloid science (the stabilization of colloidal particles in solutions), petrochemical technology (the enhanced oil recovery) and in biological systems (the drug delivery by vesicles). Therefore, the bending elastic moduli of membranes has been extensively studied both experimentally and theoretically, since their values are typically of a few k_BT, and their effects can be probed by analysis of the thermal fluctuations. We can divide these studies is three main categories depending on the polymer affinity towards the surfactant membranes:

- non-adsorbing polymers;
- adsorbing polymers;
- anchored polymers.

Experimental aspects about the bending elastic modulus

The effect of **non-adsorbing** polymer on the bending elastic moduli of membranes has been studied by Bouglet et al. [12]. A neutral water-soluble nonadsorbing polymer

polyvinilpyrolidone (PVP) was incorporated in CPCL/hexanol/water system. The bending modulus was obtained from the measurement of quadrupolar splittings of perdeuterated hexanol by deuterium NMR. The authors found that κ is insensitive to the amount of polymer in the lamellar phase, while the Gaussian modulus $\bar{\kappa}$ is strongly decreasing.

The effects of **adsorbing** polymer PEG (M_w = 20 000) and NaCl concentrations on the stability of bicontinuous microemulsions and lamellar phases formed in AOT-water-isooctane mixtures are discussed in [95]. From the conductivity measurement the authors reported a phase transformation L_α - bicontinuous microemulsion with increasing C_p at constant surfactant and salt concentrations, which they suggested may be due to a decrease of the bending constant κ or/and to an increase of the Gaussian elastic constant $\bar{\kappa}$. These authors investigated in [96] as well the effect of PEG on the bending elastic modulus of membranes in sponge phase (SDS/hexanol/water system in brine and glycerol) by dynamic light scattering technique. The bending elastic modulus was extracted from the Zilman-Granek theory for fluctuating membranes. The obtained bending modulus decreases from 3.1 k_BT (for a polymer-free sponge phase) to 1.7 k_BT (C_{PEG} = 40 g/L).

The same dynamic light scattering experiment has been performed in the work [62] in order to investigate the effect of PEG (M_w = 20 000) on the bending elastic modulus of SDS/hexanol/brine system, in this case without glycerol. The result of this study shows that the dynamics of surfactant membranes are slowed down by the addition of polymer. They showed that with increasing the PEG concentration κ *increases*. For a polymer-free sponge phase they obtained κ = 3.1 k_BT and when polymer is added the bending modulus reaches the value of 5.7 k_BT (at polymer concentration of 0.4 mM). The reasons for the discrepancy of this result and the one obtained in [96] could be related to the presence of glycerol and the different value for the solvent viscosity in the system of reference [96]. The authors suggest that the increase in the bending modulus may be due to the internal rearrangement of membranes. Because PEG penetrates the membranes and may interact in different ways with SDS and hexanol molecules, leading to a local change in SDS/hexanol molar ratio.

Warriner et al. [132] have been investigated the influence of polymer molecular weight in lamellar gels based on PEG-lipids (PEG-DMPE mixtures). In the system the linear polymer chains anchor with one end to the membranes. They observe a phase transition from the lamellar to gel phase which occurs with increasing the polymer content. This effect is explained by the changes of the membrane elastic constants [131, 132].

Theoretical aspects about the bending elastic modulus

Effect of polymer inclusions on the membrane curvature elastic constants have been discussed in several theoretical studies, in whose the attention is directed to adsorbed [15, 16, 23, 36, 121] and end-grafted flexible polymers [13, 59, 60].

De Gennes approach (1990)

In the earlier study de Gennes [36] investigated the elastic moduli of surfactant bilayer, which exposed to a solution of neutral, flexible strongly adsorbing polymer. He correctly determined the functional form for the osmotic contribution to the bending elastic modulus in the adsorbing polymer system:

$$K \sim K_0 + \beta k_B T \ln(\frac{R_F}{D}) \tag{4.3}$$

where the first term K_0 is a bilayer contribution, and the second term is the effect of diffuse cloud [35](β is a numerical constant, R_F is Flory radius of single coil, $R_F \sim N^{3/5}a$), D is the length, which characterizes the strength of the surface attraction to monomers). However, this approach does not give the sign of polymer effect. Nevertheless De Gennes predicted the rigidification of the interfaces in the situation, when polymer solute suppresses the membrane undulations.

Brooks et al. approach (1991)

Brooks et al. [15, 16] studied the effect of adsorbed polymer using both a mean-field and scaling functional approach. The attention was restricted to the cases where polymer homogeneously and reversibly adsorbs onto the surfactant bilayer without penetrating it. Their result reached a surprising conclusion: the adsorption of polymer always leads to a *decrease* in the mean curvature rigidity K and an *increase* in the Gaussian rigidity $\bar{K}$. In the limit of strong adsorption authors showed that scaling and mean-field approached give significantly different results: the latter predicts (for a good solvent) maximum shifts in the elastic constants that are small fractions of $k_B T$, whereas the scaling approach gives the contributions that can be arbitrarily large and at least comparable to the thermal energy [16]. Note however that the framework is that of mean-field, that is correlations of counterions are not taken into account.

Clement and Joanny approach (1997)

F. Clement ant J.-F. Joanny in their study [23] extended the work of Brooks et al. [16] using the same mean-field theory and calculated analytically the polymer contribution to the curvature moduli in the case of strong reversible and irreversible adsorption. A similar result was found: the adsorbed polymer always makes the membrane less stiff in both cases of polymer adsorption. The numerical prefactors given by the mean field theory are however very small and the polymer contribution to the moduli always seems smaller than $k_B T$. In an irreversibly adsorbed layer the total adsorbed polymer amount was kept constant and that the chain conformation in the layer can equilibrate freely. However, if the constraint imposed by the irreversibility is stronger, the rigidification of the membrane has been expected as for a polymer brush. Authors mention also that the use of mean field theory is not a good approximation in a good solvent conditions, where the concentration fluctuations are known to be relevant.

Skau and Blokhuis approach (2002)

In [121], K.I. Skau and E.M. Blokhuis consider irreversible polymer adsorption in the

context of the mean-field model and compare to earlier results [15,16,23]. They investigate directly the influence of polymer on the curvature properties of bilayer, the amount of polymer adsorbed varied away from equilibrium value. They argue their choice by the fact that in experimental situation for many polymer systems the desorption-adsorption kinetics are slow. So, for the time scales of the experiment, the adsorbed polymer is not necessarily in equilibrium with the bulk polymer and can be considered as irreversibly adsorbed. Authors extend the work of Clement and Joanny [23] considering the presence of free polymers in the bulk in the case of irreversible polymer adsorption; to achieve this they apply a local external field to keep the adsorbed amount fixed, whereas Clement et Joanny remove the polymer in the bulk. The result of their calculation is that the value of the bending rigidity κ is reduced by the adsorption of the polymer, so that the membrane becomes more flexible. Hovewer, what is new, that when the adsorption is fixed to a value larger than the equilibrium one, the reduction also becomes less, and ultimately changes sign leading to an *increased* bending rigidity [121]. Authors mentioned, that one can deal with more strict irreversible adsorption like fixed locations on the membrane, which may lead to a change in the sign of polymer contribution to the bending modulus. However, such models require more challenging mathematics and remain open to discussions.

Lipowsky et al.
Lipowsky et al. [59, 60] determined the effective elastic constants and the spontaneous curvature of the system, where polymers anchored (see Figure 4.34) onto a fluid membrane to both sides. The authors analyze the excess entropy of the polymer anchored to a curved surface relative to the polymer anchored to a flat substrate in both the mushroom and the brush regime. They showed that the anchored polymers stiffen the membrane, thus the effective bending rigidity increases: $\kappa_{eff} = \kappa + 0.21\ k_BT$ and the effective Gaussian modulus decreases: $\bar{\kappa} = \bar{\kappa} - 0.17\ k_BT$.

The adsorption of polymers anchored to one side of the membrane was studied in [13]. In the strongly adsorbed state, the anchored polymer forms a pancake, which are tightly bound onto the membrane surface. It turns out that the membrane now bends towards the polymer in order to maximize the number of contact points with the pancake [13,60]. This pancake induces a spontaneous curvature with an opposite sign compared to the mushroom case (Figure 4.35).

It was studied in [76] the membrane spontaneous curvature induced by flexible/semi-flexible polymer adsorption. Similar picture was observed as in Figure 4.35 for the case of non-anchored strongly adsorbed polymer. They showed even the possibility of encapsulation of polymer by the membrane (more details in [76]).

In summary, we have shown that the bending elastic modulus of surfactant membranes increases upon addition of adsorbing polymer PEG. The measured increase in κ (Figure 4.33) is not expected from the mean-field theory on the effect of adsorbing polymers on the elasticity of surfactant bilayers [15,16,23]. The works of Skau et al. [9] and Lipowsky et al. [60] predict the tendency of increase of κ, but for the case of stong irreversible adsorption

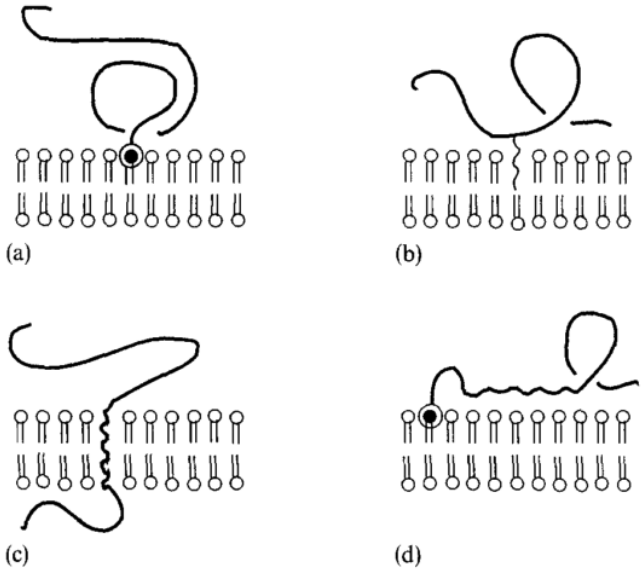

Figure 4.34: Different ways to attach polymer chains to bilayer membranes: (a) lipid anchor; (b) hydrophobic side chain; (c) membrane-spanning polymer segment; and (d) anchored and adsorbed chain. Taken from [91].

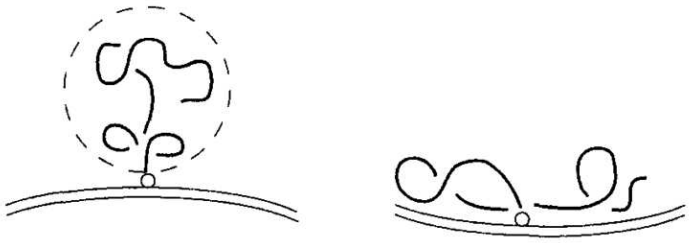

Figure 4.35: Schematic picture of the membrane bending through the interaction with anchored polymer: positive spontaneous curvature for desorption (left), and an negative curvature for strong adsorption (right) of polymer [91].

and for end-grafted polymers respectively. Indeed, the theoretical prediction of mean-field theory is a decrease in the bending modulus when polymer is adsorbed onto the surfactant membrane. This may indicate that our experimental system does not meet the theoretical assumptions of available models. The main assumption in the theory is the homogeneous, nonpenetrating adsorption of the polymer onto the membranes. However, it was shown that PEG has a special binding interaction with SDS molecules and nonnegligible degree of penetration in surfactant micelles and membranes [27]. This discrepancy maybe due to a more complex adsorption mechanism of PEG chains.

Further experiments and computer simulations are needed in order to have a better insight into these effects. The experimental results presented in this Chapter may already be useful in the development of theories necessary for a better understanding of this complex system.

4.5 Lamellar and MLVs region in the phase diagram

4.5.1 NMR spectra simulations

In this section, the deuterium NMR data concerning samples in the most diluted region of the phase diagram are presented. The main attention is given to those samples, for which the corresponding NMR spectra displays a biphasic behaviour. We have estimated the amount of isotropic phase relatively to lamellar phase along dilution lines in the phase diagram, as well as the effect of polymer addition.

Quadrupole NMR is well known to be a powerful technique in the study of liquid crystalline phase behaviours and in identifying one-phase and multiple-phases samples [8, 32, 73, 116, 126]. The spectra of multiple-phases samples are composed of the sum of the individual phases spectra, which are normally distinguishable. In the study of multilamellar vesicles (MLVs) to lamellar phase transition in [129] it was shown that for those samples which consist of MLVs the resulting spectrum is a broad singlet (see Figure 4.36b), whereas in the case where lamellar unoriented domains coexist with MLVs the corresponding spectrum is a superposition of the constituents (Figure 4.36c). The amount of each phase, or more precisely the amount of deuterium nuclei occupying each phase in a sample is proportional to the integral of that portion in the spectrum.

Interestingly, we have found similar spectra shapes for those samples, which are located in the most diluted part of the phase diagram. The spectra simulation, which were discussed in section 4.3.2 permitted us to measure the relative amount of each phase in mesophases.

As an example, Figure 4.37 shows the experimental spectrum (in black) and simulated (in red) for quite diluted sample with membrane fraction $\Phi_m = 10$ wt. % (periodicity, $d = 25.9$ nm) and without polymer. In order to fit the central part of the spectrum in Figure 4.37 we added to the chemical shift of water (DHO) an isotropic phase. Finally, the simulated spectrum, which is displayed in red is a sum of 8 quadrupolar powder patterns, chemical shift and MLVs isotropic singlet (in green). The portion of isotropic phase relatively to the lamellar phase was found to be equal to 9.6 %.

From these observations, new questions appear: does polymer favours MLVs formation? Does the location of the mesophase in the proximity of the phase boundary plays a more important role? Using the spectra simulations technique we can as well investigate the effect of PEG addition on the amount of isotropic phase in the mesophase.

Figure 4.38 shows the superimposed experimental spectra for the mesophases at constant membrane fraction $\Phi_m = 10$ wt. % and at different polymer concentrations $C_p = 0$ wt. %; $C_p = 5$ wt. % and $C_p = 10$ wt. %. One sees that with addition of polymer the central isotropic peak intensity increases, whereas the quadrupolar splitting varies

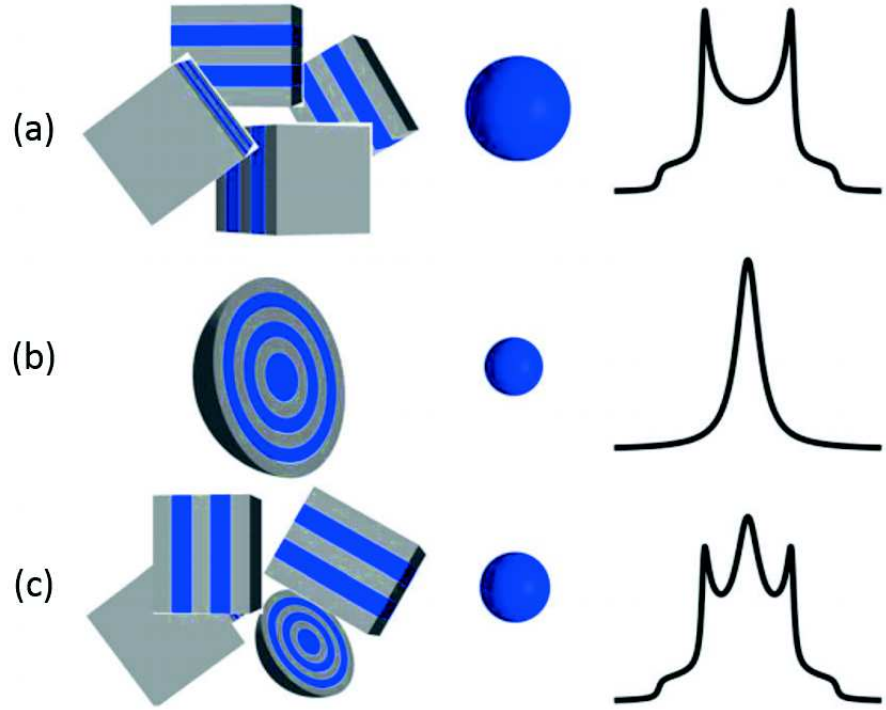

Figure 4.36: Picture of lamellar phase morphologies with corresponding diffusion tensors and quadrupolar ^{2}H spectra (taken from [129]). Column 1 : lamellar phase domains with water and surfactant shown in blue and gray, respectively. Column 2: diffusion tensors displayed as superquadrics [77]. Column 3: ^{2}H spectra. Row (a): random orientations of the lattice planes. Row (b): Multi-lamellar vesicles (MLVs). Row (c): Mixture of MLVs and randomly oriented domains.

slightly, but non-monotonically. In order to trace the effect of polymer addition on the amount of MLVs presented in each mesophase, we have performed the simulation for all the samples which appear biphasic.

Figure 4.39 shows the simulation result for the mesophase at Φ_m = 10 wt. % and C_p = 5 wt. %. The amount of isotropic phase appears to be higher than in the case without polymer and is equal to 19.6 %. The further increase of polymer concentration to C_p = 10 wt. % (Figure 4.40) leads as well to an increase of the isotropic phase amount in the mesophase to 22.9 %.

However, these mesophases are located very close to the phase boundary with L/L_α (see Figure 3.4). Therefore, it was important to check if one observes the same behaviour in the case when the mesophases become more concentrated. The results are shown in Figure 4.41, which gives a more complete, though semi-quantitative summary of NMR simulation (the quantitative information is contained in Table 4.3). The contour lines — perhaps somewhat arbitrarily drawn in a few places in the phase diagram — separate regions with nearly constant values for the amount of MLVs.

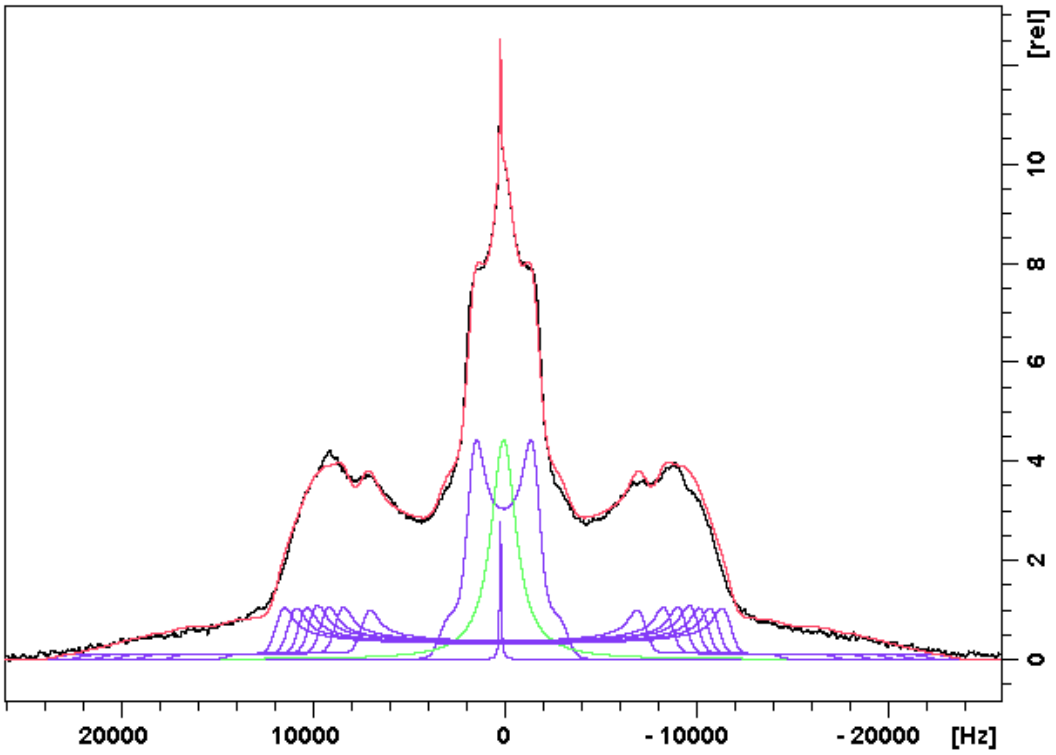

Figure 4.37: Experimental spectrum (in black) and calculated (in red) for the sample at $\Phi_m = 10$ % without polymer. The spectra overlap equals to 97 %. The fitting parameters are the quadrupolar splitting pake patterns of CD_3 and 7 CD_2 bonds; the chemical shift of the water DHO and isotropic phase (in green). The amount of isotropic phase in the mesophase is about 9.6 %.

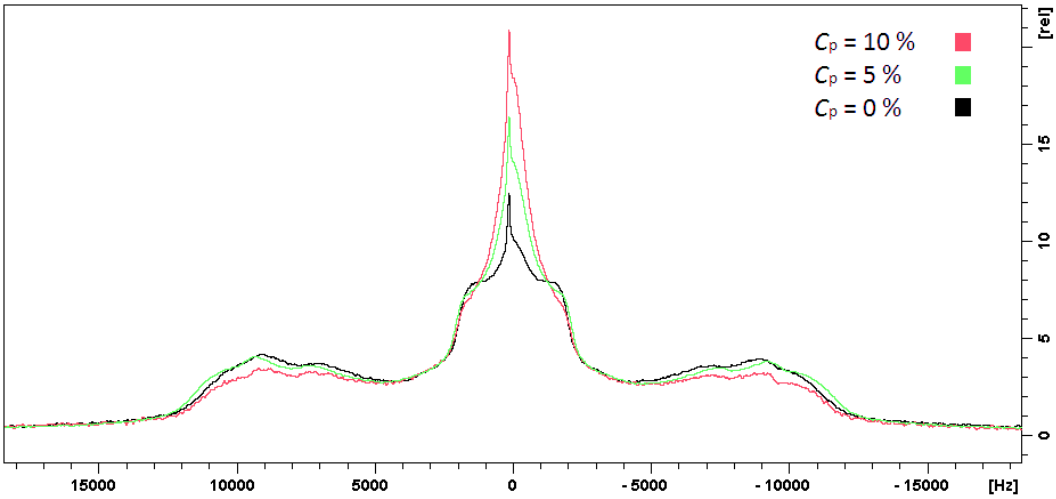

Figure 4.38: Spectra at constant membrane mass fraction $\Phi_m = 10$ wt. % at $C_p = 0$ wt. % (in black); $C_p = 5$ wt. % (in green); $C_p = 10$ wt. % (in red).

In summary, one sees from the spectrum simulations that MLVs coexist with lamellar phase in the range of the membrane mass fraction from 10 to 20-22 wt. %. There is no specific polymer effect on the amount of MLVs in the mesophases, except for the

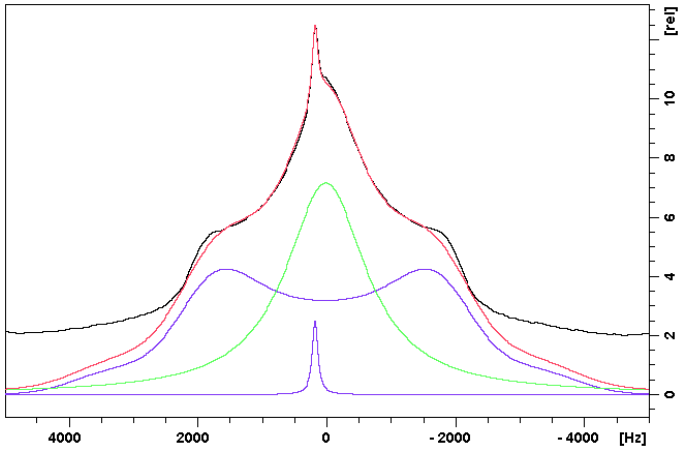

Figure 4.39: Fit of the central part of the spectrum in the range from 2535.5 to -2535.5 Hz for the mesophase at $\Phi_m = 10$ wt. % at $C_p = 5$ wt. %. The fitting parameters are a quadrupolar splitting of CD_3; a chemical shift of the water DHO and isotropic phase.

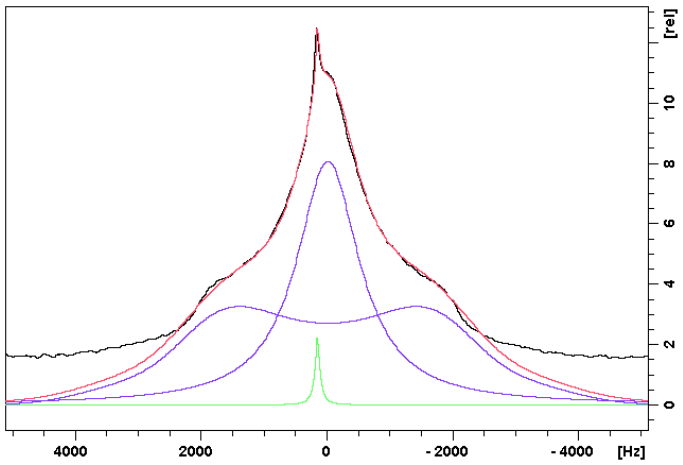

Figure 4.40: Fit of the central part of the spectrum in the range from 2535.5 to -2535.5 Hz for the mesophase at $\Phi_m = 10$ wt. % at $C_p = 10$ wt. %. The fitting parameters are a quadrupolar splitting of CD_3; a chemical shift of the water DHO and isotropic phase.

Table 4.3: The relative amount of MLVs as a function of composition of the mesophases. The values are given in %.

	$C_p = 0$	3.8	5	10	15
$\Phi_m = 10$	9.6	-	19.6	22.9	13.5
12	6.9	13.9	-	-	13.0
14	3.6	7.1	3.1	4.6	8.5
16	2.2	4.8	2.2	1.0	3.4
18	2.2	6.2	0.4	0.8	1.1
20	1.4	1.5	0	0	0
22	0	0	0	0	0

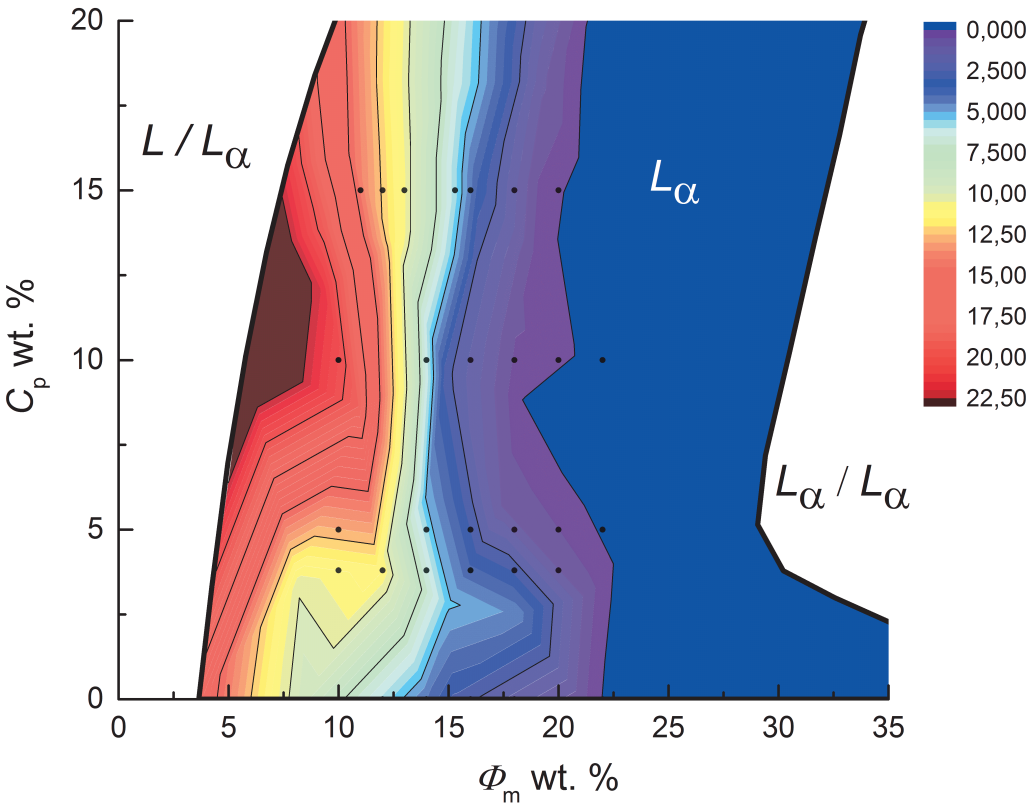

Figure 4.41: Schematic contour plot for the relative amount of MLVs in the mesophase. The color scale is given in % (the relative amount of isotropic phase in the mesophase). Black dots correspond to the location of mesophases in the phase diagram.

mesophases with $\Phi_m = 10$ wt. %, where the amount of MLVs increases drastically. In turn, the amount of HDO which gives a chemical shift signal is calculated to be from 0.10 to 0.25 % in all mesophases and located in the spectrum in the range 3.5 to 3.7 ppm.

4.5.2 Freeze fracture electron microscopy results

The observations of the biphasic behaviour in the NMR spectra have pursued us to investigate the mesophases as well by electron microscopy. Thus, we have performed freeze fracture electron microscopy (FFEM) on two different groups of mesophases.

In the first group the samples are situated on the axis parallel to the water/PEG axis in the dilute part of the phase diagram, thus their membrane mass fraction is the same: Φ_m = 10 wt. % without polymer and with 3.8; 7.5; 10; 15 wt. % of polymer in water. Note that the periodicity of the lamellar stack for these mesophases is in the range from 18 to 25 nm (inferred from SAXS).

The second group represents the samples in a more concentrated part of the phase diagram, that is to say at Φ_m = 20 wt. % and with 0 wt. %; 7.5 wt. % and 15 wt. % of polymer in water. The periodicity of the mesophases from this group is in the range from 10 to 12 nm.

The studied mesophases are presented in Figure 4.42. The section of the phase diagram shows the locations of the mesophases marked as crosses and circles. We have performed as well the freeze-fracture scanning electron microscopy (SEM) on the mesophases at Φ_m = 12 wt. % and C_p = 10 wt. %; Φ_m = 20 wt. % and C_p = 15 wt. % (white circles). In some of our mesophases 30 % in volume of water content was replaced by glycerol (yellow crosses).

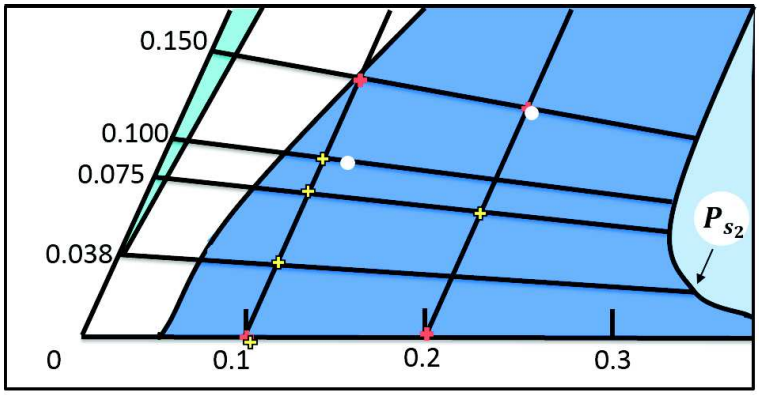

Figure 4.42: Section of the phase diagram in Figure 3.3. Red crosses represent samples studied by FFEM, yellow crosses - samples studied by FFEM, but containing glycerol, white circles - samples studied by SEM.

Figures 4.43a and 4.43b show the freeze fracture electron micrographs from the mesophases at constant membrane fraction Φ_m = 10 wt. % without polymer. Figure 4.3b shows a typical texture for a lamellar phase with a perfect stacking of bilayers. The steps (arrow in Figure 4.43b) are the signature of the lamellar structure [2]. They represent the fracture surface, which is perpendicular to the bilayer. The texture of the mesophase in Figure

4.43a consists of the defects where the lamellae are bent. The mesophase with $\Phi_m = 10$ wt. % and with polymer, $C_p = 15$ wt. %, exhibits a modified texture (Figure 4.43c and d). One observes some spherical objects (indicated by stars in Figure 4.43c) which are dispersed in the lamellar phase matrix. These objects are likely to be unilamellar vesicles of different size (about 50 nm). Note that this mesophase is located on the phase boundary and thus the system reveals biphasic. The small unilamellar vesicles can come from the L_α/L phase (see the phase diagram in Figure 3.4). Figure 4.43d shows the lamellar structure (arrow) and the unilamellar vesicles (stars).

In order to examine the influence of the phase boundary we go from diluted to more concentrated mesophases. Figure 4.44 shows the pictures from the mesophases at constant membrane fraction $\Phi_m = 20$ wt. % without polymer and at $C_p = 10$ and 15 wt. % of polymer in the water layers. It can be seen that lamellar organization is retained in all samples on the scales up to a few microns. Only for the mesophase at $C_p = 15$ wt. % the micrograph shows some defects (Figure 4.44(d)).

Freeze fracture electron microscopy experiments have been performed in the lamellar phase of the water-SDS-octanol system in the work of Auguste et al. [6]. The authors have found two types of bilayer organisations: stack of flat parallel bilayers at high surfactant and alcohol concentrations and multilayered vesicles of large size in the dilute part. The mesophases in [6] were prepared with a cryoprotectant - glycerol. Thus, in order to compare our results with the latter, we replaced as well the water content by glycerol (30 % in volume).

Figure 4.45 represents the electron micrographs obtained for the mesophases at constant membrane fraction $\Phi_m = 10$ wt. % and different polymer content with glycerol. Micrographs in Figures 4.45a and 4.45b show that without polymer the mesophase contains many defects. One sees on the fracture face (Figure 4.45a) the bilayers (arrow), which are somehow wrapped. The vesicles embedded in the lamellar matrix are very polydisperse in size (star) ranging from small unilamellar vesicles of about 50 nm diameter to MLV (onions) of more than 1 μm (Figure 4.45b). The large multilayered vesicle is shown in micrograph in Figure 4.45c for the mesophase at $C_p = 7.5$ wt. %. The fracture face (Figure 4.45c) shows a multilayered object, which is commonly called spherulite of a diameter about 1.5 μm. Figure 4.45d shows that the mesophase ($C_p = 3.8$ wt. %) has a domain-like structure, where the largest domains are about 10-15 μm. Note that the smaller domains could represent the MLVs. For example, if one does the fracturing perpendicularly to the image plane, the same kind of picture as in Figure 4.45c may be observed.

An optional etching step, involving vacuum sublimation of ice, has been carried out after fracturing. The etching process is defined as the removal of ice from the surface of the fractured specimen by vacuum sublimation (freeze drying) [118]. Then, the mesophases topography were observed by means of the scanning electron microscope. In freeze-dried material ice damage appears as small etching holes or clear or dark spaces in the mi-

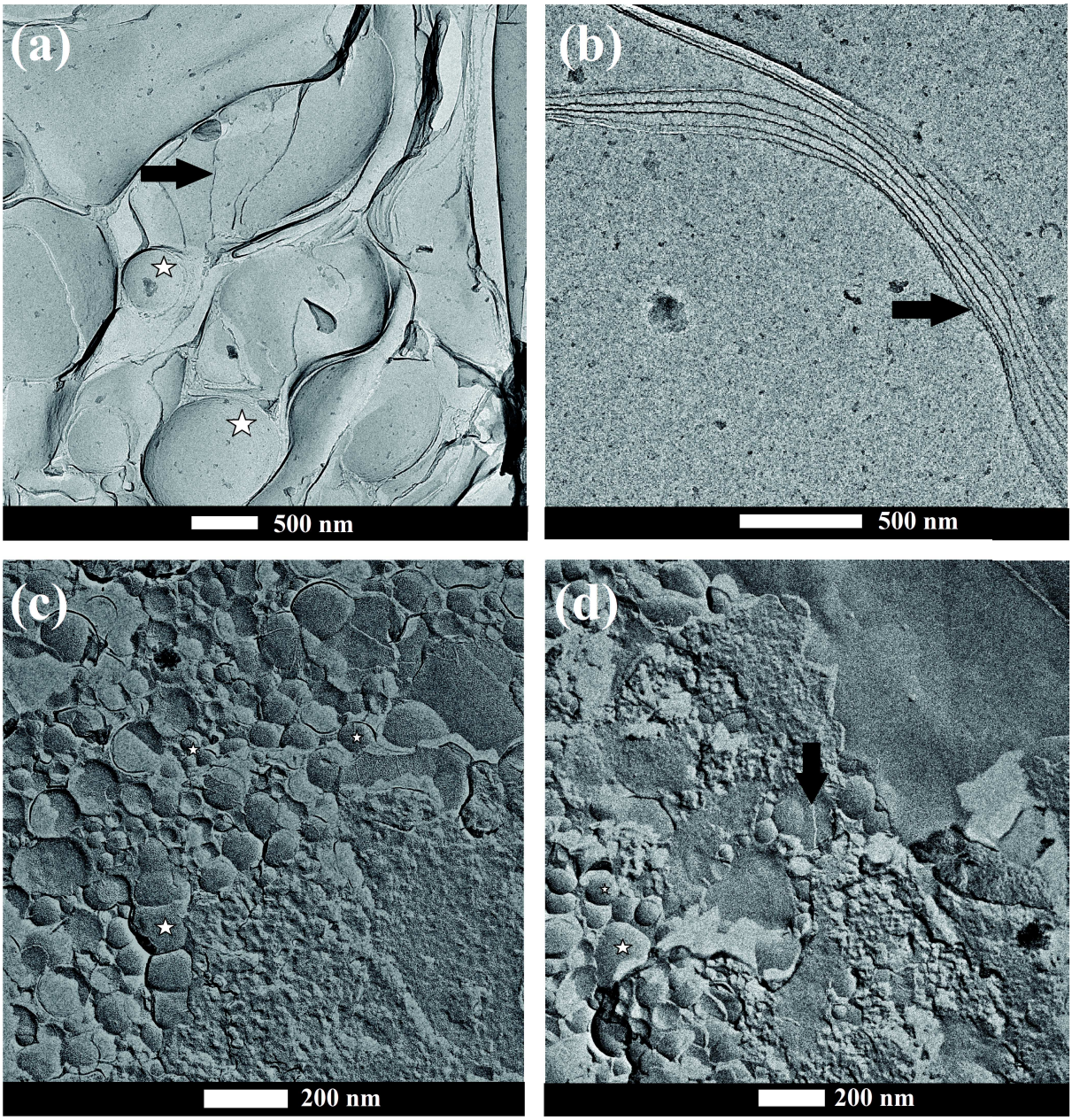

Figure 4.43: Freeze fracture micrographs visualized by FFEM for mesophases at constant membrane fraction Φ_m = 10 wt. % and different polymer content: (a) C_p = 0 wt. % stacks of planar lamellar (arrow) with the regions where bilayers are bent (stars); (b) C_p = 0 wt. % stacks of planar lamellar with steps (arrow); (c) and (d) C_p = 15 wt. % unilamellar vesicles (stars) dispersed in the lamellar matrix (arrow).

crographs. The material outlining such clear spaces consists of polymers that have been excluded from and pushed to the periphery of the growing ice crystals (Figure 4.46(c,d) arrow). A corresponding network of excluded polymers is shown in Figure 4.47(c,d). One observes small and larger water channels (etching holes) in Figure 4.47 (c), which may correspond to the places where the unilamellar and large MLVs were located.

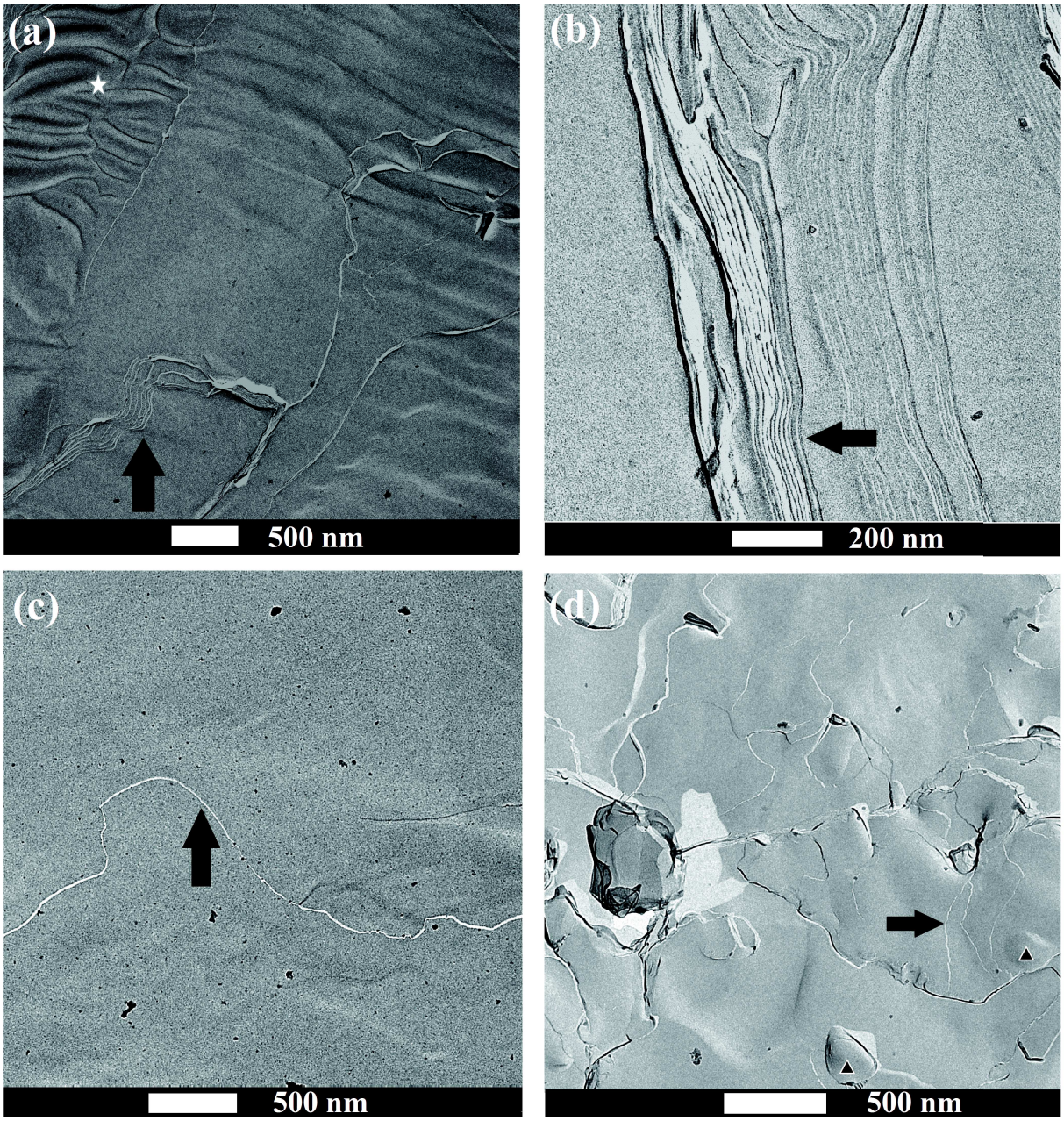

Figure 4.44: Freeze fracture micrographs visualized by FFEM for the mesophases at constant membrane fraction $\Phi_m = 20$ wt. % and different polymer content: (a) $C_p = 0$ wt. % lamellar structure, steps (arrow) and defects (star); (b) $C_p = 0$ wt. % stack of planar lamellar (arrow); (c) $C_p = 10$ wt. % (d) lamellar structure, steps (arrow); $C_p = 15$ wt. % lamellar stack (arrow), note the presense of defects where lamellae are bent (triangles).

4.5.3 Discussion

All the above results give evidence of the existence of multi- and unilamellar vesicles at high dilutions progressing into flat layers at a lower water content in the lamellar phase of the water/SDS/octanol/PEG system. As already mentioned this behaviour

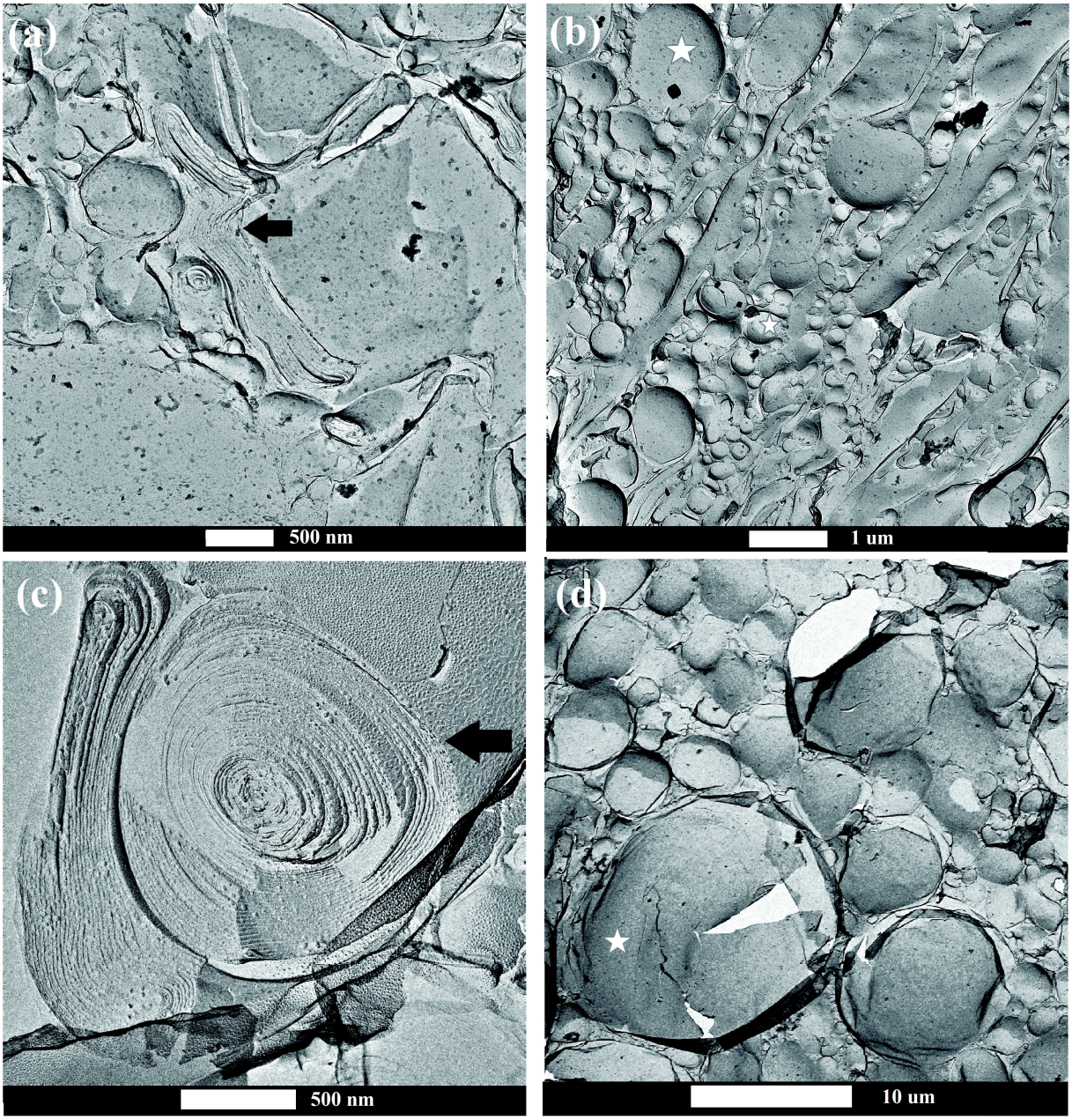

Figure 4.45: Freeze fracture micrographs visualized by FFEM for the mesophases at constant membrane fraction $\Phi_m = 10$ wt. % in the presence of cryoprotectant (30 % in volume of water is replaced by glycerol) and at different polymer concentrations (a) $C_p =$ 0 wt. % the fracture face with steps (arrow), the membranes are bent and the structure contains the defects; (b) $C_p = 0$ wt. % vesicles of different size dispersed in a lamellar matrix (stars); (c) $C_p = 7.5$ wt. % the membranes are wrapped creating an onion-like structure of about 1.5 μm(arrow) in diameter; (d) $C_p = 3.8$ wt. % large scale view shows the domain (star) of lamellae of about 10 to 15 μm, surrounded by the smaller domains, or it can be the MLVs.

was found before for the water/SDS/octanol lamellar phase in [6]. In that system the separation between the lamellar phase and the spherulites was mainly controlled by the

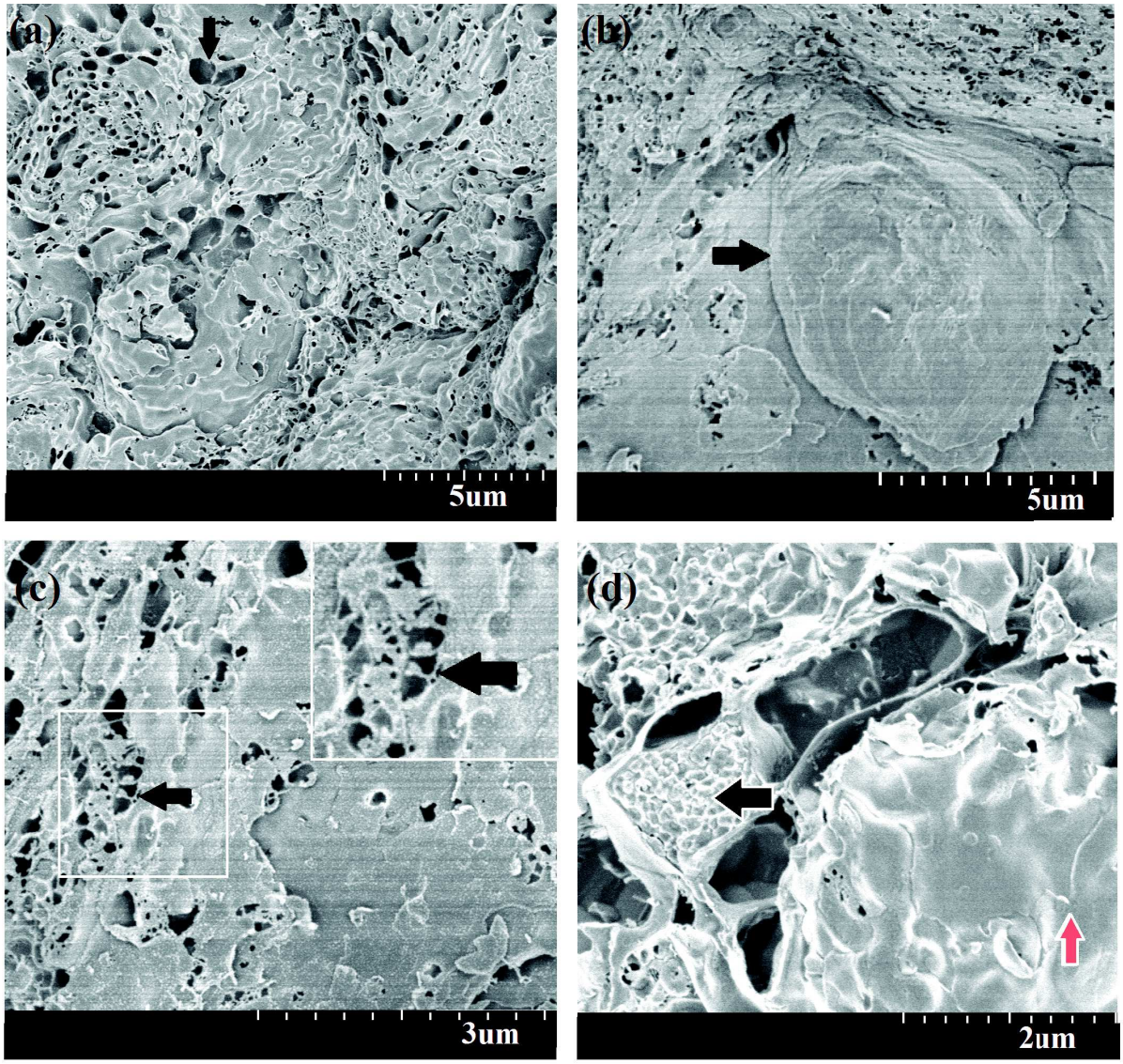

Figure 4.46: Freeze fracture scanning electron micrographs after etching for the mesophases at constant membrane fraction $\Phi_m = 12$ wt. % at $C_p = 10$ wt. %. (a) fracture face with etching holes or pockets (arrow) of different size; (b) lamellar structure with steps (arrow) surrounded by small etching holes; (c) one supposes that it could be the polymer (arrow), which collapses during the etching process; (d) may be the etching hole, which contains polymer (black arrow) and lamellar step (red arrow).

amount of alcohol in the membranes. The authors suggested that the spherulites are not thermodynamically stable and can be described as textural defects of the lamellar phase.

It is known that the topological transformation from spherical to planar structures is triggered by an increase of the $\bar{\kappa}$. It was proposed in [103] that $\bar{\kappa}$ increases with the A/S ratio. In some other studies the L_α to vesicle transition was observed under the influence of shear [43, 119]. In our system the alcohol/surfactant ratio was fixed in all prepared samples. One can propose several explanations for the observed spherulite texture at

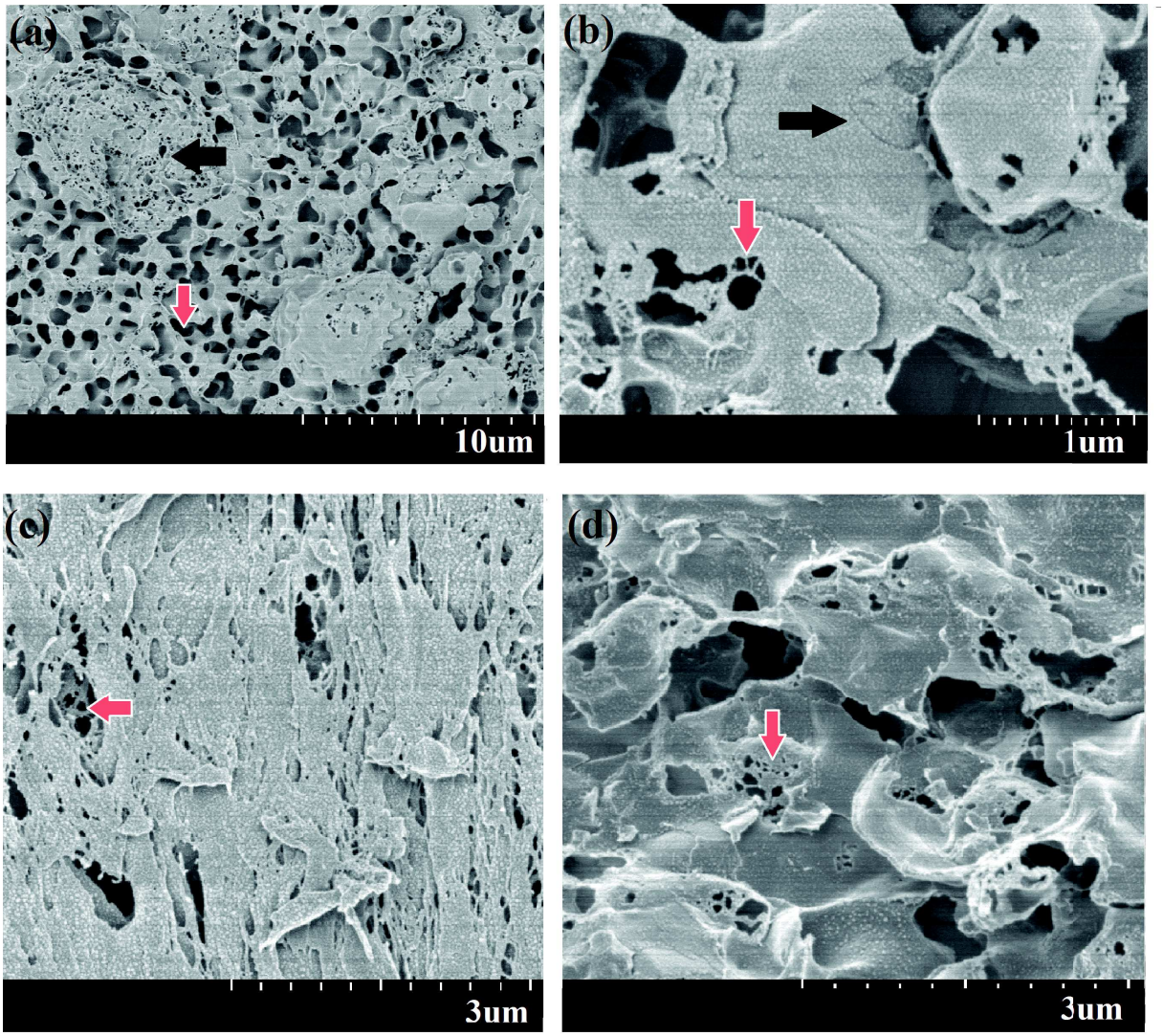

Figure 4.47: Freeze fracture scanning electron micrographs after etching for the mesophases at constant membrane fraction Φ_m = 20 wt. % at C_p = 15 wt. %. (a) two kinds of organization: big spherical object with small etching holes (black arrow) can possible be a MLV; smaller etching holes (red arrow) may represent the unilamellar vesicles; (b) lamellar step (black arrow) and polymer (red arrow); (c) etching holes with polymer (red arrow); (d) etching holes containing the polymer network (red arrow).

high dilution (Φ_m = 10 wt. %):

- it suggests that the small unilamellar and multilamellar vesicles (Figure 4.43) can come from L/L_α phase. We should not exclude as well a quenching artifact (the main quenching problem is the growth of ice crystals, which destroy the structure). However, in order to avoid the ice crystal formation, the water content was replaced by glycerol (30 % in volume). The spherulites texture is still preserved (Figure 4.45) in the presence of glycerol. Interestingly, the presence of glycerol can disorder the membrane packing, because glycerol can display a cosurfactant-like behaviour [6].

- it may be the result of polymer addition. In the study of the effect of nonadsorbing polymer on the lamellar phase stability [12,82], it was shown that the presence of polymer strongly modifies the texture. The spontaneous spherulite formation was observed in the presence of polymer. Spherulites may form due to the interaction between polymer and cosurfactant, leading to the asymmetry in the composition of the inner and outer monolayers. Polymer can induce the spontaneous curvature of the bilayer and create a kind of "water pockets" with high polymer concentration.

Numerous studies have been dedicated to lamellar $\rightarrow$ vesicles transition [6, 24, 43, 82, 119, 131, 132]. Nonetheless this problem is still not fully understood and we can not go further on this point. This is important to note, that we did not include the mesophases, which display the biphasic behaviour in the bending modulus calculations. Because we can not take into account the topology change corresponding to the appearance of spherulites in the theoretical model that has been established in [5].

Chapter 5

The diffusion coefficient of PEG in confinement

5.1 Fluorescence recovery after photobleaching pattern: principle

The Fluorescence Recovery After Photobleaching (FRAP) is an optical technique which allows to measure the diffusion coefficient of a labelled species by means of a fluorophore. The experiment consists in definitive destroying the fluorescence properties of the particles (photobleaching) in a given zone and in monitoring, over time, the recovery of the fluorescence which occurs as a result of the diffusional exchange between bleached and unbleached molecules.

In its turn, the photobleaching is the photochemical alteration of a dye or a fluorophore molecule, such that it loses its ability to fluoresce irreversibly. It is a chemical degradation induced by exposure to a photon flux. The molecular mechanisms involved are complex and depend on the type of molecule considered. Generally speaking, by passing from the excited singlet state to a triplet state, the fluorophores can react with other molecules (in particular oxygen), resulting in irreversible changes [64]. The bleaching rate of the fluorescent molecules is proportional to the number of received photons, thus to the power of the illumination and the time of exposure.

The technique was initially used to measure the translation diffusion and the lateral mobility of the fluorescent lipid analogues in phospholipid multibilayers [135]. It was implemented via a simple laser beam (FRAP [7, 135]). After the technique was modified by formation of planar fringe pattern (FRAPP [32]). A system of FRAPP, similar to that described by Davoust et al. [32] is used in our study (Figure 5.1), which was performed

in collaboration with Thierry Charitat[‡]. This geometry allows to work in the reciprocal space by using two coherent laser beams in order to create the fringes. This method has many advantages: it is very sensitive, which allows to study very thin samples, typically of a molecular thickness and also it permits to study the diffusion laws at a very wide range of scales and to distinguish different diffusive species [71].

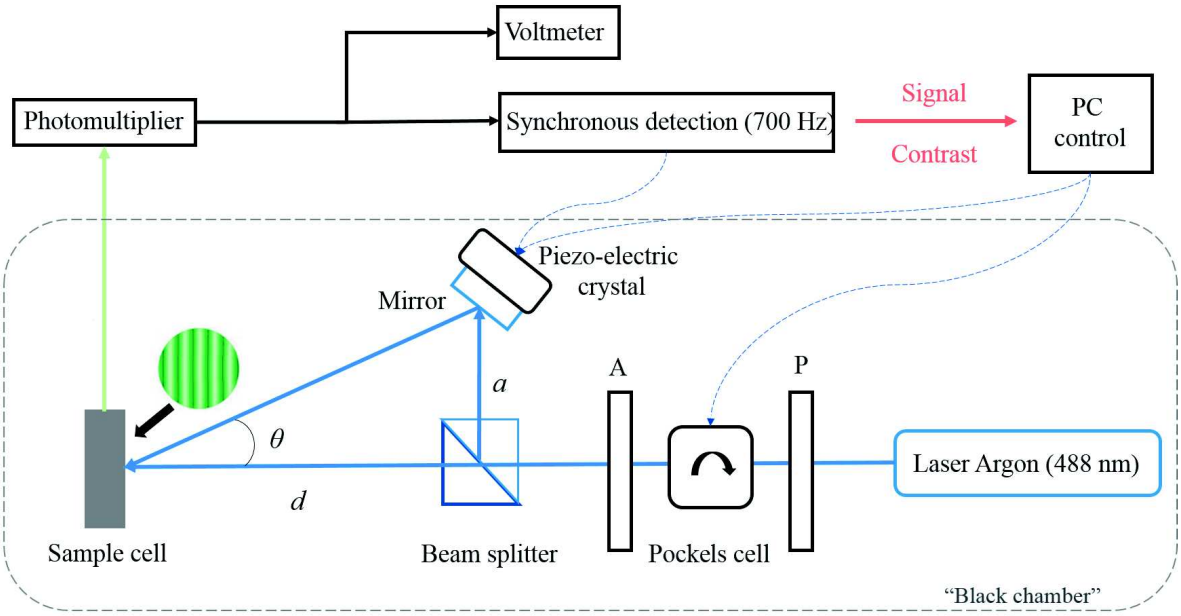

Figure 5.1: Experimental setup of FRAPP. The distances a and d are adjustable.

The principle of FRAPP is illustrated in Figure 5.1. The incident light beam of an Argon laser ($\lambda = 488$ nm, Spectra Physics, optimal power 1 W) is divided in two by a semi-reflective mirror. One part continues its trajectory directly towards the fluorescent sample, while the other will be reflected on a mirror placed at variable distance a from the semi-reflective mirror, before being reoriented to the studied sample. The two coherent beams cross in the sample cell providing an interference fringe pattern, where the fringe spacing i is given by:

$$i = \frac{\lambda}{2 \sin \frac{\theta}{2}} \tag{5.1}$$

where θ is the crossing angle between the two beams. In the following, to work in the reciprocal space, one has to determine the characteristic wave vector, which is given by:

$$q = \frac{2\pi}{i} = \frac{4\pi}{\lambda} \sin \frac{\theta}{2} \tag{5.2}$$

The adjustment of the distance a between the beam splitter and the mirror (see Figure 5.1) allows to vary the angle θ and to choose the size of the fringes i in the interval from 8 to 120 μm. The interfringe spacing can be measured through the projection of the fringe pattern if the photomultiplier in the experimental setup is replaced with a CCD

[‡]MCUBE research group in the Institute Charles Sadron, Strasbourg, France

camera or directly from the half angle θ. Figure 5.2 shows the image of the fringes taken with the camera of spacing, i, which equals to 100 $\pm$ 3 μm. It defines the wave vector, $q = 2\pi/i = 628 \pm 20$ cm^{-1}. Typically, the relative uncertainty of i is of order 3 %.

Figure 5.2: The measurement of the fringe spacing through the projection of the fringe pattern on a CCD camera. 1 fringe is equal to 100 $\pm$ 3 μm.

The intensity of the laser beam can be varied by means of a Pockels cell between two polarizers. It is a device containing an oriented crystal, which under the effect of a high voltage, becomes strongly birefringent. It is therefore possible to rotate the polarization of the incident beam by an angle related to the voltage. Applying a voltage across the cell allows to increase greatly the input power, from a few milliwatts to several hundreds of milliwatts, thus effectively photobleaching the fluorescent molecules.

The mirror is attached to a piezo-electric crystal. The application of a sinusoidal voltage to the crystal allows the phase shift between the two beams and has the effect of oscillating the position of the fringes on the sample (without varying the fringe spacing).

The fluorescence emitted by the sample is integrated and collected by the photomultiplier through an optical lens.

An experiment is performed in three stages:

- before the photobleaching the fluorescent molecules are distributed homogeneously in the sample;

- a fluorescence bleaching is obtained by producing a short ($t = 0.1 - 1$ s) full intensity pulse. A high frequency voltage is applied to the Pockels cell, causing the polarization of the beam to be rotated to arrive at the sample cell with maximum intensity. The concentration profile of fluorophores immediately after the photobleaching is periodic (Figure 5.3);

- after the photobleaching, the contrast of the fringe pattern is detected by modulation of the low intensity light fringes position at 700 Hz (with the help of piezoelectrically

modulated mirror). In other words the moments when the intensity collected by the optical fiber is maximal (I_{max}) alternate with those where it is minimum (I_{min}). The difference between I_{max} and I_{min} gives the contrast of the fringes (see Figure 5.3). A synchronous detection makes possible to filter the received signal by limiting itself to the characteristic frequency of vibration of the piezoelectric (700 Hz). This makes possible to eliminate most noise sources and considerably improves the quality of the measurements.

(a) (b)

Figure 5.3: Principle of reading of the contrast of the fringes. In black: fringes "printed" on the sample by bleaching. In blue: reading fringes at 700 Hz. (a) the fringes are in phase, the emission of fluorescence is maximum. (b) the fluorescence emitted is minimal (the concentration profile of fluorescent molecules is assimilated to a sinusoidal for the sake of simplicity).

After the bleaching, marked molecules (as well as unmarked molecules) are subjected to Brownian motion and diffuse, moving from one fringe to another one. The distribution of the fluorescent molecules is rehomogenized and the contrast of the fringes decreases with a characteristic time τ_q related to the diffusion of the molecules on the spatial scale i.

The final experimental signal gives the mean contrast $C(t)$ between dark and bright fringes. The contrast decreases with time as a result of the diffusional exchange between the bleached and unbleached molecules. The fraction of fluorescent molecules that participates in the exchange is referred to as the mobile fraction [125]. It has been shown by the authors in [32, 71] that $C(t)$ follows a simple exponential decay in the case of a single mobile population which diffuses due to the Brownian dynamics:

$$C(t) = C_0 + C_1 e^{-t/\tau_q} \tag{5.3}$$

where τ_q is a relaxation time. In the case of a Brownian motion:

$$\tau_q = \frac{1}{Dq^2}. \tag{5.4}$$

with D the coefficient of diffusion of the molecule. Consequently, by varying the spatial periodicity of the fringe pattern, hence q, it is possible to check the validity of the Brownian diffusion law and to determine precisely the diffusion coefficient of the mobile molecules. The constants C_0 and C_1 are related to the relative fractions of mobile and

immobile molecules: $f_m = C_1/(C_1 + C_0)$ and $f_i = C_0/(C_1 + C_0)$.

If the sample has N different mobile populations (e.g. different molecules, or different domains in bulk sample):

$$C(t) = C_0 + \sum_{i=1}^{N} C_i e^{-t/\tau_{q,i}} \tag{5.5}$$

with

$$\tau_{q,i} = \frac{1}{D_i q^2}. \tag{5.6}$$

5.1.1 Data analysis by the inverse Laplace transformation

The inverse Laplace transform (ILT) of the intensity contrast versus time can give an indication of the multiexponential decays and is a good way to analyse data. ILP is an integral transform that for a given function $F(t)$ gives a function $f(s)$ whose Laplace transform is equal to $F(t)$:

$$F(t) := L[f(s)] = \int_a^b f(s)e^{-st}\,\mathrm{d}s. \tag{5.7}$$

Following the ILT(Mellin inversion theorem [134]):

$$f(s) := L^{-1}[F(t)] = \frac{1}{2\pi i} \lim_{T\to\infty} \int_{\gamma-iT}^{\gamma+iT} F(t)e^{st}\,\mathrm{d}t \tag{5.8}$$

For a multiexponential decay the ILP consists of peaks (see Figure 5.5b) whose heights are proportional to coefficients near corresponding exponents and equal:

$$L^{-1}[\sum_{i=1}^{N} C_i e^{-t/T_i}] = \sum_{i=1}^{n} C_i \delta(s - 1/T_i) \tag{5.9}$$

The CONTIN software package was written by S. Prowencher [104,105] and performs a numerical ILT for a given data set. It plots an ILT as a function of $1/s$, hence the peaks will be situated at $1/s = T_i$. We analyse our data using a MATLAB script [93], which is an emulation of S. Provencher CONTIN program, written in Fortran language.

5.2 PEG in water

As a first step we determined the diffusion coefficient of the PEG chains in water solution. We used a standard cell with size 10 mm x 4 mm from Hellma. The experiments were performed with 2; 3.8; 5; 7.5 and 15 wt. % of PEG in water.

Figure 5.4a shows a typical curve of the fluorescence intensity contrast as a function of time, for a given fringe spacing $i = 49.5$ μm (or $q = 126.9$ cm^{-1}) after bleaching. The contrast decays exponentially toward zero, with characteristic time of decay τ_q, which equals about 2.54 s. Figure 5.4b shows the corresponding numerical inverse Laplace transform of the intensity contrast as a function of time. It indicates that the decay can be described by a single exponent with one peak at $\tau = 2.5$ s.

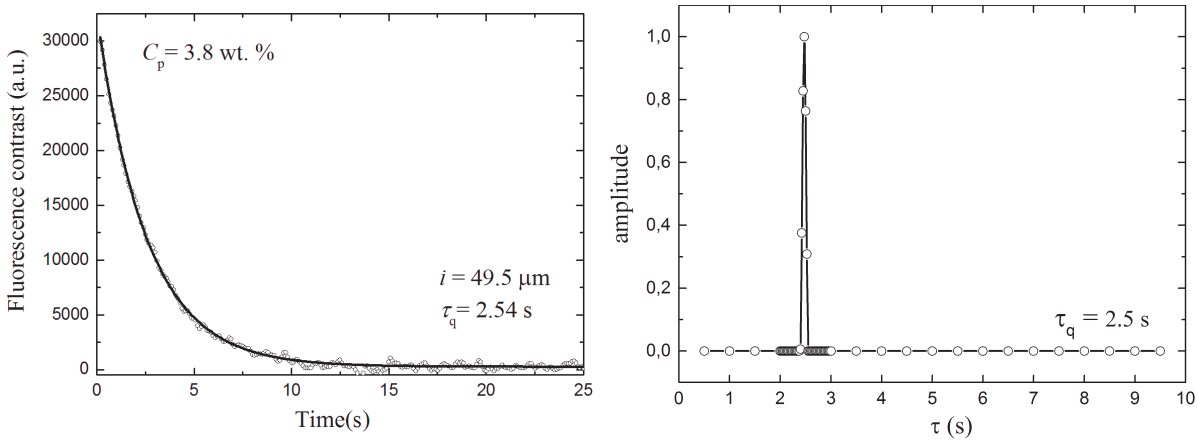

(a) (b)

Figure 5.4: PEG solution with $C_p = 3.8$ wt. %: (a) example of contrast intensity decay after bleaching, corresponding to the fringe spacing $i = 49.5$ μm ($q = 126.9$ cm^{-1}) and the best exponential fit with Eq.(5.3) $\tau_q = 2.54 \pm 0.01$ s. (b) Analysis of data in terms of inverse Laplace transform. We observe one peak at $\tau = 2.5 \pm 0.1$ s.

However, for large fringe spacing, i, we found that the fit with two exponents reproduces better the fluorescence intensity contrast decay at short times (Figure 5.5a). Indeed, the inverse Laplace transform of the data in Figure 5.5b shows a two-peak time distribution with $\tau_{q,1} = 0.8 \pm 0.1$ s and $\tau_{q,2} = 7.3 \pm 0.2$ s proving the validity of the interpretation in terms of a two-exponential decay.

We suggest that in our sample a second mobile fraction is presented, which is much faster than polymer chains and can be due to the unattached fluorescent markers (FITC). The diffusion coefficient of FITC was studied in [81] on the same system, giving the value of D about (53 ±20) $\times 10^{-11}$ μm^2/s. The value of diffusion coefficient of FITC in pure water was obtained in [98] and reads $D = 23 \times 10^{-11}$ μm^2/s. The hydrodynamic radius of FITC is 9 Å [98].

Thus, one can plot the evolution of the largest decay time τ_q as a function of $1/q^2$

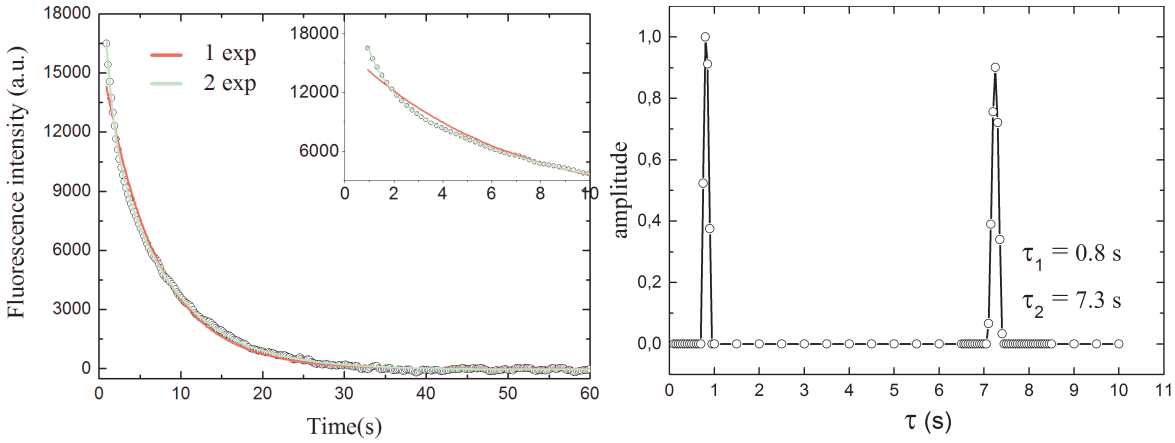

(a) (b)

Figure 5.5: (a) The contrast intensity decay for the fringe spacing $i = 104$ μm ($C_p = 3.8$ wt. %). The one exponential fit (red curve) gives $\tau_{q,1} = 6.5 \pm 0.05$ s. Whereas the two exponential fit (green curve) gives two decay times: $\tau_{q,1} = 0.87 \pm 0.03$ s and $\tau_{q,2} = 7.44 \pm 0.04$ s and better reproduces the decay at short times (see the insert). (b) the corresponding inverse Laplace transform. We observe two-peak time distribution in agreement with a two-exponential decay analysis.

(Figure 5.6). The slope corresponds to the inverse of the diffusion coefficient of polymer with a mass fraction in water $C_p = 3.8$ wt. %. The data points align along a line. This proves that the motion of the PEG chains in water is diffusive and gives a diffusion coefficient for PEG equals to $D = 2.8 \times 10^{-11}$ m^2/s (much smaller in comparison to unattached FITC).

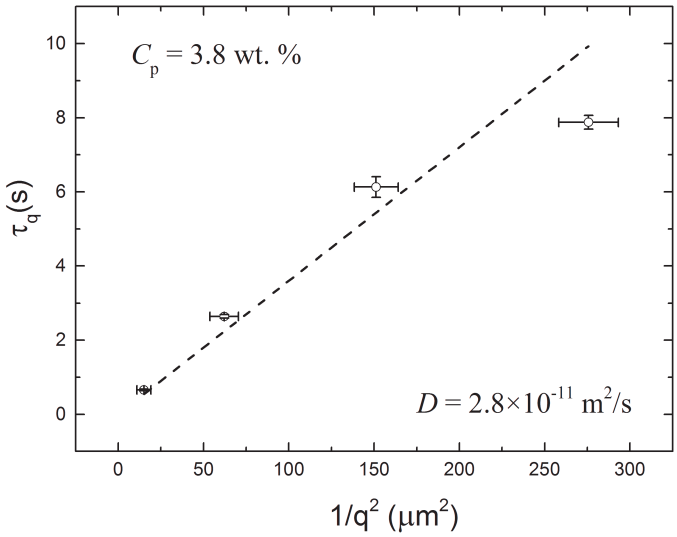

Figure 5.6: Decay time τ_q as a function of the inverse of squared interfringe spacing and the diffusion law fit with Eq.(5.4) leading to $D = 2.8 \times 10^{-11}$ m^2/s.

Using the Stokes-Einstein relationship of the diffusion coefficient:

$$D = \frac{k_B T}{6\pi\eta R_H} \tag{5.10}$$

we can estimate the hydrodynamic radius of polymer using the viscosity of water $\eta = 1.002 \times 10^{-3}$ kg/m·s at 20°C, $D = 2.8 \times 10^{-11}$ m^2/s, hence $R_H = 77 \pm 10$ Å.

Next, we investigated the effect of polymer concentration on the diffusive behaviour of the chains. All the results are summarized in Figure 5.7, where the decay time, τ_q is plotted as a function of $1/q^2$ for polymer solutions with C_p : (a) 2 wt. %; (b) 5 wt. %; (c) 7.5 wt. %; (d) 15 wt. %. Table 5.1 gives the values of the diffusion coefficient of PEG chains.

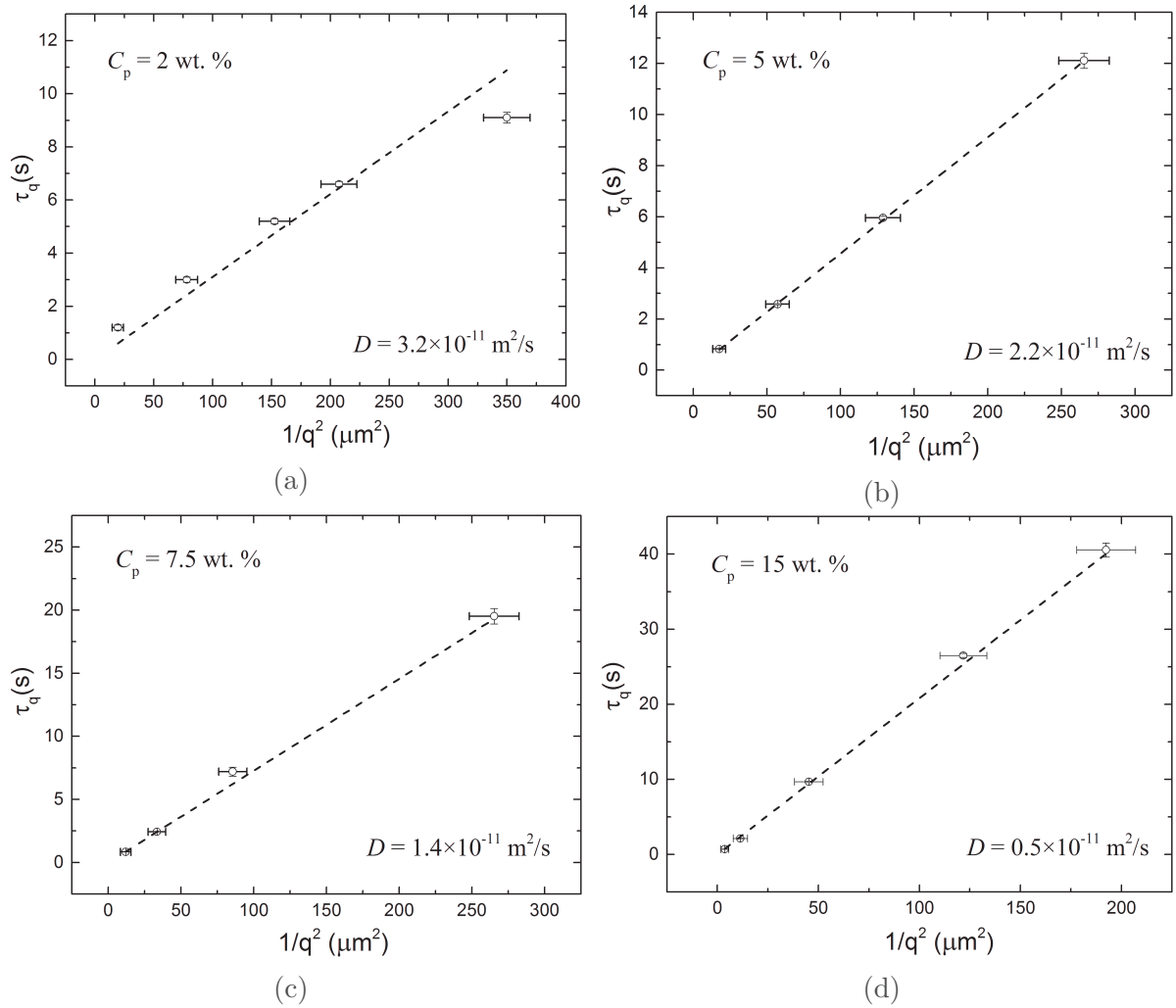

Figure 5.7: Diffusion law and the best fits with Eq.(5.4) for a PEG solutions with (a) C_p = 2 wt. %; (b) C_p = 5 wt. %; (c) C_p = 7.5 wt. %; (d) C_p = 15 wt. %.

The resulting diffusion coefficients are plotted in Figure 5.8 as log D vs. log concentration. The self-diffusion coefficient of polymer in a good solvent is given in de Gennes

Table 5.1: Values of diffusion coefficient of PEG-FITC chains determined for various weight fractions of polymer in water, C_p.

C_p (wt. %)	2	3.8	5	7.5	15
Diffusion coefficient ($\times 10^{-12}$ m$^2/s$)	32 ± 2	28 ± 3	21.9 ± 0.2	13.7 ± 0.3	4.8 ± 0.1

reptation + scaling model [34] by: $D \sim M^{-2}c^{-1.75}$, where M is the molecular weight of the diffusant and c the polymer concentration in g/cm^3.

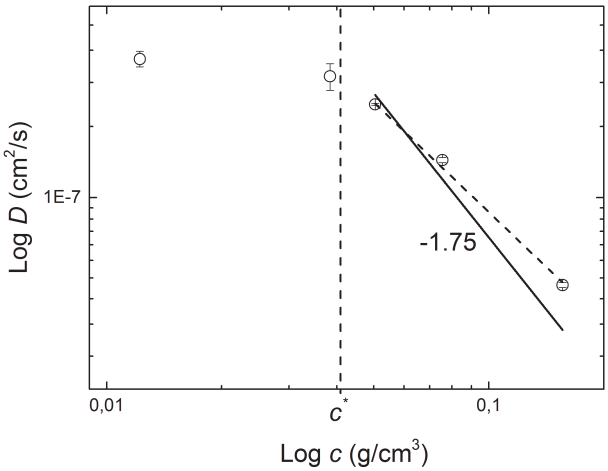

Figure 5.8: Variation of diffusion coefficient D as a function of concentration c. The solid line represents the scaling prediction of the -1.75 power law dependence of self-diffusion coefficient on concentration [34]. c^* represents the overlap concentration (defined as $c^* = \frac{3M_w}{4\pi N_A R_G^3} = 0.042$ g/cm^3). The dashed line is a linear fit with a slope equals to -1.33.

5.3 PEG in lamellar phase

The first preliminary results on the PEG diffusion in the lamellar phase were obtained by Laure Herrmann in her PhD thesis [55], where the standard Hellma cell was used for the experiment. In her study several diffusing polymer populations were observed. In order to confirm confidently these trends we repeated the experiment. However, lamellar mesophases are highly viscous, thus the use of a standard cell from Hellma is very challenging and it does not allow to orient the membranes.

In order to study the diffusion of polymer chains confined in the lamellar mesophase a new sample cell has been designed (see Figure 5.9). This kind of design was inspired from the Surface Force Apparatus and satisfies the main requirements: the need of homeotropic (parallel) alignment of membranes and the chamber sealing. The sample is confined between a flat plane and a sphere (the upper surface) as it is shown in Figure 5.9. The alignment of the mesophase can be performed by displacement of the upper surface in x, y, z directions. Before each experiment samples were centrifuged in order to avoid bubbles, and transferred into the designed cell and sealed. Just afterwords, the upper surface was positioned at a separation about $D \sim 50$ μm from the lower surface and equilibrated during one day at room temperature. The homeotropic alignment of the membranes was performed by displacement of the upper sphere in x-y directions, a movement equivalent to the shearing of membranes.

The samples were prepared using the same procedure as described in section 3.1.5. In every sample around 1 % of polymer mass fraction was replaced by PEG fluorescently labeled mPEG-FITC.

Figure 5.10 shows the typical behaviour of intensity contrast of lamellar mesophase with $\Phi_m = 10$ wt. % and $C_p = 2$ wt. % in the sphere-flat geometry. One observes an exponential decay at short times (see Figure 5.11) and long time oscillations. As it is seen from Figure 10, this geometry allows to align only partially the sample, but not enough to have a perfect alignment. The immobile fraction of polymer is quite large (50-70 %) and can be due to the adsorption on membranes and due to the textured confinement in domains, which means the lack of alignment.

First we made an attempt to extract the decay time of the mobile part. Figure 5.11 shows the two exponential fit of the intensity contrast, which gives $\tau_{q,1} \sim 3.2$ s and $\tau_{q,2} \sim 35$ s. The first decay time for few q values comparing to water solution of polymer is illustrated in Figure 5.12. The diffusion coefficient is found to be 3 times smaller and is equal to 11 $\mu m^2/s$.

We observed long time oscillations for each lamellar sample. These oscillations are caused by a change in the spatial phase shift between the intense fringe pattern, which bleaches the fluorophore and the attenuated measuring fringe pattern [32]. A small me-

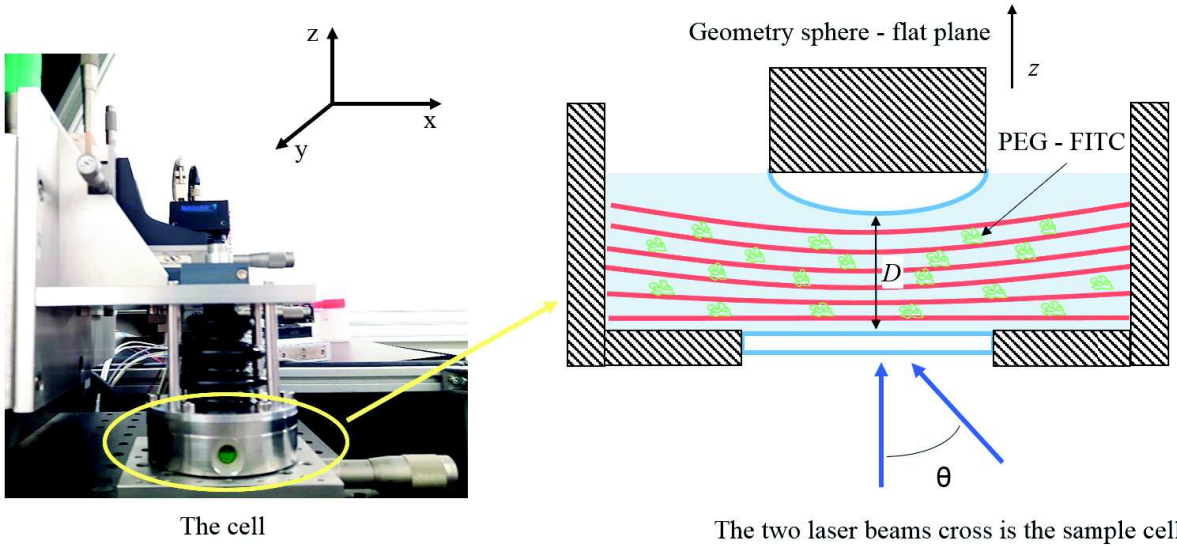

Figure 5.9: An image of the FRAPP chamber and a schematic cross-section of the confinement geometry in which the membranes (in red) are aligned all parallel. The upper surface is a spherical lens of $R = 18$ mm and the lower surface is a glass flat window. The laser cross-section is about 1-2 mm^2.

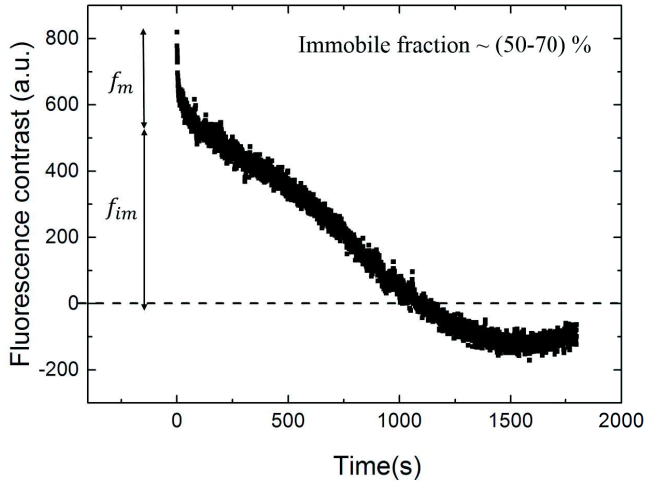

Figure 5.10: Intensity contrast as a function of time of a lamellar mesophase $\Phi_m = 10$ wt. % and $C_p = 2$ wt. %. The fringe spacing $i = 33.66$ µm. The imobile fraction equals to 64 %.

chanical drift of the mirror ($\sim$ 10 nm/min) is one of the cause of the phase shift. We should note here, that the large oscillations are observed only in presence of an immobile (or very slow) population of polymer chains.

$$C(t) = C_0 e^{-Dq_0{}^2 t} \cos(\vec{V}\vec{q_0}t) \tag{5.11}$$

where $\vec{V}$ is the relative drift velocity of bleached fringes with respect to the measuring fringes.

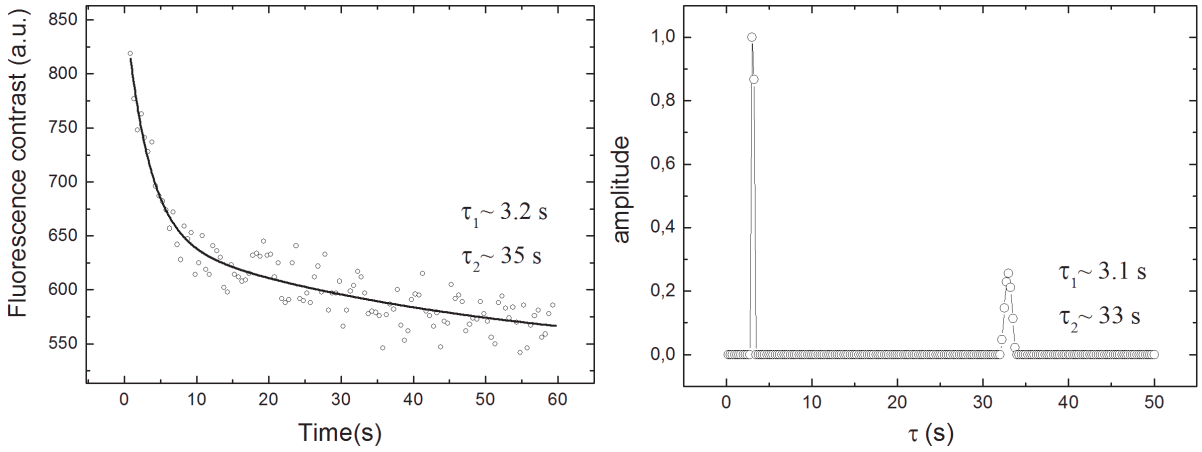

(a) (b)

Figure 5.11: The two exponential fit of the intensity contrast in the range from 0 to 60 s of sample with $\Phi_m = 10$ wt. % and $C_p = 2$ wt. % and corresponding ILT.

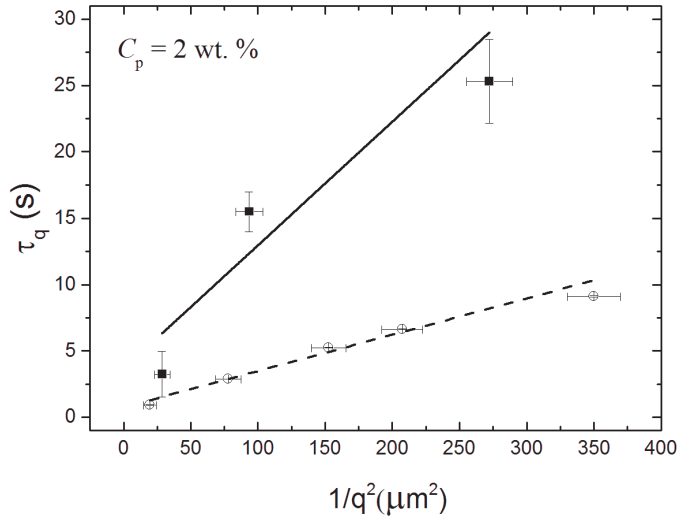

Figure 5.12: Diffusion law and the best fits. The square points correspond to the 1st peak of the Inverse Laplace transform of the lamellar sample ($\Phi_m = 10$ wt. % and $C_p = 2$ wt. %) and the circles - to bulk PEG ($C_p = 2$ wt. %). The diffusion coefficients from the fit are 11 and 37 $\mu m^2/s$ respectively.

As it was mentioned before the lamellar sample consists of domains with different orientations of size around 20 μm (in the absence of alignment). The diffusion between different domains is not allowed. Thus, if we have the interfringe spacing i superior to 20 μm most of the domains will fully lie in bleached or non bleached zone, and the mobile fraction of polymer is not able to restore the fluorescence.

Unfortunately, we were not able to achieve a perfect homeotropic alignment of the membranes using the sphere-flat geometry over an area of about 1 mm^2 (the cross-section of the laser beam). Therefore, we tried to confine the membranes in a different way using the same sealed chamber, but without the upper surface.

Figure 5.13 shows the lamellar mesophase sandwiched between two flat glasses, with cleaved mica sheets used as spacers (thickness about 20 μm). In this configuration we obtained the fluorescence contrast intensity decay as a function of time for two fringe spacing $i = 19.8$ and 39.6 μm. Figure 5.14 shows that the intensity difference decreases towards zero, which was not achieved before if we compare with the result of Figure 5.10. The oscillations are still present but their period is much smaller; it decreases from 1500 s to 200 s. One may interpret this result due to better alignment of the membranes. This means that the main contribution to the oscillations has been due to the polymers confined in different lamellar domains.

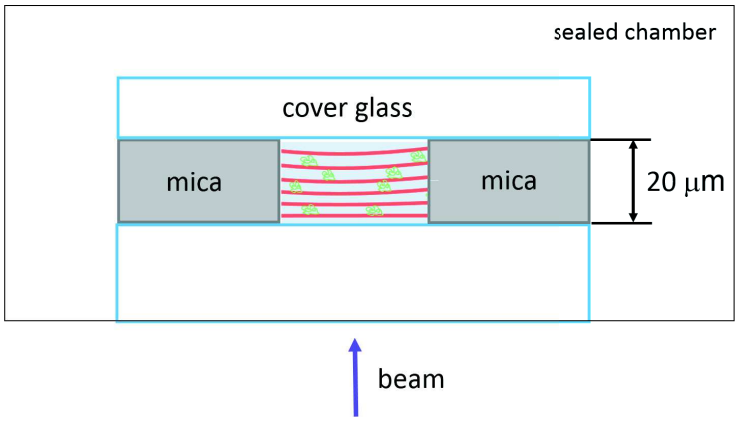

Figure 5.13: The alignment of the sample between two glasses. Mica sheets of thickness $\sim$ 20 μm are used as spacers. The chamber is sealed to prevent any evaporation and shift of the mesophase in the phase diagram.

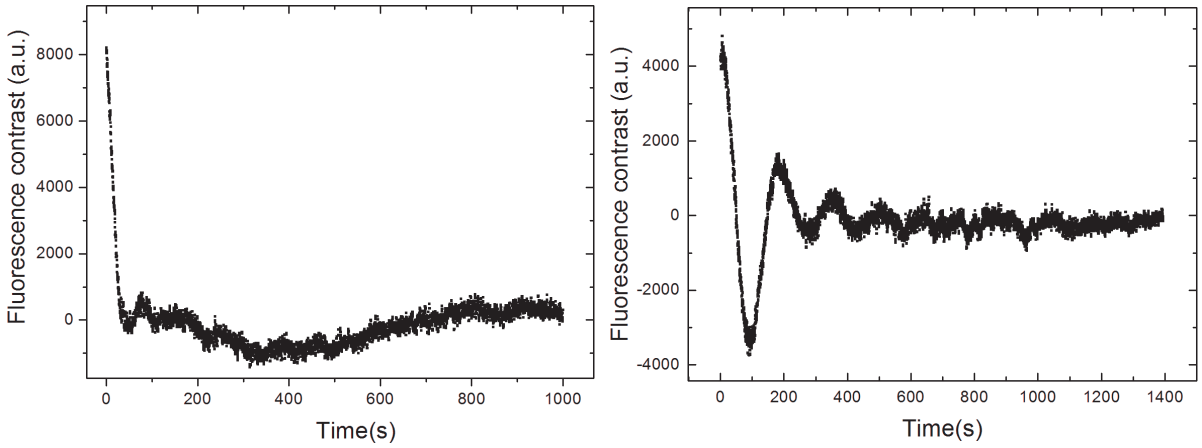

(a) (b)

Figure 5.14: Intensity contrast as a function of time for a lamellar mesophase $\Phi_m = 10$ wt. % and $C_p = 2$ wt. %. With fringe spacing $i = 19.8$ μm (a) and $i = 39.6$ μm (b).

5.4 Conclusions and perspectives

Using the Fluorescence Recovery after Photobleaching Pattern technique we have studied the diffusion coefficient of PEG chains in water. We observed the existence of two mobile populations: the first one is the PEG chains, the second one is due to the unattached FITC.

We obtained the self-diffusion coefficient of PEG chains as a function of polymer concentration. One sees from the power-law dependence (Figure 5.8) that the slope is less steep than -1.75 defined by the de Gennes reptation model [34]. However in our case the concentration of polymer solutions is very close to the crossover c^* [86]. Thus, we can suggest that our solution are too dilute to be defined by reptation. Also PEG is considered to have complex interactions with water [41]. To our knowledge the diffusive properties of PEG in water were studied by dynamic light scattering for PEG chains with molecular weight higher than 10^5 [40] and the hydrodynamic radius of PEG 2×10^4 was studied in [90].

Concerning lamellar mesophases we showed that about 50-70 % of PEG chains contribute to immobile fraction, which can be due to partially adsorbed polymer onto the membranes and polymers confined in the lamellar domains. The contrast intensity decay exhibits several diffusing polymer populations: one suggest that there are one population that diffuses about three times slower than the free polymer and two others populations diffuse much more slower. One may interpret very slow populations as exchanging populations between the not adsorbed polymer population, which are present in the middle of the interlayer spacing and the adsorbed polymer population, which is immobile.

The main problem in the work with lamellar sample is to obtain perfectly aligned membranes and to separate different mobile fractions of PEG in the lamellar mesophase, which becomes more complicated if the long range oscillations appear in the FRAPP signal. The new geometry is promising, because we succeeded to decrease the period of these oscillations drastically and to control the gap thickness of the confined sample using the mica spacers of known thickness. Unfortunately, the Laser major breakdown is not allowed us to perform more experiments. They should be repeated in the future. There is also a possibility to improve a FRAPP set-up stability by using a electro-optic modulation of the fringe pattern rather that a mechanical one in order to avoid the "mirror drift" problem.

Chapter 6

SFA results

In this chapter, the experimental results concerning lamellar mesophases with membrane volume fraction $\Phi_m = 10$ % at $C_p = 3.8$ wt. % and $C_p = 5$ wt. % are presented. The main goal is to get insights into the effect of the polymer concentration in water on the elastic compressibility modulus of the membranes and to obtain the scaling law: $\bar{B} \sim C_p^{\alpha}$ (where α is unknown constant). The present chapter is a continuation of the work, which has been done by Herrmann L. et al. [55–57] on the mesophases with membrane mass fraction $\Phi_m = 10$ % and $C_p = 0$ wt. %; $C_p = 15$ wt. %.

6.1 Force calculation

Two independent quantities are measured during an SFA experiment: the surface separation and the piezoelectric device position on which the upper surface is attached, and consequently can be moved to approach or to move away from the opposite surface. Figure 6.1 shows an example of an inward run measurement upon the approach of the surfaces.

The force in the experiment is usually calculated using the following equation:

$$F_i = F_0 + K_C(C(z_i - z_0) - (l_0 - l_i)) \tag{6.1}$$

where F_i is the force calculated at the $M_i(l_i, z_i)$ point, F_0 is the unknown force at the starting point $M_0(l_0, z_0)$ and l_i, l_0, z_i, z_0 are the coordinates defined from Figures 6.1 and 6.2. K_c is the cantilever spring constant and C is the calibration coefficient of the experiment, defined as a slope of the graph (l, z) far from the contact position: $C = -\Delta l/\Delta z$, where no force is detected. This coefficient allows us to take into account a possible drift of the surfaces due to temperature fluctuations, vibrations, etc. Far from the contact position, the interaction between the surfaces is assumed to be negligible and below the sensitivity of the SFA. Thus, the change in the surface separation should be equal to the displacement of the piezoelectric device and C should be strictly equal to -1 in the absence

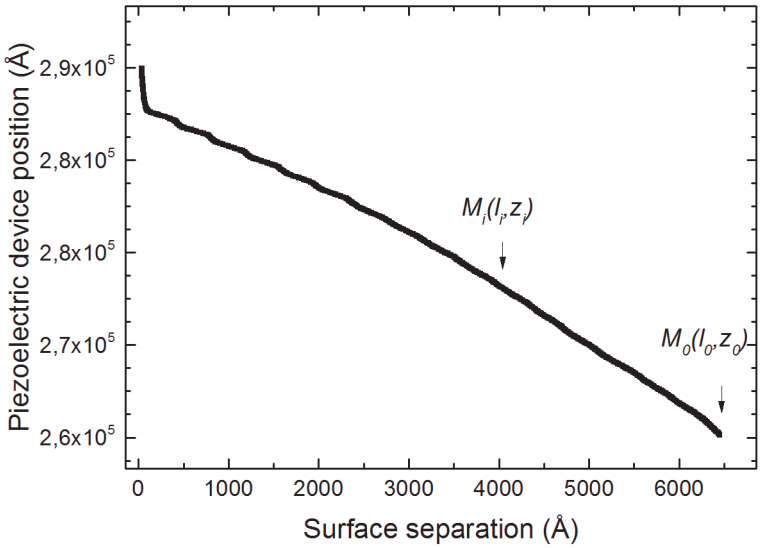

Figure 6.1: Piezo position as a function of the surface separation upon approach of the surfaces for the mesophase at $\Phi_m = 10$ wt. % and $C_p = 5$ wt. %.

of any surface drift.

However, in Figure 6.1 one observes a straight line on which oscillations superimpose, with a slope $C = -0.31$. This means that even far from the contact position some interactions must occur between the surfaces. This effect has been observed in independent measurements on all mesophases of our system as well as in other systems [48]. The slope of the linear background is sensitive to the speed and to the initial surface separation: the slope increases when the initial starting surface separation decreases (for more details refer to Herrmann L. PhD thesis [55]).

6.2 Results: the compressibility modulus

Figure 6.3 shows the resulting force-distance profile for the mesophase at $\Phi_m = 10$ wt. % and $C_p = 5$ wt. %. The linear background has already been subtracted from the total force profile. One sees that the force profile is oscillatory and constituted of regular oscillations. The first 16th oscillations were tracked with inward movement of the piezo-electric device. Due to the mechanical instability of the cantilever the forces profiles are discrete and jumps from one stable position to next one occur. The oscillations superimpose on the attractive background below 370 nm, which turns to be repulsive below about 20 nm. The amplitude of the oscillations increases when the surface separation decreases.

The lamellar structure experiences an elastic stress upon approach or separation of the confining surfaces. One assumes that the stack of membranes is equivalent to a series of springs, whose stiffnesses are all equal and depend on the intermembrane interaction, and whose lengths correspond to the mesophase periodicity. For a layered structure of

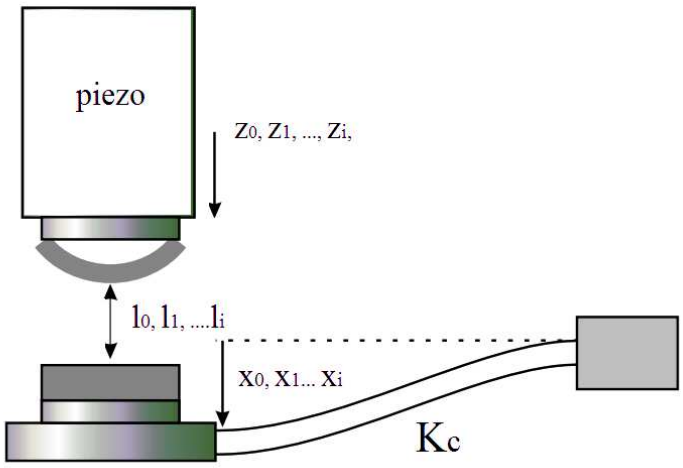

Figure 6.2: Representation of the surfaces and cantilever. When the upper surface is moved from the point M_{i-1} to M_i, the cantilever spring is deviated from an additional quantity $\Delta x_i = x_i - x_{i-1} = (z_i - z_{i-1}) - (l_{i-1} - l_i)$. The total deformation at the point M_i is $x_i - x_0 = (z_i - z_0) - (l_0 - l_i)$.

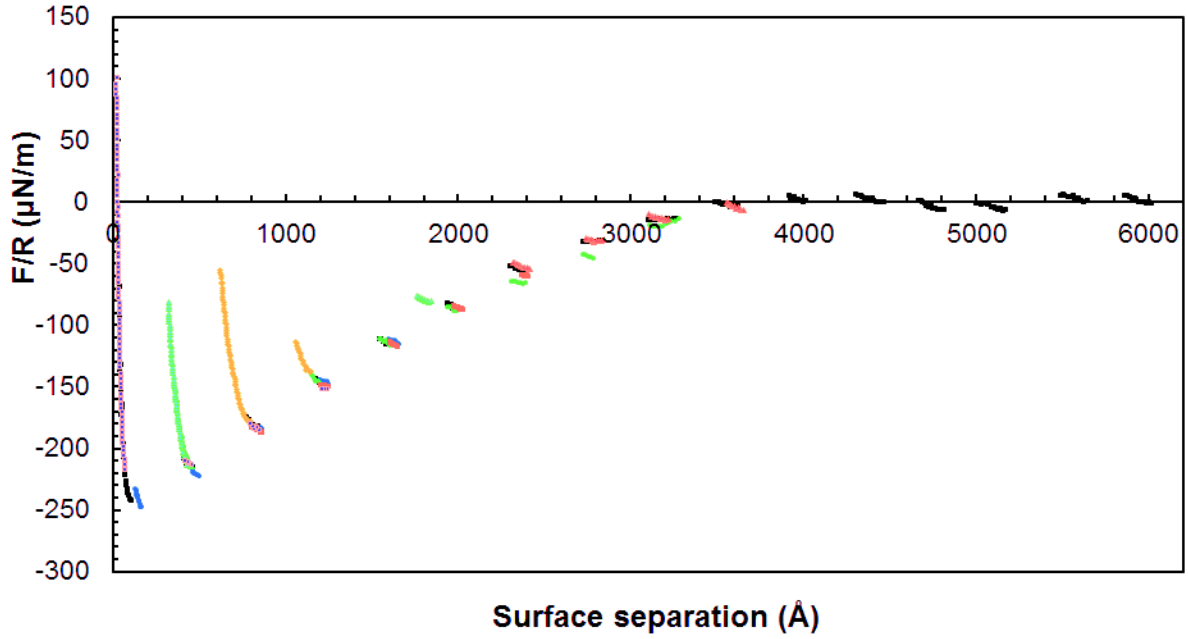

Figure 6.3: Force F normalized by the mean radius of curvature R of the surfaces as a function of sufrace separation. The colors show different force measurements ($\Phi_m = 10$ % and $C_p = 5$ wt. %).

thickness l_n at zero stress (l_n is an integral multiple of periodicity d), the corresponding elastic energy per unit of surface has a parabolic shape centered around l_n:

$$E = \frac{1}{2}\bar{B}\frac{\Delta l_n^2}{l_n} \tag{6.2}$$

where $\Delta l_n = l_n - l$, and l is a surface separation. The minima of the parabolae correspond to the l_n positions; the inward jumps correspond to positions at which two neighbouring parabolae would intersect and are denoted l_n^i. The parabolic shape of the oscillations allows the layer compressibility modulus to be extracted, using the relationship between the measured force-distance profile and the elastic free energy of the membrane stack, E (using the Derjaguin approximation):

$$(F - F_n)\frac{l_n}{\pi R} = \bar{B}\Delta l_n^2 \tag{6.3}$$

where F_n are the forces at the minima l_n. This method has been firstly used in order to analyze the force-distance profile measured for the lamellar phase of SDS/pentanol/water system [107, 108].

In order to obtain valid information, it is crucial that the thermodynamic equilibrium is maintained throughout the force run. Creation or annihilation of edge dislocations involve structural rearrangements and energetic changes which are propagating from the nucleation site throughout the mesophase [107]. At the thermodynamic equilibrium, the outward jump positions must be a linear function of n, the order of parabola. In a set of intersecting parabola, the minima l_n and inward jump positions l_n^i are defined as following:

$$l_n = nd \tag{6.4}$$

$$l_n^i = \sqrt{n(n-b)}d \tag{6.5}$$

where b is the Burger vector of the dislocation (see Figure 3.15). For each oscillation in Figure 6.3, the position of the minima and the inward jump positions are plotted in Figure 6.4 and 6.5 for mesophase at $\Phi_m = 10$ % and $C_p = 5$ wt. %.

The solid lines are the best fit to the data:

$$l_n = (10 \pm 1) + (19.8 \pm 0.1)(n - 2)$$

$$l_n^i = (-27 \pm 3) + (19.9 \pm 0.2)\sqrt{n(n-2)}$$

and give a reticular distance $d \sim 20$ nm, this value is in agreement with the periodicity inferred from the SAXS measurements.

Equation 6.3 is plotted in Figure 6.6 for the 1st, 2nd and 13th oscillations (i.e. 2, 4 and 26 bilayers confined) for a lamellar mesophase at $C_p = 5$ wt. % (similar plots for the pure lamellar mesophase and at $C_p = 15$ wt. % are reported in Herrmann L. PhD thesis [55]). All the points lie along straight lines, whose slopes are collected in Figure 6.7. The values of $\bar{B}$ are taken from the average of the slopes for each oscillation ($n \geqslant 4$), and the uncertainty is the largest deviation from the mean value; $\bar{B}$ appears to take the value of 4.9 ± 1.8 kPa. At smaller separations ($n < 4$), the magnitude of $\bar{B}$ increases. This effect has been observed observed in other systems [75]. The confining rigid mica

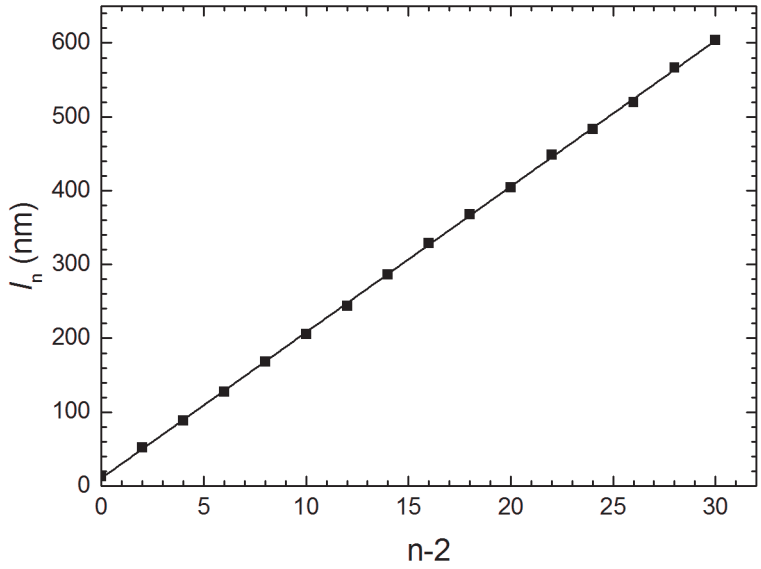

Figure 6.4: Location of the minima, l_n, of the oscillations seen in Figure 6.3 as function of the number of layers from contact $n-2$ (since the last two bilayers that remain between the surfaces have a reduced periodicity). The solid line is the best fit to the data, giving a reticular distance $d = 19.8 \pm 0.1$ nm ($\Phi_m = 10$ wt. % and $C_p = 5$ wt. %).

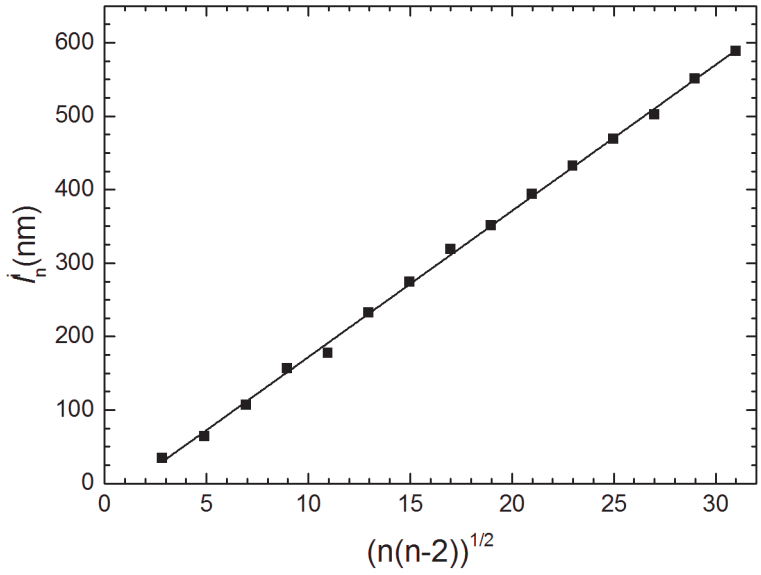

Figure 6.5: Location of the inwards jumps, l_n^i, of the oscillations seen in Figure 6.3 as a function of $\sqrt{n(n-2)}$. The solid line is the best fit to the data, giving a reticular distance $d = 19.9 \pm 0.2$ nm. ($\Phi_m = 10$ wt. % and $C_p = 5$ wt. %).

surfaces prevent the low number of confined membranes to exhibit their bulk properties as fluctuations and undulations of the membranes are reduced.

It was found that the force profiles exhibit a so-called "avalanches" phenomena (Figure 6.8) for the mesophase with $\Phi_m = 10$ wt. % and $C_p = 3.8$ wt. %. One sees that at the beginning of the measurement the force evolves around zero, after that the force increases

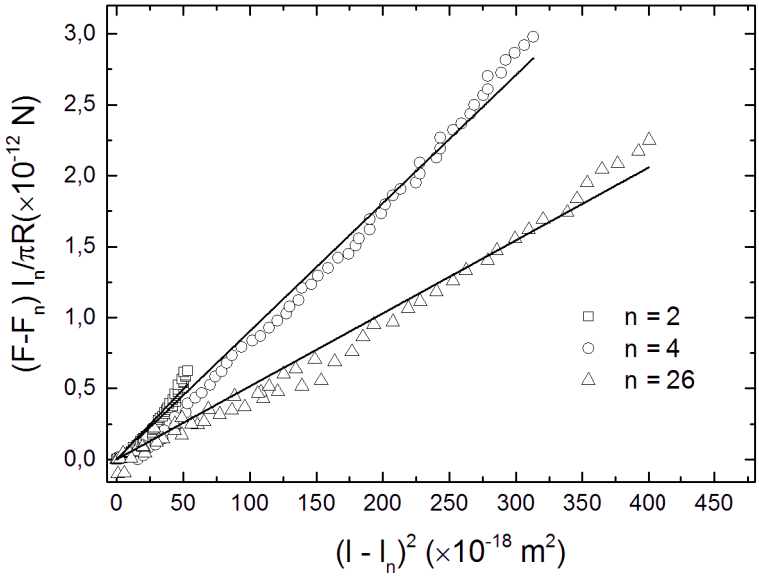

Figure 6.6: Plot of data for the 1nd (□), 2nd(∘), 13th(+) oscillations from contact position (Figure 6.3). Using Eq. (6.3) the slope of the straight line gives a layer compressibility $\bar{B}$ of 10, 9 and 5 kPa respectively ($\Phi_m = 10$ wt. % and $C_p = 5$ wt. %).

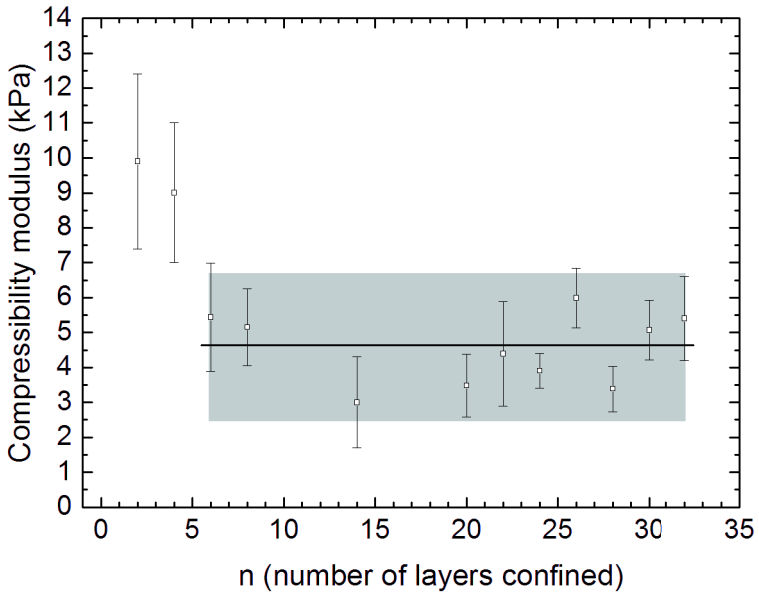

Figure 6.7: Elastic compressibility modulus from each oscillation as a function of the number of layers confined, for the mesophase $\Phi_m = 10$ wt. % and $C_p = 5$ wt. %.

progressively and becomes steeper and steeper, then the stress is released by one or two inward jumps (Figure 6.8a). Note, that the relaxation process may even lead to a "cascade", when the force is decreasing very rapidly (Figure 6.8b, the unstable points are kept).

This kind of behaviour may be due to the presence of a high energy barrier preventing the dislocations to nucleate and the creation of an edge dislocation loop is hence delayed.

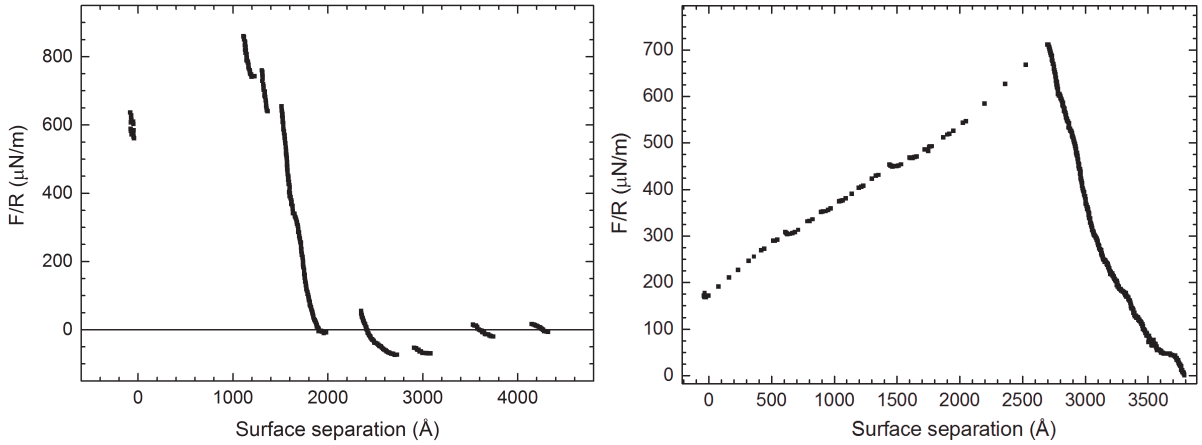

(a) (b)

Figure 6.8: Resulting force as a function of the surface separation for a mesophase with $\Phi_m = 10$ wt. % and $C_p = 3.8$ wt. %. (b): the unstable points are kept to show the avalanches phenomena.

In order to overcome the barrier, the large strains (more than a few bilayer thicknesses) must be applied before the stress is released by the occurrence of a more likely nucleation. The force-distance profile deviates rapidly from the pure elastic parabolic shape. The strain is large enough to promote the nucleation process and the stress may be partly released by expelling one or more bilayers (Figure 6.8a). When the force increases again steeply until the strain is large enough, at this point, it happens that the system has enough energy to expel the stack of remaining bilayers all at the same time and the avalanches phenomena occurs.

The resulting force-distance profile for the mesophase $\Phi_m = 10$ wt. % and $C_p = 3.8$ wt. % is shown in Figure 6.9. Note, that we were not able to collect inward runs where all parabolae are described all together, thus the force profile presented in Figure 6.9 contains the oscillations measured from different inward runs, and the exact values of the parabolae minima are thus uncertain. To overcome this difficulty their force minima were set to zero arbitrarily (different runs have revealed some scatter in the absolute force values). Note that this choice does not affect the inferred value of the elastic compressibility constant $\bar{B}$ as Eq. (6.3) shows that only relative force (with respect to the minimum value of the parabolae) must be taken into account. For each oscillation in Figure 6.9 the positions of the minima l_n and the inward position l_n^i are plotted against $n-1$ and $\sqrt{n(n-1)}$ respectively in Figure 6.10 and 6.11. The choice of -1 rather than -2 (as in Figure 6.4 and 6.5) is justified bellow. The solid lines are the best fit to the data:

$$l_n = (10\pm3)+(19.6\pm0.2)\cdot n$$

$$l_n^i = (8 \pm 4) + (19.2 \pm 0.2)\sqrt{n(n-1)}$$

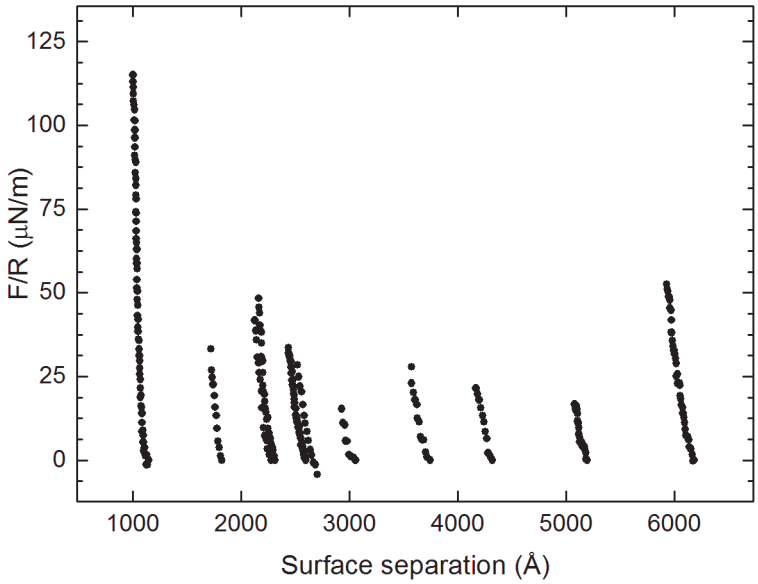

Figure 6.9: Force F nornalized by the mean radius of curvature R of the surfaces as a function of separation for the mesophase at $\Phi_m = 10$ wt. % and $C_p = 3.8$ wt. %.

which give a reticular distance $d = 19.6 \pm 0.2$ nm and 19.2 ± 0.2 nm respectively. These values are in agreement with the periodicity inferred from SAXS measurement: $d = 19.8 \pm 0.2$ nm. Burgers vector $b = 2$ is the most favourable for this lamellar structure. However, one observes that system nucleate a $b = 1$ dislocation loop. Here the value of the burger vector, $b = 1$, is an assumption, however the full oscillations profile was not obtained for this mesophase. Taking $b = 1$ one sees that the last confined membrane at the steric wall position at $l_0 = 10$ nm.

In Figure 6.12 the values obtained for $\bar{B}$ are plotted against the number of layers confined between the surfaces.

6.3 Discussion

The elastic compressibility modulus extracted from the parabolic fit of each oscillation of the force-distance profles (Figures 6.3 and 6.9) shows a dependence with the rank of the oscillation (Figure 6.7 and 6.12). At short separations the rigid walls have a significant influence on the few remaining confined lamellae. Such effect was also observed by L. Herrmann on the same system [55] and in other lamellar systems [3, 4, 73, 107]. As discussed previously the increased in $\bar{B}$ for the last remaining lamellae results from a combined effect. First, the structures of the rigid surfaces and that of the free membranes have no resemblance. Since there is no adsorbed surfactant on the mica surfaces, the surface charge of the mica is much larger than the one of its adjacent bilayer; as a result the electrostatic repulsion is enhanced. Secondly, as shown by Monte Carlo simulations the proximity of the rigid walls reduces the amplitude of fluctuations of the confined

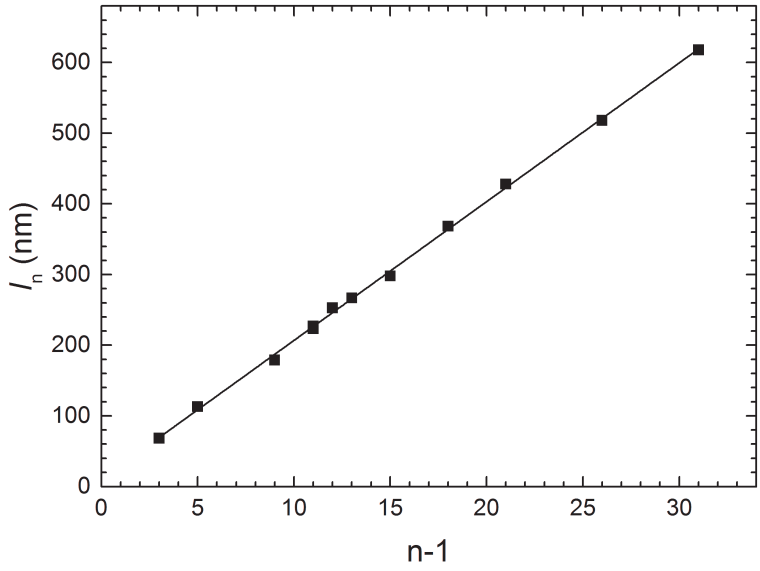

Figure 6.10: Location of the minima, l_n, of the oscillations seen in Figure 6.9 as function of the number of layers from contact $n-1$ ($b=1$). The solid line is the best fit to the data, giving a reticular distance $d = 19.6 \pm 0.2$ nm ($\Phi_m = 10$ wt. % and $C_p = 3.8$ wt. %).

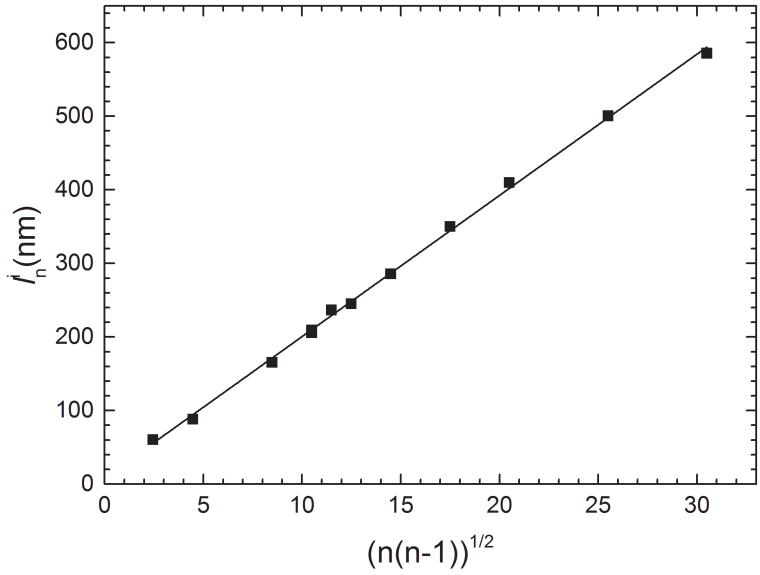

Figure 6.11: Location of the inwards jumps, l_n^i, of the oscillations seen in Figure 6.9 as a function of $\sqrt{n(n-1)}$. The solid line is the best fit to the data, giving a reticular distance $d = 19.2 \pm 0.2$ nm ($\Phi_m = 10$ wt. % and $C_p = 3.8$ wt. %).

membrane interfaces compared to those exhibited in bulk [68]. As the gap between the two mica surfaces gets larger the influence of the rigid mica surfaces begins to vanish out. At these large separations where there were a larger number of membranes far enough from their walls to exhibit their bulk properties, the elastic compressibility modulus is constant as shown in Figures 6.7 and 6.12. This constant value can thus be considered as the bulk value of the compressibility modulus for the lamellar mesophase (the influence

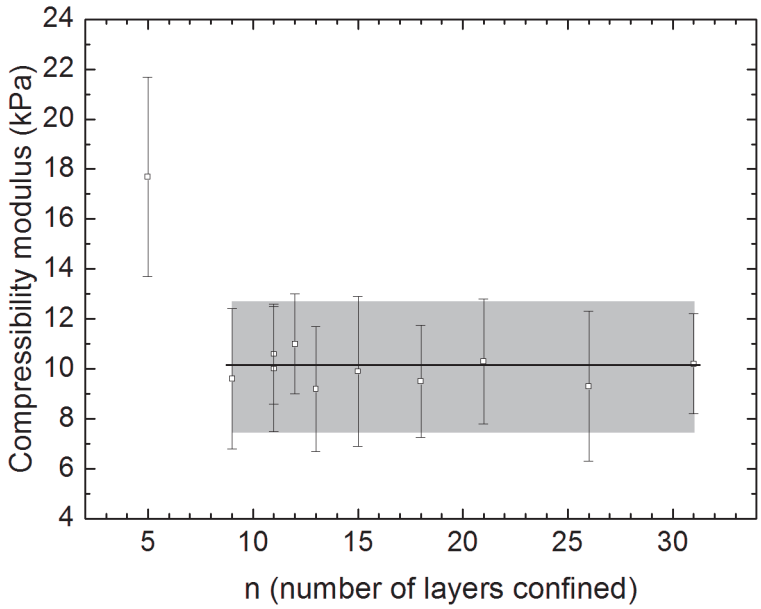

Figure 6.12: Plot of the elastic compressibility modulus from each oscillation as a function of the number of layers confined, for the mesophase $\Phi_m = 10$ wt. % and $C_p = 3.8$ wt. %.

of the rigid mica surfaces has vanished out): it is $\bar{B} = 4.9 \pm 1.8$ kPa for the mesophase at $\Phi_m = 10$ wt. and $C_p = 5$ wt. % and $\bar{B} = 10 \pm 3$ for the mesophase with $\Phi_m = 10$ wt. % and $C_p = 3.8$ wt. %. Since the number of oscillations measured was small (around 6-11), the uncertainty in $\bar{B}$ was taken as the largest deviation from the mean value. Obviously, more data are called for to improve the statistics in the measurement.

All the interlayer interactions are contained in the coefficient $\bar{B}$, and its magnitude reflects the interactions responsible for the stability of the stack. In the present system the mixed SDS/octanol bilayers are known to be charged (with a surface area per charge $\Sigma \cong 1$ nm^2 due to the dissociation of the sodium counterion from the polar head of the SDS molecules) and to undulate. For a stack of rigid charged planes of surface charge area separated by counterions only in water (no added salt; water layer thickness $\bar{d} = d - \delta$ with the bilayer thickness $\delta = 2.3$-2.5 nm as inferred from SAXS (Appendix A.1, section 4.1), the elastic compressibility modulus $\bar{B}$ is known from the mean-field, Poisson-Boltzmann approximation as [56]:

$$\bar{B}_{PB} = \frac{\pi k_B T d}{2 L_B \bar{d}^3} \left(1 - \frac{6}{\tilde{d}} + \frac{24}{\tilde{d}^2} + ...\right) \tag{6.6}$$

where $L_B = \frac{e^2}{4\pi\varepsilon_0\varepsilon_r k_B T}$ is the Bjerrum length of the solvent (≈ 0.7 nm for water at room temperature), $\lambda = \frac{\Sigma}{2\pi L_B}$ is the Gouy-Chapman length for monovalent counterions, and the correction terms ($\frac{1}{\tilde{d}} = \frac{\lambda}{\bar{d}} \ll 1$) arise from the boundary conditions. Remarkably, $\bar{B}_{PB}$ determined by the counterions pressure in the mid-plan does not depend on the surface charge to leading order. For swollen lamellar structures of large periodicities $d \gg \delta$, $\bar{B}_{PB}$ scales as $1/d^2$. For the pure lamellar phase without polymer the water thickness is $\bar{d} = 20.4$ nm (so $1/\tilde{d} = 0.0109$, $\tilde{d} = 91.5$) and thus we obtain $\bar{B}_{PB} = 22.6$ kPa. When the

membranes undulate due to their flexibility, the steric hindrance of a membrane bound between two neighbors induces an entropic repulsion as first shown by Helfrich [54] and $\bar{B}_{und}$ is given by:

$$\bar{B} = \frac{9\pi^2 (k_B T)^2 d}{64\kappa \bar{d}^4} \tag{6.7}$$

Note that steric hindrance decays with distance as $1/\mathrm{d}^3$ and can be safely neglected at larger distances. For highly charged membranes with bending modulus $\kappa \cong 2.5 k_B T$ according to our measurements (Chapter 4) the contribution of the undulations is at most 2 % of the Poisson Boltzmann compressibility. For the pure lamellar mesophase without polymer the elastic compressibility modulus was measured by Herrmann [55] to have the right order of magnitude: $\bar{B} = 16.6 \pm 2.8$ kPa, despite the fact that its value appears smaller (by about 30%) than the expected $\bar{B}_{PB} = 22.6$ kPa calculated for charged rigid plates. Recalling that the Surface Force Apparatus technique allows $\bar{B}$ to be measured free of any parameter, the discrepancy can only result from the approximation set by the mean-field Poisson-Boltzmann framework. Indeed, the weak organization of the counterions (correlations in their locations) near the membranes leads to an attractive contribution to the electrostatic inter-membrane interaction. This detailed analysis, reported in [56] has allowed the authors to evaluate this negative contribution to the elastic compressibility modulus, yielding to a theoretical expectation of $\bar{B} = 17.7$ kPa, now in a remarkable good agreement with the measured one for the pure lamellar mesophase without polymer. In the following, one considers that this value can be considered as the reference value for the electrostatic contribution of the $\bar{B}$ for the stack of interacting lamellae without any polymer at that membrane mass fraction (10%).

As shown in Fig 6.12, replacing water by a PEG solution softens the interactions between the membranes. This result is in agreement with the measurement of Herrmann et al. [57] on the same system by SFA for $C_p = 15$ wt. % polymer, and with the results of Ficheux et al. by neutron and X-ray scatterings on the same system for different polymer contents [46]. Comparing with the results of Herrmann et al. obtained at the same membrane volume fraction (10%) and for $C_p = 0$ wt. % and at $C_p = 15$ wt. % we note that the $\bar{B}$ magnitude measured in our work at $C_p = 3.8$ wt. % locates in between these two ones. Our measurement confirms the negative polymer contribution to the total elastic compressibility modulus. At $C_p = 3.8$ wt. % it would amount to about -6 kPa compared to -10 kPa at C_p =15 wt. % [57] compared to the lamellar mesophase without added polymer. As the same membrane fraction constitutes the pure- and the doped-lamellar mesophases, the presence of PEG in the aqueous layers causes either a significant enhancement of an attractive contribution which superimposes to the ever present electrostatic repulsion between the bilayers or a decrease in this inter-bilayer interaction.

Within the first hypothesis one considers the additivity of the contributions in the interaction potential, and thus $\bar{B} = \bar{B}_{elec} + \bar{B}_{pol}$ by noting that the steric contribution, $\bar{B}_{und}$, due to the undulations of the membranes is still negligible compared to the elec-

trostatic contribution of the charged membranes, $\bar{B}_{elec}$. Assuming that the presence of the macromolecules in the aqueous layers does not affect the charge distribution along the membrane interface and within the electrical double layer, $\bar{B}_{elec}$ amounts to about 17 kPa, the value measured for the pure lamellar phase with the same membrane fraction, or equivalently the magnitude predicted by the full electrostatics theory beyond Poisson-Boltzmann (see above in [57]). As a consequence, the polymer contribution to the elastic compressibility modulus is negative and $\bar{B}_{pol}$ would amount to about -6 kPa. We note that the PEG chains are in a semi-dilute regime since their volume fraction in water, $\bar{\Phi} = 0.032$, which is very close to the overlapping volume fraction, $\bar{\Phi}^* \simeq 0.034$. To our knowledge the only theoretical approach dealing with confined polymers in lyotropic lamellar phases has been proposed by Ligoure et al. [87]. However non adsorbing polymers have been considered, which is not the case of the present experimental situation, as it is known that PEG chains can adsorb at the SDS / water interface. This precludes any meaningful comparison for our experimental results.

It should also be stressed that the case of adsorbing polymers questions the validity of the additivity assumption of the contributions since the electrostatic part of the interaction potential must be affected. Indeed, when macromolecules adsorb at the membranes / aqueous solution interface, some segments of the chains may slot into the membrane between the polar heads inducing a rearrangement of the SDS and octanol molecules within the bilayers. As a consequence the distribution of the charges is likely to be affected, not only along the interface but also within the electrical double layer. Therefore the correlations in the positions of the counterions are changed and an inhomogeneous surface charge distribution may arise. These effects are non negligible as the experimental situation deals with highly charged interfaces. While the general picture is quite straightforward, namely the coupling between the electrostatics and polymer contributions to the interaction potential and thus to the elastic compressibility modulus, the microscopic features require closer scrutinity. In particular the density profile of the polymer chains within the aqueous interlayer spacing must be determined. Some insights have been inferred by investigating the dynamics of the PEG chains (see Chapter on Fluorescence Recovery after Photobleaching technique (FRAPP)) where our preliminary experimental results show that there are several diffusing polymer populations: there are chains that diffuse as quickly as is they were free in bulk, chains that appear as almost immobile, and chains that diffuse slowly with diffusion coefficients smaller by two or three orders of magnitude compared to the bulk one. This intermediate diffusing population, can be viewed as an exchanging population between the free polymer population (not adsorbed, in the middle of the aqueous interlayer spacing) and the adsorbed polymer population on the membrane interface (immobile fraction). Further experimental investigations are called for drawing definitive conclusions about all the aforementioned effects.

Considering the mesophase with $\Phi_m = 10$ wt. % and $C_p = 5$ wt. % the value of the compressibility modulus is 4.9 ± 1.8 kPa. This value seems much too weak compared with what was expected. Unfortunately, we noted some evolution of the mesophase sample

during few weeks of SFA measurements. This observation has called for caution, as the weak B measured value could result from the hydrolysis of SDS, which produces dodecanol and sodium hydrogen sulfate. This means that the system may have contained more alcohol and thus the compressibility modulus is reduced. Despite this frustrating observation, not allowing us to add another data point with confidence in the study of $\bar{B}$ as a function of polymer content, the result is nevertheless quite valuable. It shows that the alcohol content modifies (reduces) greatly the electrostatic contribution of the elastic compressibility modulus, since it increases the surface charge Σ in Eq. (6.6). This is in agreement with the X-ray scattering works of Roux et al. [110, 111] the presence of alcohol in surfactant membranes increase the undulation forces. There, the authors showed that the dilution of the lamellar phase with dodecane and with brine exhibit very similar behaviour: the electrostatic interactions between the membranes are short range and the undulation fluctuations dominates.

A final remark concerns the observation of avalanches phenomena. This was first observed by Herrmann et al., but the mechanism remains still not understood. Their origin may be found in the confinement of the macromolecules: the layer of confined polymer between the membranes may induce a stiffening of the stack by bridging two neighbouring membranes for example, or due to the topological defects (handles) in the mesophase. The avalanches phenomena is exciting and needs to be explored in more details.

Chapter 7

Conclusions

The effect of the incorporation of the adsorbing polymer PEG on the structural and elastic properties of lyotropic lamellar mesophases of the system SDS/octanol/water/PEG has been explored in the course of this thesis.

The deuterium solid state NMR technique was used to study the fluctuations of the membrane in the lamellar mesophases. Angular undulations have been obtained from the quadrupolar splitting, which was measured on NMR spectra by two methods. The additional spectrum simulations technique was developed for our system and used in order to extract the quadrupolar splitting. The bending elastic modulus κ of the membranes has been investigated along different dilutions lines of polymer. It is inferred from the measurement of quadrupolar splittings by deuterium solid state NMR of the perdeuterated cosurfactant molecule embedded in the membrane. We have shown that the bending elastic modulus of surfactant membranes increases upon addition of adsorbing polymer PEG. An increase of about 20 % is observed as soon as the regime becomes semi-diluted. While, the theoretical prediction of the mean-field theory is a decrease in the bending modulus. This may indicate that our experimental system does not meet the theoretical assumptions of available models. The main assumption in the theory is the homogeneous, nonpenetrating adsorption of the polymer onto the membranes. Note also that the NMR technique allows to extract κ almost independently of the knowledge of $\bar{B}$, the compressibility elastic modulus, which can be measured experimentally by the SFA technique.

Concerning the mesophases located in the most diluted part of the phase diagram (Φ_m = 10 wt. %) we have been able to interpret the biphasic behaviour in the NMR spectra by the presence of the spherulites of different sizes. The freeze-fracture electron microscopy study has confirmed the presence of onion-like structures and smaller unilamellar vesicles.

Using the Fluorescence Recovery after Photobleaching we obtained the self-diffusion coefficient of PEG chains in water as a function of polymer concentration. We obtained

a power-law dependence very close to the crossover regime. Concerning the lamellar mesophases we showed that about 50-70 % of PEG chains contribute to immobile fraction, which can be due to partially adsorbed polymer onto the membranes or/and polymers confined in the lamellar domains. The contrast intensity decay exhibits several diffusing polymer populations: one suggest that there are one population that diffuses about three times slower than the free polymer chains and two others populations that diffuse much more slowly. One may interpret the very slow populations as exchanging chains between the not adsorbed polymer population, which is present in the middle of the interlayer spacing and the adsorbed polymer population, which is immobile. The main difficulty in the work with lamellar mesophases was two-fold: one must obtain perfectly aligned membranes and secondly needs to separate different mobile fractions of PEG in the lamellar mesophase, which becomes more complicated if long range oscillations appear in the FRAPP signal. Therefore, a new set-up geometry was proposed in order to achieve a better alignment and to control the gap thickness of the confined sample using mica spacers of known thickness. Unfortunately the laser broke down the last year and by lack of money it has not been replaced yet. Therefore the results could not be completed during the framework of this Ph.D Thesis. Further experimental investigations are called for drawing definitive conclusions about all the aforementioned effects.

Direct measurements of the elastic compressibility modulus of the lamellar mesophases were also carried out. The main goal was to get insights into the effect of the polymer concentration in water on the elastic compressibility modulus of the membranes and to obtain the scaling law in the case of adsorbing polymer: $\bar{B} \sim C_p^{\alpha}$ (where α is unknown constant). The Chapter 6 of this thesis is a continuation of the work, which has been done by Herrmann L. et al. [55–57]. It has been shown that the polymer induces a priori a softening of the intermembranes interactions, as already observed on similar systems [48]. Also, the mechanism of avalanches phenomena, again observed, remains still not understood and needs to be explored in more details.

Polymer-doped lamellar phases are interesting objects of study, for fundamental issues as well as for practical applications. The polymer, which is confined in a lamellar mesophase induces many effects. The membranes are slightly thinned, the curvature fluctuations are effected by adsorption of the polymer chains at the membrane/water interface, some polymer-water pockets may even be created in between adjacent membranes, and likely the distribution of alcohol molecules along the surfactant interface is modified. In addition the dynamics of the polymer chains is slowed down upon confinement in the water layers. All these local effects combine for destabilizing the lamellar stack macroscopically and ultimately lead to the coexistence of two lamellar phases of different periodicities as observed in the phase diagram. This Ph.D Thesis work has shed some light into these destabilizing effects even if more work is called for getting a comprehensive understanding of the doped-polymer lamellar phase behaviour.

Appendix A

A.1 Small angle X-ray scattering results

In this Appendix the results of SAXS along the dilution lines at constant polymer amount are presented. Each of the 2D scattering patterns have the following dimensions: 0.33×0.33 Å^{-1}.

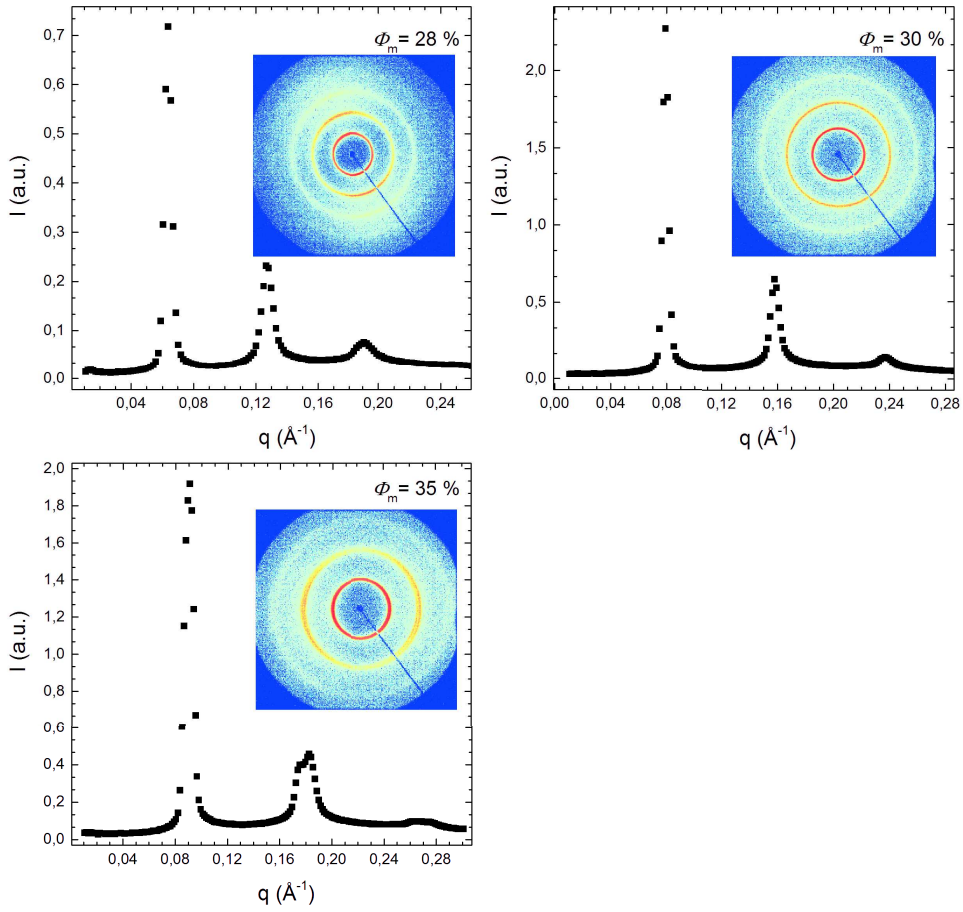

Figure A.1: The intensity scattered by the mesophases along the dilution line without polymer ($C_p = 0$ wt. %).

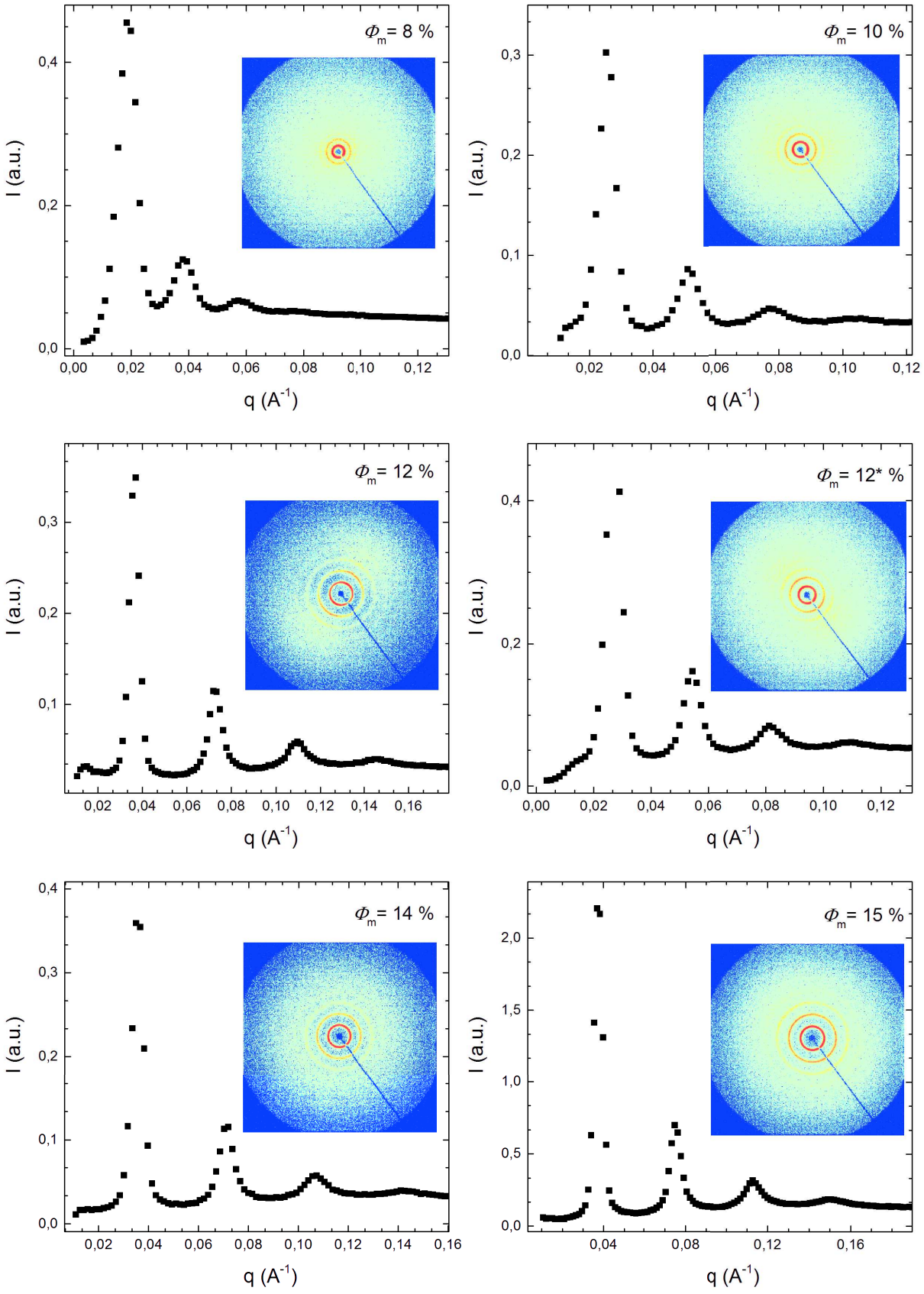

Figure A.2: The intensity scattered by the mesophases along the dilution line without polymer ($C_p = 0$ wt. %).

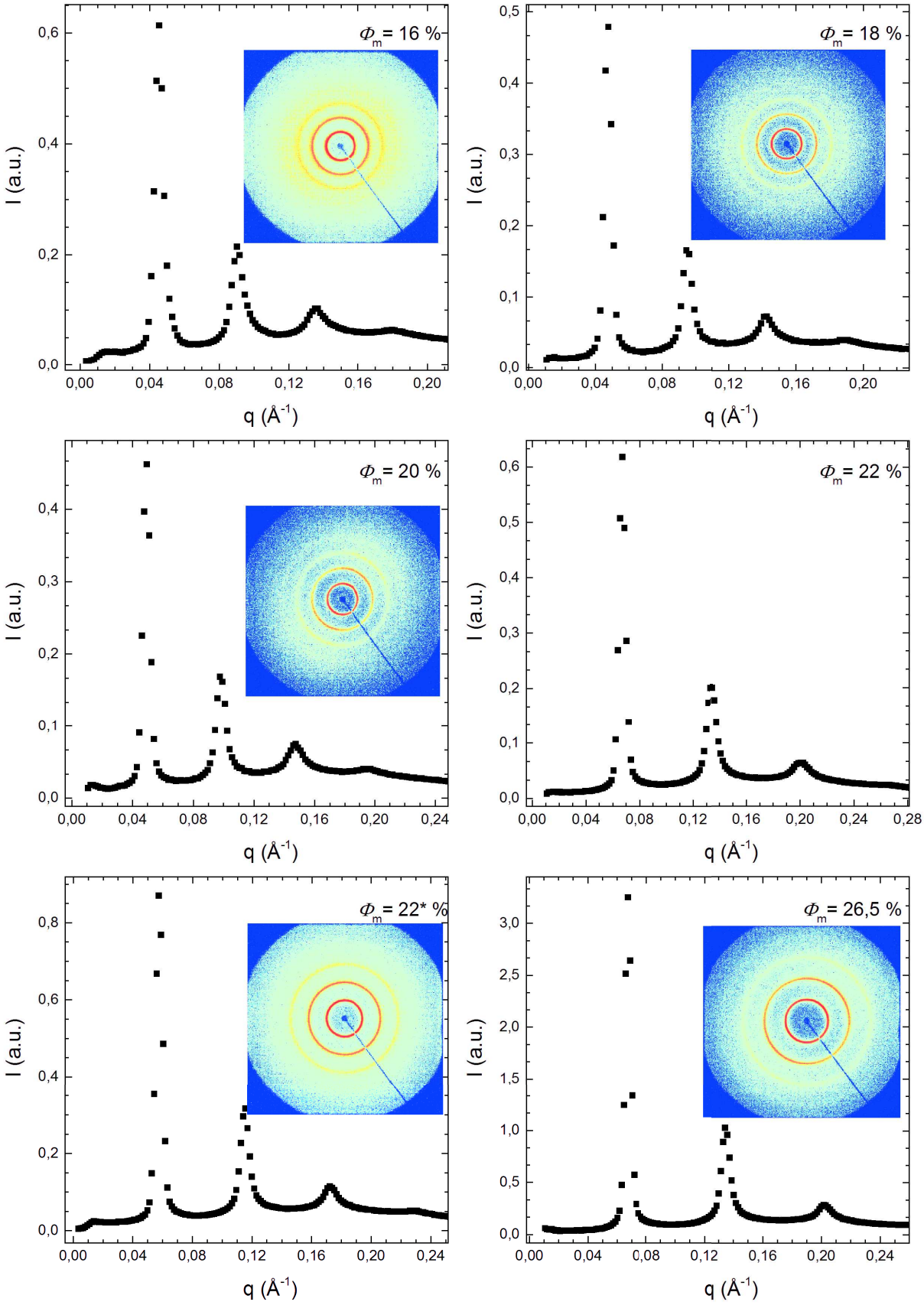

Figure A.3: The intensity scattered by the mesophases along the dilution line without polymer ($C_p = 0$ wt. %).

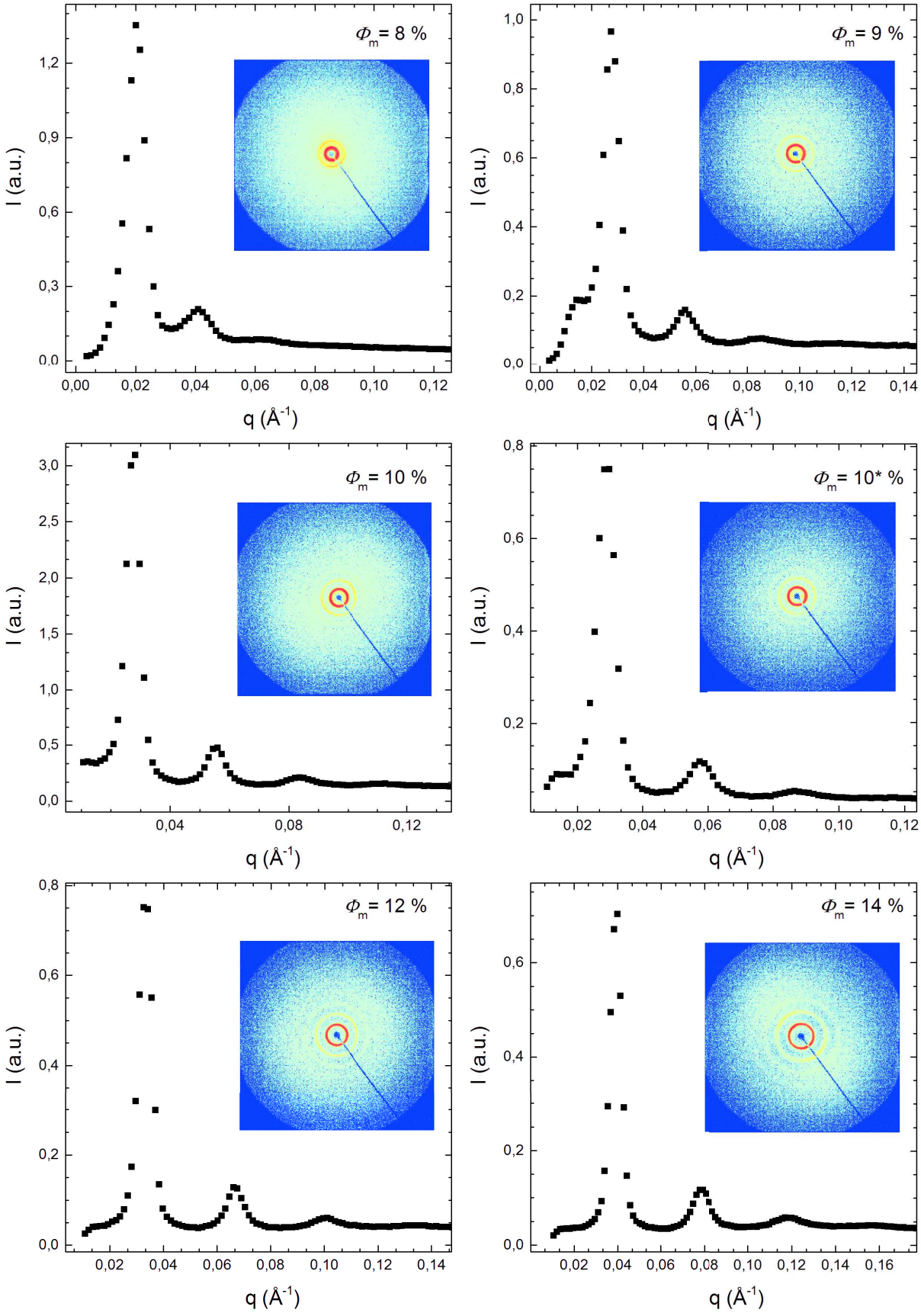

Figure A.4: The intensity scattered by the mesophases along the dilution line at constant polymer amount ($C_p = 3.8$ wt. %).

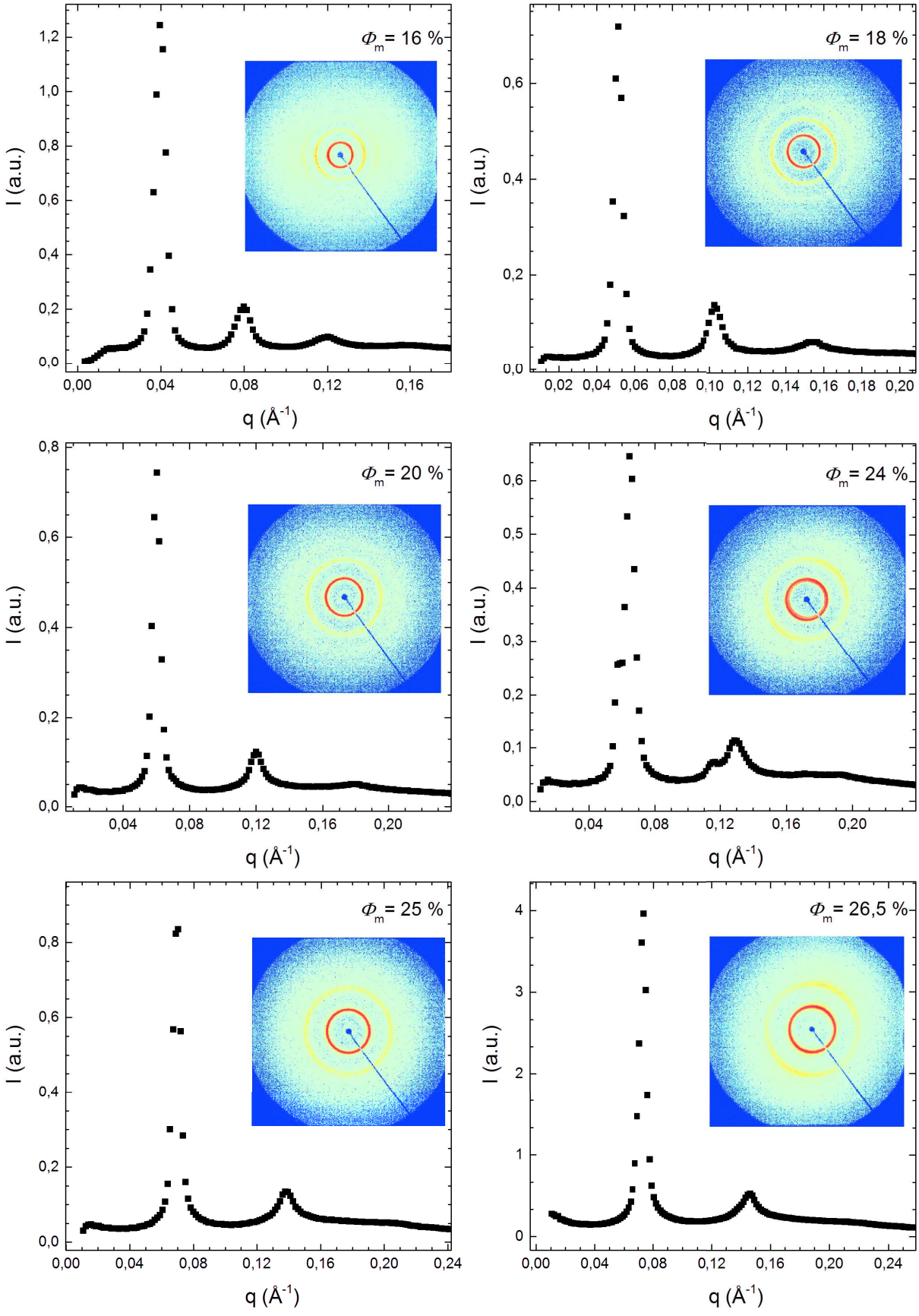

Figure A.5: The intensity scattered by the mesophases along the dilution line at constant polymer amount ($C_p = 3.8$ wt. %).

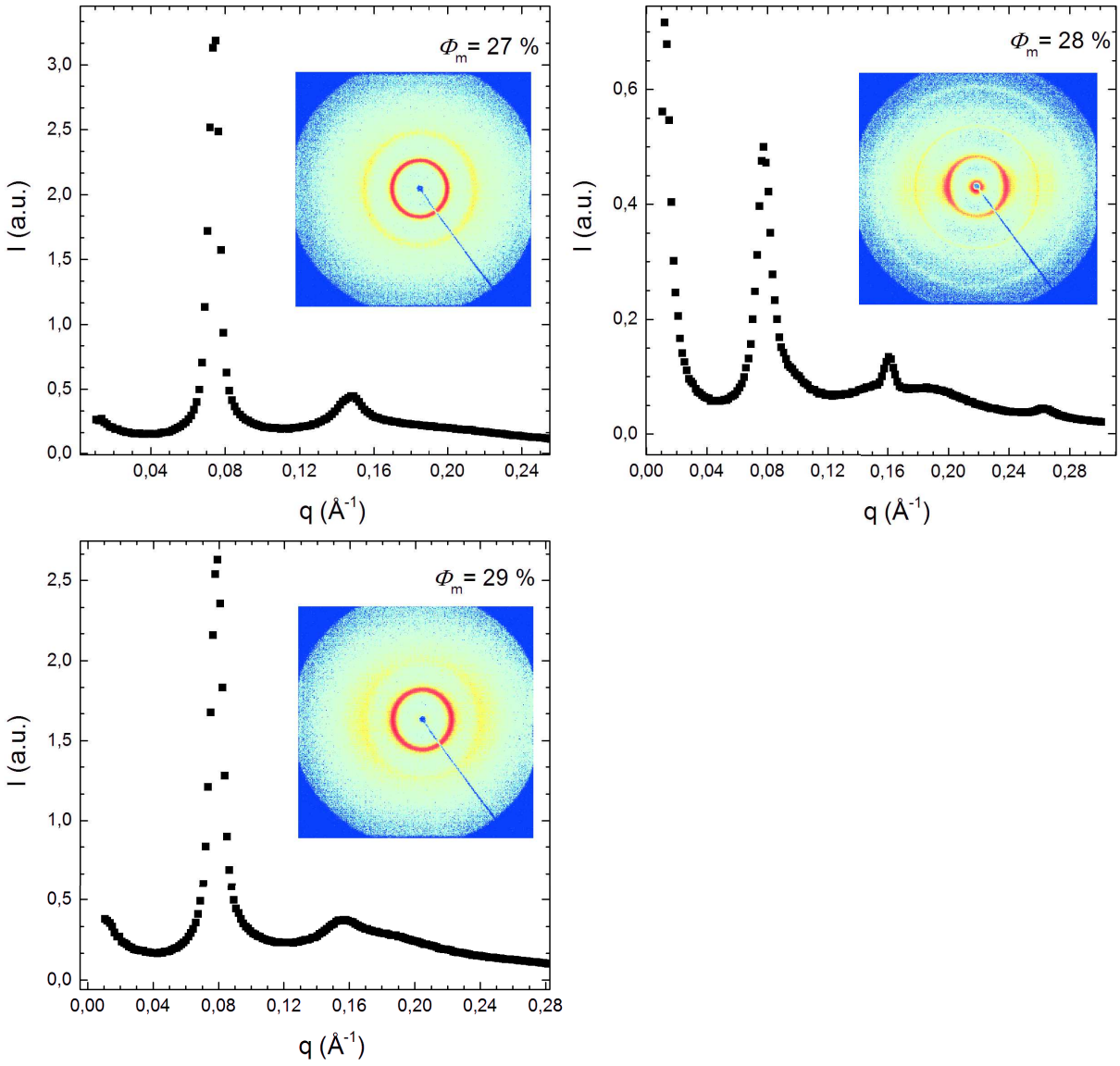

Figure A.6: The intensity scattered by the mesophases along the dilution line at constant polymer amount ($C_p = 3.8$ wt. %).

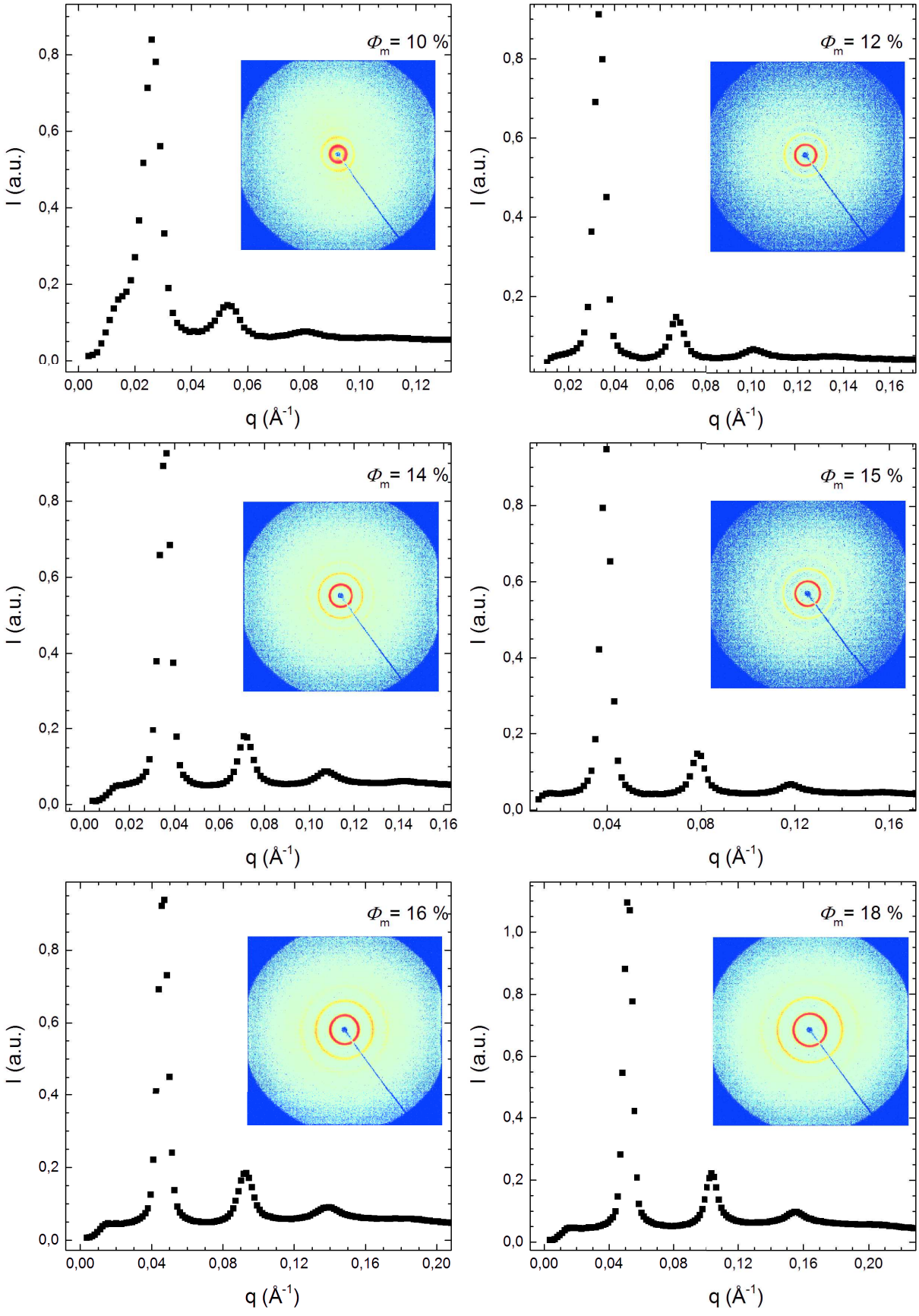

Figure A.7: The intensity scattered by the mesophases along the dilution line at constant polymer amount ($C_p = 5$ wt. %).

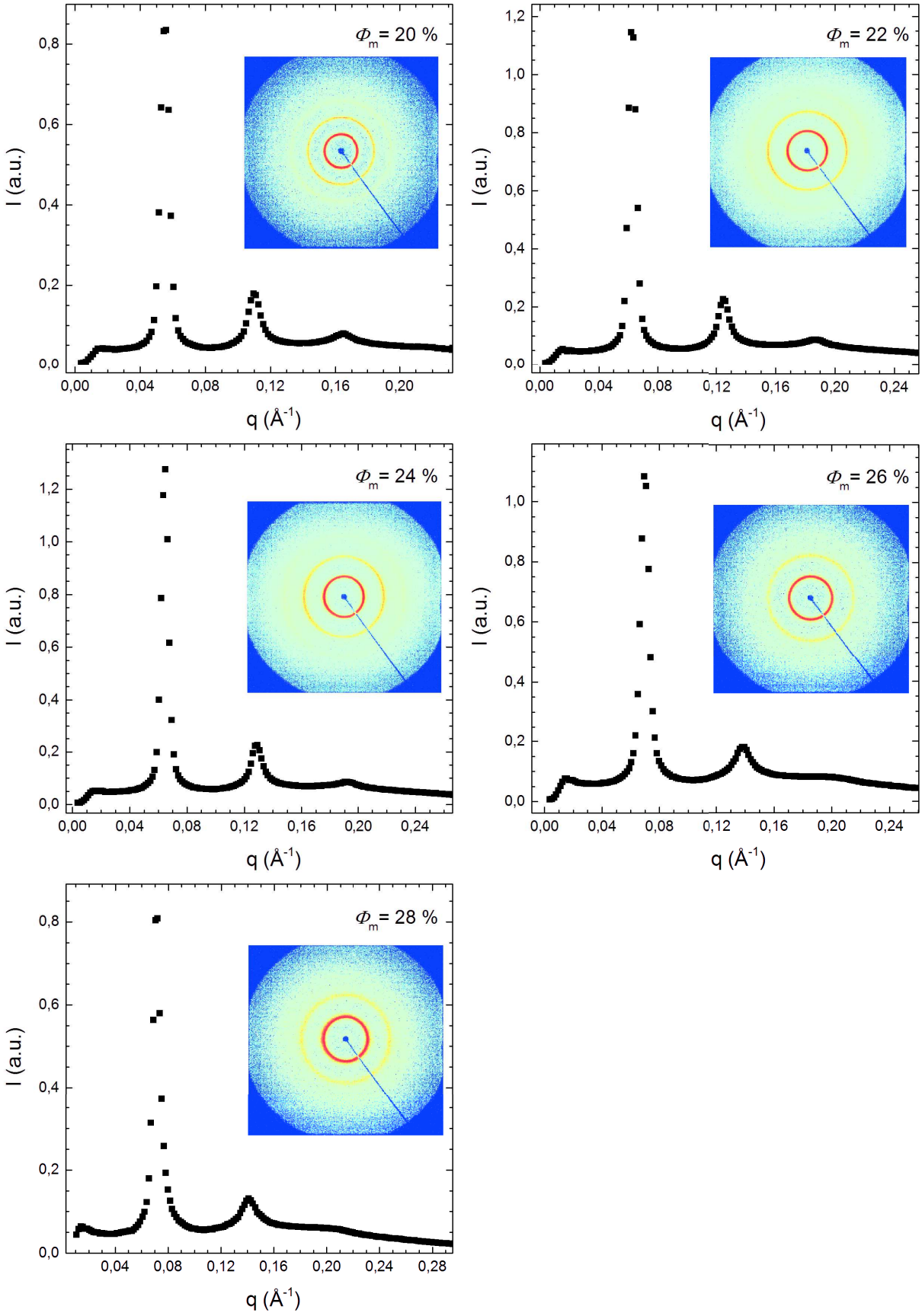

Figure A.8: The intensity scattered by the mesophases along the dilution line at constant polymer amount ($C_p = 5$ wt. %).

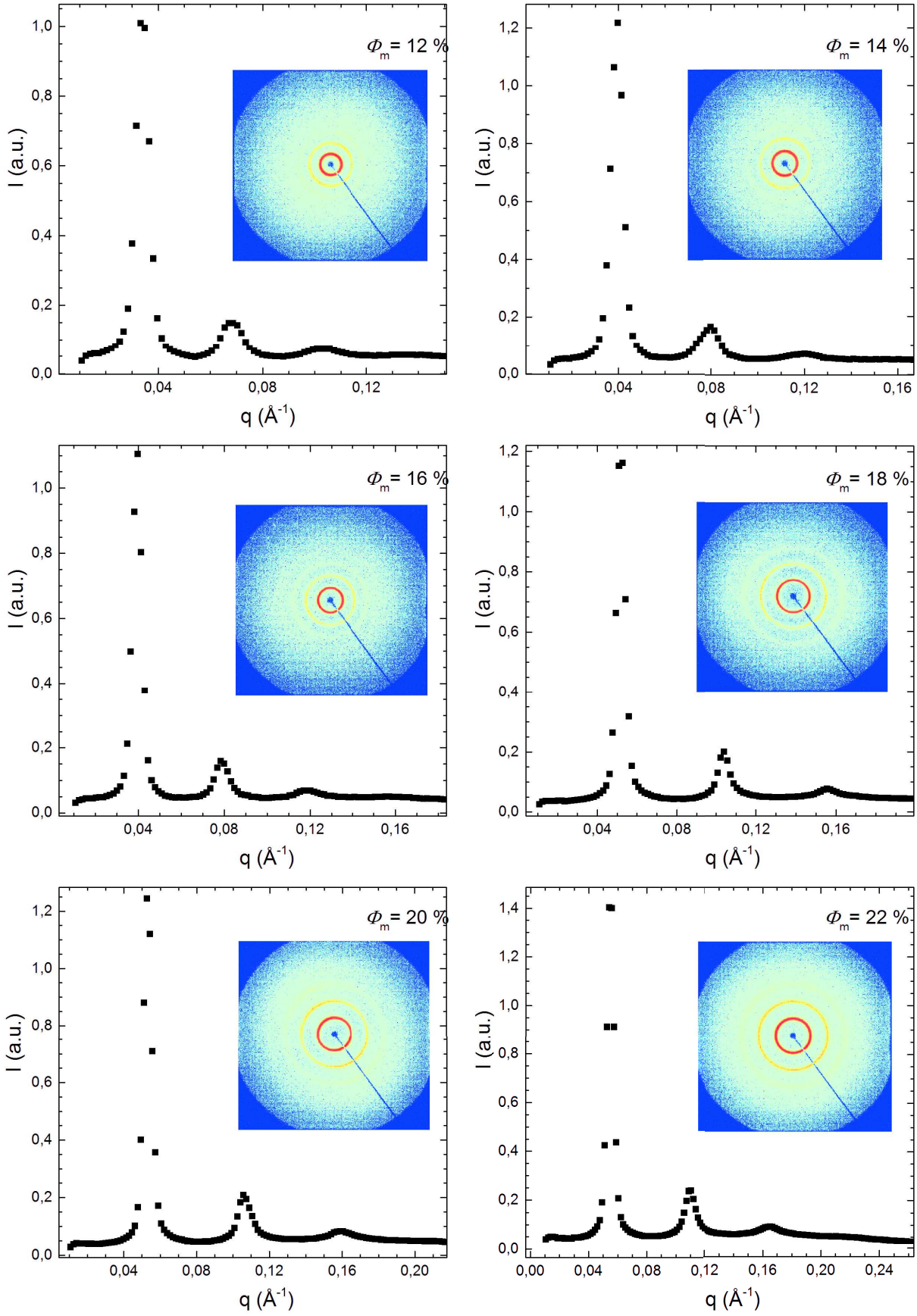

Figure A.9: The intensity scattered by the mesophases along the dilution line at constant polymer amount ($C_p = 7.5$ wt. %).

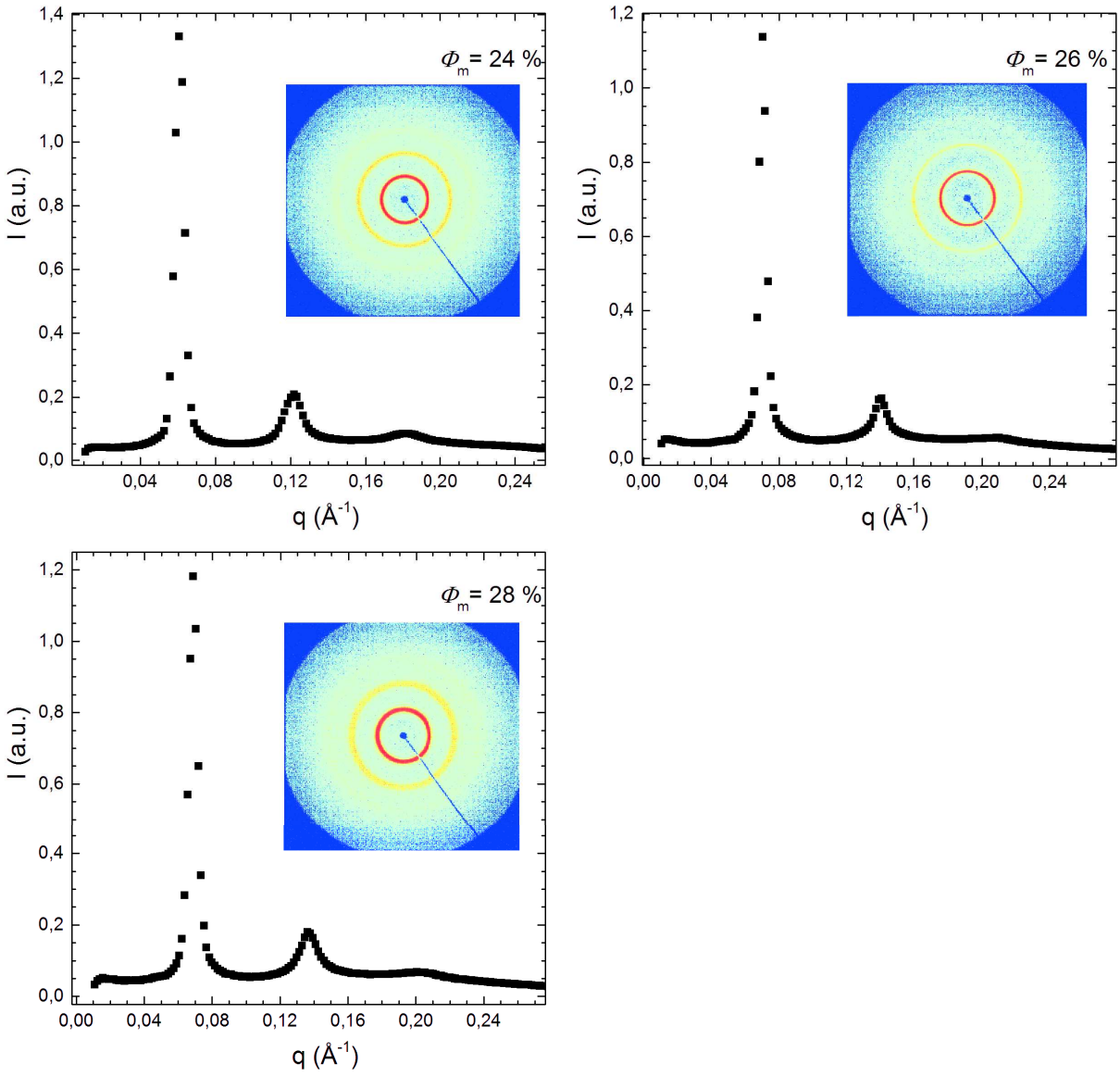

Figure A.10: The intensity scattered by the mesophases along the dilution line at constant polymer amount ($C_p = 7.5$ wt. %).

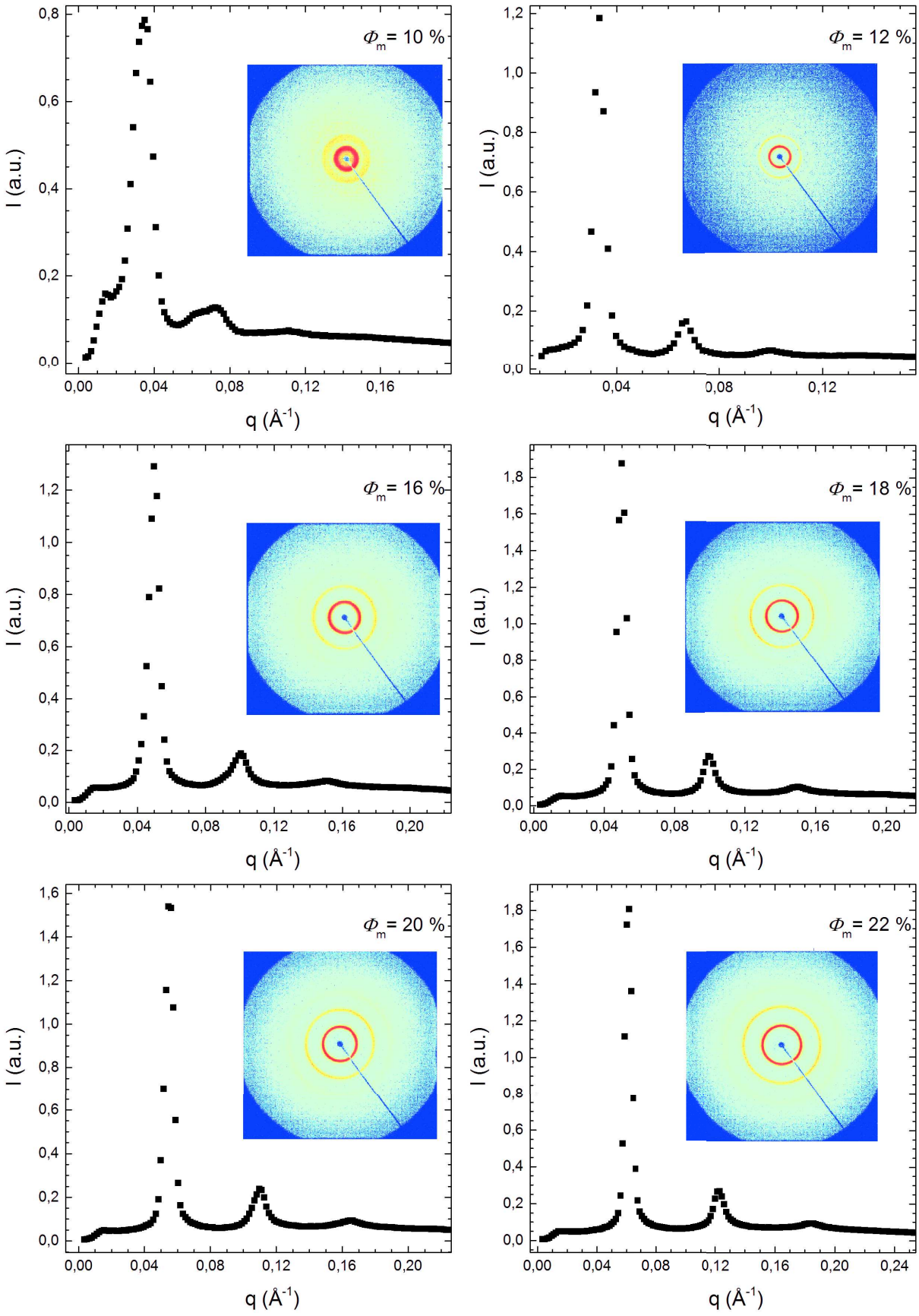

Figure A.11: The intensity scattered by the mesophases along the dilution line at constant polymer amount ($C_p = 10$ wt. %).

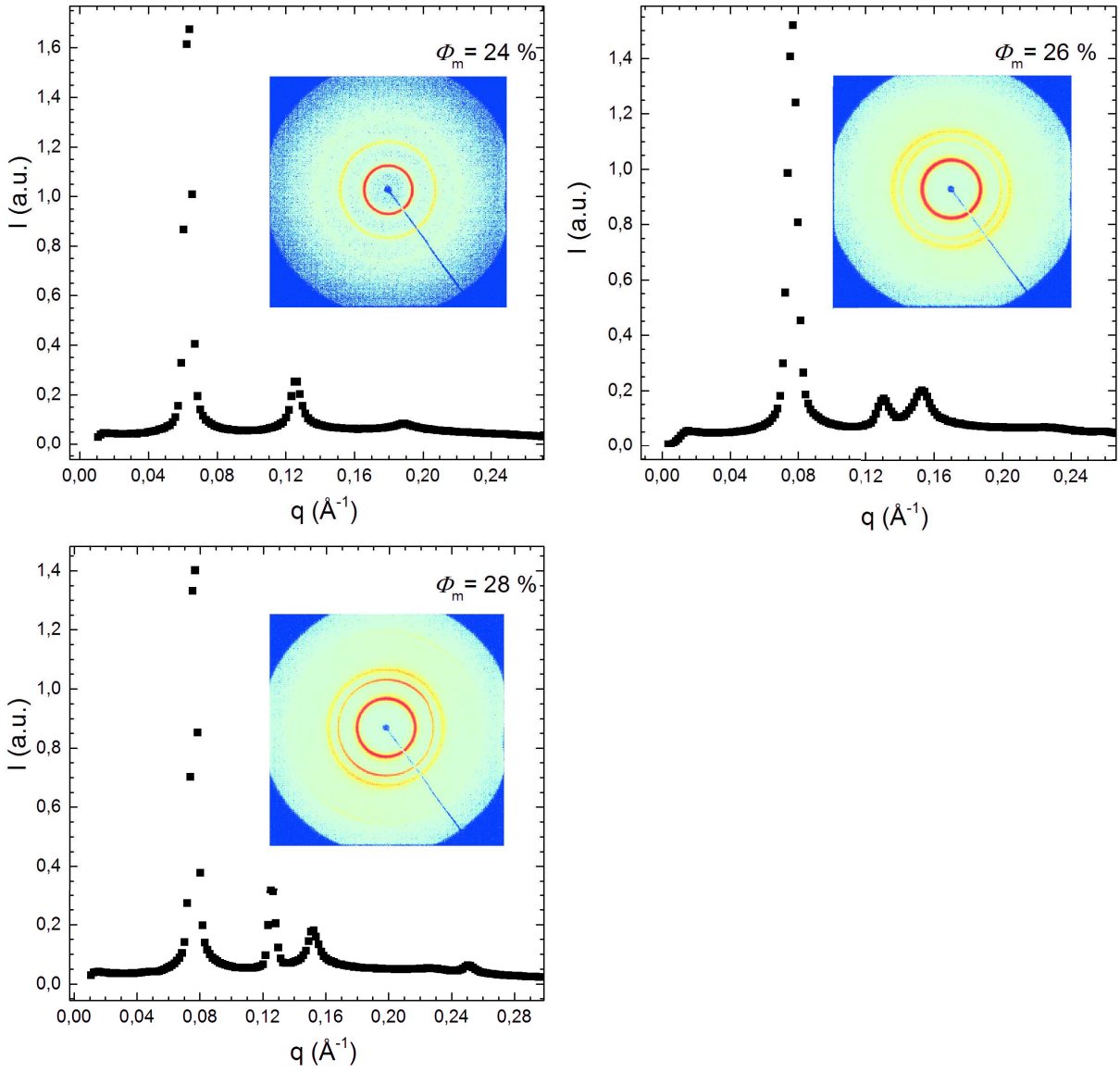

Figure A.12: The intensity scattered by the mesophases along the dilution line at constant polymer amount ($C_p = 10$ wt. %).

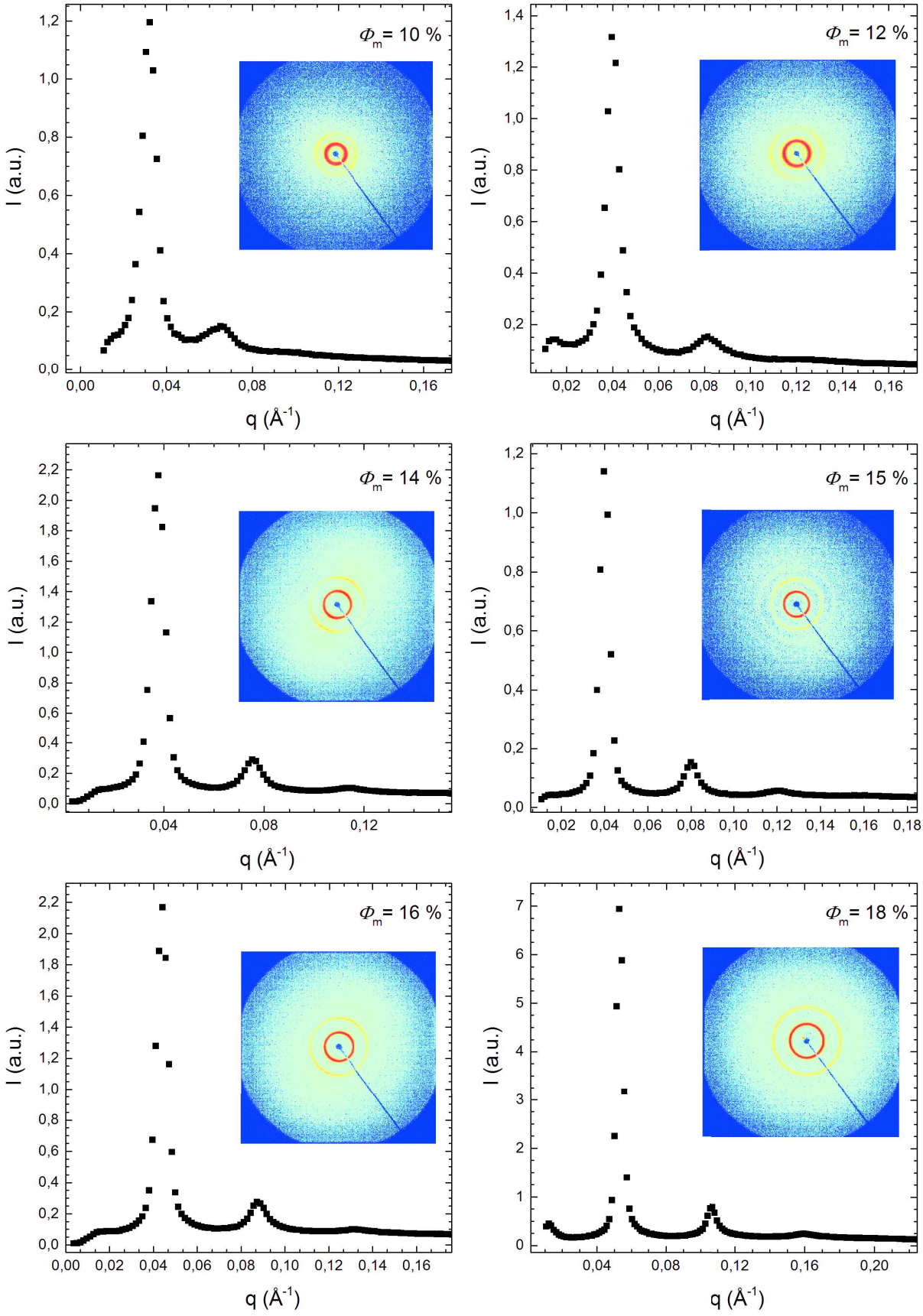

Figure A.13: The intensity scattered by the mesophases along the dilution line at constant polymer amount ($C_p = 15$ wt. %).

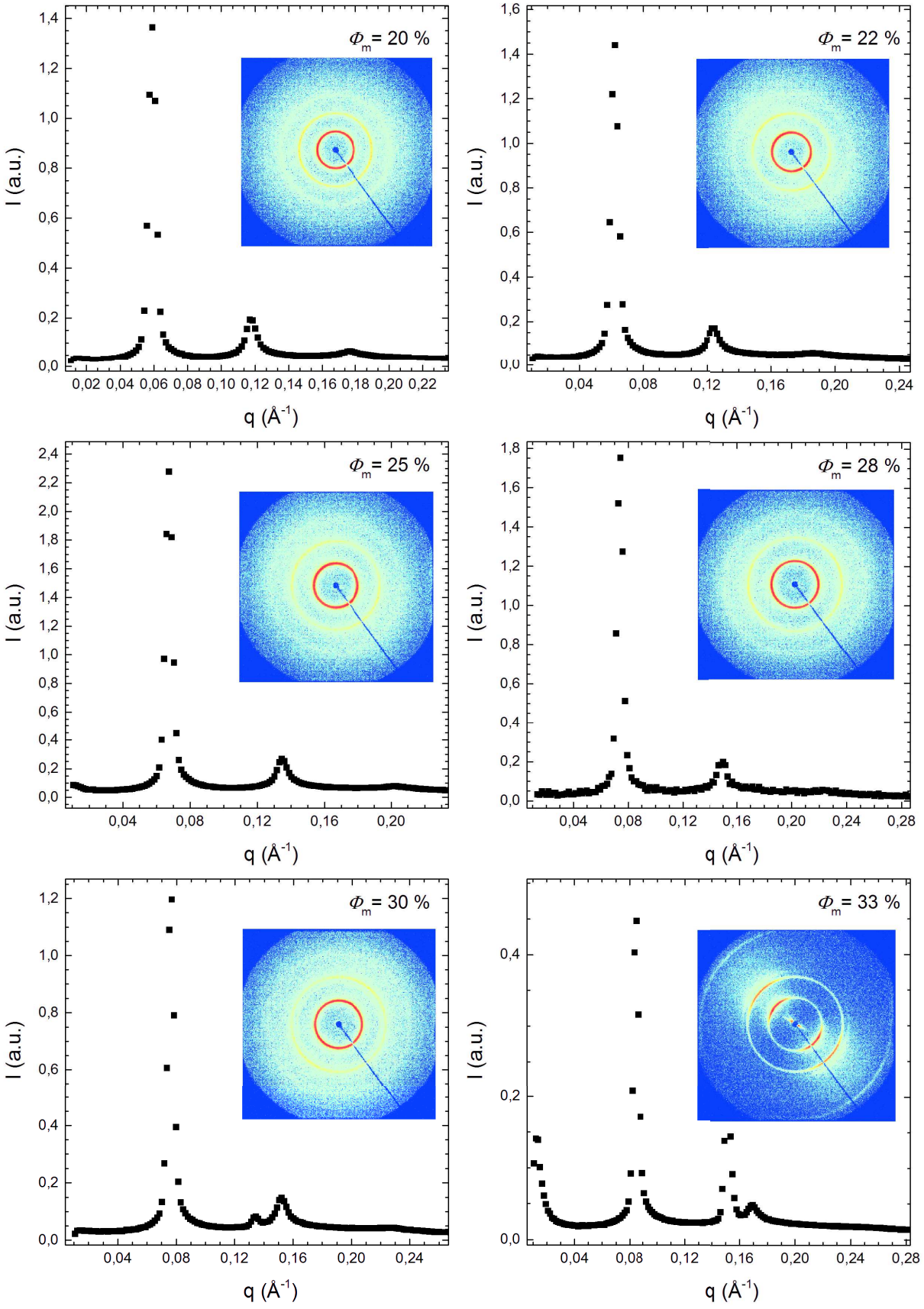

Figure A.14: The intensity scattered by the mesophases along the dilution line at constant polymer amount ($C_p = 15$ wt. %).

Bibliography

[1] *Surfactant Chemistry*, Dr. Julian EASTOE, Bristol UK, 2002.

[2] M. Allain, *Défauts dans des phases lamellaires lyotropes observés par cryofracture et microscopie électronique*, Journal de Physique, 46 (1985), pp. 225–234.

[3] D. A. Antelmi and P. Kékicheff, *Measurement of the compressibility modulus in a lyotropic lamellar phase stabilized by undulation forces*, Journal of Physical Chemistry B, 101 (1997), pp. 8169–8179.

[4] D. A. Antelmi, P. Kékicheff, and P. Richetti, *Confinement-induced sponge to lamellar phase transition*, Langmuir, (1999), pp. 7774–7788.

[5] F. Auguste, P. Barois, L. Fredon, B. Clin, E. J. Dufourc, and a. M. Bellocq, *Flexibility of molecular films as determined by deuterium solid state NMR*, J. Phys. II France, 4 (1994), pp. 2197–2214.

[6] F. Auguste, J. P. Douliez, a. M. Bellocq, and a. J. Dufourc, *Evidence of Multilamellar Vesicles in the Lamellar Phase of an Electrostatic Lyotropic Ternary System. A Solid State 2H-NMR Freeze-Fracture Electron Mycroscopy*, Langmuir, 13 (1997), pp. 666–672.

[7] D. Axelrod, D. E. Koppel, J. Schlessinger, E. Elson, and W. W. Webb, *Mobility measurement by analysis of fluorescence photobleaching recovery kinetics*, Biophysical Journal, 16 (1976), pp. 1055–1069.

[8] J. C. Blackburn and Peter K. Kilpatrick, *Using Deuterium NMR Line Shapes To Analyze Lyotropic Liquid Crystalline Phase Transitions*, Langmuir, 8 (1992), pp. 1679–1687.

[9] E. M. Blokhuis, K. I. Skau, and J. B. Avalos, *Free energy formalism for polymer adsorption: Self-consistent field theory for weak adsorption*, The Journal of Chemical Physics, 119 (2003), pp. 3483–3494.

[10] N. Boden and S. A. Jones, *Solubilizate-Bilayer Interactions in Lamellar Mesophases*, in Nuclear Magnetic Resonance of Liquid Crystals, Springer Netherlands, Dordrecht, 1985, pp. 497–532.

[11] G. Bouglet and C. Ligoure, *Polymer-mediated interactions of fluid membranes in a lyotropic lamellar phase: a small angle x-ray and neutron scattering study*, The European Physical Journal B - Condensed Matter and Complex Systems, 9 (1999), pp. 137–147.

[12] G. Bouglet, C. Ligoure, a. Bellocq, E. Dufourc, and G. Mosser, *Bending moduli of a nonadsorbing-polymer-containing lyotropic lamellar phase: An experimental study*, 1998.

[13] M. Breidenich, R. Netz, and R. Lipowsky, *Adsorption of polymers anchored to membranes*, The European Physical Journal E, 5 (2001), pp. 403–414.

[14] J. T. Brooks and M. E. Cates, *The role of added polymer in dilute lamellar surfactant phases*, The Journal of Chemical Physics, 99 (1993), pp. 5467–5480.

[15] J. T. Brooks, C. M. Marques, and M. E. Cates, *Role of Adsorbed Polymer in Bilayer Elasticity*, Europhysics Letters, 14 (1991), pp. 713–718.

[16] ——, *The effect of adsorbed polymer on the elastic moduli of surfactant bilayers*, J. Phys. II France, 1 (1991), pp. 673–690.

[17] B. Cabane, *Structure of some polymer-detergent aggregates in water*, The Journal of Physical Chemistry, 81 (1977), pp. 1639–1645.

[18] B. Cabane and R. Duplessix, *Organiztion of surfactant micelles adsorbed on a polymer molecule in water: a neutron scattering study*, Journal de Physique, 43 (1982), pp. 1529–1542.

[19] A. Caillé, *Remarks on the Scattering of X-Rays by A-Type Smectics*, C.R. Seances Acad. Sci., Ser. B, 274 (1972), pp. 891–893.

[20] A. A. Carrington and A. D. McLachlan, *Introduction to magnetic resonance : with applications to chemistry and chemical physics*, London : Chapman and Hall [etc.], 1979.

[21] J. Charvolin, P. Manneville, and B. Deloche, *Magnetic resonance of perdeuterated potassium laurate in oriented soap-water multilayers*, Chemical Physics Letters, 23 (1973), pp. 345–348.

[22] M. Clauzel, *Désorption forcé de tensioactifs à l'interface polymr̀e-eau*, PhD thesis, Universitè Louis Paster Starasbourg I, 2006.

[23] F. Clement and J. Joanny, *Curvature Elasticity of an Adsorbed Polymer Layer*, J. Phys. II France, 7 (1997), pp. 973–980.

[24] B. A. Coldren, H. Warriner, R. Van Zanten, J. A. Zasadzinski, and E. B. Sirota, *Lamellar gels and spontaneous vesicles in cationic surfactant mixtures.*, Langmuir, 22 (2006), p. 10296.

[25] D. Constantin and P. Oswald, *Diffusion coefficients in a lamellar lyotropic phase: evidence for defects connecting the surfactant structure*, Physical Review Letters, (2000).

[26] H. W. D. Evans, *The colloidal domain*, J. Wiley and Sons, 53 (1999), p. 1—87.

[27] S. Dai and K. C. Tam, *Isothermal Titration Calorimetric Studies on the Temperature Dependence of Binding Interactions between Poly (propylene glycol)s and Sodium Dodecyl Sulfate*, Langmuir, 20 (2004), pp. 2177–2183.

[28] M. Daoud and P.-G. De Gennes, *Statistics of macromolecular solutions trapped in small pores*, Journal de Physique, 38 (1977), pp. 85–93.

[29] J. Davis, *Deuterium magnetic resonance study of the gel and liquid crystalline phases of dipalmitoyl phosphatidylcholine*, Biophysical Journal, 27 (1979), pp. 339–358.

[30] J. Davis, K. Jeffrey, and M. Bloom, *Spin-lattice relaxation as a function of chain position in perdeuterated potassium palmitate*, Journal of Magnetic Resonance (1969), 29 (1978), pp. 191 – 199.

[31] J. H. Davis, *The description of membrane lipid conformation, order and dynamics by 2H-NMR.*, Biochimica et biophysica acta, 737 (1983), pp. 117–171.

[32] J. Davoust, P. F. Devaux, and L. Legerl, *Fringe pattern photobleaching, a new method for the measurement of transport coefficients of biological macromolecules*, The EMBO Journal, 1 (1982), pp. 1233–1238.

[33] P.-G. de. Gennes, *The Physics of Liquid Crystals*, Clarendon Press, Oxford, 1974.

[34] ——, *Scaling concepts in polymer physics*, Cornell University Press, 1979.

[35] P.-G. de Gennes, *Polymers at an interface; a simplified view*, Advances in Colloid and Interface Science, 27 (1987), pp. 189–209.

[36] P.-G. De Gennes, *Interactions between polymers and surfactants*, The Journal of Physical Chemistry, 94 (1990), pp. 8407–8413.

[37] P.-G. De Gennes and C. Taupin, *Microemulsions and the flexibility of oil/water interfaces*, The Journal of Physical Chemistry, 86 (1982), pp. 2294–2304.

[38] B. V. Derjaguin, *Theorie des anhaftens kleiner teilchen*, Kolloid Z., 69 (1934), pp. 155–164.

[39] B. V. Derjaguin, A. S. Titijevskaia, I. I. Abricossova, and A. D. Malkina, *Investigations of the forces of interaction of surfaces in different media and their application to the problem of colloid stability*, Discuss. Faraday Soc., 18 (1954), pp. 24–41.

[40] K. Devanand and J. C. Selser, *Asymptotic behavior and long-range interactions in aqueous solutions of poly (ethylene oxide)*, Macromolecules, 24 (1991), pp. 5943–5947.

[41] E. E. Dormidontova, *Role of competitive PEO-water and water-water hydrogen bonding in aqueous solution PEO behavior*, Macromolecules, 35 (2002), pp. 987–1001.

[42] M. J. Duer, *Introduction to Solid-State NMR Spectroscopy*, Blackwell Science, 2004.

[43] J. I. Escalante, M. Gradzielski, H. Hoffmann, and K. Mortensen, *Shear-induced transition of originally undisturbed lamellar phase to vesicle phase*, Langmuir, 16 (2000), pp. 8653–8663.

[44] M.-F. Ficheux, *Etude de systèmes mixtes polymère/tensioactif en phases organisées: diagrammes de phases et interactions*, PhD thesis, Université Bordeaux I, 1995.

[45] M.-F. Ficheux, a. M. Bellocq, and F. Nallet, *Experimental Study of a Lyotropic Lamellar Phase Swollen with Polymer Solutions*, Journal de Physique II, 5 (1995), pp. 823–834.

[46] M.-F. Ficheux, A.-M. Bellocq, and F. Nallet, *Elastic properties of polymer-doped dilute lamellar phases: A small-angle neutron scattering study*, The European Physical Journal E, 4 (2001), pp. 315–326.

[47] E. Freyssingeas, *Diffusion du rayonnement par des phases de membranes: phases lamellaires, phases éponges*, PhD thesis, Université Bordeaux I, 1994.

[48] E. Freyssingeas, D. Antelmi, P. Kékicheff, P. Richetti, and A.-M. Bellocq, *Softening of the interactions between surfactant bilayers in a lamellar phase due to the presence of a polymer*, The European Physical Journal B, 9 (1999), pp. 123–136.

[49] J. C. Froberg and T. Ederth, *On the Possibility of Glue Contaminations in the Surface Force Apparatus*, Journal of Colloid and Interface Science, 217 (1999), pp. 215–217.

[50] J. C. Gilkey and L. A. Staehelin, *Advances in ultrarapid freezing for the preservation of cellular ultrastructure*, Journal of Electron Microscopy Technique, 3 (1986), pp. 177–210.

[51] A. Guinier, *X-ray Diffraction in Crystals, Imperfect Crystals, and Amorphous Bodies*, 1965.

[52] B. Hammouda, *Probing Nanoscale Structures - the SANS Toolbox*, 2009, ch. SANS from polymer solutions, p. 670.

[53] P. L. Hansen, J. A. Cohen, R. Podgornik, and V. A. Parsegian, *Osmotic Properties of Poly(Ethylene Glycols): Quantitative Features of Brush and Bulk Scaling Laws*, Biophysical Journal, 84 (2003), pp. 350–355.

[54] W. Helfrich, Naturforsch, 1973.

[55] L. Herrmann, *Polymères confinés dans des mésophases lamellaires lyotropes*, PhD thesis, Université de Strasbourg, 2013.

[56] L. Herrmann, A. Johner, and P. Kékicheff, *Interactions between Charged Lamellae in Aqueous Solution*, Physical Review Letters, 268302 (2014), pp. 1–5.

[57] L. Herrmann and P. Kékicheff, *Effect of Dissolved Polymer on the Elasticity and Plasticity of a Lyotropic Lamellar Mesophase*, Macromolecular Symposia, 359 (2016), pp. 88–103.

[58] M. Heuberger, G. Luengo, and J. Israelachvili, *Topographic Information from Multiple Beam Interferometry in the Surface Forces Apparatus*, Langmuir, 13 (1997), pp. 3839–3848.

[59] C. Hiergeist, V. A. Indrani, and R. Lipowsky, *Membranes with anchored polymers at the adsorption transition*, Europhysics Letters, 36 (1996), pp. 491–496.

[60] C. Hiergeist and R. Lipowsky, *Elastic Properties of Polymer-Decorated Membranes*, Journal de Physique II, 6 (1996), pp. 1465–1481.

[61] K. Holmberg, B. Jönsson, B. Kronberg, and B. Lindman, *Surfactants and Polymers in Aqueous Solution*, John Wiley & Sons, Ltd, 2003.

[62] R. Iñiguez-Palomares, H. Acuña-Campa, and A. Maldonado, *Effect of polymer on the elasticity of surfactant membranes: A light scattering study*, Physical Review E, 84 (2011), pp. 1–6.

[63] R. Íñiguez-Palomares and A. Maldonado, *Topology change by screening the electrostatic interactions in a polymer-surfactant system*, Colloid and Polymer Science, 287 (2009), pp. 1475–1479.

[64] H. C. Ishikawa-Ankerhold, R. Ankerhold, and G. P. C. Drummen, *Advanced fluorescence microscopy techniques - FRAP, FLIP, FLAP, FRET and FLIM*, Molecules, 17 (2012), pp. 4047–4132.

[65] J. Israelachvili, *Thin film studies using multiple-beam interferometry*, Journal of Colloid and Interface Science, 44 (1973), pp. 259–272.

[66] J. Israelachvili, *The different faces of poly(ethylene glycol)*, Proc. Natl. Acad. Sci., 94 (1997), pp. 8378–8379.

[67] J. N. Israelachvili, *Intermolecular and surface forces*, Academic Press, 1985.

[68] W. Janke, H. Kleinert, and M. Meinhard, *Monte carlo study of a stack of self-avoiding surfaces with extrinsic curvature stiffness*, Phys. Lett. B, (1989), pp. 525–529.

[69] I. Javierre, *Polymère confiné en phases de membranes: influences sur la stabilité, la structure et la dynamique*, PhD thesis, Université Bordeaux I, 1999.

[70] I. Javierre, A. M. Bellocq, and F. Nallet, *Effect of confinement of a polymer on the phase behavior of ternary and quaternary lyotropic mixtures*, Langmuir, 17 (2001), pp. 5417–5425.

[71] L. Jourdainne, S. Lecuyer, Y. Arntz, C. Picart, P. Schaaf, B. Senger, J. C. Voegel, P. Lavalle, and T. Charitat, *Dynamics of poly(L-lysine) in hyaluronic acid/poly(L-lysine)multilayer films studied by fluorescence recovery after pattern photobleaching*, Langmuir, 24 (2008), pp. 7842–7847.

[72] P. Kékicheff, *Des cylindres aux bicouches : étude structurale des transformations de phase dans un cristal liquide lyotrope*, PhD thesis, Université Paris-Sud, 1987.

[73] ——, *Phase diagram of sodium dodecyl sulfate-water system*, Journal of Colloid and Interface Science, 131 (1989), pp. 133–152.

[74] P. Kékicheff, B. Cabane, and M. Rawiso, *Macromolecules dissolved in a lamellar lyotropic mesophase*, Journal of Colloid and Interface Science, 102 (1984), pp. 51–70.

[75] P. Kékicheff and H. Christenson, *Forces measured in a swollen lyotropic lamellar mesophase confined between solid surfaces*, Physical review letters, 63 (1989), p. 2823.

[76] Y. Kim and W. Sung, *Membrane curvature induced by polymer adsorption*, Physical Review E, 63 (2001), p. 041910.

[77] G. Kindlmann, *Superquadric Tensor Glyphs*, The Eurographics Association, (2004).

[78] M. Kléman, *Lamellar Lyotropic Phases: Rheology, Defects*, in Physics of Amphiphilic Layers, Proceedings of the Workshop, Les Houches, France February 10–19, 1987, pp. 164–170.

[79] A. Kolate, D. Baradia, S. Patil, I. Vhora, G. Kore, and A. Misra, *Peg — a versatile conjugating ligand for drugs and drug delivery systems*, Journal of Controlled Release, 192 (2014), pp. 67 – 81.

[80] F. Krafft and D. B. G. Berichte, *Ueber die krystallisationsbedingungen colloïdaler salzlösungen*, Berichte der deutschen chemischen Gesellschaft, 32 (1899), pp. 1596–1608.

[81] I. Kriuchevskyi, *Diffusion of confined polymers in lyotropic lamellar mesophases*, master's thesis, Université de Strasbourg, 2004.

[82] L. Porcar, J. Marignan, C. Ligoure, *Effect of a nonadsorbing polymer on the stability of a two-solvent lamellar phase: Experimental and theoretical study of critical points of lamellar/lamellar phase separations.*

[83] O. D. Lavrentovich, *Defects in Liquid Crystals: Surface and Interfacial Anchoring Effects*, in Patterns of Symmetry Breaking, Springer Netherlands, Dordrecht, 2003, pp. 161–195.

[84] J. H. Lee, H. B. Lee, and J. D. Andrade, *Blood compatibility of polyethylene oxide surfaces*, Progress in Polymer Science, 20 (1995), pp. 1043–1079.

[85] S. Leikin, V. A. Parsegian, D. C. Rau, and R. P. Rand, *Hydration forces*, Annual Review of Physical Chemistry, 44 (1993), pp. 369–395.

[86] J. Li, M. Turesson, C. A. Haglund, B. Cabane, and M. Skepö, *Equation of state of PEG/PEO in good solvent. Comparison between a one-parameter EOS and experiments*, Polymer (United Kingdom), 80 (2015), pp. 205–213.

[87] C. Ligoure, G. Bouglet, and G. Porte, *Polymer induced phase separation in lyotropic smectics*, Physical Review Letters, 71 (1993), pp. 3600–3603.

[88] C. Ligoure, G. Bouglet, G. Porte, and O. Diat, *Smectic Compressibility of Polymer-Containing Lyotropic Lamellar Phases: An Experimental Tool to Study the Thermodynamics of Polymer Confinement*, Journal de Physique II, 7 (1997), pp. 473–491.

[89] B. Lindman and H. Wennerström, *Micelles. amphiphile aggregation in aqueous solution*, Topics in current chemistry, 87 (1980), p. 1—87.

[90] K. L. Linegar, A. E. Adeniran, A. F. Kostko, and M. A. Anisimov, *Hydrodynamic radius of polyethylene glycol in solution obtained by dynamic light scattering*, Colloid Journal, 72 (2010), pp. 279–281.

[91] R. Lipowsky, *Flexible membranes with anchored polymers*, Colloids and Surfaces A: Physicochemical and Engineering Aspects, 128 (1997), pp. 255–264.

[92] C. Loison, *Numerical Simulations of a Smectic Lamellar of Amphiphilic Molecules*, PhD thesis, Ecole Normale Supérieure de Lyon, 2003.

[93] I.-G. Marino, *Regularized inverse laplace transform.* `https://fr.mathworks.com/matlabcentral/fileexchange/6523-rilt`. Accessed April 27, 2017.

[94] D. Massiot, F. Fayon, M. Capron, I. King, S. Le Calvé, B. Alonso, J. O. Durand, B. Bujoli, Z. Gan, and G. Hoatson, *Modelling one- and two-dimensional solid-state NMR spectra*, Magnetic Resonance in Chemistry, 40 (2002), pp. 70–76.

[95] M. Maugey and a. M. Bellocq, *Effect of Added Salt and Poly (ethylene glycol) on the Phase Behavior of a Balanced AOT - Water - Oil System*, Langmuir, 15 (1999), pp. 8602–8608.

[96] M. Maugey and A. M. Bellocq, *Effect of adsorbed and anchored polymers on membrane flexibility: A light scattering study of sponge phases*, Langmuir, 17 (2001), pp. 6740–6742.

[97] S. A. McNelles, S. D. Knight, N. Janzen, J. F. Valliant, and A. Adronov, *Synthesis, radiolabeling, and in vivo imaging of pegylated high-generation polyester dendrimers*, Biomacromolecules, 16 (2015), pp. 3033–3041.

[98] P. Moreau, *Diffusion Moléculaire d'un dopant hydrosoluble dans une phase lamellaire lyotrope — transition smectique - cholestérique dans un mélange de molécules amphiphiles*, PhD thesis, Université de Bordeaux, 2004.

[99] F. Nallet, D. Roux, and J. Prost, *Dynamic light scattering study of dilute lamellar phases*, Phys. Rev. Lett., 62 (1989), pp. 276–279.

[100] F. Nallet, D. Roux, C. Quilliet, P. Fabre, and S. T. Milner, *Elasticity and hydrodynamic properties of "doped solvent" dilute lamellar phases*, Journal de Physique II France, 4 (1994), pp. 1477–1499.

[101] P. Oswald and P. Pieranski, *Smectic and Columnar Liquid Crystals: Concepts and Physical Properties Illustrated by Experiments*, New York: Taylor & Francis, Boca Raton, London, 2006.

[102] J. Pope, L. Walker, and D. Dubro, *On the ordering of N-alkane and N-alcohol solutes in phospholipid bilayer model membrane systems*, Chemistry and Physics of Lipids, 35 (1984), pp. 259–277.

[103] G. Porte, J. Appell, P. Bassereau, and J. Marignan, *Lα to L3 : a topology driven transition in phases of infinite fluid membranes*, Journal de Physique, 50 (1989), pp. 1335–1347.

[104] S. Provencher, *Contin*. `http://s-provencher.com/contin.shtml`. Accessed April 27, 2017.

[105] S. W. Provencher, *Inverse Problems in Polymer Characterization: Direct Analysis of Polydispersity with Photon Correlation Spectroscopy*, Die Makromolekulare Chemie, 180 (1979), pp. 201–209.

[106] E. Z. Radlinska, T. Gulik-Krzywicki, F. Lafuma, D. Langevin, W. Urbach, C. E. Williams, and R. Ober, *Polymer Confinement in Surfactant Bilayers of a Lyotropic Lamellar Phase*, Physical Review Letters, 74 (1995), pp. 4237–4240.

[107] P. Richetti, P. Kékicheff, and P. Barois, *Measurement of the Layer Compressibility Modulus of a Lamellar Mesophase with a Surface Forces Apparatus*, Journal de Physique II, 5 (1995), pp. 1129–1154.

[108] P. Richetti, P. Kékicheff, J. Parker, and B. Ninham, *Measurement of the interactions between membranes in a stack*, Nature, 346 (1990), p. 252.

[109] D. Roux, F. Nallet, E. Freyssingeas, G. Porte, P. Bassereau, M. Skouri, and J. Marignan, *Excess area in fluctuating-membrane systems*, EPL (Europhysics Letters), 17 (1992), p. 575.

[110] D. Roux and C. Safinya, *A synchrotron X-ray study of competing undulation and electrostatic interlayer interactions in fluid multimembrane lyotropic phases*, Journal de Physique, 49 (1988), pp. 307–318.

[111] Roux, D. and Safinya, C.R., *A synchrotron x-ray study of competing undulation and electrostatic interlayer interactions in fluid multimembrane lyotropic phases*, J. Phys. France, 49 (1988), pp. 307–318.

[112] M. A. Sani, D. K. Weber, F. Delaglio, F. Separovic, and J. D. Gehman, *A practical implementation of de-Pake-ing via weighted Fourier transformation*, PeerJ, 1 (2013), p. 30.

[113] H. Schäfer, B. Mädler, and F. Volke, *De-Pake-ing of NMR Powder Spectra by Nonnegative Least-Squares Analysis with Tikhonov Regularization*, Journal of Magnetic Resonance Series A, 116 (1995), pp. 145–149.

[114] M. Schmutz and P. Mésini, *Cryo-fracture of self-assembled systems in organic solvent*, 2008.

[115] A. Seelig and J. Seelig, *The dynamic structure of fatty acyl chains in a phospholipid bilayer measured by deuterium magnetic resonance.*, Biochemistry, 13 (1974), pp. 4839–4845.

[116] J. Seelig, *Deuterium magnetic resonance: theory and application to lipid membranes*, Quarterly reviews of biophysics, 10 (1977), pp. 353–418.

[117] J. Seelig and W. Niederberger, *Deuterium-labeled lipids as structural probes in liquid crystalline bilayers. Deuterium magnetic resonance study*, Journal of the American Chemical Society, 96 (1974), pp. 2069–2072.

[118] N. J. Severs, *Freeze-fracture electron microscopy*, Nat. Protocols, 2 (2007), pp. 547–576.

[119] P. Sierro and D. Roux, *Structure of a Lyotropic Lamellar Phase under Shear*, Physical Review Letters, 78 (1997), pp. 24–27.

[120] M. Singh, R. Ober, and M. Kleman, *Polymer in a lyotropic lamellar system: an experimental study*, The Journal of Physical Chemistry, 97 (1993), pp. 11108–11114.

[121] K. Skau and E. Blokhuis, *Mean-field theory for polymer adsorption on curved surfaces*, The European Physical Journal E, 7 (2002), pp. 13–22.

[122] E. Sternin, M. Bloom, and A. L. Mackay, *De-pake-ing of NMR spectra*, Journal of Magnetic Resonance (1969), 55 (1983), pp. 274–282.

[123] R. Strey, R. Schomäcker, D. Roux, F. Nallet, and U. Olsson, *Dilute lamellar and l3 phases in the binary water $c_1 2 e_5$ system*, Journal of the Chemical Society, Faraday Transactions, 86 (1990), pp. 2253–2261.

[124] W. Sung and P. J. Park, *Polymer translocation through a pore in a membrane*, Phys. Rev. Lett., 77 (1996), pp. 783–786.

[125] S. R. Swift and L. Trinkle-Mulcahy, *Basic principles of FRAP , FLIM and FRET*, Proceedings of the Royal Microscopical Society, 39 (2004), pp. 3–10.

[126] J. L. Thewalt, *Deuterium NMR Studies of model membranes containing 1-alkanol anestetics or alpha-tocopherol*, PhD thesis, Simon Fraser University, 1979.

[127] R. L. Thurmond, G. Lindblom, and M. F. Brown, *Curvature, order, and dynamics of lipid hexagonal phases studied by deuterium nmr spectroscopy*, Biochemistry, 32 (1993), pp. 5394–5410.

[128] S. Tolansky, *Multiple-beam interferometry of surfaces and films*, Clarendon Press, 1948.

[129] D. Topgaard, D. Bernin, V. Koch, and M. Nyde, *Multi-Scale Characterization of Lyotropic Liquid Crystals Using 2H and Diffusion MRI with Spatial Resolution in Three Dimensions*, PLoS ONE, 9 (2014), pp. 1–11.

[130] N. Tsapis, R. Ober, A. Chaffotte, D. E. Warschawski, J. Everett, J. Kauffman, P. Kahn, M. Waks, and W. Urbach, *Modification of the elastic constants of a peptide-decorated lamellar phase*, Langmuir, 18 (2002), pp. 4384–4392.

[131] H. E. Warriner, P. Davidson, N. L. Slack, M. Schellhorn, P. Eiselt, S. H. J. Idziak, H.-W. Schmidt, and C. R. Safinya, *Lamellar biogels comprising fluid membranes with a newly synthesized class of polyethylene glycol-surfactants*, Journal of Chemical Physics, 107 (1997), pp. 3707–3722.

[132] H. E. Warriner, S. L. Keller, S. H. J. Idziak, N. L. Slack, P. Davidson, J. A. Zasadzinski, and C. R. Safinya, *The Influence of Polymer Molecular Weight in Lamellar Gels Based on PEG-Lipids*, Biophysical journal, 75 (1998), pp. 272–293.

[133] W. D. Wheeler, *Processing nmr data: Window functions*, tech. report, University of Wyoming, 2010.

[134] Wikipedia, *Mellin inversion theorem — wikipedia, the free encyclopedia*. `https://en.wikipedia.org/w/index.php?Mellin_inversion_theorem&oldid=710434256`. Accessed April 27, 2017.

[135] E. S. Wu, K. Jacobson, and D. Papahadjopoulos, *Lateral diffusion in phospholipid multibilayers measured by fluorescence recovery after photobleaching.*, Biochemistry, 16 (1977), pp. 3936–3941.

[136] B. S. Yang, J. Lal, P. Richetti, C. M. Marques, W. B. Russel, and R. K. Prud'homme, *Interaction of hydrophobically modified polymers and surfactant lamellar phase*, Langmuir, 17 (2001), pp. 5834–5841.

Viktoriia MEKLESH

Effect of confined polymer on the properties of lyotropic lamellar mesophases

Résumé

Cette thèse porte sur l'effet de l'incorporation du polymère adsorbant polyéthylène glycol (PEG) sur les propriétés structurelles et élastiques des mésophases lamellaires lyotropes. En particulier, ces phases lamellaires dopées au polymère sont d'un grand intérêt pour la compréhension des interactions inter-membranaires médiées par la macromolécule. Dans un premier temps, le module élastique de courbure des membranes a été étudié le long de plusieurs lignes de dilution de polymère. Il a été obtenu à partir des mesures des couplages quadrupolaires par spectroscopie de résonance magnétique nucléaire (RMN) à l'état solide de deutérium des molécules de cotensioactif perdeuteré incorporée dans la membrane. En présence du polymère adsorbé, nous avons constaté que la valeur du module élastique de courbure augmentait d'environ 20% dès que la solution de polymère était semi-diluée. Deuxièmement, nous discutons le coefficient de diffusion du polymère dans l'eau et confiné dans la phase lamellaire. La structure des mésophases a été étudiée par diffusion aux petits angles par rayons X et par microscopie électronique après cryofracture. Finalement, les mesures directes du module de compressibilité des mésophases lamellaires ont également été réalisées.

Mots clés : phase lamellaire, structure, interactions, polymère, diffusion, sphérulites

Résumé en anglais

This thesis deals with the effect of the incorporation of the adsorbing polymer polyethylene glycole (PEG) on the structural and elastic properties of lyotropic lamellar mesophases. In particular, these polymer doped-lamellar phases are of great interest for understanding the intermembrane interactions mediated by the macromolecule. Firstly, the bending elastic modulus of the membranes has been investigated along several dilution lines of polymer. It was obtained from the measurements of quadrupolar splittings by deuterium solid state Nuclear Magnetic Resonance (NMR) spectroscopy of the perdeuterated cosurfactant molecule embedded in the membrane. In the presence of the adsorbed polymer the value of the bending elastic modulus was found to increase of about 20% as soon as the polymer solution becomes semi-diluted. Secondly, the diffusion coefficient of the polymer in water and confined in the lamellar phase is discussed. The structure of the mesophases was investigated by small angle X-ray scattering and freeze-fracture electon microscopy. Finally, the direct measurements of the compressibility modulus of the lamellar mesophases were also carried out.

Keywords : lamellar phase, structure, interactions, polymer, diffusion, spherulites